

HOMO- AND HETEROMETALLIC MANGANESE CLUSTERS: NEW METAL
ARCHITECTURES, SINGLE-MOLECULE MAGNETS, AND PHYSICAL PHENOMENA

By

CHRISTOS LAMPROPOULOS

A DISSERTATION PRESENTED TO THE GRADUATE SCHOOL
OF THE UNIVERSITY OF FLORIDA IN PARTIAL FULFILLMENT
OF THE REQUIREMENTS FOR THE DEGREE OF
DOCTOR OF PHILOSOPHY

UNIVERSITY OF FLORIDA

2009

© 2009 Christos Lampropoulos

To my parents Athanasios and Aggeliki

ACKNOWLEDGMENTS

First and foremost, I would like to thank my advisor, Professor George Christou, for his guidance, help, and understanding all these years. His imposing figure hoards an intriguing personality, and a mentor full of energy, ready to always pass his knowledge onto his students. His unique attitude about science always stimulates interesting discussions, facilitates independent creative thinking, and induces deeper understanding of the subject at hand. Also, I would like to acknowledge Dr. Benjamin Smith, Prof. Daniel R. Talham, Prof. Michael J. Scott, and Prof. Mark Meisel for serving as my graduate committee, for all their help, as well as for all the interesting and stimulating discussions. Special thanks go to professors Stephen O. Hill and Naresh D. Dalal for all the spectroscopic studies on $\text{Mn}_{12}\text{Bu}^t$, as well as working closely with me and Prof. Christou on several other projects, most of them included in this dissertation. I would also like to acknowledge Dr. Jon Lawrence, Saiti Datta, and Changyun Koo, from Prof. Hill's group, and Dr. Andrew Harter, from Prof. Dalal's group, for working on my samples; they were the people who covered my mind gaps with some interesting physics. I would also like to acknowledge Dr. Wolfgang Wernsdorfer for providing essential single crystal measurements on the Mn_{12} compound below 1.8 K using his micro-SQUID apparatus, and answering all my questions to help bring these results together. I would like to express my gratitude to Dr. Khalil A. Abboud, and all the staff of the Center for X-ray Crystallography at UF, as well as Dr. Anastasios J. Tassiopoulos, and Dr. Manolis J. Manos (University of Cyprus) for all the crystal structures, and the patience and time that the x-ray analysis requires.

I would like to thank the entire Christou group, past and present, for their friendship, and support, no matter how different we were. Special thanks go to Rashmi, Shreya, and Taketo for the fun discussions, and the development of lab-philosophy during coffee breaks, and hallway chatting. Also, my gratitude goes to Jenn who proof-read this document. During my time in UF I

made many friends, some of whom need special mention: my travel partners Heeshan “Grasshopper” Illangoon and Roberto Laos, as well as Konstantinos and Ninetta Efthymiou, and Angelo and Eleni Barboutis; they made life in Gainesville fun, and interesting, and I thank them for that. Additionally, my work was highly stimulated by two post-doctoral fellows that I had the pleasure to work with, and learn a lot from, Dr. Muralee Murugesu and Dr. Theocharis C. Stamatatos. Especially, I would like to acknowledge Theocharis for his unconditional friendship and support throughout my career, as well as the vast amount of information that he bombarded me with every day in the lab, during coffee breaks, and at home (since he was my roommate). At this point, I would like to express my gratitude to Prof. Spyros P. Perlepes, who visited us from Greece, and even though he stayed with us for only a couple of months, he was an inexhaustible source of information, inspiration, great stories, and positive energy.

Moving to the United States was a big vault for me, and I would like thank my family here, my uncle Peter, my aunt Stella, my cousins Vicky and Lena, as well as my aunt Kiki, for all their essential help especially at the beginning of my career, as well as for making the US a home away from home. Also, I would like to thank my dear Eva for caring about me, for being so understanding and sweet, for brightening my dark days, and making my life more beautiful. Finally, I thank my parents for all the support, unconditional love and patience throughout the years I have lived away from them, for always being there in every situation, every bad moment, as well as for every celebration in my life. This dissertation is dedicated to them for everything they have done for me, and for all the love they will continue to offer me in the years to come.

TABLE OF CONTENTS

| | <u>page</u> |
|---|-------------|
| ACKNOWLEDGMENTS..... | 4 |
| LIST OF TABLES..... | 10 |
| LIST OF FIGURES..... | 12 |
| LIST OF ABBREVIATIONS..... | 18 |
| ABSTRACT..... | 19 |
| CHAPTER | |
| 1 GENERAL INTRODUCTION..... | 21 |
| 2 A NEW DODECANUCLEAR SINGLE-MOLECULE MAGNET WITH AXIAL SYMMETRY: SYNTHESIS, AND PHYSICAL AND SPECTROSCOPIC CHARACTERIZATION..... | 41 |
| 2.1 Introduction..... | 41 |
| 2.2 Experimental Section..... | 46 |
| 2.2.1 Synthesis..... | 46 |
| 2.2.2 X-Ray Crystallography..... | 47 |
| 2.2.3 DC and AC Magnetometry..... | 47 |
| 2.2.4 High-Frequency Electron Paramagnetic Resonance (HF-EPR) Spectroscopy..... | 48 |
| 2.2.5 ⁵⁵ Mn Nuclear Magnetic Resonance (NMR) Spectroscopy..... | 49 |
| 2.2.6 Other Studies..... | 49 |
| 2.3 Results and Discussion..... | 50 |
| 2.3.1 Synthesis..... | 50 |
| 2.3.2 Description of Structure..... | 51 |
| 2.3.3 Magnetochemistry..... | 52 |
| 2.3.3.1 Direct current magnetic susceptibility studies..... | 52 |
| 2.3.3.2 Alternating current magnetic susceptibility studies..... | 54 |
| 2.3.3.3 Arrhenius plot using AC and DC data..... | 56 |
| 2.3.3.4 Hysteresis studies..... | 57 |
| 2.3.3.5 High-frequency EPR spectroscopy..... | 58 |
| 2.3.3.6 Single crystal ⁵⁵ Mn NMR spectroscopy..... | 64 |
| 2.4 Recent Evidence for Non-Linear Arrhenius Behavior in Single-molecule Magnets..... | 72 |
| 2.5 Conclusions..... | 77 |
| 3 NEW PENTA- AND HEXANUCLEAR MIXED-VALENT MANGANESE CLUSTERS FROM THE USE OF OXIMATO LIGANDS AND AZIDES..... | 97 |
| 3.1 Introduction..... | 97 |
| 3.2 Experimental Section..... | 99 |

| | |
|---|-----|
| 3.2.1 Syntheses..... | 99 |
| 3.2.1.1 [Mn ₆ O ₃ (N ₃) ₃ (mpko) ₆ (H ₂ O) ₃](ClO ₄) ₂ (5) | 99 |
| 3.2.1.2 [Mn ₆ O ₃ (N ₃) ₅ (mpko) ₆ (H ₂ O)]·4H ₂ O (6)..... | 100 |
| 3.2.1.3 [Mn ₅ O ₂ (OMe) ₂ (N ₃) ₃ (dapdo) ₃ (py) ₂]·py MeOH (7) | 101 |
| 3.2.1.4 [Mn ₅ O ₂ (N ₃) _{3.5} (O ₂ CMe)(dapdo) ₃ (py) _{2.5}](N ₃) _{0.5} (8)..... | 101 |
| 3.2.2 X-Ray Crystallography | 102 |
| 3.2.2.1 X-ray crystal structure of complex 5 | 103 |
| 3.2.2.2 X-ray crystal structure of complex 6 | 103 |
| 3.2.2.3 X-ray crystal structure of complex 7 | 103 |
| 3.2.2.4 X-ray crystal structure of complex 8 | 103 |
| 3.2.3 Other studies..... | 104 |
| 3.3 Results and Discussion | 104 |
| 3.3.1 Syntheses..... | 104 |
| 3.3.2 Description of Structures | 107 |
| 3.3.3 Magnetochemistry | 110 |
| 3.3.3.1 Direct current magnetic susceptibility studies | 110 |
| 3.3.3.2 Reduced magnetization studies..... | 112 |
| 3.3.3.3 Alternating current magnetic susceptibility studies..... | 113 |
| 3.4 Conclusions | 115 |
| | |
| 4 BUILDING UP THE SMALL FAMILY OF 3d/4f METAL COMPLEXES: HETERROMETALLIC HEXA, ENNEA, AND DECANUCLEAR Mn-Ce CLUSTERS . | 127 |
| 4.1 Introduction | 127 |
| 4.2 Experimental Section..... | 129 |
| 4.2.1 Syntheses..... | 129 |
| 4.2.1.1 [Ce ₆ Mn ₄ O ₁₂ (O ₂ CMe) ₁₀ (NO ₃) ₄ (py) ₄]·py·9MeCN (9 ·py·9MeCN). | 129 |
| 4.2.1.2 [Mn ₈ CeO ₈ (O ₂ CCH ₂ Bu ^t) ₁₂ (DMF) ₁₄]·1.5DMF (10 ·1.5DMF). | 130 |
| 4.2.1.3 [Ce ₂ Mn ₄ O ₂ (O ₂ CMe) ₆ (NO ₃) ₄ (hmp) ₄]·H ₂ O·6MeCN (11 ·H ₂ O·6MeCN). | 130 |
| 4.2.2 X-Ray Crystallography | 130 |
| 4.2.3 Other Studies | 132 |
| 4.3 Results and Discussion | 132 |
| 4.3.1 Syntheses..... | 132 |
| 4.3.2 Description of Structures | 136 |
| 4.3.1 X-ray crystal structure of complex 9 | 136 |
| 4.3.2 X-ray crystal structure of complex 10 | 137 |
| 4.3.3 X-ray crystal structure of complex 11 | 139 |
| 4.3.3 Magnetochemistry | 140 |
| 4.3.3.1 Direct current magnetic susceptibility studies | 140 |
| 4.3.3.2 Alternating current magnetic susceptibility studies..... | 144 |
| 4.4 Conclusions | 150 |

| | | |
|---------|--|-----|
| 5 | PROBING MAGNETIC INTERACTIONS WITH TRIANGULAR CLUSTERS: HOMO- AND HETERROMETALLIC OXIDE-CENTERED MANGANESE TRIANGLES | 158 |
| 5.1 | Introduction | 158 |
| 5.2 | Experimental | 161 |
| 5.2.1 | Syntheses..... | 161 |
| 5.2.1.1 | [NEt ₃ (CH ₂ Cl)] ₂ [Mn ₃ O(hmcH) ₃ (hmcH ₂) ₃] (13) | 161 |
| 5.2.1.2 | [MnGd ₂ O(O ₂ CPh) ₃ (O ₂ CMe)(dapdo)(dapdoH) ₂] (14)..... | 162 |
| 5.2.2 | X-Ray Crystallography | 162 |
| 5.2.3 | Other Studies | 163 |
| 5.3 | Results and Discussion | 164 |
| 5.3.1 | Syntheses..... | 164 |
| 5.3.2 | Description of Structures | 165 |
| 5.3.3 | Magnetochemistry | 166 |
| 5.3.3.1 | DC magnetic susceptibility of complex 13 | 166 |
| 5.3.3.2 | Reduced magnetization study of complex 13 | 168 |
| 5.3.3.3 | AC magnetic susceptibility of complex 13 | 168 |
| 5.3.3.4 | Magnetostructural correlation between 13 and other oxo-centered Mn ^{III} ₃ triangles | 169 |
| 5.3.3.2 | DC Magnetic susceptibility of complex 14 | 172 |
| 5.3.3.3 | AC Magnetic susceptibility of complex 14 | 174 |
| 5.3.3.4 | Theoretical analysis of the spin frustration in complex 14 | 174 |
| 5.4 | Conclusions | 176 |
| 6 | SYNTHESIS, MAGNETISM, AND HIGH-FIELD EPR SPECTROSCOPY OF A FAMILY OF MIXED-VALENT CUBOCTAHEDRAL Mn ₁₃ COMPLEXES WITH 1,8-NAPHTHALENEDICARBOXYLATE LIGANDS | 186 |
| 6.1 | Introduction | 186 |
| 6.2 | Experimental Section..... | 187 |
| 6.2.1 | Syntheses..... | 187 |
| 6.2.1.1 | [Mn ₁₃ O ₈ (OH) ₆ (ndc) ₆] (16) | 187 |
| 6.2.1.2 | [Mn ₁₃ O ₈ (OEt) ₅ (OH)(ndc) ₆] (17) | 188 |
| 6.2.1.3 | [Mn ₁₃ O ₈ (OEt) ₆ (O ₂ CPh) ₁₂] (18)..... | 188 |
| 6.2.1.4 | [Mn ₁₃ O ₈ (OMe) ₆ (ndc) ₆] (19)..... | 189 |
| 6.2.2 | X-ray Crystallography..... | 189 |
| 6.2.3 | Other Studies | 191 |
| 6.3 | Results and Discussion | 192 |
| 6.3.1 | Syntheses..... | 192 |
| 6.3.2 | Description of Structures | 193 |
| 6.3.3 | Structural Comparison of Complexes 16-18 | 196 |
| 6.3.4 | Magnetochemistry | 198 |
| 6.3.4.1 | DC Magnetic Susceptibility Studies on Complexes 16-19 | 198 |
| 6.3.4.2 | AC Magnetic Susceptibility Studies of Complexes 16-19 | 201 |
| 6.3.4.3 | Single-crystal, High-Field EPR Spectroscopy of Complex 16 | 202 |
| 6.4 | Conclusions | 204 |

APPENDIX

| | | |
|---|--|-----|
| A | LIST OF COMPOUNDS..... | 213 |
| B | VAN VLECK EQUATIONS | 214 |
| C | STRUCTURE AND MAGNETIC PROPERTIES OF COMPLEX 15 | 220 |
| D | X-RAY CRYSTALLOGRAPHY TABLES | 224 |
| E | BOND VALENCE SUM (BVS) CALCULATIONS | 236 |
| | LIST OF REFERENCES | 239 |
| | BIOGRAPHICAL SKETCH | 254 |

LIST OF TABLES

| <u>Table</u> | <u>page</u> |
|--|-------------|
| 2-1 ^{55}Mn NMR Peak parameters for 3 | 66 |
| 2-2 Variation of the calculated U'_{eff} and U''_{eff} for complex 3 ·MeOH..... | 75 |
| 3-1 Structural differences between complexes 5 and 6 | 108 |
| 4-1 Magnetostructural correlation between 10 and other CeMn_8 clusters with general formula $[\text{CeMn}_8\text{O}_{12}(\text{O}_2\text{CR})_{12}(\text{L})_4]$ | 148 |
| 4-2 Structural types, core descriptions, and ground state S values for heterometallic Mn-Ce clusters..... | 149 |
| 5-1 Magnetostructural correlation between complexes 13 and 15 | 170 |
| 6-1 Structural Comparison between Complexes 16 , 17 , and 18 | 197 |
| D-1 Crystallographic Data for 3 | 224 |
| D-2 Selected Bond Distances (Å) and Angles (deg) for 3 ·MeOH..... | 224 |
| D-3 Crystal Data and Structure Refinement Parameters for Complexes 5-8 | 225 |
| D-4 Selected bond distances (Å) and angles (°) for complex 5 | 226 |
| D-5 Selected bond distances (Å) and angles (°) for complex 6 | 227 |
| D-6 Selected bond distances (Å) and angles (°) for complex 7 | 227 |
| D-7 Selected bond distances (Å) and angles (°) for complex 8 | 228 |
| D-8 Crystal data and structure refinement parameters for complexes 9 , 10 , and 11 | 229 |
| D-9 Selected bond distances (Å) and angles (°) for complex 9 | 230 |
| D-10 Selected bond distances (Å) and angles (°) for complex 10 | 231 |
| D-11 Selected bond distances (Å) and angles (°) for complex 11 | 232 |
| D-12 Crystal Data and Structure Refinement Parameters for Complexes 13 and 14 | 232 |
| D-13 Selected Core Interatomic Distances (Å) and angles (°) for complex 13 | 233 |
| D-14 Selected Core Interatomic Distances (Å) and angles (°) for Complex 14 | 233 |
| D-15 Crystal Data and Structure Refinement Parameters for Complexes 16-18 | 234 |

| | | |
|------|---|-----|
| D-16 | Selected Core Interatomic Distances (Å) for Complex 16 . | 234 |
| D-17 | Selected Core Interatomic Distances (Å) for 17 . | 235 |
| D-18 | Selected bond distances (Å) and angles (deg) for 18 . | 235 |
| E-1 | Bond valence sum calculations for the Mn ions for complexes 5 and 6 . | 236 |
| E-2 | Bond valence sum calculations for the Mn ions for complexes 7 and 8 . | 236 |
| E-3 | Bond valence sum calculations and assignments for the Ce and Mn ions in 9 , 10 , and 11 . | 236 |
| E-4 | Bond valence sum calculations and assignments for the μ_3 -O ^a in complexes 9 , and 10 . | 237 |
| E-5 | BVS Calculations for the Mn ^a atoms of 13 and 14 . | 237 |
| E-6 | Bond valence sum calculations for the Mn ions for complexes 16 , 17 and 18 . | 237 |
| E-7 | Bond valence sum calculations for the μ_3 -O ^a ions for complex 16 . | 238 |

LIST OF FIGURES

| <u>Figure</u> | <u>page</u> |
|---------------|--|
| 1-1 | Representation of the different ways the magnetic field lines of flux change in the absence of a sample, in the presence of a diamagnetic sample, and in the presence of a paramagnetic sample 36 |
| 1-2 | Plot of the $\chi_M T$ product (χ_M is the molar susceptibility) vs. temperature 37 |
| 1-3 | Magnetic dipole arrangements in different types of materials 37 |
| 1-4 | Typical hysteresis loop of a magnet, where M is magnetization, H is the applied magnetic field and M_s is the saturation value of the magnetization 37 |
| 1-5 | ORTEP representation in Pov-Ray format showing the structure of the $[\text{Mn}_{12}\text{O}_{12}(\text{O}_2\text{CMe})_{16}(\text{H}_2\text{O})_4]$ complex 38 |
| 1-6 | ORTEP representation in Pov-Ray format of the metal core of a typical $[\text{Mn}_{12}\text{O}_{12}(\text{O}_2\text{CR})_{16}(\text{H}_2\text{O})_4]$ complex, showing the relative disposition of the JT elongation axes 38 |
| 1-7 | Representative plots of the potential energy barrier for an SMM 39 |
| 1-8 | In-phase (as $\chi_M' T$) and out-of-phase (as χ_M'') AC susceptibility signals for a dried, microcrystalline sample of $[\text{Mn}_{12}\text{O}_{12}(\text{O}_2\text{CR})_{16}(\text{H}_2\text{O})_4]$ 39 |
| 1-9 | Magnetization hysteresis loops for a typical $[\text{Mn}_{12}\text{O}_{12}(\text{O}_2\text{CR})_{16}(\text{H}_2\text{O})_4]$ complex in the 1.3-3.6 K temperature range at a 4 mT/s field sweep rate 40 |
| 1-10 | Schematic representation of the change in energy of m_s sublevels as the magnetic field is swept from zero to a non-zero value 40 |
| 2-1 | Representations of the structure of 1 79 |
| 2-2 | Magnetization (M) vs field of a single crystal of complex 1 at the indicated field sweep rate at 0.04 K 80 |
| 2-3 | Edge dislocation along the y axis with the extra plane y, z inserted at $z > 0$ 80 |
| 2-4 | ORTEP representation in PovRay format of the two-fold disorder of the MeCO_2H solvent molecules of crystallization in complex 1 81 |
| 2-5 | ORTEP representation in PovRay format of the hydrogen-bonding interaction in complex 1 81 |
| 2-6 | ORTEP representation in PovRay format of $[\text{Mn}_{12}\text{O}_{12}(\text{O}_2\text{CMe})_{16}(\text{H}_2\text{O})_4]$ and $[\text{Mn}_{12}\text{O}_{12}(\text{O}_2\text{CCH}_2\text{Br})_{16}(\text{H}_2\text{O})_4]$ 82 |

| | | |
|------|--|----|
| 2-7 | Packing diagram of $[\text{Mn}_{12}\text{O}_{12}(\text{O}_2\text{CCH}_2\text{Bu}^t)_{16}(\text{MeOH})_4] \cdot \text{MeOH}$ (3) with MeOH solvent molecules of crystallization..... | 82 |
| 2-8 | PovRay representations of the partially labeled core and a stereopair of complex 3 | 83 |
| 2-9 | Side view of complex 3 , emphasizing the disposition of the Jahn-Teller (JT) axes..... | 84 |
| 2-10 | Plot of $\chi_M T$ vs temperature for a dried, microcrystalline sample of complex 3 | 85 |
| 2-11 | Plot of $M/N\mu_B$ vs H/T for complex 3 | 85 |
| 2-12 | Two dimensional contour plot of the fitting error surface vs D and g for 3 | 86 |
| 2-13 | Plot of the in-phase (as $\chi_M' T$) and out-of-phase (χ_M'') AC susceptibility signals vs temperature for dried, microcrystalline complex 3 | 86 |
| 2-14 | Argand plot of m' vs m'' of dried crystals of 3 •2H ₂ O at 4.6 K | 87 |
| 2-15 | Plot of relaxation time (τ) vs $1/T$ for complex 3 using AC χ_M'' and DC magnetization decay data..... | 87 |
| 2-16 | Plot of the magnetization versus time decay data for crystals of complex 3 | 88 |
| 2-17 | Magnetization hysteresis loops for a single crystal of 3 | 88 |
| 2-18 | Temperature dependence of the easy-axis HFEP spectra obtained for complex 3 at a frequency of 336 GHz..... | 89 |
| 2-19 | Angle dependence of the hard-plane HFEP spectra obtained for complex 3 at 15 K and a color contour plot of the data..... | 90 |
| 2-20 | The full-width-at-half-maximum (FWHM) deduced from Gaussian fits to easy-axis HFEP data obtained for three different $S = 10$ SMMs for a range of frequencies | 91 |
| 2-21 | A comparison between the hard-plane HFEP spectra obtained for 1 and complex 3 , at 15 K and 51.5 GHz..... | 91 |
| 2-22 | Zero-field ⁵⁵ Mn spectrum of 3 | 92 |
| 2-23 | Line fits for the Mn(1), Mn(2) and Mn(3) resonances..... | 92 |
| 2-24 | Comparison of the line width and peak area of the Mn(2) peaks for 2 and 3 | 93 |
| 2-25 | Spin-Lattice relaxation rate (T_1^{-1}) of the Mn(1) peak for a single crystal of 3 down to He-3 temperatures | 93 |
| 2-26 | T_1^{-1} fits extended down to 100 mK..... | 94 |
| 2-27 | Plot of the natural logarithm of the magnetization relaxation rate vs $1/T$ for 3 •MeOH..... | 94 |

| | | |
|------|--|-----|
| 2-28 | Plot of the natural logarithm of the magnetization relaxation rate vs $1/T$ for 2 | 95 |
| 2-29 | The fit of all the data for 2 | 95 |
| 2-30 | Plot of $\ln(1/\tau)$ vs $1/T$ for 3 ·MeOH and the fit to the double-exponential function; the inset shows the deviation $\Delta\ln(1/\tau_1)$ of the data from the straight line | 96 |
| 2-31 | Plot of $\ln(1/\tau)$ vs $1/T$ for 2 and the fit to the double-exponential function; the inset shows the deviation $\Delta\ln(1/\tau)$ of the data from the straight line..... | 96 |
| 3-1 | A schematic representation of selected pyridine methanols and pyridyl oximes | 116 |
| 3-2 | The structure and a stereopair of complex 5 | 116 |
| 3-3 | The labeled core of complex 5 | 117 |
| 3-4 | The bridging-chelating mode of the mpko ⁻ ligand in complexes 5 and 6 | 117 |
| 3-5 | The structure and a stereopair of complex 6 | 118 |
| 3-6 | The labeled core of complex 6 | 118 |
| 3-7 | The structure and a stereopair of complex 7 | 119 |
| 3-8 | The labeled extended core of complex 7 | 119 |
| 3-9 | The bridging-chelating mode of the dapdo ²⁻ ligand in complexes 7 and 8 | 120 |
| 3-10 | The structure and a stereopair of complex 8 | 120 |
| 3-11 | The labeled extended core of complex 8 | 121 |
| 3-12 | $\chi_M T$ vs T plots for complexes 5-8 in the temperature range 5.0-300 K in a 0.1 T applied dc field | 122 |
| 3-13 | Plots of the reduced magnetization, $M/N\mu_B$, vs H/T for complexes 5 and 6 | 123 |
| 3-14 | $M/N\mu_B$, vs H/T plot for 6 | 124 |
| 3-15 | Plots of the reduced magnetization, $M/N\mu_B$, vs H/T for complexes 7 and 8 | 124 |
| 3-16 | Plots of the in-phase (χ'_M) (as $\chi'_M T$) and out-of-phase (χ''_M) ac susceptibility signals of complexes 5 and 6 | 125 |
| 3-17 | Plots of the in-phase (χ'_M) (as $\chi'_M T$) ac susceptibility signals of complexes 7 and 8 | 126 |
| 4-1 | The structure and a stereopair of complex 9 | 151 |
| 4-2 | Fully labeled core of complex 9 | 151 |

| | | |
|------|--|-----|
| 4-3 | The structure of complex 10 | 152 |
| 4-4 | Partially labeled core of complex 10 | 152 |
| 4-5 | The structure and a stereopair of complex 11 | 153 |
| 4-6 | The partially labeled core of 11 | 153 |
| 4-7 | Schematic representation of the metal core of 11 | 154 |
| 4-8 | Plot of $\chi_M T$ vs temperature for complex 9 | 154 |
| 4-9 | Plots of $\chi_M T$ vs temperature for complexes 10 and 11 | 155 |
| 4-10 | Plots of the in-phase ac susceptibility signals for complexes 9 , 10 , and 11 | 155 |
| 4-11 | Plot of the out-of-phase (χ''_M) AC susceptibility signals of complex 9 | 156 |
| 4-12 | Plot of the out-of-phase (χ''_M) AC susceptibility signals of complex 10 | 156 |
| 4-13 | Plot of the out-of-phase (χ''_M) AC susceptibility signals of complex 11 | 157 |
| 5-1 | Schematic representation of polyalcohols used as ligands..... | 178 |
| 5-2 | Schematic representation of methyl-2-pyridyl ketone oxime, and 2,6-diacetylpyridine dioxime (dapdoH ₂)..... | 178 |
| 5-3 | The structure, a stereopair, and the partially labeled core of complex 13 | 179 |
| 5-4 | The structure, a stereopair, and the labeled core of complex 14 | 180 |
| 5-5 | $\chi_M T$ vs T plot for complexes 13 in the temperature range 5.0-300 K in a 0.1 T applied dc field..... | 181 |
| 5-6 | Plot of the reduced magnetization, $M/N\mu_B$, vs H/T for complex 13 in the 0.1 – 7 T field range..... | 181 |
| 5-7 | Plot of the in-phase (χ'_M) ac magnetic susceptibility as $\chi'_M T$ vs T for complex 13 | 182 |
| 5-8 | $\chi_M T$ vs T plot for complex 14 in the temperature range 5.0-300 K in a 0.1 T applied dc field..... | 182 |
| 5-9 | Plot of the in-phase (χ'_M) ac magnetic susceptibility as $\chi'_M T$ vs T for complex 14 | 183 |
| 5-10 | Depictions of the indicated $ S_T, S_A\rangle$ states, showing different levels of frustration for complex 14 | 184 |
| 5-11 | Variation of the spin state energies of 14 with the J/J' ratio, showing multiple changes in the ground state; the states are labelled as $ S_T, S_A\rangle$ | 185 |

| | | |
|------|--|-----|
| 6-1 | Schematic representation of 1,8-naphthalene dicarboxylic acid (ndcH ₂)..... | 205 |
| 6-2 | The structure and a stereopair of complex 16 | 205 |
| 6-3 | Fully labeled core of complex 16 | 206 |
| 6-4 | Alternate views of complex 16 | 206 |
| 6-5 | Alternate views of the Mn ₁₃ topology..... | 207 |
| 6-6 | The labeled core of complex 17 | 208 |
| 6-7 | The complete molecule of complex 18 | 208 |
| 6-8 | Representation of the core of complex 18 | 209 |
| 6-9 | $\chi_M T$ vs T plots for complexes 16-19 in the temperature range 5.0-300 K in a 0.1 T applied dc field | 209 |
| 6-10 | Plot of the reduced magnetization, $M/N\mu_B$, vs H/T for complex 16 in the 0.1 – 0.8 T field range | 210 |
| 6-11 | Two-dimensional contour plot of the fitting-error surface vs D and g for 16 | 210 |
| 6-12 | Plot of the in-phase (χ_M') ac magnetic susceptibility as $\chi_M' T$ vs T for complexes 16-19 | 211 |
| 6-13 | High-field EPR data for complex 16 | 211 |
| 6-14 | Frequency dependence of the EPR spectrum | 212 |
| B-1 | Dimeric model used to fit the dc magnetic susceptibility of complex 9 | 214 |
| B-2 | The ordering of the energy states for each dimer within 9 | 215 |
| B-3 | Triangular model used to fit the dc magnetic susceptibility of complex 13 | 216 |
| B-4 | Triangular model used to fit the dc magnetic susceptibility of complex 14 | 218 |
| C-1 | The structure, a stereopair, and the partially labeled core of complex 15 | 220 |
| C-2 | $\chi_M T$ vs T plot for complex 15 in a 1 kG field..... | 221 |
| C-3 | Plot of the reduced magnetization, $M/N\mu_B$, vs H/T for complex 15 in the 0.1 – 7 T field range | 221 |
| C-4 | Representations of the error surface for the D vs g fit of reduced magnetization ($M/N\mu_B$) vs H/T for complex 15 | 222 |

C-5 Plot of the in-phase (χ'_M) (as $\chi'_M T$) and out-of-phase (χ''_M) AC susceptibility signals of complex **15** 223

LIST OF ABBREVIATIONS

| | |
|---------------------|--|
| BVS | bond valence sum |
| HFEPR | high frequency electron paramagnetic resonance |
| NMR | nuclear magnetic resonance |
| ZFS | zero-field splitting |
| DC | direct current |
| AC | alternating current |
| RM | reduced magnetization |
| TIP | temperature independent paramagnetism |
| WOC | water oxidizing complex |
| PS II | photosystem II |
| Py | pyridine |
| DMF | dimethyl formamide |
| Bu ^t | tertiary butyl |
| mpkoH | methyl-2-pyridyl ketone oxime |
| dapdoH ₂ | 2,6-diacetylpyridine dioxime |
| hmpH | 2-hydroxymethyl pyridine |
| hmcH ₃ | 2,6-bis(hydroxymethyl)- <i>p</i> -cresol |
| ndcH ₂ | 1,8-naphthalene dicarboxylic acid |
| JT | Jahn-Teller |

Abstract of Dissertation Presented to the Graduate School
of the University of Florida in Partial Fulfillment of the
Requirements for the Degree of Doctor of Philosophy

HOMO- AND HETEROMETALLIC MANGANESE CLUSTERS: NEW METAL
ARCHITECTURES, SINGLE-MOLECULE MAGNETS, AND PHYSICAL PHENOMENA

By

Christos Lampropoulos

May 2009

Chair: George Christou

Major: Chemistry

Polynuclear discrete clusters incorporating transition metals have been attracting a lot of attention, due to their aesthetically pleasing chemical structures, and their magnetic properties, such as single-molecule magnetism (SMM); this is a property intrinsic to the individual molecules, which makes them capable of functioning as nanoscale magnetic particles. The first species to exhibit such properties was $[\text{Mn}_{12}\text{O}_{12}(\text{O}_2\text{CMe})_{16}(\text{H}_2\text{O})_4]$ (Mn_{12}), which now serves as the “drosophila” of molecular magnetism. Extension of this chemistry has led to a new high-symmetry Mn_{12} derivative ($\text{Mn}_{12}^t\text{Bu}$) with no intermolecular communication. The thorough investigation of its physical and spectroscopic properties has led to exciting new physics. The use of Mn_{12} clusters as models has allowed for accurate measurement of the magnetization reversal barriers, with the latter finding addressing several misconceptions about SMMs.

In the synthesis of clusters, organic groups are often used as ligands, such as oximes, which in this work have been used in Mn chemistry either alone or with azide groups known to be ferromagnetic couplers. The use of methyl 2-pyridyl ketone oxime (mpkoH) in combination with azides has afforded a family of half-integer spin hexanuclear SMMs.

Extending this work to the bifunctional form of mpkoH, the use of 2,6-diacetylpyridine oxime has provided an entry into new cluster types, including a pentanuclear family of

$\text{Mn}^{\text{IV}}_2\text{Mn}^{\text{III}}\text{Mn}^{\text{II}}_2$ clusters, as well as a $\text{Mn}^{\text{IV}}_2\text{Gd}^{\text{III}}$ triangular complex with an unusual combination of metal oxidation states. The thorough study of the latter, using both physical and theoretical methods, allowed for spin-frustration effects to be investigated and understood.

Ferromagnetic Mn^{III}_3 triangles have also been important in the recent literature, since some of them behave as SMMs. Thus, a new Mn^{III}_3 triangle was synthesized, from the use of bis(hydroxymethyl)-*p*-cresol (hmcH_3), which is ferromagnetically coupled but not a SMM, which is in contrast with other literature examples. The comprehensive magnetostructural correlation between Mn^{III}_3 triangles has led to insights in the structure / property relationship, and to important conclusions about the origin of ferromagnetism and molecular anisotropy.

Another ligand used in this work is the non-flexible 1,8-naphthalene dicarboxylate, which has afforded a family of Mn_{13} clusters, resembling the body-centered cubic structure of mineral salts, and the mathematic model of the Archimedian solid, cuboctahedron. A magnetostructural correlation was possible for these Mn_{13} cages, which proved that small “tweaking” of the structures can affect the magnetic properties, and change the ground states of the molecules.

The incorporation of lanthanides could also lead to novel structures, while high oxidation-state clusters could be potentially useful in the chemical industry instead of metal oxides, i.e. in the catalysis of nitric oxides. To replicate these conditions in a molecule a Ce_6Mn_4 , a Mn_4Ce_2 , and a Mn_8Ce clusters were synthesized. The $\text{Ce}^{\text{IV}}_6\text{Mn}^{\text{III}}_2\text{Mn}^{\text{IV}}_2$ complex possesses a central Ce^{IV} octahedron, capped by two Mn/Ce cubane units, while the Mn_4Ce_2 cage is a snub octahedron, both unprecedented structural motifs. This work has also afforded the fifth isolated member of a Mn_8Ce family of clusters with a saddle-like topology. From the challenging magnetostructural correlation a previously-ignored magnetic pathway was found to dictate the overall spin ground state, and thus the SMM properties.

CHAPTER 1 GENERAL INTRODUCTION

Molecular nanoscience is a fast-developing field of study, which even though is less than a century old, it has influenced our lives in a plethora of ways. Nanoscience in general was introduced by Richard Feynman in his lecture given in 1959 at an American Physical Society meeting. Feynman's seminal lecture entitled "There's Plenty Of Room At The Bottom" was his solution to the struggling at the time top-down technologies. Eric Drexler later coined the term and promoted the significance of "nano-scale" through lectures and books. These two legendary figures of modern science were the main chisellers of the term and its current sense. Nanoscience and nanotechnology describe the study of phenomena and manipulation of materials at the nanoscale, leading to an understanding and control of nanostructures, and pertain broadly to fields such as biology, physics, chemistry, or any existing research area relevant to the nanoscale. Although nanotechnology deals with everything that is small (typically 10^{-9} m and beyond), this is not the case with grants associated with this burgeoning field. It has become such an appealing field that the funding of projects has grown from 464 million in 2001 to estimates of 1.45 billion dollars for 2008.¹

The top-down approach has been spectacularly successful and has underpinned much of the progress of our modern society. Scientists and engineers have learned to fabricate and organize progressively smaller and smaller pieces of matter using techniques such as photolithography.² However, photolithography is typical of many 'top-down' approaches in being of limited applicability for dimensions much smaller than 100 nanometers or so. Of course, this size is still very small by the standards of our everyday experience, but is very large on the scale of atoms and molecules. The molecular nanoscience approach depends on the ability of chemists to synthesize from small, simple starting materials the target molecules with the desired

properties. In most cases, these are previously unknown molecules that are new forms of matter and may be patented as such. They usually also require the development of new synthetic methodologies for their synthesis, and it is this that makes synthetic chemistry a most enjoyable act of creation as much akin to art as to science. The essence of synthetic chemistry, and particularly synthetic (supra)molecular chemistry, finds its full expression in the words of that epitome of the artist-scientist Leonardo da Vinci, as quoted by Nobel laureate Jean-Marie Lehn in his book on supramolecular chemistry³ “*Where Nature finishes producing its own species, man begins, using natural things and with the help of this nature, to create an infinity of species.*”

The synthesis of molecular nanostructures is a process similar to the building of a house. A plan, or at least an envisagement, is required for both: for the building of an architectural structure this takes the form of blueprints, whereas in the synthesis of molecular compounds this is the basis of designed assembly. In both cases certain situations require shifting of the original direction or change of plans, since not everything can be predicted; in molecular synthesis this is the serendipitous assembly method. Furthermore, the use of the appropriate building materials usually ensures strong structures, and in synthesis the use of the suitable combination of synthetic components directs serendipity to desirable products. Similarly, the making of buildings involves bricks or steel beams, while preformed building blocks are used as a route to molecular architectures. Finally, protection of a house is provided by a fence or a surrounding brick wall: the bigger the fence, the more the protection and privacy. Analogously, molecular clusters have a protective shell, separating them from their neighbors: the bulkier the protecting envelope, the lesser the molecular communications.

An architect or engineer needs to be particularly careful when designing and executing the building of a house, while it seems logical that building larger structures is more challenging than small single-family homes. Similarly, synthetic chemists ought to be particularly careful in their choices of metals, ligands, atomic bridges, and protective peripheral groups for the synthesis of desired molecular complexes. The rationale of larger molecules being more challenging than smaller ones is true here as well. However, additional parameters need to be defined for the synthesis of molecular complexes, which add further challenges for a synthetic chemist. For an engineer, the weather does not usually affect the building of a house, whereas for a synthetic chemist the choice of reaction conditions is a determinative reaction-specific parameter, which needs special attention. Since designed synthesis is far more difficult than serendipitous assembly, one must carefully choose the reaction components in order to direct various equilibria to the desired products. Thus, in synthesis there is no “right or wrong” choice, since the possible directions are plentiful; because of this fact, however, there is limited amount of control on the final product. Such a challenge is absent in the case of building a house, since the choices are palpable depending on the type of structure one intends to make, i.e. for a large commercial building the use of steel beams is an obvious choice, whereas for a small house bricks are more appropriate. Additionally, chemists have to face a different problem: thermodynamically favored products versus kinetically fast-forming products. It is well known that carbon has different allotropes, two of which are diamond and graphite. The transformation of a diamond to graphite is a thermodynamically favored process; however kinetics are particularly slow for this reaction, and thus diamonds are known. In the industry, the synthesis of ammonia is a challenging one, involving high pressures and temperatures, because there is a thermodynamic barrier to be overcome; once this barrier is reached, ammonia forms quite easily.

Similarly, in molecular synthesis (mostly solution chemistry) thermodynamics and kinetics take control of the reaction equilibria: even though a variety of products are present in solution, the most thermodynamically stable and kinetically attainable product will precipitate. It is therefore easily understood that synthetic chemistry is synonymous to many challenges, arising from both the reaction-specific parameters, and the apparent confrontation of kinetics and thermodynamics.

On the contrary, molecular chemistry presents many advantages: (i) Once purified, all the molecules in the sample are identical. Such a single-size (monodisperse) collection of nanosized particles is extremely difficult to achieve with traditional top-down approaches, and is important because there is a greater variation of properties with size at the nanoscale than is found at the everyday macroscale. Thus, a distribution of nanoparticle sizes means a significant distribution of properties. In contrast, each molecule in a monodisperse collection will have identical properties; (ii) the low-energy synthetic methods allow the periphery of the molecule to comprise organic groups of various types. Ligands may be altered at will, and this provides a means to finetune important properties of the molecule, such as their solubility, which is important to their purification, crystallization, and study; (iii) molecular solubility is a major advantage, in contrast to classical nanoparticles which form colloidal suspensions. True solubility provides major benefits for purification, processing (e.g. deposition on surfaces, removal from surfaces, etc.) and controlled modification; (iv) the formation of crystals represents the formation of three-dimensional ordered arrays of identical, monodisperse particles, each usually even with the same orientation. They thus all display the same response to an external influence, such as an applied magnetic field. Crystallization of traditional nanoparticles is extremely difficult to achieve; (v) the peripheral organic groups provide a protective coat that prevents significant interactions

between adjacent molecules, and ensures the absence of surface variations, roughness, defects, etc., common with traditional nanoparticles.

Nanoscience is a highly multidisciplinary field, and molecular nanoscience involves the reproducible assembly of addressable nano-sized molecular entities and the characterization of their properties. Nanomagnetism is a relatively new topic, which nevertheless has been attracting a great deal of attention for at least three decades. Since the term “nanomagnetism” includes the term “magnetism”, it would be wise to introduce magnetic materials first and then follow the history to the present day and the current efforts in nanomagnetism.

Magnetic materials have been influencing humanity since the ancient times. The discovery and subsequent utilization of magnetic materials have been central to significant technological advancements that have affected civilization and humankind.⁴ Thales of Miletus (about 634-546 BC) was one of the first to recognize that the mixed-valent iron oxide (Fe_2O_3), magnetite, attracts elemental iron. Since then, magnetic materials have been in the spotlight of research worldwide because magnetism is one of the few phenomena that thrust the technological development. Historically, approximately two thousand years ago the Chinese developed the first magnetic device: the compass. Considering the importance and contribution of the compass to world trade and travel via land, sea or air, one can easily realize the role of magnetic materials to the progress of our civilization. Following this early development, magnets have become almost essential to every modern society and have found uses in several magnetomechanical applications, acoustic instruments, information and telecommunication devices, electrical motors and generators, magnetic shielding, as well as numerous others.⁵ Modern day magnetic materials include magnetic alloys and oxides, particularly ferrites, such as MgFe_2O_4 , which can function in transformer cores, magnetic recording and/or information storage devices.^{5,6}

The motion of electrical charge and specifically the spin and orbital angular momenta of electrons within the atoms of a material are responsible for the magnetic field associated with the magnetic substance. One would anticipate that since all matter is composed of electrons, there should be plenty of magnetic materials. However, this is not true and there are actually very few materials that behave as magnets. Closed electron shells is the most common configuration of electrons in most substances, i.e. electrons with magnetic fields aligned in opposite directions are paired with each other and there is no overall net-magnetization. Such materials with negligible magnetic moment are termed diamagnets.^{7,8} Hence, the crucial element that distinguishes a magnetic substance, or a paramagnet, from a diamagnet is the existence of a magnetic moment that arises from at least one unpaired electron.

There are various types of magnetic materials depending on their response to an external applied magnetic field. As a consequence, the magnetic susceptibility, χ , of the material also changes. In Figure 1-1a, the magnetic field lines of flux are shown for a magnet in vacuum. Interaction of the electron pairs of a diamagnet and an applied field generates a repulsive field which weakly repels the diamagnet from the applied field and causes the flux lines to divert around the diamagnetic substance (Figure 1-1b); the sign of χ is negative and its magnitude is small (-10^{-5}). In contrast, a paramagnet is drawn by an applied magnetic field; the sign of χ is small positive (10^{-3} to 10^{-5}) and hence, the lines of flux are attracted by the paramagnetic substance (Figure 1-1c). The strength of the attraction is governed both by the number of unpaired electrons in the material as well as the nature of the interactions of its electron spins. Diamagnetic susceptibilities are independent of field and temperature while paramagnetic susceptibility varies inversely with temperature, $\chi = C/T$, where C is the Curie constant.⁹ The various types of paramagnetism are distinguished by both the temperature dependence as well as

the absolute magnitude of χ .⁹ Simple paramagnetic behavior is observed in substances in which the magnetic moments of unpaired electrons are independent of each other. In the absence of a magnetic field, individual magnetic moments are randomly oriented. The electron spins of paramagnetic materials align parallel, albeit weakly, to any applied magnetic field, and this effort is opposed to the randomizing effect of thermal energy. Removal of the field results in the subsequent randomization of the spins, which is an entropy-driven process. Therefore, availability of unpaired electrons does not necessarily result in a magnetic material, since a paramagnet can have a net zero magnetization.

In paramagnetic substances that contain multiple metal centers, the magnetic moments of the unpaired spins are not independent, but rather interact with each other, either in a cooperative manner when there is a parallel alignment of the magnetic moments, or in a non-cooperative way, when there is an overall anti-parallel alignment of the magnetic moments. The former describes ferromagnetic behavior while the latter is associated with an antiferromagnetic or ferrimagnetic response; antiferromagnetism refers to a complete canceling of magnetic moments while ferrimagnetism corresponds to the situation in which magnetic moments align in an antiparallel fashion but resulting in a non-zero magnetization.^{4,5,8-10} Examples of classical ferromagnets include iron, cobalt, nickel and several rare earth metals and their alloys while magnetite, Fe_3O_4 , is a ferrimagnet.⁸ Plots of the $\chi_M T$ product, where χ_M is the molar susceptibility, vs. temperature (T) are commonly used as a probe for ferromagnetic or antiferromagnetic responses in molecular and/or classical systems. Ferromagnets exhibit increase of the $\chi_M T$ signals as temperature decreases (Figure 1-2a), whereas antiferromagnets display decrease of the $\chi_M T$ signals with decreasing temperature, as shown in Figure 1-2b.

At all temperatures, ferro-, antiferro- and ferrimagnets (Figure 1-3) are composed of domains, or tiny regions in which all the spins are aligned parallel. Each domain aligns randomly with respect to its neighbors. Application of a strong external magnetic field induces the alignment of all the domains with the field. As alignment occurs, the interactions of spins become strong enough to overcome dipole interactions and entropy considerations that maintain the random alignment of the domains. Effectively, a domain of a specific alignment grows at the expense of a neighboring domain and thus the material becomes magnetized. Finally, when the magnetization reaches a saturation value all the spins align parallel in one particular direction.

Preservation of this parallel spin alignment after the applied field is removed (i.e. remnant magnetization) is not surprisingly dependent on the system's temperature. The system should be lying below a critical temperature T_C in order to retain its ferromagnetic response, in the absence of an external magnetic field. Above T_C , the thermal energy (kT) is large enough to cause the random alignment of the electron spins and change the behavior of the material to simple paramagnetic; this fact also explains the $\chi_M T$ vs. T behavior of ferro- and antiferromagnets at higher temperatures (Figure 1-2). For suppression of the remnant magnetization, a coercive field in the opposite direction is applied, inducing the realignment of the spins in the opposite direction and resulting in a hysteresis loop (Figure 1-4). Because an additional field is required to reverse the direction of magnetization, magnetic storage of information is possible in ferromagnetic and ferrimagnetic materials. For information storage, a small coercive field (high permeability) with a relatively rectangular-shaped hysteresis loop is crucial so that the two magnetic orientations of the spin can represent zero and one in the binary digital system used by current technology.⁸⁻¹⁰ One of the requirements for information storage is the retention of the

system at a temperature in which the material exhibits hysteresis while the removal of the stored information involves heating to a temperature above T_C .⁹

In addition to the ferri- and ferromagnetic behavior, other magnetic-ordering phenomena, such as metamagnetism, canted ferromagnetism, and spin-glass behavior may occur.¹¹ The transformation from an antiferromagnetic state to a high moment state is called metamagnetism. A canted antiferromagnet (or weak ferromagnet) results from the relative canting of antiferromagnetically coupled spins that leads to a net moment. A spin glass occurs when local spatial correlations with neighboring spins exist, but long-range order does not. The spin alignment for a spin glass is that of paramagnet; however, unlike paramagnets, for which spin directions vary with time, the spin orientations of a spin glass remain fixed or vary only very slowly with time.¹²

Magnetic materials have been used for information storage since the early days of computing. Following the development of these materials, today we rely on nanotechnology for more efficient information storage methods. The United States' National Nanotechnology Initiative website defines nanotechnology as "...the understanding and control of matter at dimensions of roughly 1 to 100 nanometers, where unique phenomena enable novel applications". The first hard disk drive, "RAMAC", introduced by IBM in 1957 had a storage capacity of only 2000 bits in⁻² while storage density reached approximately 10 Gbits in⁻² in 2000 – an increase by a factor of five million.¹³ This stunning advance in information technology has been heavily dependent on the dramatic miniaturization of the components employed in the construction of such devices and machines.¹⁴ From the first computer, weighing some 30 tons, to the present state-of-the art supercomputer containing more than 40 million microprocessors, the progress has been simply stupendous.¹

It is therefore no surprise that some of the forefront research areas in magnetism today are driven by the “smaller and faster” mantra of advanced technology. Due to this increasing need for the storage of greater quantities of digital information on smaller surfaces areas, the development of magnetic particles of nanoscale dimensions is one of the current intensive interests. Progress in that direction involves the use of smaller materials of nanoscale dimensions that behave as “permanent” magnets with functional temperatures in the practical range for technological use. In order for scientists to bring magnetic materials to the range of nano, two main approaches have been followed: the top-down and the bottom-up approach. The top-down route involves the fragmentation of bulk ferro- or ferrimagnets to a size smaller than a single domain (20-200nm), therefore all the spins within the particle always remain parallel. These particles, also known as superparamagnets, are composed of randomly oriented spins unless induced by an applied magnetic field. Superparamagnets retain their magnetization when their magnetic relaxation is slowed below a blocking temperature, T_B . Unfortunately this approach has been problematic due to the wide distribution of shapes and sizes of these nanoparticles.¹⁵ Besides, there is a distribution of barrier heights for the interconversion of the spins and these materials are insoluble in organic solvents and thus unstable for some applications and studies. Recently, new fragmentation techniques based on scanning tunneling microscopy and biomineralization have been devised as a method of improvement of the non-uniform particle size obstacle.^{16,17}

Alternatively, one can look at the challenge of further miniaturization from the bottom and say that the top-down approach is reaching the size scale at which molecular chemists have been working for centuries. Thus maybe an easier, or at least complementary, approach to further miniaturization is to re-direct this vast expertise in molecular science towards the synthesis of

larger molecules and related species that can be employed in new generations of nanoscale devices and machines. Therefore, another strategy currently being explored in detail is the development of new magnets using molecules as building blocks. Materials of this kind are also called molecule-based magnets, and have the potential to demonstrate characteristics that are unattainable by the conventional metal/intermetallics and metal-oxide magnets used so far. These materials present properties such as low-temperature processability, high magnetic susceptibilities, high solubility, compatibility with polymers for composites, biocompatibility, transparency, semiconducting and insulating properties, high remnant magnetizations, as well as several other desirable characteristics.^{4,18} Paramagnetic organic or inorganic molecules with a large number of unpaired electrons are typically used as the building blocks for the preparation of these molecule-based magnets, which rely on long-range intermolecular interactions to account for their magnetic behavior. Reported in 1967, the first molecule-based magnet, $[\text{Fe}(\text{dtc})_2\text{Cl}]$, where dtc = diethyldithiocarbamate, was found to have an $S = 3/2$ ground state with ferromagnetic ordering at 2.46 K.^{9,19} This area of multidisciplinary scientific research was subsequently silent, as far as scientific publication is concerned, until 1987 when Miller and co-workers reported a molecular ferromagnet composed of alternating stacks of metallocenium donor cations (D^+) and organic radical acceptor anions (A^-), each with a single unpaired electron. For the complex $[\text{Fe}(\text{C}_5\text{Me}_5)_2]^+$, where D^+ is the decamethylferrocenium cation and A^- is the tetracyanoethylene anion, $[\text{TCNE}]^-$, the ordering temperature was found to be 4.8 K.^{20,21} From these studies, it was determined that the position of adjacent chains relative to one another had a significant effect on the bulk magnetic properties of the material. Thus, Kahn and coworkers studied the effect of the chain arrangement on magnetic properties, by designing, synthesizing and studying the magnetism of a series of mixed-metal $\text{Cu}^{\text{II}} - \mu\text{-L} - \text{Mn}^{\text{II}}$ chains, where L is a

bridging ligand.²² For example, antiferromagnetic coupling was observed between the chains of $[\text{Mn}^{\text{II}}\text{Cu}^{\text{II}}(\text{pba})(\text{H}_2\text{O})_3]$, where pba = 1,3-propylenebis(oxamate). By changing the ligand only very slightly, contrasting data were observed as the compound $[\text{Mn}^{\text{II}}\text{Cu}^{\text{II}}(\text{pbaOH})(\text{H}_2\text{O})_3]$, where pbaOH = 2-hydroxy-1,3-propylenebis(oxamate), showed overall ferromagnetic coupling with $T_c = 4.6 \text{ K}$.²² Such studies emphasized the importance of the selected bridging groups in the formation of 2D or 3D lattices and as well as the communication between the magnetic centers in the molecular building blocks.

After this original work, an attractive direction became apparent: the synthesis of molecules containing several transition metal ions, such as Mn, Fe, V, Ni, and Co, which can potentially exhibit behavior similar to that of superparamagnets. After years of struggle with the reactivity of metal sources, redox chemistry that was taking place during the synthesis of such compounds, and finding the appropriate combination of solvents, molar ratios, and crystallization techniques, in 1993 the first example of a molecule $[\text{Mn}_{12}\text{O}_{12}(\text{O}_2\text{CMe})_{16}(\text{H}_2\text{O})_4]$ (**1**), abbreviated as Mn_{12}ac , able to behave as a magnet by itself was discovered.^{23,24} This discovery led to a totally new approach: the synthesis of nanoscale magnetic materials in which the magnetism was intrinsic to the molecule and not due to interactions between molecules. In fact, complex **1** was first synthesized nearly two decades before its exciting properties were identified.²⁵ Mn_{12}ac thus represents proof-of-feasibility of this approach, and by performing magnetic studies in polyethylene matrix of Mn_{12}ac the absence of any kind of long-range three-dimensional interactions was demonstrated.

Ever since several polynuclear metal complexes that behave as nanoscale magnetic particles have been prepared, resulting in the rapid development of a venerable new area of high-spin metal clusters, termed single-molecule magnets (SMMs).²⁶ For numerous reasons, SMMs

represent a stimulating area of research, promising several advantages over conventional nanoscale magnetic particles. Such advantages include (i) the preparation of purified compounds by solution methods, resulting in a product with a single, sharply defined size; (ii) possible variation in the peripheral ligation such that small or bulky, hydrophilic or hydrophobic ligands can be incorporated into the synthesis; (iii) solubility in several organic solvents, providing access to a variety of industrial applications; and (iv) the possibility of reaching sub-nanoscale dimensions, resulting in the potential development of even better memory storage devices.²⁶

The magnetic behavior of a SMM arises from the combination of a large ground state spin, S , and a large and negative magnetic anisotropy as gauged by the axial zero-field splitting parameter (ZFS), D .^{27,28} In the fields of both inorganic and organic chemistry, there is an intense search underway for such potentially useful high-spin molecules. The first SMM was Mn_{12}ac and it was shown that this exceptional combination of high-spin ground state and large, negative magnetic anisotropy displayed by the complex, resulted in nanoscale-like magnetic behavior and the subsequent classification of the molecule as a SMM (Figure 1-5).^{23,24,27,29} Probably the most intensely studied SMM, $[\text{Mn}_{12}\text{O}_{12}(\text{O}_2\text{CMe})_{16}(\text{H}_2\text{O})_4]$ has an $S = 10$ ground state spin and is just one in a class of well-characterized Mn_{12} complexes of the general formula, $[\text{Mn}_{12}\text{O}_{12}(\text{O}_2\text{CR})_{16}(\text{H}_2\text{O})_4]$, where $R = \text{Me, Et, Ph}$, as well as numerous other groups.²⁶

In these dodecanuclear mixed-valence Mn(III/IV) complexes, a non-planar ring composed of eight alternating Mn^{III} and eight triply bridging oxide ions surrounds a central $[\text{Mn}_4^{\text{IV}}\text{O}_4]^{8+}$ cubane unit. Sixteen bridging carboxylate ligands and four terminal water molecules complete the peripheral ligation. The large ground state spin ($S=10$) arises from exchange interactions between the $S = 3/2$ spins of the Mn^{IV} ions and the $S = 2$ spins of the Mn^{III} ions. Each of the eight Mn^{III} ions on the outer periphery of the complex undergoes a Jahn-Teller (JT) distortion as

expected for a high-spin d^4 ion in near-octahedral geometry. The distortion takes place in the form of an elongation of two *trans* bonds. The approximately parallel alignment of the elongation axes of the eight Mn^{III} ions accounts for a high degree of molecular anisotropy. Molecular anisotropy is defined by the tensorial sum of the single ion anisotropies of the metal ions and therefore the overall anisotropy of a cluster is primarily a consequence of the single-ion anisotropies of the constituent ions within the cluster and of the relative orientations of the magnetic axes of these ions with respect to each other (Figure 1-6).

Hence, the magnetic anisotropy of a Mn_{12} cluster is primarily of the axial type, with the x and y directions approximately equivalent to each other while different from the z direction. Consequently the magnetic moment of an individual Mn_{12} molecule preferentially lies in the z direction, or the easy-axis, of the molecule. As a result of this Ising type of zero-field splitting, the $S = 10$ ground state spin is divided into 21 ($2S + 1$) sublevels, each characterized by a spin projection quantum number, m_s , where $-S \leq m_s \leq S$. The energy of each sublevel is given as $E(m_s) = m_s^2 D$, giving rise to a double well potential (Figure 1-7). Because the value of the axial ZFS parameter D for a SMM is negative (i.e. $D = -0.50 \text{ cm}^{-1}$ for **1**), the $m_s = \pm 10$ sublevels lie lowest in energy while the $m_s = 0$ sublevel lies highest. For the reversal of the spin direction from “spin-up” ($m_s = -10$) to “spin-down” ($m_s = +10$) orientations of the magnetic moment, there is a potential energy barrier, defined as $U = S^2 |D|$ for integer spins, such as $Mn_{12}ac$ ($S=10$) and $U = S^2 |D| - 1/4$ for half-integer spins as it will be shown later for other molecular systems.

For **1**, the potential energy barrier for the reversal of the spin orientation is $\approx 72 \text{ K}$. For this reason, SMMs exhibit slow magnetization relaxation at low temperatures. Experimental evidence for this behavior is supported by the appearance of frequency-dependent signals (χ_M'' signals) in

out-of-phase AC magnetic susceptibility measurements, as shown in Figure 1-8b, and of hysteresis loops in magnetization versus DC field scans (Figure 1-9).^{27,30}

In contrast to the hysteresis loops of traditional ferri- or ferromagnetic materials, such as those of magnetite or chromium dioxide, respectively, the plots of magnetization versus magnetic field of SMMs show steps that correspond to an increase in the relaxation rate of magnetization that occurs when the energy of m_s sublevels coincide on the opposite sides of the potential energy barrier (Figure 1-10).^{26,31-34} Such predicted, but never before observed behavior was first reported in 1996 for molecules of $[\text{Mn}_{12}\text{O}_{12}(\text{O}_2\text{CMe})_{16}(\text{H}_2\text{O})_4]\cdot 2\text{MeCO}_2\text{H}\cdot 4\text{H}_2\text{O}$.³¹ Hence, the relaxation of the magnetization of a SMM occurs not just by thermal activation over the energy barrier, but also by quantum tunneling of the magnetization through the energy barrier.

This quantum phenomenon is not unique to **1**, but is also exhibited by many other SMMs, including the octanuclear Fe^{III} oxo-hydroxo cluster, $[\text{Fe}_8\text{O}_2(\text{OH})_{12}(\text{taccn})_6]^{8+}$ (taccn = 1,4,7-triazacyclononane), where ground state tunneling was first observed, i.e., tunneling between the lowest energy m_s levels.³⁵ In the case of **1**, quantum tunneling of magnetization (QTM) is thermally assisted and occurs between m_s sublevels higher in energy than the lowest lying $m_s = \pm 10$ states. Although tunneling provides a route for rapid reversal of magnetization and, hence, a less attractive memory storage device, an investigation into the gap between the quantum and classical understanding of magnetism can be made using these complexes as models.

Due to the strong need for new SMMs with even larger S values and more negative D values, numerous synthetic strategies aiming at the improvement of these materials have been employed. However, even if these strategies seem feasible on paper, they have been proven a considerable challenge to synthetic chemists worldwide. One of the primary goals of this

research is the development of new synthetic methods for the subsequent preparation of new SMMs. One of the strategies employed towards this goal is the introduction of bulky organic ligands to the synthesis of polynuclear compounds and stabilization of new geometries and nuclearities which might afford new SMMs. Also, a relatively new approach to this effort is the incorporation of heavier metals, such as lanthanides and actinides, in polynuclear clusters. The advantages of such mixed-metal complexes include the incorporation of highly anisotropic metal ions that could aid our efforts for better SMMs, the high coordination affinity of such heavier metals, which could lead to interesting metal assemblies with new coordination environments, and exciting magnetic properties. Finally, due to the multidisciplinary nature of this area of research, a variety of spectroscopic, physical, and theoretical methods are often used, in order to identify, quantify, and explain several interesting physical phenomena. Thus, such methods constitute a big part of the area of molecular magnetism, and SMM-related research.

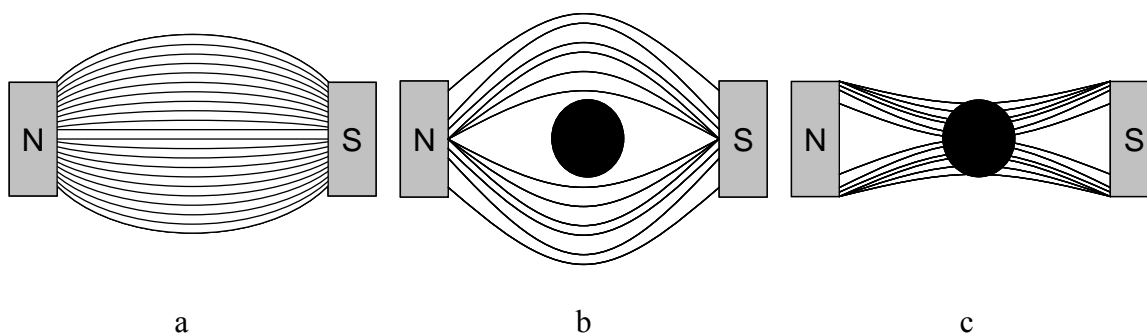


Figure 1-1. Representation of the different ways the magnetic field lines of flux change in the absence of a sample, in the presence of a diamagnetic sample, and in the presence of a paramagnetic sample. (a) magnetic field lines of flux (i.e. contour lines of constant field values) in vacuum; (b) the lines of flux for a diamagnetic substance in a magnetic field; (c) the lines of flux for a paramagnetic substance in a magnetic field

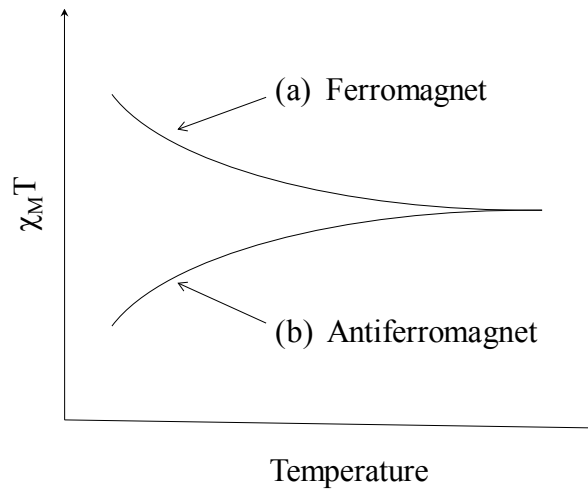


Figure 1-2. Plot of the $\chi_M T$ product (χ_M is the molar susceptibility) vs. temperature. (a) Plot of $\chi_M T$ vs. T for a ferromagnet. (b) Plot of $\chi_M T$ vs. T for an antiferromagnet

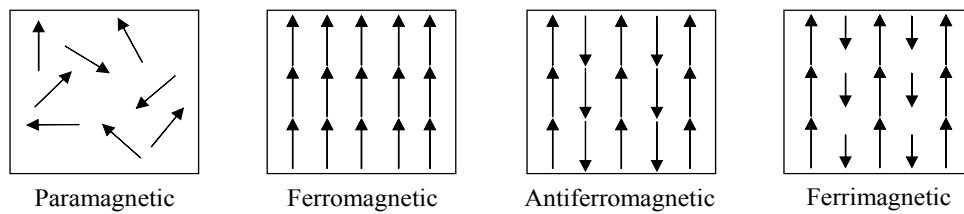


Figure 1-3. Magnetic dipole arrangements in different types of materials. (a) Paramagnetic, (b) ferromagnetic, (c) antiferromagnetic, and (d) ferrimagnetic materials

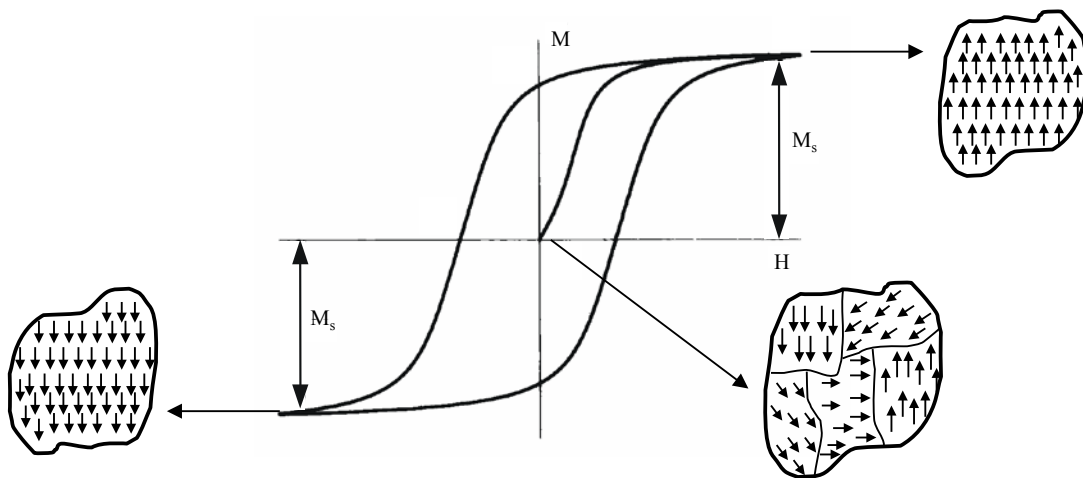
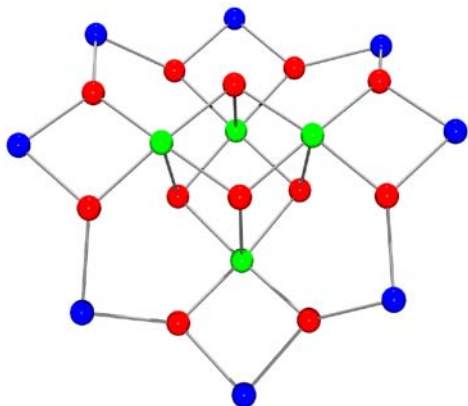


Figure 1-4. Typical hysteresis loop of a magnet, where M is magnetization, H is the applied magnetic field and M_s is the saturation value of the magnetization

(a)



(b)

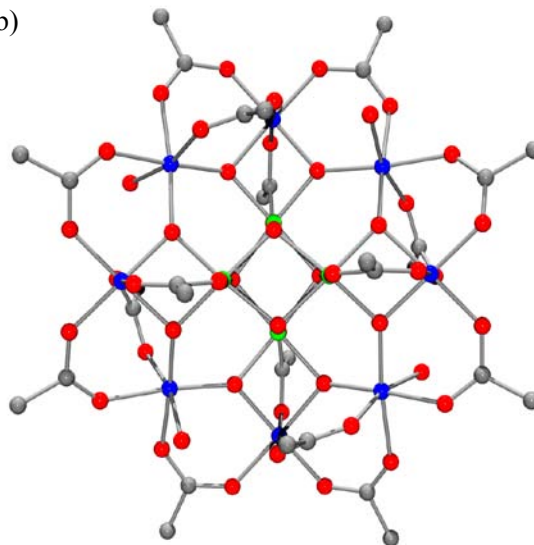


Figure 1-5. ORTEP representation in Pov-Ray format showing the structure of the [Mn₁₂O₁₂(O₂CMe)₁₆(H₂O)₄] complex. (a) The [Mn^{III}₈Mn^{IV}₄(μ₃O²⁻)₁₂]¹⁶⁺ core and (b) the [Mn₁₂O₁₂(O₂CMe)₁₆(H₂O)₄] complex with acetates as peripheral ligands. Mn^{IV} green; Mn^{III} blue; O red; C gray

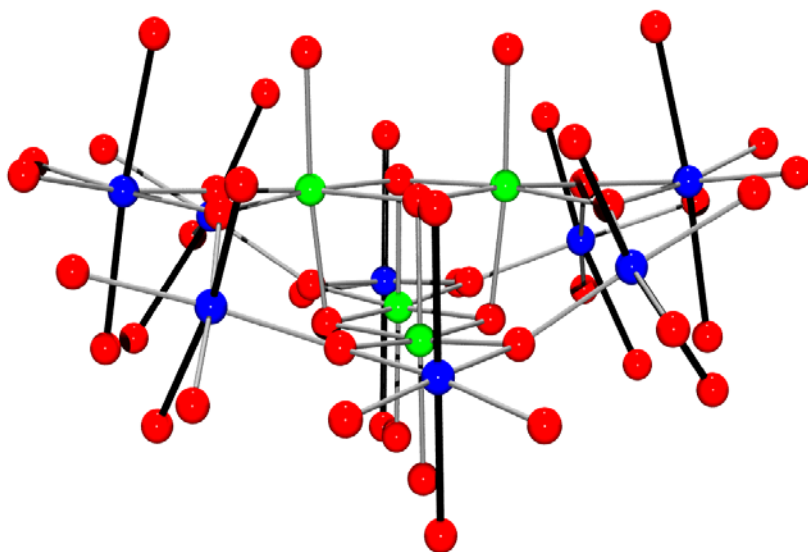


Figure 1-6. ORTEP representation in Pov-Ray format of the metal core of a typical [Mn₁₂O₁₂(O₂CR)₁₆(H₂O)₄] complex, showing the relative disposition of the JT elongation axes indicated as solid black bonds. Mn^{IV} green; Mn^{III} blue; O red

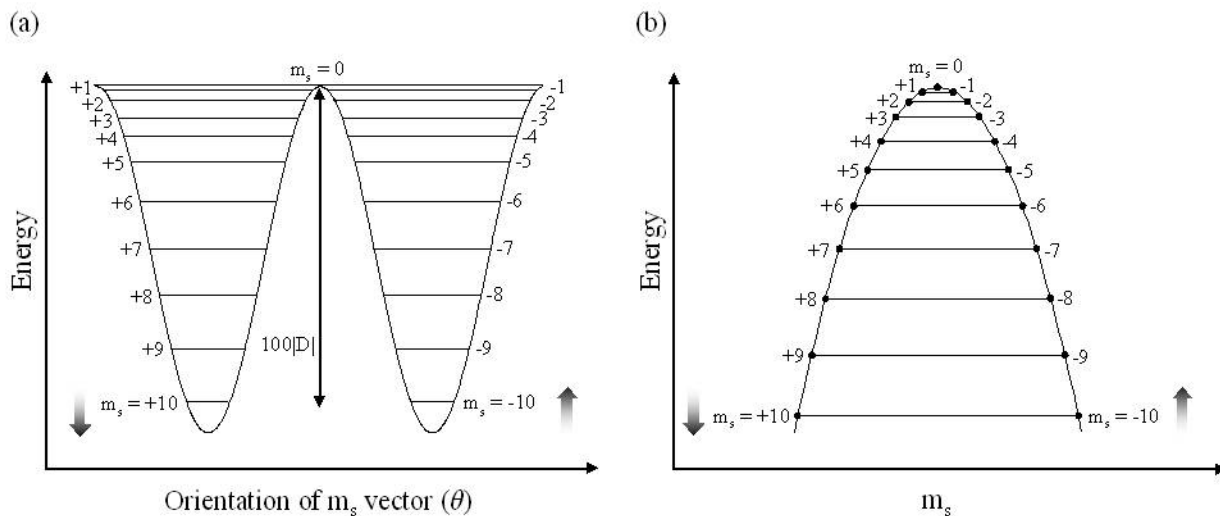


Figure 1-7. Representative plots of the potential energy barrier for an SMM. (a) Plot of the energy versus the orientation of the m_s vector (θ) along the z axis and (b) plot of the energy versus the m_s sublevel for a Mn_{12} complex with an $S = 10$ ground state, experiencing zero-field splitting, $D\hat{S}_z^2$

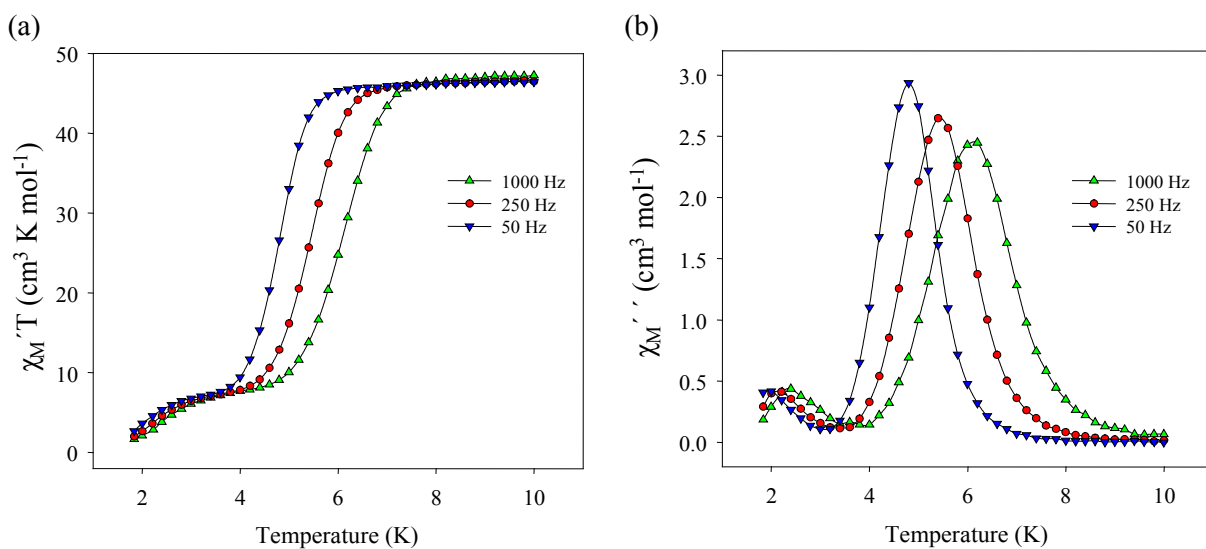


Figure 1-8. In-phase (as $\chi_M' T$) and out-of-phase (as χ_M'') AC susceptibility signals for a dried, microcrystalline sample of $[Mn_{12}O_{12}(O_2CR)_{16}(H_2O)_4]$ at the indicated oscillation frequencies

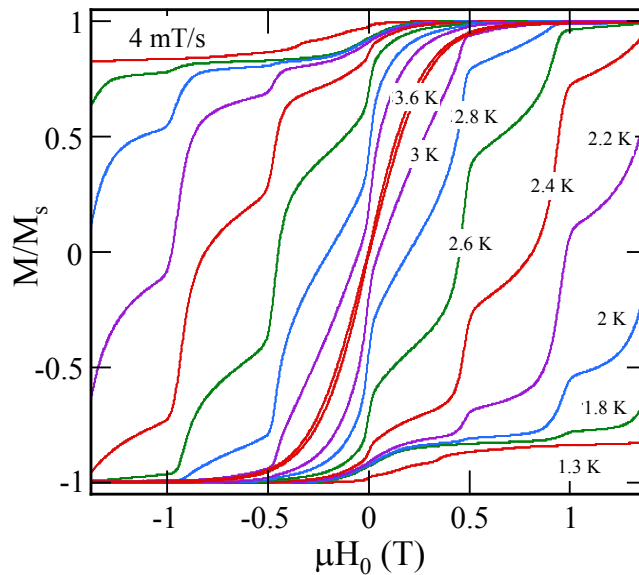


Figure 1-9. Magnetization hysteresis loops for a typical $[\text{Mn}_{12}\text{O}_{12}(\text{O}_2\text{CR})_{16}(\text{H}_2\text{O})_4]$ complex in the 1.3-3.6 K temperature range at a 4 mT/s field sweep rate. M is normalized to its saturation value, M_s

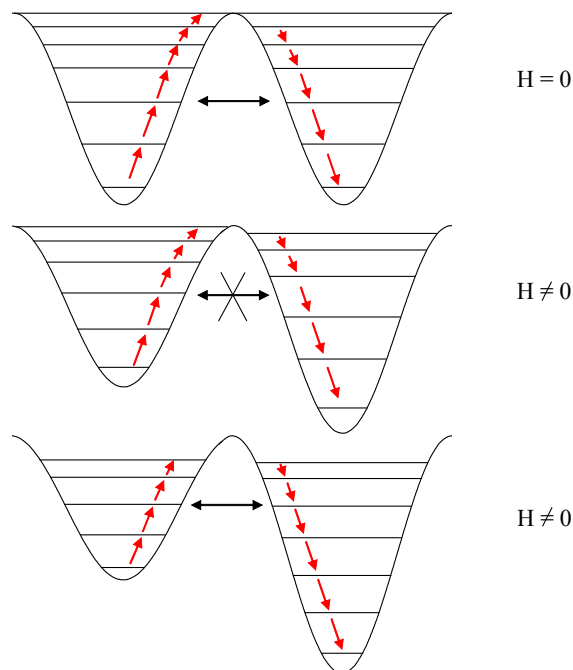


Figure 1-10. Schematic representation of the change in energy of m_s sublevels as the magnetic field is swept from zero to a non-zero value. Resonant magnetization tunneling occurs when the m_s sublevels are aligned between the two halves of the diagram

CHAPTER 2
A NEW DODECANUCLEAR SINGLE-MOLECULE MAGNET WITH AXIAL SYMMETRY:
SYNTHESIS, AND PHYSICAL AND SPECTROSCOPIC CHARACTERIZATION

2.1 Introduction

The crossover between classical and quantum physics is a very attractive area of modern research, and has been termed mesoscopic physics. The boundary between classical and quantum behavior is the focus of a plethora of studies performed around the globe using many different physical methods. Since the discovery of quantum effects in single-molecule magnets (SMMs) in 1996, it was apparent that SMMs were one of the most promising candidates for observing the limits between classical and quantum physics.^{26,31,36-41} The crossover between the classical and quantum regimes can be explored experimentally by observing signatures of quantum mechanical behavior, including quantum tunneling of magnetization (QTM), quantum phase interference and quantum coherence, in macroscopic systems.^{39,42,43} Quantum computing and magnetic information storage are among the many technological applications for materials that exhibit such mesoscopic quantum phenomena,^{37,44,45} and as such, are actively investigated for both fundamental scientific and for technological interests.^{28,32,46,47}

In order for experimental physicists to investigate clearly the quantum effects on macroscopic magnetization, a sufficiently simple system is required, and this is the advantage of using SMMs for such detailed studies. Single-molecule magnets, or molecules that function as single-domain magnetic particles, are ideal systems for the investigation of quantum effects on macroscopic magnetization, offering numerous advantages over higher dimensionality, more complex magnetic systems. One interesting aspect of SMMs is that their study as monodisperse, crystalline assemblies allows quantum properties to be observed that are not easy to detect for traditional top-down nanomagnets. These advantages are largely a consequence of their well-defined structure; a single crystal of a SMM is an ordered ensemble of non-interacting molecules

with a defined orientation with respect to the cell axes (Figure 2-1). The magnetic response is amplified by the number of molecules in the crystal and macroscopic measurements give direct access to single-molecule properties.

The dodecanuclear mixed-valence, trapped-valence manganese-oxo cluster $[\text{Mn}_{12}\text{O}_{12}(\text{O}_2\text{CCH}_3)_{16}(\text{H}_2\text{O})_4] \cdot 2\text{CH}_3\text{CO}_2\text{H} \cdot 4\text{H}_2\text{O}$ (**1**; $\text{Mn}_{12}\text{-Ac}$) was the first single-molecule magnet (SMM), comprising a magnetic core with a diameter of ~ 1 nm. In 1993 $\text{Mn}_{12}\text{-Ac}$ was reported to exhibit slow magnetization relaxation of its $S = 10$ spin ground state, which is split by axial zero-field splitting.⁴⁸ It was also the first system to show quantum tunneling of magnetization (QTM) showing up as periodic “steps” in the hysteresis loops (Figure 2-2).¹⁶ During the last several years, many more SMMs have been discovered and studied, but the Mn_{12} family of compounds remains the most widely studied SMM family, with **1** being the most studied compound to date.⁴⁹

With the observation of quantum tunneling of magnetization as step-like features in the hysteresis loops of **1**, the interface between classical and quantum behavior was finally bridged. Such behavior was also observed in the octanuclear Fe^{III} oxo-hydroxo cluster $[\text{Fe}_8\text{O}_2(\text{OH})_{12}(\text{tacn})_6]^{8+}$ ($\text{tacn} = 1, 4, 7\text{-triazacyclononane}$)³⁵ and has since been seen in numerous other SMMs.⁵⁰⁻⁵⁶ In-depth understanding of the magnetic behavior of SMMs has subsequently been the focus of vast physical research, using **1** as the most popular model. Until recently, **1** was the most ideal candidate for study by numerous techniques, due to its crystallographic tetragonal symmetry.

The symmetry of a SMM strongly influences its magnetic behavior, dictating selection rules as described by certain terms in the spin Hamiltonian of the molecule, an example of which is given in eq 2-1.

$$\hat{H} = D\hat{S}_z^2 + E(\hat{S}_x^2 + \hat{S}_y^2) + \mu_B \vec{H} \cdot \vec{g} \cdot \hat{S} + B_4^0 \hat{O}_4^0 + B_4^4 \hat{O}_4^4 + \hat{H}' \quad (2-1)$$

The first term represents the second order uniaxial magnetic anisotropy of the molecule (D is the axial anisotropy (zero-field splitting, ZFS) constant and \hat{S}_z is the spin projection operator along the easy-axis of the molecule); the second term represents the second order transverse anisotropy (E is the rhombic anisotropy (ZFS) constant, and \hat{S}_x and \hat{S}_y are the x and y projections of the total spin operator \hat{S}); the third term represents the Zeeman interaction with an applied magnetic field H ; the fourth and fifth terms represent the fourth-order uniaxial and transverse anisotropy (B_4^0 and B_4^4 are the fourth order uniaxial and transverse anisotropy constants, respectively), and \hat{H}' represents environmental couplings such as hyperfine, dipolar and exchange interactions.⁵⁷

Quantum tunneling of magnetization is predicted when there are transverse terms in the spin Hamiltonian that do not commute with \hat{S}_z . Such terms are provided by: (i) allowed transverse anisotropy terms for systems in which $x \neq y \neq z$ directions; (ii) transverse components of the magnetic fields due to dipolar interactions and/or hyperfine nuclear fields; and (iii) the Zeeman interaction associated with the transverse component of the external magnetic field. Mixing of degenerate m_s sublevels on opposite sides of the double well potential describing the $S = 10$ ground state spin of the Mn_{12} molecule (Figure 1-7) occurs in the presence of transverse interactions, causing a small tunnel splitting, Δ , and allowing relaxation of the magnetization by quantum tunneling through the two m_s sublevels separated in energy by the tunnel splitting. Among others, the techniques that have been used to study the magnetic behavior of the model Mn_{12} system **1** include inelastic neutron scattering (INS), high-frequency electron paramagnetic resonance (HFEP), low-temperature hysteresis/magnetization measurements, and ^{55}Mn nuclear magnetic resonance. Even though these techniques have afforded substantial insight about the

magnetic properties of the cluster, many questions still remain concerning certain abnormal features exhibited by **1** at low temperatures. These include the absence of tunneling selection rules and multiple, broad EPR absorption peaks.

So far, strict axial symmetry was assumed for **1** on the basis of X-ray diffraction studies, i.e., the second order transverse anisotropy constant, E , is zero. The remaining terms in the spin Hamiltonian allow quantum tunneling of magnetization only from even-numbered m_s to odd-numbered m_s sublevels. However, these are not the only steps observed in the hysteresis loops collected on single crystals of **1**. The hysteresis studies reveal that in addition to even-to-odd resonances, there are also steps that correspond to tunneling from odd-to-even m_s sublevels. These resonances are forbidden by a spin Hamiltonian that assumes strict axial symmetry, and hence there is not an obvious explanation to account for these resonances. Throughout the years of study, several reasons have been proposed to account for this strange magnetic behavior of **1**. These include crystal dislocations that give rise to local rotations of the anisotropy axes (Figure 2-3). These local rotations would give rise to a broad distribution of tunneling rates and account for odd tunneling resonances. Unfortunately, using this model, the predicted distributions are considerably broader than those observed experimentally.^{58,59} Only recently, on the basis of X-ray studies, Cornia and others have proposed a more realistic model involving a discrete disorder associated with the acetic acid molecule of crystallization of **1**. This disorder also gives rise to a locally varying rhombicity and hence a distribution of tunneling rates; the predicted distribution in this case more closely resembles that which is experimentally observed.⁶⁰

Study of the reactivity of the Mn_{12} complex has afforded a great variety of related Mn_{12} compounds. However, very few of these meet the requirement of strict axial symmetry, with the majority of Mn_{12} clusters crystallizing in space groups with the crystallographic symmetry of

two-fold or less. So far only three Mn_{12} clusters with 3-fold or greater symmetry are known: $[Mn_{12}O_{12}(O_2CMe)_{16}(H_2O)_4] \cdot 2MeCO_2H \cdot 4H_2O$ (**1**), $[Mn_{12}O_{12}(O_2CCH_2Br)_{16}(H_2O)_4]$ (**2**) and $[Mn_{12}O_{12}(O_2CCH_2Bu^t)_{16}(MeOH)_4] \cdot MeOH$ (**3**).^{25,30,61-64} **1** and **3** crystallize in the tetragonal space group, $I\bar{4}$ whereas **2** crystallizes in $I4_1/a$, with all the molecules possessing S_4 crystallographic symmetry. The molecular structure of **3** is very similar to the other two. In **3**, the acetate (ac) and H_2O groups have been replaced by $Bu^tCH_2CO_2$ (tBuAc) and MeOH groups respectively. The increased bulk of the $Bu^tCH_2CO_2$ groups leads to a unit cell volume for **3** of 7.06 nm^3 that is almost double that of **1** (3.72 nm^3), and thus to greater intermolecular separations and decreased intermolecular interactions relative to **1**. In addition, the interstitial MeOH solvent molecules in **3** are not disordered and neither are they hydrogen-bonding with the Mn_{12} molecules. As a result, the site symmetry of the latter in **3** is truly axial with a resulting small distribution of environments. This is in stark contrast to **1** where each of the acetic acid molecules in the crystal is disordered over sites with two-fold symmetry, so the site occupancy is 50:50% (Figure 2-4). This disorder was proposed to give rise to a locally varying rhombic anisotropy which breaks the true axial symmetry of the molecule.⁶⁵ Additionally in **1**, each acetic acid forms a strong $OH \cdots H$ hydrogen-bond with an acetate ligand in the cluster that bridges two Mn^{III} ions (Figure 2-5) [$O(15) \cdots O(6) = 2.866(6) \text{ \AA}$ and $O(15)-H(15)-O(6) = 174.6(3)^\circ$], but will do so with only one of the two Mn_{12} molecules next to it.

Complex **2** also possesses crystallographic axial symmetry, but instead of having acetic acid molecules of crystallization, the molecule crystallizes with four dichloromethane molecules that are not interacting with the Mn_{12} molecules (Figure 2-6b). Complex **3** has the lowest solvent content of the three compounds; it crystallizes with one methanol of crystallization per Mn_{12} molecule, which is non-interacting with any of the surrounding Mn_{12} molecules, thus retaining

the S_4 symmetry even when one considers the solvents of crystallization. It was therefore considered of importance to study the magnetic behavior of a high symmetry Mn_{12} cluster that consists of only one species with strict axial symmetry, i.e. $Mn_{12}O_{12}(O_2CCH_2Bu^t)_{16}(MeOH)_4] \cdot MeOH$ to complement previous studies with complex **2**.³⁰ We herein describe the synthesis, single crystal X-ray structure, single crystal ^{55}Mn NMR spectra, high-frequency electron paramagnetic resonance (HFEP) spectra, and magnetic properties of this new high symmetry Mn_{12} complex. From the detailed latter study significant evidence for non-Arrhenius-type kinetic behavior was discovered, which was found to be also present in other Mn_{12} derivatives.

2.2 Experimental Section

2.2.1 Synthesis

All manipulations were performed under aerobic conditions using materials as received, except where otherwise noted. $[Mn_{12}O_{12}(O_2CMe)_{16}(H_2O)_4] \cdot 2MeCO_2H \cdot 4H_2O$ (**1**) was prepared as described elsewhere.²⁵ $[Mn_{12}O_{12}(O_2CCH_2Bu^t)_{16}(H_2O)_4] \cdot CH_2Cl_2 \cdot CH_3NO_2$ (**4**) was prepared using the published procedure.^{66,67}

Freshly prepared crystals of complex **4** (0.18 g, 0.06 mmol) were dissolved in Et_2O (5 cm^3). Methanol was then allowed to slowly diffuse into the ether solution over the course of 4 days. The resulting black crystals were collected by filtration, and dried in vacuo; yield 12%. A sample for crystallography was maintained in contact with the mother liquor to prevent the loss of interstitial solvent. Vacuum-dried solid analyzed as **3**·2 H_2O . Anal. Calcd (found) for **3**·2 H_2O ($C_{101}H_{200}Mn_{12}O_{51}$): C, 41.98 (41.86); H, 6.98 (6.84); N, 0.00 (0.02). Selected IR data (cm^{-1}): 3419 (w), 2954 (vs), 2905 (mw), 2868 (mw), 1572 (vs), 1519 (s), 1412 (vs), 1366 (vs), 1275 (s), 1233 (s), 1198 (s), 1143 (m), 1032 (m), 977 (m), 906 (m), 709 (w), 642 (w), 606 (w), 547 (w), 423 (m).

2.2.2 X-Ray Crystallography

Data were collected by Dr. K. A. Abboud at 173 K on a Siemens SMART PLATFORM equipped with a CCD area detector and a graphite monochromator utilizing MoK α radiation ($\lambda = 0.71073 \text{ \AA}$). A suitable crystal of **3** was attached to a glass fiber using silicone grease and transferred to the goniostat where it was cooled to -100°C for characterization and data collection. The structure was solved by the Direct Methods in *SHELXTL6*, and refined using full-matrix least squares. The non-H atoms were treated anisotropically, whereas the hydrogen atoms were calculated in ideal positions and refined using with the use of a riding model. Cell parameters were refined using up to 8192 reflections. A full sphere of data (1850 frames) was collected using the ω -scan method (0.3° frame width). The first 50 frames were remeasured at the end of data collection to monitor instrument and crystal stability (maximum correction on I was $< 1\%$). Absorption corrections by integration were applied based on measured indexed crystal faces.

An initial survey of reciprocal space revealed a set of reflections with a tetragonal lattice. Analysis of the full data set revealed that the space group was $I\bar{4}$. The asymmetric unit consists of one-quarter of the Mn₁₂ cluster located on a -4 rotary axis and a one-quarter molecule of methanol on another -4 axis. A total of 369 parameters were refined in the final cycle of refinement using 7144 reflections with $I > 2\sigma(I)$ to yield R_1 and wR_2 of 3.64% and 10.35%, respectively. Refinement was done using F^2 . The crystallographic data and structure refinement details are collected in Table D-1.

2.2.3 DC and AC Magnetometry

Variable-temperature DC magnetic susceptibility data down to 1.80 K were collected on a Quantum Design MPMS-XL SQUID magnetometer equipped with a 70 kG (7 T) DC magnet at

the University of Florida. Pascal's constants were used to estimate the diamagnetic corrections, which were subtracted from the experimental susceptibility to give the molar magnetic susceptibility (χ_M). Samples were embedded in solid eicosane, unless otherwise stated, to prevent torquing. AC magnetic susceptibility data were collected on the same instrument employing a 3.5 G field oscillating at frequencies up to 1500 Hz. Magnetization vs field and temperature data were fit using the program MAGNET,⁶⁸ and contour plots were obtained using the program GRID,⁶⁹ both written at Indiana University by E. R. Davidson. Low temperature (< 1.8 K) hysteresis loop and DC relaxation studies were performed at Grenoble using an array of micro-SQUIDs.³⁶ The high sensitivity of this magnetometer allows the study of single crystals of SMMs of the order of 10-500 μm . The field can be applied in any direction by separately driving three orthogonal coils.

2.2.4 High-Frequency Electron Paramagnetic Resonance (HF EPR) Spectroscopy

HF EPR measurements were performed at various frequencies in the 50-360 GHz range. Single-crystal spectra were obtained at fixed microwave frequencies and temperatures using a sensitive cavity-perturbation technique, and a Millimeter-wave Vector Network Analyzer (MVNA) was employed as a source and detector (this instrumentation is described in detail elsewhere).^{70,71} Hard-plane, angle-dependent measurements were performed in a 7 T horizontal field magnet with a vertical access. This setup also allows rotation about an orthogonal axis using a rotating cavity^{57,71} thereby enabling measurements with the field parallel to the magnetic easy-axis of the sample. The hard-plane measurements were performed on higher-order modes of the cavity. Needle-shaped single crystals were removed directly from their mother liquor and protected with vacuum grease before cooling at 10 K/min under 1 atm of helium gas; the crystals were exposed to air for no more than a few seconds, and they were then cooled below 270 K

within minutes of removal from the mother liquor. Temperature control was achieved within the variable-flow cryostat belonging to a Quantum Design PPMS system.

2.2.5 ^{55}Mn Nuclear Magnetic Resonance (NMR) Spectroscopy

Crystals of **3** of suitable dimensions for single-crystal studies were coated in fast-setting epoxy to allow for easier manipulation of the brittle material and to help prevent damage from thermal cycling. NMR coils for the single crystal sample were made by wrapping Cu wire directly around the encapsulated samples. The single crystal was aligned in the coil such that the c-axis (easy axis) was perpendicular to the H_1 field produced by the coil. The probe used for zero-field frequency scans was inductively matched and could be tuned over a large range, 200 – 400 MHz, without having to adjust the matching. Because the breadth of the signal was so large, scans could take anywhere from 3 hours to 1 day. Utilizing a stepper motor controlled by the spectrometer to aid in tuning greatly increased the efficiency of this process. The spectrometer, a MagRes 2000, was home-built with quadrature detection. $\pi/2$ - $\pi/2$ pulse sequences were utilized for frequency scanning and spin-lattice relaxation time (T_1) measurements, with pulse times ranging from 500-1500 ns. Low temperature T_1 studies were conducted with a Janis ^3He system; T_1 was measured over a 0.365 - 1.5 K range with the coil mounted such that it was in thermal contact with a brass plate touching the thermometer and heater.

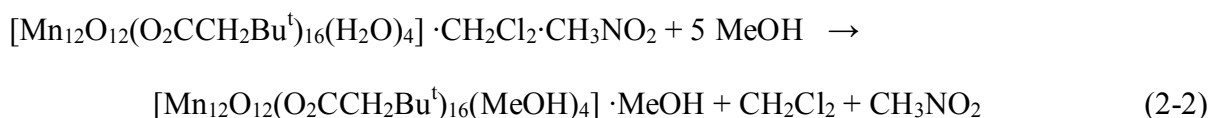
2.2.6 Other Studies

Infrared spectra were recorded in the solid state (KBr pellets) on a Nicolet Nexus 670 FTIR spectrophotometer in the 400-4000 cm^{-1} range. Elemental analyses (C, H, N) were performed at the in-house facilities of the University of Florida Chemistry Department.

2.3 Results and Discussion

2.3.1 Synthesis

The very efficient methodology we have previously developed for the substitution of all the acetate groups of readily available $[\text{Mn}_{12}\text{O}_{12}(\text{O}_2\text{CMe})_{16}(\text{H}_2\text{O})_4] \cdot 2\text{MeCO}_2\text{H} \cdot 4\text{H}_2\text{O}$ (**1**, $\text{Mn}_{12}\text{-Ac}$) with essentially any other carboxylate of choice has opened up access to a large family of Mn_{12} derivatives.^{17,30,72-80} Modification of the properties of interest, such as the solubilities of the products, their redox potentials, crystallinity, and others have been successfully achieved through this process. In the present work, we describe a new synthetic route for the alteration of the coordinated and non-coordinated solvent molecules. Unfortunately this method applies only to the highly soluble complex **4** since it involves recrystallization from a mixture of diethyl ether and methanol. Complex **4** is the only member of the Mn_{12} family that is readily soluble in diethyl ether. During the course of the recrystallization solvent exchange takes place, where both the coordinated and the lattice solvents of complex **4** being replaced by methanol. We are aware of only one previous report of a Mn_{12} complex with non-aqueous terminal ligands,⁸¹ in addition to a complex we recently synthesized and characterized.⁸² The preparation of **3**·MeOH is summarized in eq 2-2.



Since SMMs, and especially the Mn_{12} family, are very sensitive to small structural perturbations, it was of interest to assess whether the replacement of bonded H_2O with MeOH had any significant effect on the properties. Further, it should be noted that we have extended this synthetic procedure to the formation of other derivatives containing other alcohols, such as chloroethanol, *n*-amyl alcohol, and tert-butanol to name a few. However, this work has yet to be

completed and it will not be further discussed. In this work we will focus in the most well-studied of those derivatives, namely complex **3**·MeOH.

2.3.2 Description of Structure

A partially labeled ORTEP plot in PovRay format (top) and stereoview (bottom) of complex **3** are presented in Figure 2-8, while a side view is shown in Figure 2-9. Selected interatomic distances and angles are listed in Table D-2. Complex **3**·MeOH crystallizes in the tetragonal space group $I\bar{4}$. The asymmetric unit consists of one quarter of a Mn_{12} molecule, and one quarter of a MeOH molecule, with each Mn_{12} located on the crystallographic fourfold rotation axis, whereas the interstitial methanol moieties lie on the fourfold screw axis. For the sake of brevity, references to specific atoms in the following discussion implicitly include their symmetry-related partners. The structure of complex **3** is nearly the same as the previously characterized complex **4** and very similar to the rest of the members of the Mn_{12} family, generally denoted as $[Mn_{12}O_{12}(O_2CR)_{16}(L)_4]$ (L = neutral terminal group). Complexes **4** and **3** differ in the identity of the terminal ligands, as well as the solvent molecules in the crystal lattice. The entire family of Mn_{12} compounds, with very few exceptions, possesses the same magnetic core, consisting of a central $[Mn_4O_4]^{8+}$ (Mn1 and O3,4) cubane unit surrounded by a nonplanar ring of Mn^{III} ions (Mn2 and Mn3) bridged to each other and to the central cubane unit via eight μ_3-O^{2-} ions (O1 and O2). Peripheral ligation is provided by sixteen $\eta^1:\eta^1-\mu-O_2CCH_2Bu^t$ anions and four terminal methanol moieties (O10), thus yielding an overall neutral Mn_{12} complex. The four methanol molecules are bound in a 1:1:1:1 fashion, namely one on each alternating Mn^{III} ion (Mn3) as dictated by the S_4 symmetry axis (*vide infra*).

All the Mn ions are six-coordinate with near-octahedral geometry. The oxidation levels of the Mn ions were assigned qualitatively by consideration of the overall charge neutrality, and the

metric parameters, and the clear presence of Jahn-Teller (JT) elongated axes ($\sim 0.1\text{-}0.2$ Å longer than the equatorial bonds of the $\text{Mn}^{\text{III}}\text{O}_6$ octahedron, as expected for a high-spin d^4 metal ion) on all the Mn^{III} ions in the complex. Bond valence sum (BVS)⁸³ calculations quantitatively confirmed the manganese oxidation states, i.e. that Mn2 and Mn3 are Mn^{III} , whereas the remaining manganese center (Mn1) is Mn^{IV} . The elongation axes are all oriented towards the axial carboxylates and/or methanol groups, and are thus positioned roughly parallel to each other and along the crystallographic c axis. This is the normal disposition of JT axes for the Mn_{12} family of complexes, the abnormal one being seen in the handful of $\text{Mn}_{12}\text{-JT}$ isomers where one or more of the elongation axes is equatorial to the disk-like core of the molecule.

The precise orientation (θ) of each JT axis will be of relevance to the ^{55}Mn NMR spectroscopic studies and analyses to be described (vide infra), and these data are therefore provided here (Figure 2-9, bottom). The JT axes at Mn2 and Mn3 are at angles of $\theta = 13.7^\circ$ and 36.6° respectively; for these calculations, the Mn^{III} JT axes are defined by the $\text{O}\cdots\text{O}$ vector between the two trans Mn – O bonds. As stated earlier, there are no hydrogen-bonds between the lattice MeOH and the MeOH molecules. There are only intramolecular hydrogen-bonds between the bound MeOH oxygen and the adjacent carboxylate oxygen ($\text{O6}\cdots\text{O10} = 2.60$ Å). Thus, the solvate molecules do not provide a hydrogen bonding pathway for intermolecular exchange interactions.

2.3.3 Magnetochemistry

2.3.3.1 Direct current magnetic susceptibility studies

Variable-temperature DC magnetic susceptibility (χ_M) data were collected on a microcrystalline powdered sample of $3\cdot 2\text{H}_2\text{O}$, restrained in eicosane to prevent torquing, in a 1.0 kG magnetic field in the 5.0-300 K range. The $\chi_M T$ versus T dependence is similar to those of

previously studied $[\text{Mn}_{12}\text{O}_{12}(\text{O}_2\text{CR})_{16}(\text{H}_2\text{O})_4]$ complexes, exhibiting a nearly temperature-independent value of $18\text{-}20 \text{ cm}^3 \text{ K mol}^{-1}$ in the $150\text{-}300 \text{ K}$ range which then increases rapidly to a maximum of $52 \text{ cm}^3 \text{ K mol}^{-1}$ at 10 K before decreasing rapidly at lower temperatures (Figure 2-10). The maximum suggests a large ground state spin (S) value for the complex of $S = 10$ ($\chi_{\text{M}}T = 55 \text{ cm}^3 \text{ K mol}^{-1}$ for $g = 2$), as is expected for a Mn_{12} complex, with the sharp decrease at low temperatures primarily due to a combination of Zeeman and zero-field splitting effects. The ground state and additional data were obtained from a fit of magnetization (M) data collected in the $1.8\text{-}4.0 \text{ K}$ range in applied DC fields (H) ranging from $1\text{-}70 \text{ kG}$. The data are plotted in Figure 2-11 as reduced magnetization ($M/N\mu_B$) versus H/T , where N is Avogadro's number, and μ_B is the Bohr magneton. The $M/N\mu_B$ versus H/T data were fit using the program MAGNET⁶⁸ to a model that assumes only that the ground state is populated at these temperatures and magnetic fields, and incorporates isotropic Zeeman interactions, axial zero-field splitting ($D\hat{S}_z^2$) and a full powder average.⁸⁴ The best fit is shown as the solid lines in Figure 2-11, and the fit parameters were $S = 10$, $g = 1.90$, and $D = -0.42 \text{ cm}^{-1} = -0.60 \text{ K}$. These values are typical for members of the Mn_{12} family.

In order to confirm that the obtained D and g parameters for $S = 10$ were the true global rather than a local minimum, and to assess the uncertainty in the obtained g and D values, a root-mean square D vs g error surface for the fit was generated using the program GRID.⁶⁹ The error surface is shown in Figure 2-12 as a 2-D contour plot for the $D = -0.50$ to -0.20 cm^{-1} and $g = 1.80$ to 2.05 ranges. One soft (poorly-defined) fitting minimum was observed, with the lowest-error contour describing a region of minimum error spanning $D \approx -0.32$ to -0.40 cm^{-1} and $g \approx 1.91$ to 1.97 , giving estimated uncertainties in the fit parameters of $D = -0.36 \pm 0.04 \text{ cm}^{-1}$ and $g = 1.94 \pm 0.03$. This level of uncertainty in D ($\sim 11\%$) is consistent with our general experience that

magnetization fits are not the most precise way to measure D values; more precise techniques such as HFEPR are required for more reliable numbers.

2.3.3.2 Alternating current magnetic susceptibility studies

Alternating current (AC) magnetic susceptibility data were collected on vacuum-dried, microcrystalline samples of $\mathbf{3} \cdot 2\text{H}_2\text{O}$ in the 1.8-10 K range in a 3.5 G AC field with eight oscillation frequencies (ν) from 5 to 1488 Hz, to probe the magnetization relaxation dynamics. In Figure 2-13 are shown the in-phase (χ_M' , plotted as $\chi_M'T$) and out-of-phase (χ_M'') AC susceptibility signals. In an AC susceptibility experiment, a weak field (typically 1-5 G) oscillating at a particular frequency (ν) is applied to a sample. The magnetization vector of the molecule oscillates with the AC field, and there is no out-of-phase AC susceptibility signal (χ_M'') unless the temperature is lowered to a value at which the barrier to magnetization relaxation is comparable to the thermal energy. A frequency-dependent χ_M'' signal is then observed and there is also a concomitant frequency-dependent decrease in the in-phase (χ_M') signal. A frequency-dependent χ_M'' signal is a necessary but not sufficient⁸⁵ indicator of the superparamagnet-like properties of a single-molecule magnet (SMM). The value of $\chi_M'T$ at the lowest temperatures is also especially useful for confirming (or otherwise) conclusions about the ground state spin of a molecule determined from DC magnetization fits, avoiding the often complicating effect of the applied DC field and/or low-lying excited states.⁸⁶⁻⁸⁹ The $\chi_M'T$ in Figure 2-13 is $\sim 54 \text{ cm}^3 \text{ K mol}^{-1}$ above $\sim 9 \text{ K}$, which is consistent with $S = 10$ and $g \approx 1.98$, in satisfying agreement with the DC magnetization fit parameters. At lower temperatures, there is a frequency-dependent decrease in $\chi_M'T$ and a concomitant increase in χ_M'' , indicating that $\mathbf{3}$ is likely an SMM, as indeed expected for a member of the Mn_{12} family. At lower temperatures, a second feature in either $\chi_M'T$ or χ_M'' is not detectable, indicating the absence of any faster-relaxing Mn_{12} species in the sample. Therefore, the phenomenon of Jahn-Teller isomerism was not observed for complex $\mathbf{3}$. Jahn-

Teller isomerism involves an abnormally oriented Mn^{III} JT axis, as mentioned earlier, which results in smaller barriers to magnetization relaxation and thus a faster-relaxing, so-called lower-temperature (LT) form, whose χ_M'' signals are at lower temperatures than the normal, higher-temperature (HT), slower-relaxing form.^{66,67,90,91}

The AC susceptibility data as a function of temperature at a constant oscillation frequency (Figure 2-13) were supplemented with AC susceptibility data of $\mathbf{3}\cdot\mathbf{2H}_2\mathbf{O}$ as a function of AC oscillation frequency at a constant temperature. Such measurements have become a common method of studying the nature of the magnetization relaxation process in SMMs.^{80,92,93} The in-phase (as m') and out-of-phase (m'') components of the AC magnetic susceptibility were measured at a fixed temperature of 4.6 K as the AC frequency was varied from 0.1 to 1488 Hz (Figure 2-14). As with similar measurements on other Mn₁₂ complexes,^{30,92,93} the data were best fit to a distribution of single relaxation processes rather than to a single relaxation process. The m' (or χ_M') and m'' (or χ_M'') as a function of angular frequency (ω) for a single relaxation process (i.e. a single relaxation barrier) is given by eqs 2-3 and 2-4, respectively, while for a distribution of single relaxation processes (i.e. a distribution of barriers), the m' and m'' behavior is given by eqs 2-5 and 2-6, respectively.

$$\chi'(\omega) = \chi_s + \frac{(\chi_T - \chi_s)}{1 + \omega^2 \tau^2} \quad (2-3)$$

$$\chi''(\omega) = \frac{(\chi_T - \chi_s)\omega\tau}{1 + \omega^2 \tau^2} \quad (2-4)$$

$$\chi'(\omega) = \chi_s + \frac{(\chi_T - \chi_s)[1 + (\omega\tau)^{1-\alpha} \sin(\alpha\pi/2)]}{1 + 2(\omega\tau)^{1-\alpha} \sin(\alpha\pi/2) + (\omega\tau)^{2(1-\alpha)}} \quad (2-5)$$

$$\chi''(\omega) = \frac{(\chi_T - \chi_s)(\omega\tau)^{1-\alpha} \cos(\alpha\pi/2)}{1 + 2(\omega\tau)^{1-\alpha} \sin(\alpha\pi/2) + (\omega\tau)^{2(1-\alpha)}} \quad (2-6)$$

In these equations, χ_s is the adiabatic susceptibility, χ_T is the isothermal susceptibility, $\omega = 2\pi\nu$ is the angular frequency, and τ is the magnetization relaxation time. A main objective of such a study is assessing the magnitude of α , a value between 0 and 1 that is included in the expressions for a distribution of single relaxation processes as a gauge of the width of the distribution. The data in Figure 2-14 for dry crystals of $\mathbf{3}\cdot 2\text{H}_2\text{O}$ were least-squares fit to these equations: the fits to eqs 2-3 and 2-4 (dashed lines) are clearly inferior to those to eqs 2-5 and 2-6 with $\alpha = 0.184$ (solid lines). The relaxation times (τ) obtained from the two fits are very similar, however: $\tau = 0.0176$ s (single relaxation process) and $\tau = 0.0181$ s (distribution of single relaxation processes), with the main difference in the fits arising from the values of the adiabatic and isothermal susceptibility.

2.3.3.3 Arrhenius plot using AC and DC data

The χ_M'' vs T plots were used as a source of kinetic data to calculate the effective energy barrier (U_{eff}) to magnetization relaxation.⁹⁴ At a given oscillation frequency (ν), the position of the χ_M'' peak maximum is the temperature at which the angular frequency ($\omega = 2\pi\nu$) of the oscillating field equals the relaxation rate ($1/\tau$, where τ is the relaxation time) at which a molecule relaxes between the halves of the double-well potential energy plot (Figure 1-17). The relaxation rates at a given temperature can thus be obtained from $\omega = 1/\tau$ at the maxima of the χ_M'' peaks. For crystalline samples of complex $\mathbf{3}\cdot\text{MeOH}$, the frequency-dependence of both sets of χ_M'' peaks was determined at eight different oscillation frequencies in the 5 – 1500 Hz range. Each single peak for every oscillation frequency was accurately fit to a Lorentzian function and the data were plotted as relaxation time τ vs $1/T$ in Figure 2-15. The magnetization relaxation of a SMM obeys the Arrhenius relationship (eq 2-7)

$$(1/\tau) = (1/\tau_0) \exp(-U_{\text{eff}}/kT) \quad (2-7a)$$

$$\ln(1/\tau) = \ln(1/\tau_0) - U_{\text{eff}}/kT \quad (2-7b)$$

the characteristic behavior of a thermally activated Orbach process, where U_{eff} is the effective anisotropy energy barrier, k is the Boltzmann constant and $1/\tau_0$ is the pre-exponential factor. To supplement these AC data and to provide for a more accurate analysis over a wider range of temperatures, DC magnetization decay data were collected and combined with the AC χ_M'' vs ν data. These data were obtained on a single crystal of **3** using a micro-SQUID apparatus. First, a large DC field of 1.4 T was applied to the sample at ~ 5 K to saturate its magnetization in one direction, and the temperature was then lowered to a chosen value between 1.3 and 4.4 K. When the temperature was stable, the field was swept from 1.4 to 0 T at a rate of 0.14 T/s, and then the magnetization in zero field was measured as a function of time (Figure 2-16). The combined AC and DC data sets were used to construct an Arrhenius plot (Figure 2-15). The fit of the thermally-activated region above ~ 3.3 K gave $\tau_0 = 8.5 \times 10^{-9}$ s and $U_{\text{eff}} = 67.8$ K. The U_{eff} value is significantly larger than that for **1** (60-64 K) and for lower-symmetry Mn_{12} derivatives, and is consistent with the high symmetry of each Mn_{12} molecule in the crystal of **3**. Such larger values of U_{eff} appear typical of high-symmetry Mn_{12} complexes.^{30,61,95}

2.3.3.4 Hysteresis studies

The realization of this clearly significant effective barrier to magnetization relaxation, and the fact that complex **3** belongs to the archetypical Mn_{12} family of SMMs, suggested that hysteresis loops should be observed. Hysteresis in magnetization vs DC field sweeps is the classical property of a magnetic material. The studies were performed on aligned single crystals of **3**·MeOH using a micro-SQUID apparatus, and the resulting hysteresis loops at temperatures < 3.6 K and with a 0.002 T/s sweep rate are shown in Figure 2-17. The hysteresis loops exhibit an increasing coercivity with decreasing temperature and with increasing field sweep rate, as expected for the superparamagnetic properties of a SMM. Hysteresis is observed up to at least

3.6 K at a 2 mT/s sweep rate. In addition, as is usually found for neutral Mn_{12} complexes such as **1** and others, the loops exhibit well-defined steps due to quantum tunneling of magnetization (QTM) at periodic field values. The latter are those at which m_S levels on one side of the potential energy double well of the $S = 10$ ground state are in resonance with m_S levels on the other side, allowing tunneling to occur through the anisotropy barrier. The steps are thus positions of increased magnetization relaxation rate. The separation between steps, ΔH , is proportional to D , as given in eq 2-8.

$$\Delta H = \frac{|D|}{g\mu_B} \quad (2-8)$$

Measurement of the step positions in Figure 2-17 gave an average ΔH of 0.45 T and thus a $|D|/g$ value of 0.20 cm^{-1} (0.29 K). Assuming $g = 2.0$, this corresponds to a D value of $0.40 \text{ cm}^{-1} = 0.58 \text{ K}$, consistent with the result of the magnetization vs field fit on dried samples of **4** ($D = -0.42 \text{ cm}^{-1}$, $g = 1.90$, $|D|/g = 0.22 \text{ cm}^{-1}$).

2.3.3.5 High-frequency EPR spectroscopy

In order to determine the effective giant-spin Hamiltonian parameters for complex **3**·MeOH, and to characterize the disorder in crystals of this compound, we have carried out extensive multi-high-frequency EPR measurements as a function of magnetic field (frequency), field orientation, and temperature. These were carried out in the UF Physics Department in collaboration with the Hill group. Experiments were performed in one of two superconducting magnets: a split-pair with a 7 T horizontal field and a vertical access, allowing smooth 180° rotation of the entire EPR probe with $< 0.1^\circ$ angle resolution; and a 17 T solenoid for high-field measurements. All of the EPR data presented in this chapter were obtained from carefully oriented single-crystals. The sensitivity of the measurements was enhanced via the use of a

unique cylindrical cavity, which additionally permits sample rotation relative to the applied field direction.⁷⁰ The quality factor of the cavity at its fundamental TE011 mode frequency of 51 GHz is 20,000. However, measurements are also feasible to frequencies well above 300 GHz on high-order modes. The use of a cavity provides additional benefits in terms of being able to control the polarization of the microwave field (H_1) at the position of the sample, and in reducing instrumental problems that can give rise to distorted lineshapes. As a source and detector, we used a Vector Network Analyzer (VNA) which enables measurement of both the in-phase (absorption) and out-of-phase (dispersion) response of the sample.^{70,71} In order to avoid solvent loss from the samples, the needle-shaped single crystals ($\sim 1 \times 0.4 \times 0.4 \text{ mm}^3$) were removed directly from their mother liquor and protected with paratone-N oil before cooling under 1 atm of helium gas.

Ignoring nuclear hyperfine interactions, the effective Hamiltonian for an isolated giant-spin molecule with strictly S_4 site symmetry is given to fourth-order as follows^{40,57,96-99}

$$\hat{H} \equiv D \left[\hat{S}_z^2 - \frac{1}{3} S(S+1) \right] + B_4^0 \hat{O}_4^0 + B_4^4 \hat{O}_4^4 + \mu_B \vec{B} \cdot \vec{g} \cdot \hat{S} \quad (2-9)$$

where $\hat{O}_4^0 = 35\hat{S}_z^4 - 30S(S+1)\hat{S}_z^2 + 25\hat{S}_z^2 - 6S(S+1) + 3S^2(S+1)^2$

and $\hat{O}_4^4 = \frac{1}{2}(\hat{S}_x^4 + \hat{S}_y^4)$,

\hat{S} is the spin angular momentum operator and \hat{S}_i the spin projection operator along the i -axis ($i = x, y, z$) of the molecule, \vec{B} is the applied magnetic field vector, and \vec{g} is the Landé g-tensor. D parameterizes the dominant axial anisotropy, while B_4^0 and B_4^4 parameterize the fourth order anisotropy terms \hat{O}_4^0 and \hat{O}_4^4 , respectively. When the applied field is aligned with the S_4 (z -) axis, and assuming \vec{g} is diagonal, the appropriate basis states are defined by the spin projection

quantum number m_s , i.e. the projection of the total spin onto the S_4 axis. In this situation, the Hamiltonian matrix is diagonal when written in an \hat{S}_z representation, apart from the transverse \hat{O}_4^4 operator, which does not commute with \hat{S}_z . However, the effect of this term on the low-lying energy levels is extremely weak for $S = 10$.^{57,99} Consequently, it can be completely neglected as far as the high-frequency EPR (HFEP) spectrum is concerned, in which case, the energy eigenvalues are given simply by the following expression:

$$E(m_s) \cong D'm_s^2 + Bm_s^4 + g_z\mu_B Bm_s. \quad (2-10)$$

The relationship between D' , B , D and B_4^0 is available elsewhere.⁵⁷ Thus, one can directly determine g_z and two of the three zero-field-splitting (ZFS) parameters in Eq. 2-9 by fitting easy-axis EPR spectra to Eq. 2-10.

Figure 2-18 displays 336 GHz easy-axis ($B//z$) HFEP) spectra for complex **3** at several temperatures between 30 K and 1.4 K. The positions of these peaks are given by the energy differences, $\Delta E = [E(m_s \pm 1) - E(m_s)]$, deduced from Eq. 2-10, i.e.

$$\Delta E(m_s) \cong \left| D'(1 \pm 2m_s) + O(m_s^3) \pm g_z\mu_B B \right|, \quad (2-11)$$

where the + and – denote transitions on the negative and positive m_s sides of the barrier, respectively. The approximately linear dependence of the transition energies (frequencies) on m_s results in $2S$ fine structures in the HFEP) spectrum, which are more-or-less evenly spaced in magnetic field, as seen in the main panel of Figure 2-18; several of the resonances have been labeled according to the m_s levels involved in the transition. A slight variation in the spacing between the resonances is due to the fourth order term in Eq. 2-10, which gives rise to a weak term of order m_s^3 in Eq. 2-11.¹⁰⁰ By plotting the positions of HFEP) peaks obtained at several different frequencies (inset to Figure 2-18), one can precisely obtain g_z and the ZFS parameters D' and B (hence D and B_4^0) from a fit to an expression similar to Eq. 2-11 which includes the full

m_s^3 dependence of the transition energies. Such a procedure leads to the following results: $g_z = 1.99(2)$, $D = -0.462(2) \text{ cm}^{-1}$, and $B_4^0 = -2.5(2) \times 10^{-5} \text{ cm}^{-1}$.¹⁰¹

As already discussed, the transverse term, \hat{O}_4^4 , in Eq. 2-9 does not significantly affect the lowest lying ZFS for $S = 10$. However, application of a large transverse magnetic field ($B_x > DS/g\mu_B$) results in a situation in which \hat{O}_4^4 operates in zeroth-order on the appropriate basis functions, i.e. its contribution to the energy is of order $B_4^4 m_s^4$ in this high-field limit.

Furthermore, since it is fourth order in the spin operators, it can contribute to a significant fraction of the anisotropy, i.e. $B_4^4 m_s^4 / D m_s^2 \sim 1\%$. More importantly, the \hat{O}_4^4 interaction possesses a very definite symmetry, which is revealed via angle-dependent HFEPR experiments in which the applied field is rotated in the hard plane of the sample.^{30,101} Figure 2-19a shows EPR spectra recorded at 51 GHz for different field orientations within the hard plane of complex **3**. These measurements were restricted to low fields, because the higher field transitions are extremely sensitive to small mis-alignments ($< 1^\circ$) of the field away from the hard plane. Perfect alignment of the sample within the cavity is not realistic. Therefore, time consuming two-axis measurements would be required in order to observe the hard-plane dependence of all transitions. However, analysis of the low-field resonances ($\alpha 0$, $\alpha 2$, $\alpha 4$) is sufficient for determining B_4^4 . In Figure 2-19b, a color contour plot of the data in Figure 2-19a is displayed, albeit spanning the full 360° of rotation. From both plots, a clear oscillatory pattern in the positions of the peaks is observed. The periodicity of the pattern is four-fold, as expected from the molecular geometry. A good fit to the peak positions is obtained (solid squares in Figure 2-19b) using a single value of the parameter $B_4^4 = \pm 4.3(2) \times 10^{-5} \text{ cm}^{-1}$, and $g_x = g_y = 1.94(2)$.

Having determined its zfs parameters, we next assess the quality of crystals of complex **3**·MeOH. Recent studies by numerous groups have demonstrated that the low-temperature

quantum dynamics of the most widely studied Mn_{12} complex (**1**) are significantly affected by solvent disorder.^{58,65,102,103} This was first recognized through measurements of so-called D -strain, which indicated a significant distribution of the axial zfs parameter D , with $\sigma_D \approx 0.02D$.¹⁰⁴⁻¹⁰⁶ Subsequently, a number of groups have shown that the likely source of disorder involves a hydrogen-bonding network of acetic acid solvent molecules, giving rise to a discrete set of solvent environments.^{60,65} Remarkably, each solvent environment can significantly influence the local anisotropy at a given Mn_{12} site in the crystal, giving rise to different Mn_{12} species exhibiting different QTM characteristics, as summarized in a recent review article.⁹⁹ The main motivation behind the present investigations was to ascertain whether such behavior is generic to all high-symmetry Mn_{12} systems, or whether the sensitivity to the solvent can be reduced by attaching bulkier ligands to the Mn_{12} core, e.g. the $\text{O}_2\text{CCH}_2\text{Bu}^+$ ligand.

The D -strain in **1** was deduced on the basis of a linear m_s dependence of the easy-axis EPR linewidth.¹⁰⁴⁻¹⁰⁶ The reason for such a dependence can be seen directly from Eq. 2-11, i.e. a distribution in D produces an energy broadening which scales linearly with m_s . Figure 2-20 displays HF EPR linewidth data for three different $S = 10$ complexes. For both **1** and Fe_8Br , a significant regime of linear dependence on m_s is observed, with the expected zero-linewidth intercept at $m_s = -0.5$; the frequency dependence is due to dipolar broadening.^{97,104,105} In both **1** and Fe_8Br , the data deviate from a linear dependence for small m_s values, approaching a minimum linewidth which is ≈ 50 mT and relatively field- (frequency-) independent for **1**. Meanwhile, the minimum linewidth for Fe_8Br is significantly less, and continues to exhibit field dependence. This ‘residual’ linewidth results from lesser inhomogeneous broadening mechanisms, which dominate the linewidth only when the influence of the static D -strain can be minimized (i.e. for transitions involving small m_s values).

The main sources of inhomogeneous broadening, after D -strain, involve local variations (at the molecular level) in the magnetic induction resulting from fluctuating dipolar and nuclear moments. Indeed, the smaller residual linewidth for Fe_8Br may in part be attributable to the weaker hyperfine coupling in this complex (^{56}Fe has no nuclear spin). The hyperfine contribution to the linewidth in **1** can be estimated to be on the order of 20 mT,¹⁰⁷ i.e. a good fraction of the observed residual linewidth. Meanwhile, calculations of the dipolar broadening for transitions involving the lowest $|m_s|$ levels also give linewidths on the order of 10-20 mT in the 20-25 K range for **1** (10 mT for Fe_8Br at 10 K). Thus, the residual linewidths for the two previously characterized $S = 10$ systems appear to be caused by a combination of fluctuating nuclear and dipolar fields, together with a residual static D -strain (~ 15 mT for **1**, ~ 6 mT for Fe_8Br). We note that all transitions are sensitive to D -strain for an integer spin system.⁴⁰

The situation for $\text{Mn}_{12}\text{-tBuAc}$ (**3**) should not be so different from $\text{Mn}_{12}\text{-Ac}$ (**1**), i.e. the residual linewidths ought to be quite similar for the two complexes. It is notable that the width for the $m_s = -10$ to -9 transition observed for complex **3**·MeOH is already quite close to the residual linewidth of **1**, and that the linewidths become comparable at about $m_s = -6$. Based on the available data for complex **3**·MeOH, it appears that the linewidth levels off for smaller m_s values, approaching an intercept on the vertical axis which is only slightly less than that of **1**, i.e. ~ 35 mT, as opposed to 50 mT. Clearly, therefore, the m_s dependence of the linewidth is much weaker for complex **3**·MeOH, implying that the D -strain is considerably weaker than in **1**. Indeed, one can estimate an upper bound of $\sigma_D < 0.0035D$ from the slope of the data for complex **3**·MeOH, i.e. a factor of 5-6 less than in **1**. Thus, it is fair to say that the static disorder has been significantly reduced in this new high-symmetry Mn_{12} complex. This reduced D strain accounts for the smaller residual linewidth (~ 35 mT) for complex **3**·MeOH.

We believe that the solvent disorder which has been extensively characterized in **1**^{57,98,99} is unique to that particular complex. As discussed earlier, the single MeOH solvent in the unit cell of complex **3**·MeOH sits on a four-fold axis, and does not interact strongly with the core of the Mn₁₂ molecule, i.e. the bulky O₂CCH₂Bu^t ligands provide added protection from the surrounding solvent environment which may or may not contain disorder. One of the clearest evidences for the solvent disorder in **1** comes from angle-dependent HFEPR measurements close to the hard plane. A discrete set of fine structures appear on the high- and low-field sides of the main EPR peaks (see Figure 2-21); each fine structure corresponds to a distinct Mn₁₂ species, and exhibits a unique angle-dependence. The main point as far as complex **3**·MeOH is concerned is that the fine structures, which are clearly associated with the solvent disorder in **1**, are completely absent in the corresponding HFEPR spectra of **3**·MeOH, as illustrated in Figure 2-21. Furthermore, the HFEPR for complex **3**·MeOH are clearly much sharper than for the **1**. These observations constitute the most direct evidence that the type of solvent disorder found in **1** is completely absent in this newer Mn₁₂ complex, though this does not rule out other weaker sources of disorder due to, e.g., solvent loss. It is interesting to note that the hard-plane HFEPR peaks for complex **3**·MeOH in Figure 2-21 fit better to a Lorentzian function than to a Gaussian. This could indicate that the linewidth is limited by the spin dephasing time, implying a T₂ value on the order of 0.3 ns. Future time-resolved HFEPR studies will be needed to resolve this issue.

2.3.3.6 Single crystal ⁵⁵Mn NMR spectroscopy

There has been great interest recently in using solid state ⁵⁵Mn NMR studies to learn more about Mn₁₂ SMMs,¹⁰⁸⁻¹¹¹ particularly at extremely low temperatures where thermal fluctuations are of diminishing importance and quantum effects take over.^{112,113} This work has mainly concentrated on the Mn₁₂-Ac complex **1**. Most of these studies have taken advantage of the ability of ⁵⁵Mn NMR spectroscopy to probe individual symmetry-equivalent groups of Mn sites,

whereas other techniques such as EPR can only probe the complete molecule. Thus, these previous NMR studies have established that there are three symmetry types of Mn within **1**,^{108,109} the central group of 4 Mn^{IV} ions and two groups of 4 Mn^{III} outer ions, as expected under S_4 symmetry. In addition, the sensitivity of the NMR signals to external magnetic fields has provided support for the spin structure of the molecule leading to the $S = 10$ ground state, namely that the spins of the central 4 Mn^{IV} ions (each $S = 3/2$) are aligned antiparallel to those of the outer 8 Mn^{III} ions (each $S = 2$), giving a molecular ground state of $S = 16 - 6 = 10$.¹⁰⁹⁻¹¹¹ Further, ⁵⁵Mn NMR studies on **1** have also been employed to probe QTM within this complex;¹¹⁰⁻¹¹³ in particular, ultralow temperature (down to 20 mK) spin-lattice relaxation time (T_1) data on an oriented microcrystalline powder of **1** were obtained by Morello et al.^{112,113} Below 800 mK, they report an essentially temperature independent T_1 region and conclude that relaxation in this region occurs only through QTM, driven by the significant number (~5%) of faster-relaxing Mn₁₂ molecules located through the crystals of **1** and which serve as relaxation sources. With the availability of the superior crystals of **3**·MeOH, we decided to carry out a full investigation of this complex by ⁵⁵Mn NMR spectroscopy. These studies were carried out in the High Magnetic-Field Lab in Tallahassee in collaboration with the Dalal group. ⁵⁵Mn NMR shows three main peaks (Figure 2-22) in the spectrum of **3**·MeOH, consistent with previously examined Mn₁₂ systems.^{30,64,108,114} The first peak, occurring at 229.6 MHz, corresponds to the four Mn⁴⁺ ions making up the core of the magnetic structure, and is labeled Mn(1). The second peak centered at 293.9 MHz, belonging to the four Mn³⁺ ions whose local Jahn-Teller orientation makes an angle of 13.7° when compared against the crystallographic c-axis, is well split by quadrupole couplings. This peak is labeled Mn(2) in the spectrum. The last four Mn³⁺ ions, labeled Mn(3), also have a Jahn-Teller axis which is canted away from the c-axis of the molecule, but at an

angle of 36.6° . The main resonance for this ion is centered at 360.8 MHz and is also split by quadrupole couplings.

Table 2-1. ^{55}Mn NMR Peak parameters for **3**.

| | Electronic Spin | Central Frequency (MHz) | Internal Field (T) | \angle JT axis makes with c-axis | Average $\Delta\nu_Q$ (MHz) | e^2qQ (MHz) |
|---|-------------------|-------------------------|--------------------|------------------------------------|-----------------------------|---------------|
| $\text{Mn}^{4+} \rightarrow \text{Mn}(1)$ | $S = \frac{3}{2}$ | 229.614 | 21.868 | 0° | 0.61 | 4.06 |
| $\text{Mn}^{3+} \rightarrow \text{Mn}(2)$ | $S = 2$ | 293.937 | 27.994 | 13.7° | 6.35 | 46.22 |
| $\text{Mn}^{3+} \rightarrow \text{Mn}(3)$ | $S = 2$ | 360.833 | 34.365 | 36.6° | 2.50 | 35.71 |

Previous work has defined the hyperfine Hamiltonian which determines the strength of the magnetic field due to interactions of the nuclei with the electrons, and in turn gives the central frequency for each of the three main peaks.¹⁰⁹ The effective hyperfine Hamiltonian is represented as: $H_{eff} = H_F + H_d + H_l$, where H_F is the Fermi contact term, H_d is the dipolar coupling, and H_l is the spin-orbit coupling. While it is possible to calculate the Fermi contact and dipolar terms if one knows the magnetic moment at each Mn site,¹⁰⁹ obtainable from neutron studies, these calculations are not important to this study, thus, we only use the effective hyperfine field.

The Fermi contact term is greatest in magnitude, followed by the dipolar coupling. The spin-orbit coupling term is negligible compared against the other hyperfine interactions and is therefore taken to be zero. The nuclei's energy levels can be further split by non-hyperfine interactions, such as quadrupole (H_Q) or Zeeman (H_0) fields; however, these contributions will be a small perturbation on the total hyperfine field. The total effective field felt at the nuclear site is then: $H_T = H_F + H_d + H_Q + H_0$. The Mn^{4+} hyperfine field only has a contribution from the Fermi contact term while the presence of quadrupolar effects, with respect to spin-lattice relaxation, is still being debated.¹¹⁵ The Mn^{3+} ions have a combination of the Fermi contact and dipolar fields

along with a strong contribution from an electric field gradient, producing quadrupolar interactions. The dominating Fermi contact term produces a range of magnetic fields from 20 T to 40 T at the nuclear site when considering all three resonances, while the magnitude of the dipolar hyperfine field and the magnitude of the quadrupolar interaction depend on the angle that the local Jahn-Teller axis of the Mn ion makes with the c-axis of the molecule.¹⁰⁹ A larger angle corresponds to a smaller dipolar contribution and a smaller quadrupolar coupling. Because the dipolar hyperfine field opposes the Fermi contact term, a smaller dipolar field results in a greater total hyperfine field. This description can clearly be appreciated when comparing the Mn(2) and Mn(3) peaks. Because the Mn(3) peak (360.8 MHz) has a smaller quadrupolar splitting and occurs at a higher frequency (larger total hyperfine field), it can be determined that these Mn³⁺ ions are bent away from the c-axis of the molecule by a larger magnitude.

Because of the nicely split quadrupolar peaks, the quadrupolar coupling parameter can be extracted by use of the equation 2-12, assuming the asymmetry parameter, η , is equal to zero:

$$E_m = -\gamma_n \hbar H_{eff} m_n + \frac{e^2 q Q}{4I(2I-1)} \left(\frac{3 \cos^2 \theta - 1}{2} \right) [3m_n^2 - I(I+1)] \quad (2-12)$$

The first term results from the effective hyperfine Hamiltonian while the second term is the quadrupole perturbation. eQ is the electric quadrupole moment, eq is the gradient of the electric field along the z-axis, and θ is the angle the Jahn-Teller axis makes with the crystallographic c-axis (Figure 2-9). Taking the energy difference between two neighboring m_n levels allows the calculation of $e^2 q Q$, the quadrupolar coupling parameter. These values have been reported in a previous publication and are tabulated in Table 2-1.⁶⁴

Close examination of the Mn(1) resonance shows the presence of fingers at its peak, an interesting discovery considering that, on first glance, the other peaks show no splitting other

than quadrupolar, suggesting that quadrupolar forces may not be suppressed at the Mn⁴⁺ sites.

The Mn(1) peak is fit to both Gaussian (eq. 2-13) and Lorentzian (eq. 2-14) line shapes, where:

$$\text{Gaussian: } y = y_0 + \frac{A}{w\sqrt{\pi/2}} \exp^{-2\left(\frac{x-x_c}{w}\right)^2} \quad (2-13)$$

$$\text{Lorentzian: } y = y_0 + \left(\frac{2A}{\pi}\right) \left(\frac{w}{4(x-x_c)^2 + w^2}\right) \quad (2-14)$$

The Gaussian line shape gives the overall best fit; however, neither line function fits well in the wings of the peak (Figure 2-23). This point will be addressed more completely after discussion of the line shapes that make up the Mn(2) and Mn(3) peaks.

The Mn(2) resonances are also fit with Lorentzian and Gaussian line shapes. In this case, the discrepancy between these two fitting functions becomes clear. The Lorentzian line shape closely matches the low frequency wing of the Mn(2) peak while a Gaussian line shape is clearly superior on the high frequency side. To resolve the line shape discrepancy, the area of each of the five resonances is plotted against their width, with both values obtained from the fitting functions. Interestingly, the areas of similar transitions are consistent with one another in **3** while the peak width constantly increases (Figure 2-24). Comparing the line width and peak area of the Mn(2) peak of **3**·MeOH against that of the Mn(2) peak for Mn₁₂-BrAc (**2**) emphasizes the inconsistency of the line shapes.

The shift from a Lorentzian to Gaussian fitting function obviously is due to the broadening of the peaks upon moving to higher frequencies. One possibility that could describe this behavior would be to have unusual quadrupole properties, such as a non-zero asymmetry parameter (η), causing the peak locations to be non-symmetrically distributed about the central transition. Diagonalization of the quadrupolar Hamiltonian was carried out to determine the effect of such

an occurrence. Comparing various η values against the peak frequency showed that the shifts present in the Mn(2) peak of $\mathbf{3}\cdot\text{MeOH}$ could not be due to quadrupolar interactions. Looking for consistency, the Mn(3) resonance was dissected.

The Mn(3) peak also is fit to Lorentzian and Gaussian line shapes, and, while there were some similarities to the unusual broadening of the Mn(2) peak, the overlap of the resonances does not allow for a unique set of fitting parameters, making it difficult to determine if in fact broadening occurs as the frequency is increased. Close examination of the line fits for the Mn(3) ions again reveals the presence of an error at the perimeter of the peak, as the fittings deviate from the baseline. This error, like that of the Mn(1) resonance, may be attributed to the lack of knowledge about the fitting parameters for the peaks that overlap.

Examination of the three main resonances as a whole leads to an inconclusive result. Because at this time it is not possible to attribute the broadening of the Mn(2) resonance to a specific physical interaction, it is difficult to understand, and therefore assign, an interpretation of the splitting that occurs at the Mn(1) peak. More likely than not, the symmetry of the Mn^{4+} ions has decreased allowing the presence of a quadrupolar splitting to be observed, presenting the first observable evidence for such an interaction in the Mn^{4+} ions for these compounds. The quadrupolar coupling parameter is then calculated in the same manner as it was for the Mn(2) and Mn(3) peaks, with the data placed in Table 2-1. A non-zero quadrupole indicates that $\text{Mn}_{12}\text{-BrAc}$ is the most symmetric Mn_{12} family member, with respect to the Mn nuclei, as no evidence for splitting is observed for its Mn(1) peak and no broadening is seen in its Mn(2) resonance. The power of NMR as a technique is obvious with this result, as neither EPR nor X-ray could detail such a fine structure change.

Spin-Lattice relaxation (T_1) was performed on the Mn(1) peak for **3**, as it is the narrowest peak, and therefore, the easiest to saturate. Even though the Mn(1) resonance is the narrowest, it is still difficult to saturate the entire peak, with a width of 2.8 MHz. Development of a special pulse sequence was necessary, and consisted of a comb pulse where the individual pulses occurred at varying frequencies. The set of frequencies were chosen such that the pulses would overlap to blanket the entire peak. Full saturation of the resonance never occurred; however, effective saturation was achieved, as the recovery curve could be fit to a single exponential function. The recovery was fit with eq 2-15:

$$M(t) = (M_\infty - M_0) \left[1 - \exp\left(-t/T_1\right) \right] + M_0 \quad (2-15)$$

where $M(t)$ is the time dependent nuclear magnetization, M_∞ is the equilibrium magnetization, t is the time between the saturation sequence and the observation spin-echo, M_0 is the remnant magnetization immediately following the saturation comb, and T_1 is the longitudinal (spin-lattice) relaxation time. The temperature was then varied and the saturation sequence run again. T_1 was extracted and plotted as a function of temperature.

The high temperature data (0.8 K to 1.8 K) is fit to equation 2-16 (Figure 2-25):

$$\frac{1}{T_1} \propto C \exp\left(-\Delta E/k_b T\right), \text{ with } C \propto \frac{\gamma_N^2 \langle h_\perp^2 \rangle}{\omega_N^2 \tau_0} \quad (2-16)$$

from which the energy barrier between the $m_s = \pm 10$ and $m_s = \pm 9$ states is extracted. This fit gives $\Delta E = 13.1$ K. A slope change occurs at 800 mK, out of which a new low temperature spin-lattice relaxation function evolves. Because it has been previously assumed that T_1 below 0.8 K is temperature independent, and that tunneling dominates the nuclear relaxation mechanism at these temperatures, no mechanism has been investigated for temperature dependence in this

range. To further understand the temperature response, Figure 2-26 shows the low temperature T_1 data which has been fit with multiple temperature dependent functions. Equally good fits arise from $T_1^{-1} = \kappa T^2$ and $T_1^{-1} = \kappa \exp\left(-\frac{\Delta E}{k_b T}\right)$, where κ is a constant, T is the temperature, k_b is the Boltzmann constant, and ΔE represents the energy barrier. The physical significance of these fits are currently under investigation. ΔE was extracted from the exponential fit and found to be 1.1 K. While the giant spin model describing this system cannot account for such an energy barrier, evidence for a similar energy gap has been observed with another technique, inelastic neutron scattering, on **1**.¹¹⁶ This study showed evidence for an energy level that exists roughly 2 K above the ground state, which they found to be magnetic in origin and tentatively associated with the excitation of a dimer, likely between the Mn^{3+} and Mn^{4+} ions. Further neutron experiments on high symmetry Mn_{12} systems must be conducted to determine if in fact any low lying energy barriers exist. If confirmation of this barrier can be shown, then the Hamiltonian describing these systems must be reinterpreted, possibly leading to a stronger understanding of the tunneling mechanism.

Another intriguing find is that ΔE between the $m_s = \pm 10$ and $m_s = \pm 9$ states found by NMR never measures up to (always less than) that observed by EPR or millimeter wave experiments.¹¹³ In fact, the difference between the values obtained by NMR and EPR are always in the range from 1 K to 2 K, when comparing **1**, **2**, and **3**·MeOH. The energy difference is very similar in magnitude to the low temperature energy barrier, possibly indicating the presence of a much more diverse energy landscape than previously considered, and further rationalizing the need for additional neutron and NMR studies.

To confirm if either of the low temperature fits is correct, T_1 measurements must be extended down to 200 mK, a formidable task considering that at 400 mK T_1 is ~1000 sec, and, if

the fitting trends continue, then T_1 will be anywhere from 5000 sec to 10,000 sec at 200 mK. Such measurements were beyond the scope of the present study, but any future success along these lines could be quite rewarding.

2. 4 Recent Evidence for Non-Linear Arrhenius Behavior in Single-molecule Magnets

Single-molecule magnets (SMMs) are molecules that below a certain temperature (T_B) function as individual nanoscale magnetic particles, exhibiting magnetization hysteresis loops.²⁶ As such, they represent an alternative and molecular (bottom-up) route to nanomagnetism, complementing the top-down approach to traditional magnetic nanomaterials.⁴⁹ SMMs also exhibit fascinating quantum behavior such as quantum tunneling of the magnetization (QTM),^{42,117} showing that they are truly mesoscale entities straddling the classical/quantum divide. The barrier causing slow magnetization relaxation arises from a combination of a large ground state spin (S) and easy-axis anisotropy (negative zero-field splitting parameter, D). Ac magnetic susceptibility studies are a convenient method of assessing whether a compound might be an SMM; frequency-dependent out-of-phase (χ''_M) signals are indicative of the superparamagnet-like properties of an SMM. The variation in signal position with ac frequency can then be used as a source of rate vs T kinetic data, because the χ''_M peak maximum is the temperature at which the angular frequency of the oscillating field equals the rate ($1/\tau$, where τ is the relaxation lifetime) of spin vector reversal. This allows construction of a $\ln(1/\tau)$ vs $1/T$ plot based on the Arrhenius relationship (eq 2-17), the behavior expected of a thermally-activated process over a single- barrier.

$$(1/\tau) = (1/\tau_0)\exp(-U_{\text{eff}}/kT) \quad (2-17)$$

From the slope of the straight line can be obtained the effective barrier to relaxation (U_{eff}), and from the intercept the pre-exponential term ($1/\tau_0$). Adherence to the Arrhenius relationship has been one defining property of a SMM, reflecting the low-dimensional origin of its magnetic

properties rather than 3-D interactions and long-range magnetic order. Deviations from linearity have been noted in the $\ln(1/\tau)$ vs $1/T$ plot for $[\text{Mn}_{12}\text{O}_{12}(\text{O}_2\text{CMe})_{16}(\text{H}_2\text{O})_4]\cdot 2\text{MeCO}_2\text{H}\cdot 4\text{H}_2\text{O}$ (1) when very high ac frequencies (from several kHz up to 1 MHz) were employed.^{118,119} In the present work, we show that non-linear Arrhenius behavior is evident even for data collected in the more typical frequency (ν) range (5 - 1500 Hz), and that the apparent U_{eff} obtained is thus distinctly dependent on the range of data constrained to a linear fit to the Arrhenius equation, giving erroneously large apparent U_{eff} values. This conclusion will be supported by comparisons of U_{eff} values with those from high-frequency EPR (HF-EPR) data (U_{EPR}).

The upper limit to the true barrier to magnetization reversal in SMMs can be calculated with knowledge of the spin Hamiltonian parameters, and a reliable method to obtain these is HF-EPR spectroscopy. This gives what we shall henceforth refer to as U_{EPR} , which should represent a theoretical upper limit to the barrier. However, this is not necessarily the same as the effective barrier, U_{eff} , measured by kinetic (ac) studies because there may be QTM through higher energy M_S levels of the ground state S multiplet, thereby effectively cutting-off part of the true barrier.^{82,117} The slope of an Arrhenius plot has thus been an invaluable way to determine U_{eff} experimentally. We have recently been carrying out determinations of U_{EPR} for various SMMs, and have been encountering significant and puzzling differences between them and the corresponding U_{eff} values obtained from linear Arrhenius plots using ac χ''_{M} vs T data with 5 - 1500 Hz frequencies; these studies consistently give $U_{\text{eff}} > U_{\text{EPR}}$ rather than the other way round.⁸² We have therefore re-examined data for many compounds and have come to the conclusion that even $\ln(1/\tau)$ vs $1/T$ plots constructed using <1500 Hz data exhibit noticeable curvature, and that fits to eq 2-17 are thus inappropriate!

To better probe this, we collected data at 25 frequencies <1500 Hz for $[\text{Mn}_{12}\text{O}_{12}(\text{O}_2\text{CBu}^t)_{16}(\text{MeOH})_4]\cdot\text{MeOH}$ (**3**·MeOH), and $[\text{Mn}_{12}\text{O}_{12}(\text{O}_2\text{CCH}_2\text{Br})_{16}(\text{H}_2\text{O})_4]\cdot 4\text{CH}_2\text{Cl}_2$ (**2**), which (like **1**) crystallize in tetragonal space groups with the Mn_{12} molecules having high (axial, S_4) symmetry. The resulting $\ln(1/\tau)$ vs $1/T$ plot for **3** is shown in Figure 2-27, , and the usual practice of fitting this to a straight line (eq 1) gives $U_{\text{eff}} = 72.0(5)$ K and $\tau_0 = 4.4 \times 10^{-9}$ s (solid line in Figure 2-27, inset). However, the fit is not great owing to the curvature. If it is assumed the high T (high ν) data represent a deviation from otherwise linear behavior,¹¹⁸ then the low T data (< 600 Hz) can be fit to give $U'_{\text{eff}} = 69.5(5)$ K and $\tau_0 = 7.1 \times 10^{-9}$ s; the high T data (\geq 600 Hz) can themselves also be fit to eq 1 to give $U''_{\text{eff}} = 81.4(7)$ K and $\tau_0 = 1.1 \times 10^{-9}$ s (solid lines in Figure 2-27). However, this approach totally ignores the overall curvature, which also makes it impossible to decide objectively where data separation should be made for a two-line fit; this, of course, affects the resulting U'_{eff} calculated from the slope. (Table 2-2). For comparison, single-crystal HFEPR spectra on **3**·MeOH were measured in the 50-360 GHz range, with the field along the easy- axis of the Mn_{12} molecule ($B//z$).⁷¹ Fitting of the resulting data gave $U_{\text{EPR}} = 67.3(13)$ K,¹²⁰ noticeably smaller than $U_{\text{eff}} = 72.0$ K from the linear fit (Figure 2-27, inset), and closer to the $U'_{\text{eff}} = 69.5$ K of the low ν (low T) fit. The latter supports the higher T (higher ν) data as being the main source of the deviation from the Arrhenius law and the resulting discrepancy between U_{EPR} and U_{eff} . Complex **2** gave similar results: $U_{\text{eff}} = 77.6(4)$ K, $U_{\text{EPR}} = 68.3(13)$ K, $U'_{\text{eff}} = 75.6(5)$ K, $U''_{\text{eff}} = 83.4(4)$ K. (Figures 2-28, 2-29) Therefore, the picture that emerges is that fits of the data to Arrhenius eq 2-17, as one or two linear regions, are either inappropriate or subjective, or both. Thus, they are unsatisfactory for obtaining reliable U_{eff} values, or ones that can be confidently compared between different workers who will likely

use different frequency sets and thus weight differently the low and high frequency data points in a linear fit.

Table 2-2. Variation of the calculated U'_{eff} and U''_{eff} for complex **3**·MeOH, considering different frequency cutoff points for the two linear fits to eq 1.

| Frequency cutoff point (Hz) | U'_{eff} (K) | U''_{eff} (K) |
|-----------------------------|-----------------------|------------------------|
| 1150 | 71.4 | 75.7 |
| 1000 | 70.8 | 79.7 |
| 800 | 70.3 | 81.1 |
| 600 | 69.5 | 81.4 |
| 400 | 69.2 | 80.8 |
| 250 | 68.4 | 78.8 |

To accommodate the high T (high ν) deviations, the modified Arrhenius relationship of eq 2-18 was employed, comprising a double-exponential function involving two barriers U_1 and U_2 , and corresponding τ_{01} and τ_{02} , respectively.

$$(1/\tau) = (1/\tau_{01})\exp(-U_1/kT) + (1/\tau_{02})\exp(-U_2/kT) \quad (2-18)$$

An excellent fit of the $\ln(1/\tau)$ vs $1/T$ data for **3**·MeOH to eq 2-18 was obtained (solid line in Figure 2-30) with $U_1 = 63(1)$ K, $\tau_{01} = 2.8(6) \times 10^{-8}$ s, $U_2 = 102(4)$ K, and $\tau_{02} = 1.3(7) \times 10^{-10}$ s. U_1 is reasonable for a Mn_{12} SMM and is close to U_{EPR} (67.3 K); as already stated, it is reasonable for $U_{\text{eff}} < U_{\text{EPR}}$ due to tunneling below the top of the EPR barrier. In Figure 2-30 (inset) is the deviation $\Delta \ln(1/\tau_1)$ of the data from the linear plot resulting from the first term in eq 2-18 and the U_1 and τ_{01} values; the deviation is non-zero at all T (ν) values, i.e. the second term affects the relaxation kinetics even at the lowest frequencies. Similar behavior was also observed for **2** (Figure 2-31), with $U_1 = 66(1)$ K, $\tau_{01} = 2.2(6) \times 10^{-8}$ s, $U_2 = 96(2)$ K, and $\tau_{02} = 1.9(4) \times 10^{-10}$ s.

Eq 2-18 represents a minimal description of what we believe to be behind the curvature of the $\ln(1/\tau)$ versus $1/T$ plots. It consists of a sum of two relaxation processes: the first term corresponds to relaxation within the $S = 10$ ground state, and the second term represents relaxation via excited S states. Under this description, U_1 is the real kinetic relaxation barrier of

the $S = 10$ Mn_{12} molecule in its ground state, and U_2 reflects the ‘average’ excitation energy to a large group of excited states that provide more efficient relaxation pathways, i.e. a faster pre-exponential factor $1/\tau_{02}$.

Relaxation through excited states will involve processes in which spins within the cluster flip independently of each other, i.e. the notion of a rigid spin $S = 10$ breaks down at higher temperatures. There is clearly only a single relaxation process over the $S = 10$ barrier for the rigid spin, whereas there will be a huge number of relaxation pathways involving independent spin-flips. We propose that this is the reason for the significantly faster pre-exponential factor. While the second term in eq 2-18 is phenomenological, the first does accurately reflect the slower relaxation within the ground state. Consequently, eq 2-18 correctly captures the low-temperature limiting behavior of the relaxation dynamics, and we thus believe that U_1 provides a reliable estimate of U_{eff} that is not dependent on factors such as the choice of ac frequencies. The value of U_2 , on the other hand, should not be taken too seriously, although it does agree quite well with the locations of excited states.¹²¹ A very large $U_{\text{eff}} = 168$ K (and $\tau_0 = 1.0 \times 10^{-11}$ s) obtained from a fit to eq 2-17 of $\ln(1/\tau)$ vs $1/T$ data collected in the 100 Hz to 1 MHz frequency range (and T up to 20 K) suggests even faster pathways at higher energies.¹¹⁹ Thus, an exact description should probably contain stretched exponentials to capture the high T behavior.

In summary, the magnetization relaxation of Mn_{12} SMMs does not follow a simple Arrhenius law, even for data collected at < 1500 Hz, due to contributions to the relaxation rate via excited S states with a larger thermal barrier but much faster spin reversal rates. We have provided a double-exponential modification of the Arrhenius equation that we consider a superior means to obtain the true barrier U_1 of an SMM in its ground state, which also avoids subjective decisions about which data to employ in a linear Arrhenius plot (eq 2-17) and thus

making comparisons between different data sets from different groups and techniques more reliable. Preliminary studies of other Mn_x SMM families are leading to the same conclusions as for Mn_{12} , i.e. non-linear Arrhenius plots at low frequencies are a general property of SMM relaxation kinetics. Note that the present results suggest published U_{eff} values obtained from Arrhenius plots using ac susceptibility data are consistently overestimated, in some cases by ~10% or more, e.g. the Mn_6 family.^{50,122} It also appears that accurate comparisons for U_{eff} values that have been obtained from ac data using eq 2-17 are not possible unless the data were collected in the same frequency ranges. Without doubt, there is a need for greater theoretical understanding in this area.

2.5 Conclusions

The synthesis of a new Mn_{12} derivative bearing bulky $O_2CCH_2Bu^t$ ligands and terminal methanols was achieved using a newly developed solvent exchange technique. The magnetization studies establish that complex **3** possesses the usual $S = 10$ ground state spin, as the vast majority of the complexes in the Mn_{12} family of SMMs. Frequency-dependent out-of-phase AC susceptibility signals, and the hysteresis loops in magnetization vs applied DC field sweeps, support our initial notion of **3** being a single-molecule magnet. It is worth noting that the overall profiles of nearly all the magnetic data of **3** are similar to the original Mn_{12} -Ac (**1**), and a recently reported Mn_{12} -BrAc (**2**).³⁰

Tetragonal symmetry is a common feature of **1**, the recent Mn_{12} -BrAc (**2**), and complex **3** discussed in this account. Even though all three compounds crystallize in a tetragonal space group, they seem to exhibit different properties, due to the disposition and/or disorder of the solvent molecules in the crystal lattice. Namely, the data for **1** are significantly compromised by an apparent mixture of isomers in the crystal. The data of Mn_{12} -BrAc (**2**) discussed elsewhere³⁰ are undeniably much cleaner than complex **1**. However, when compared with complex **3** it is

apparent that the data of the latter is perceptibly superior, as evident from the sharper signals in the EPR, and the ^{55}Mn NMR spectra. Complex **3** possesses no remarkable disorder in the environment of the Mn_{12} magnetic core, nor is the overall S_4 symmetry lowered by the lattice solvent, since one methanol molecule is shared equally by four Mn_{12} complexes, as dictated by the crystal symmetry, without hydrogen-bonding to only one of them. Furthermore, the intermolecular interactions are practically absent due to the increased steric bulk of the peripheral ligands, thus enhancing the magnetic insulation of the Mn_{12} core. Therefore, **3** is much closer to an ideal situation of a three-dimensional ensemble of identical, monodisperse molecular particles in identical environments. Detailed ^{55}Mn NMR experiments have revealed unique features within the NMR peaks of **3**; namely, some level of asymmetry was realized for the NMR peak of the Mn^{4+} ions. This is the first time such quadrupolar splitting has been observed on this peak for a Mn_{12} , and we propose it originates from decreased local symmetry around the Mn^{4+} ions. Even though such an interaction is not yet understood thoroughly, it could pave the way to more interesting physics, and overall understanding of the relaxation mechanism and QTM. High-frequency EPR spectroscopy is a very powerful tool for studying the dynamic parameters in SMMs, and in the case of **3** was also used to address the quality of the crystals with respect to the symmetry. EPR data provided the values of all the thermodynamic parameters with great accuracy, and respectively realized the retention of the cubic symmetry using a 360° field-rotation experiment. Furthermore, the smaller residual linewidth of the EPR signal suggested the significant weakening of the D -strain compared to its predecessors, and thus proved the significance of the local symmetry to the quality of the data.

Herein we suggest that both the crystal and the local symmetries are major contributors to the similar behavior of all Mn_{12} complexes. Furthermore, as evidenced by non-linear Arrhenius

plots of complexes **2** and **3**, excited state tunneling seems to be the origin of this curvature even at this frequency / temperature range. The suggested modified Arrhenius equation allows for accurate comparisons between U_{eff} obtained for different molecules, by different workers. This initial observation suggests that the spins within the clusters flip independently of each other, i.e. notion of the rigid spin breaks down at higher temperatures. Further theoretical studies are undoubtedly needed in order to address this behavior.

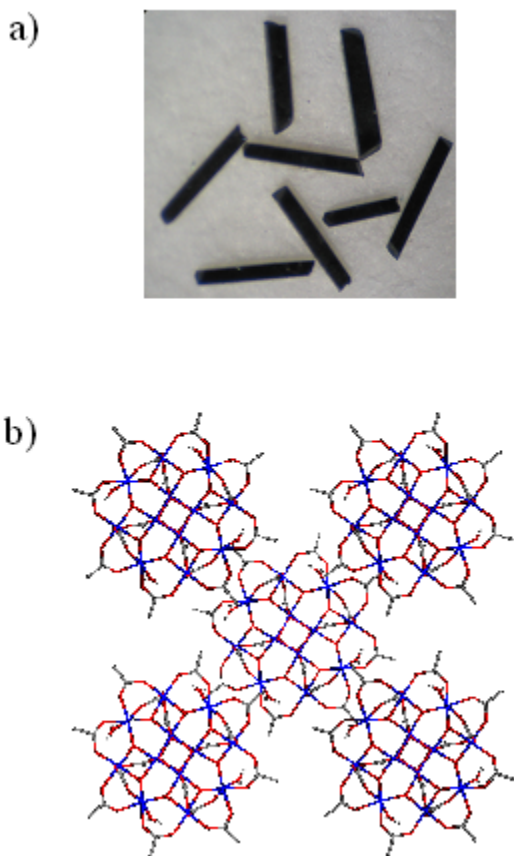


Figure 2-1. Representations of the structure of **1**. (a) Photograph of eight crystals and (b) packing diagram showing the orientation of molecules of **1** relative to each other with respect to the z axis (long axis) of an individual crystal.

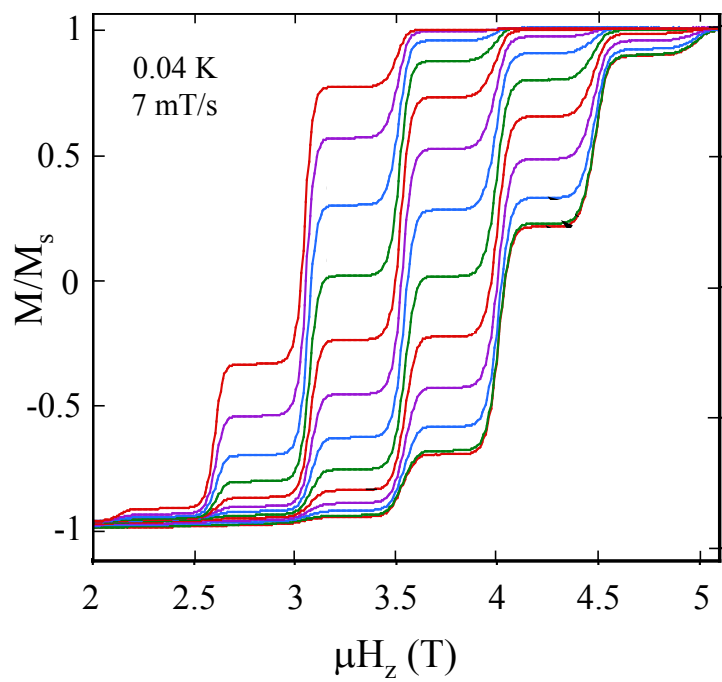


Figure 2-2. Magnetization (M) vs field of a single crystal of complex **1** at the indicated field sweep rate at 0.04 K. Transverse fields are applied along the z axis of the crystal and M is normalized to its saturation value, M_s .

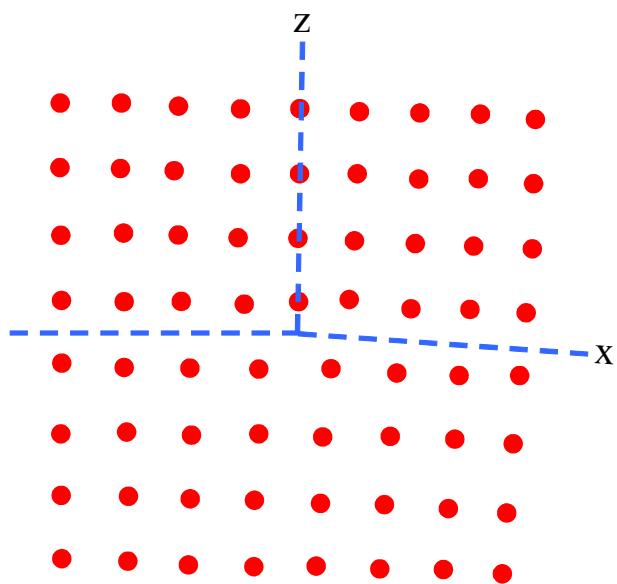


Figure 2-3. Edge dislocation along the y axis with the extra plane y, z inserted at $z > 0$.

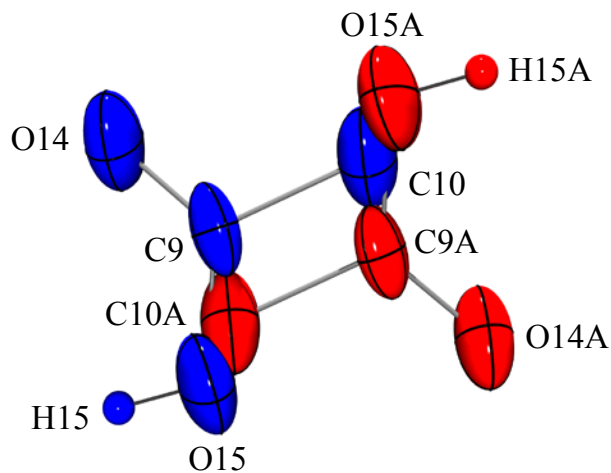


Figure 2-4. ORTEP representation in PovRay format of the two-fold disorder of the MeCO₂H solvent molecules of crystallization in complex **1**. A crystallographic C₂ rotation axis (not shown) passes through the center of the two MeCO₂H molecules.

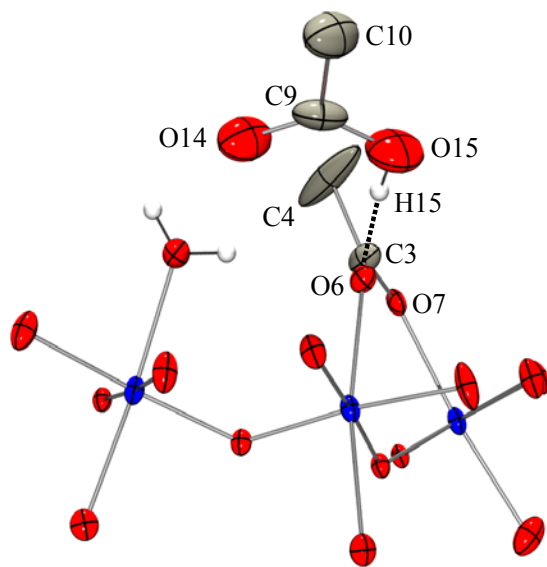


Figure 2-5. ORTEP representation in PovRay format of the hydrogen-bonding interaction between an MeCO₂H molecule of crystallization [O(14), O(15), C(9), C(10), H(15)] and an MeCO₂⁻ ligand [O(6), O(7), C(3), C(4)] bridging Mn^{III}Mn^{III} pairs in complex **1**.

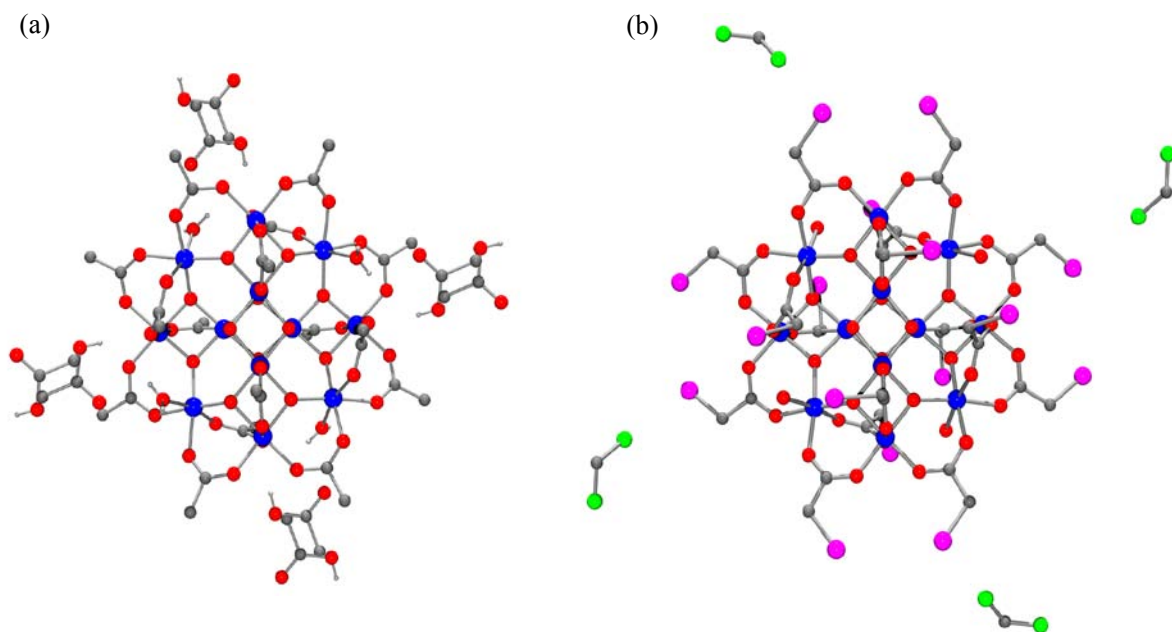


Figure 2-6. ORTEP representation in PovRay format of (a) $[\text{Mn}_{12}\text{O}_{12}(\text{O}_2\text{CMe})_{16}(\text{H}_2\text{O})_4]$ with MeCO_2H solvent molecules of crystallization and (b) $[\text{Mn}_{12}\text{O}_{12}(\text{O}_2\text{CCH}_2\text{Br})_{16}(\text{H}_2\text{O})_4]$ with CH_2Cl_2 solvent molecules of crystallization. Mn blue; O red; C gray; Br pink; Cl green; H light gray.

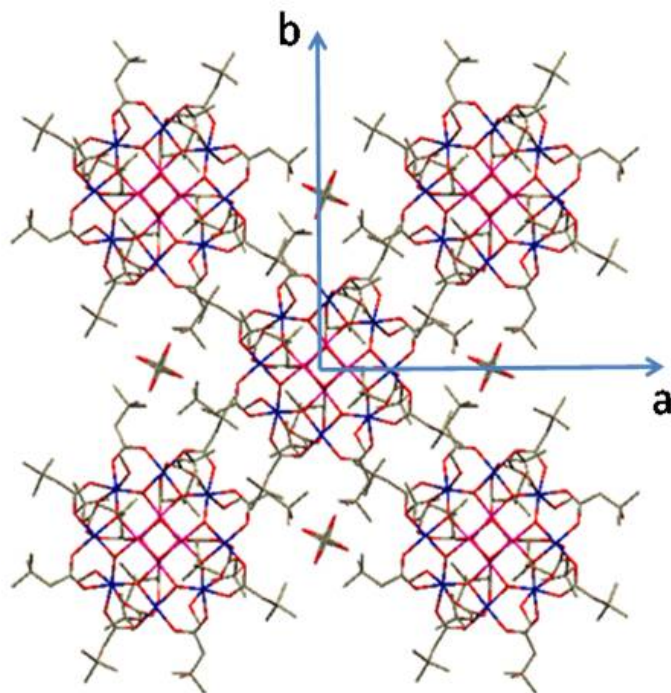


Figure 2-7. Packing diagram of $[\text{Mn}_{12}\text{O}_{12}(\text{O}_2\text{CCH}_2\text{Bu})_{16}(\text{MeOH})_4] \cdot \text{MeOH}$ (**3**) with MeOH solvent molecules of crystallization.

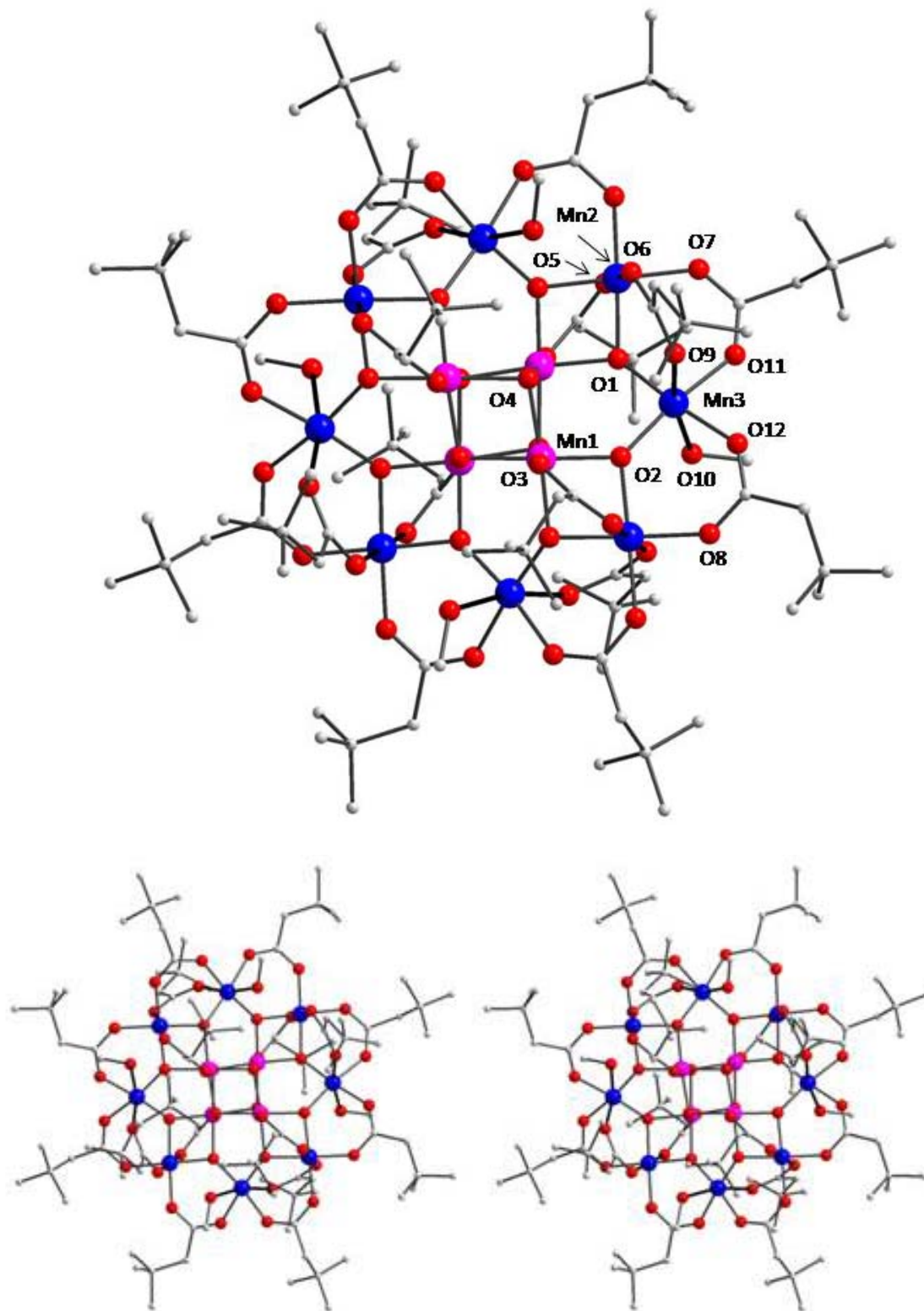


Figure 2-8. PovRay representations of the partially labeled core (top) and a stereopair (bottom) of complex 3. Mn^{IV} purple; Mn^{III} blue; O red; C gray.

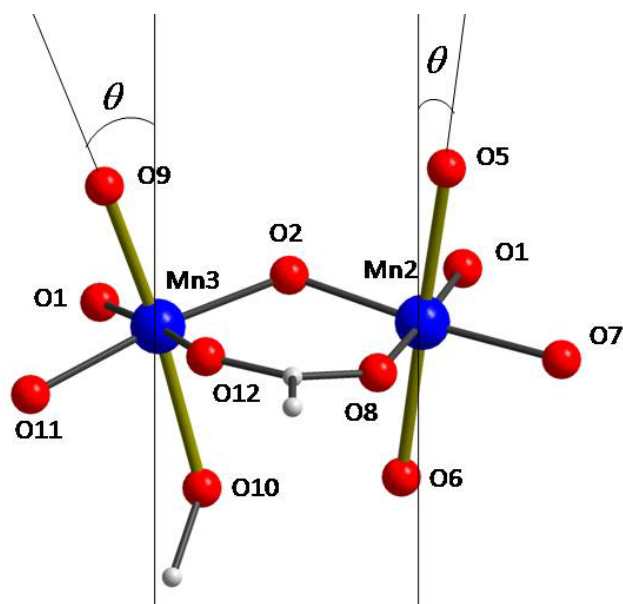
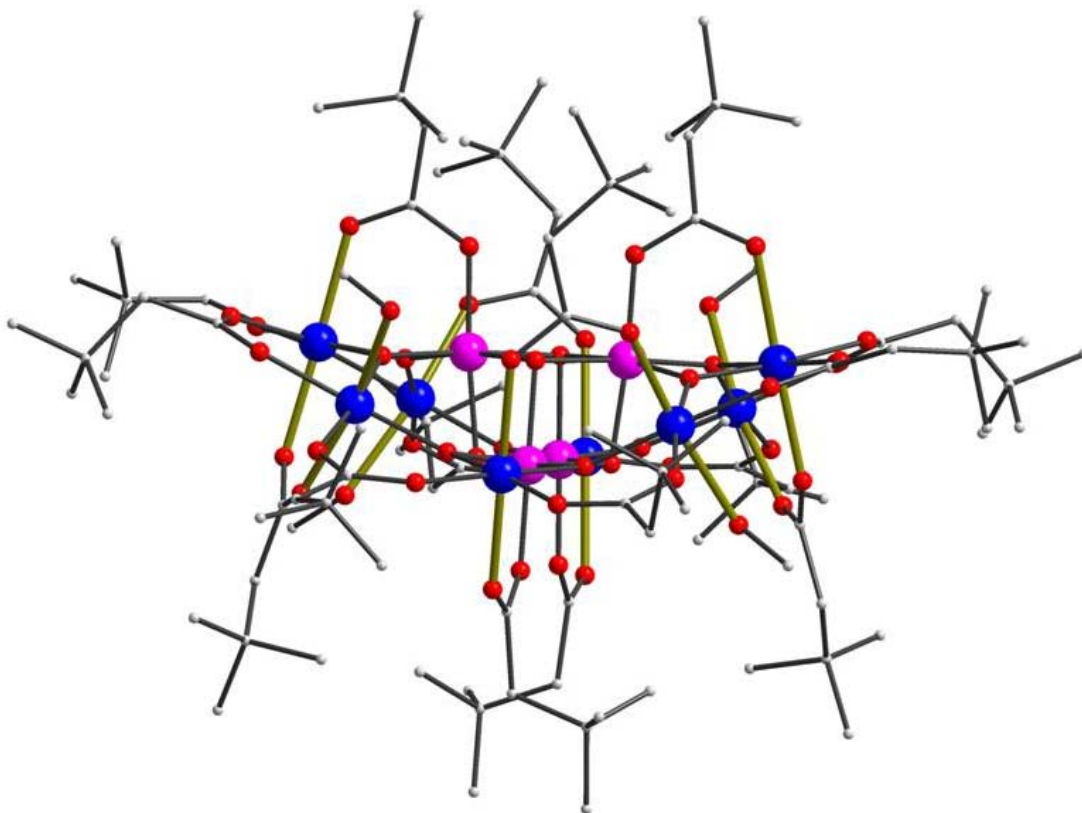


Figure 2-9. Side view of complex **3**, emphasizing the disposition of the Jahn-Teller (JT) axes (top) and the anisotropy (JT) axes of Mn2 and Mn3, where θ is the angle of the local Mn^{III} anisotropy axis with respect to the crystallographic z axis (bottom). JT axes are shown in dark green for emphasis. Mn^{IV} purple; Mn^{III} blue; O red; C gray.

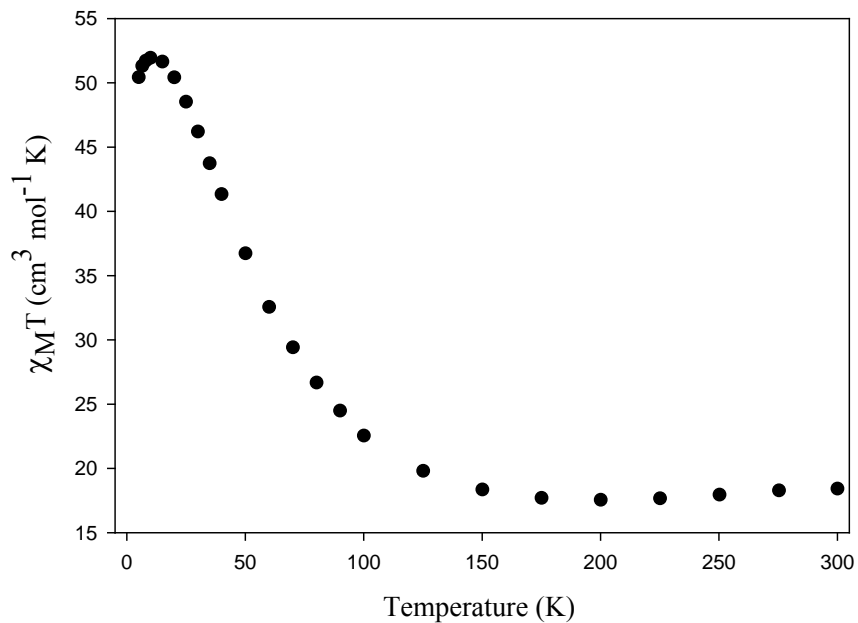


Figure 2-10. Plot of $\chi_M T$ vs temperature for a dried, microcrystalline sample of complex **3** in eicosane. χ_M is the DC molar magnetic susceptibility measured in a 1.0 kG field.

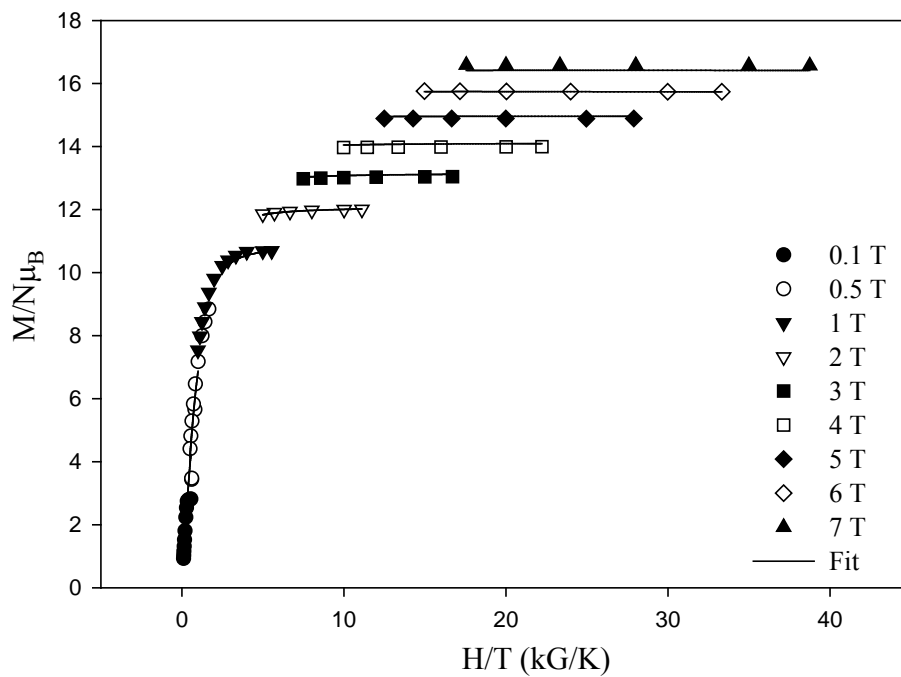


Figure 2-11. Plot of $M/N\mu_B$ vs H/T for complex **3** at the indicated applied fields. The solid lines are the fit of the data; see text for the fit parameters.

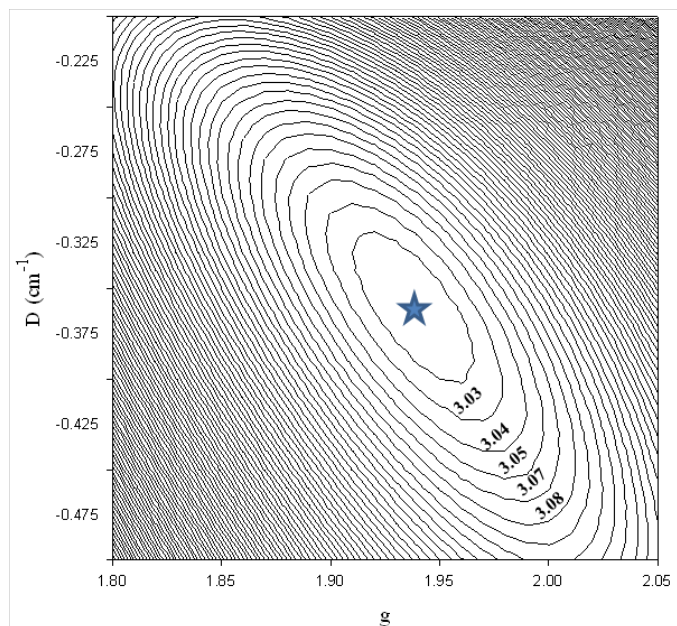


Figure 2-12. Two dimensional contour plot of the fitting error surface vs D and g for **3**.

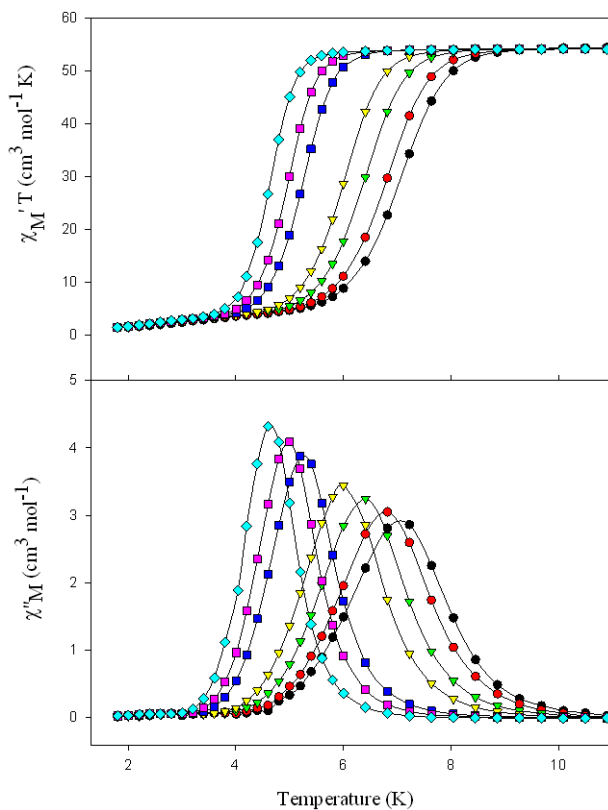


Figure 2-13. Plot of the in-phase (as $\chi_M' T$) and out-of-phase (χ_M'') AC susceptibility signals vs temperature for dried, microcrystalline complex **3** at the indicated oscillation frequencies.

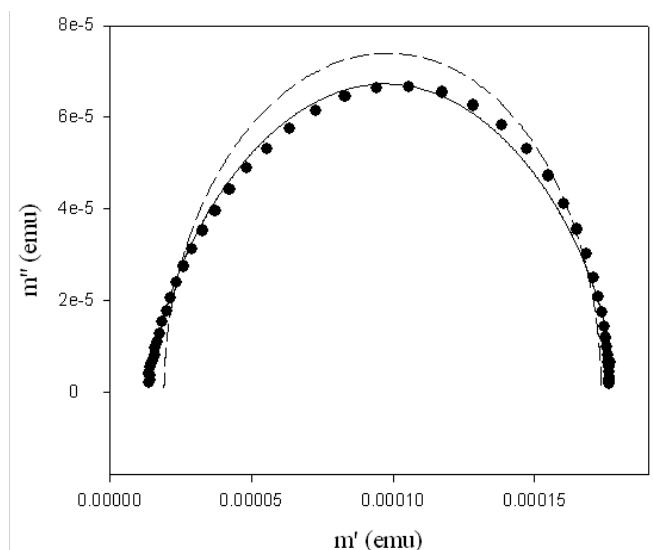


Figure 2-14. Argand plot of m' vs m'' of dried crystals of $3 \cdot 2\text{H}_2\text{O}$ at 4.6 K. The dashed line is a least-squares fitting of the data to a single relaxation process as described by eqs 2-3 and 2-4. The solid line is a least-squares fitting of the data to a distribution of single relaxation processes as described by eqs 2-5 and 2-6.

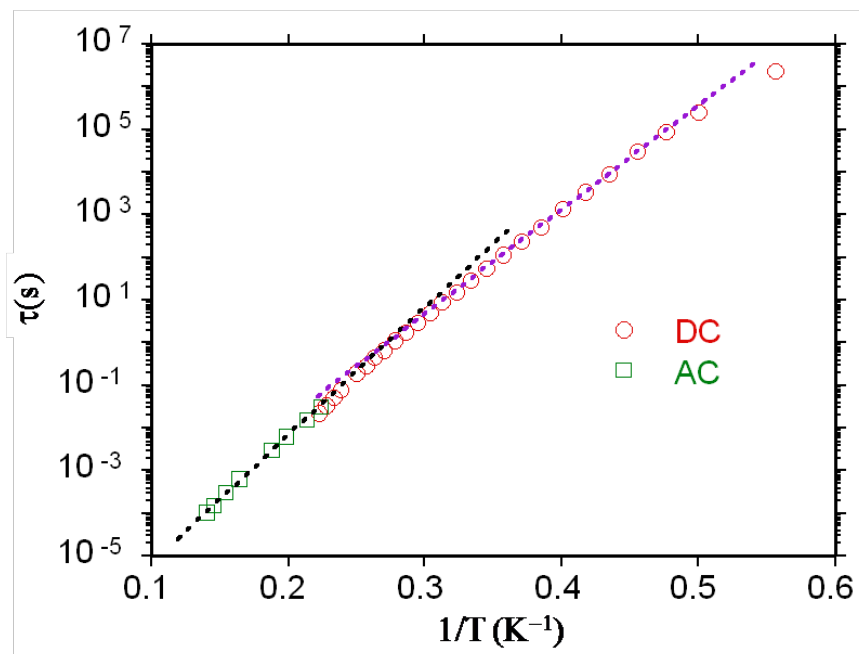


Figure 2-15. Plot of relaxation time (τ) vs $1/T$ for complex **3** using AC χ_M'' and DC magnetization decay data. The solid line is a fit to the Arrhenius equation. See text for the fit parameters.

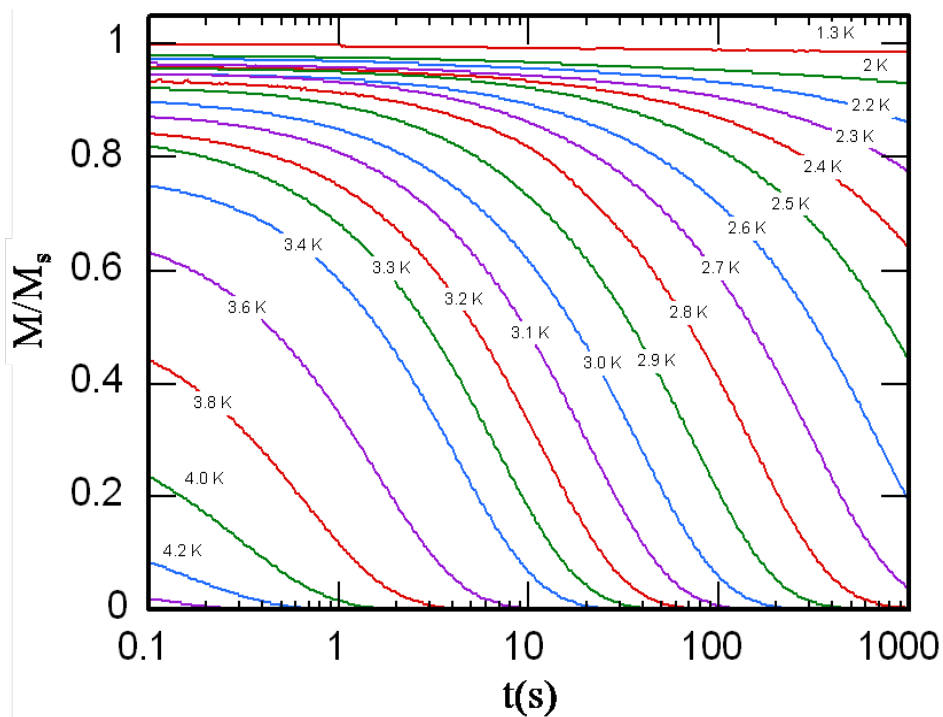


Figure 2-16. Plot of the magnetization versus time decay data for crystals of complex **3**, at the indicated temperatures. M is normalized to its saturation value, M_s .

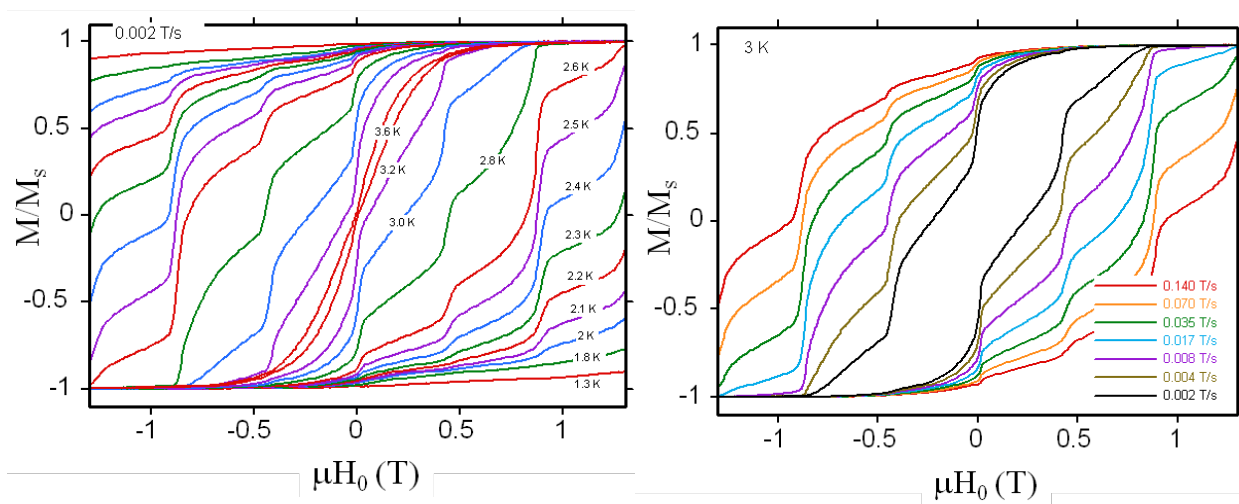


Figure 2-17. Magnetization hysteresis loops for a single crystal of **3**: (left) temperature dependence at a fixed scan rate of 2 mT/s; (right) scan-rate dependence at a fixed temperature of 3.0 K. M is normalized to its saturation value, M_s .

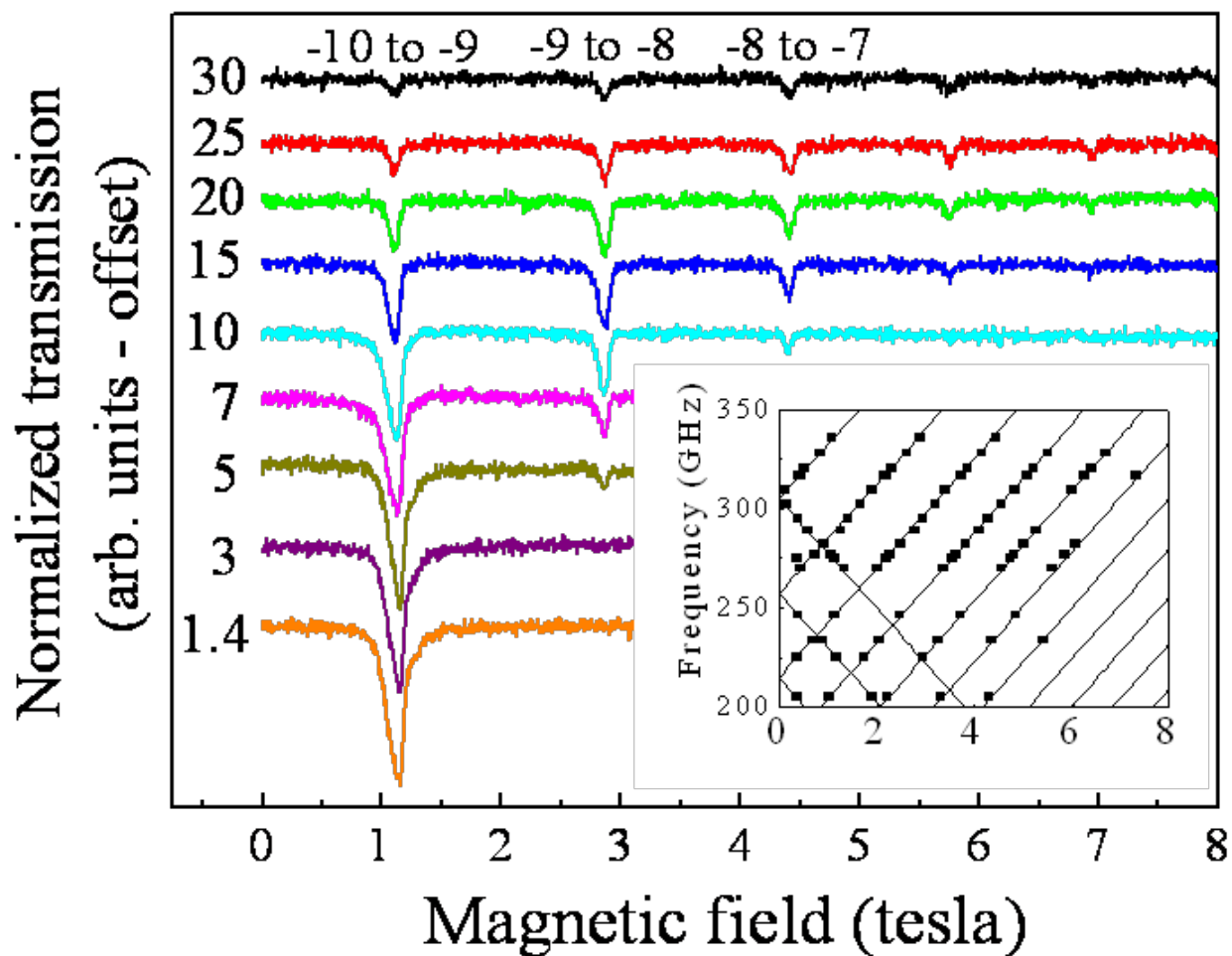


Figure 2-18. Temperature dependence of the easy-axis HFEPR spectra obtained for complex **3** at a frequency of 336 GHz. The temperatures are given in kelvin on the left-hand side of the figure, and several of the resonances have been labeled according to the m_s levels involved in the transition. The inset shows the positions (in field) of resonances deduced from 25 K spectra taken at many different frequencies. The solid lines are fits to the data points using Eq. 2-11. In order to improve the quality of the fit, a long range dipolar contribution to the local magnetic induction was included in the analysis.

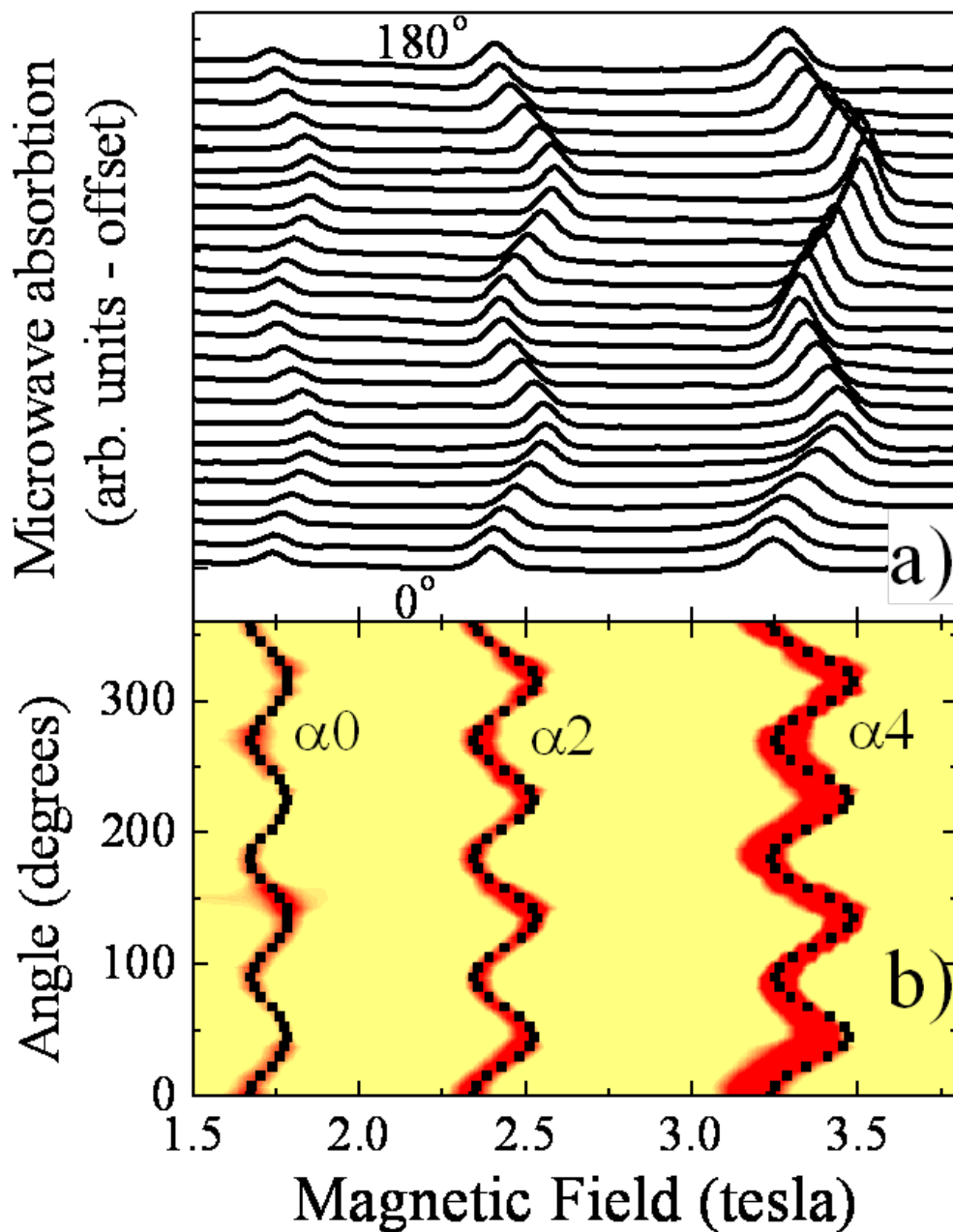


Figure 2-19. (a) Angle dependence of the hard-plane HFEPR spectra obtained for complex **3** at 15 K and a frequency of 51.5 GHz, for different orientations of the applied field within the hard plane; the angle step is 7.5° , and 0° corresponds to the field parallel to one of the medium axes associated with the 4th order transverse anisotropy. (b) A color contour plot of the data in (a); the resonances have been labeled according to the scheme in ref. 57. The data points represent the best fit to the angle-dependence of the peak positions. From these fits, a unique value for the B_4^4 parameter is obtained.

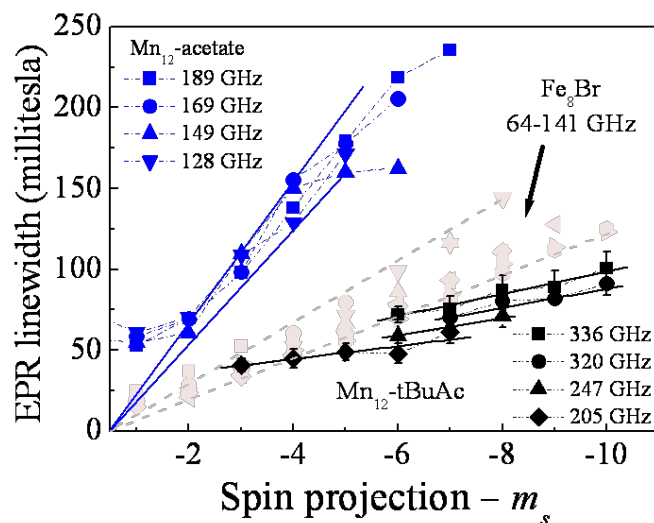


Figure 2-20. The full-width-at-half-maximum (FWHM) deduced from Gaussian fits to easy-axis HF-EPR data obtained for three different $S = 10$ SMMs for a range of frequencies: **1** at 20 K (blue data); Fe₈Br at 10 K (light gray); and Mn₁₂-tBuAc (complex **3**) at 25 K (black data). The horizontal axis denotes the m_s value for the level from which the EPR transition was excited. See main text and Eq. (2-11) for explanation of the data.

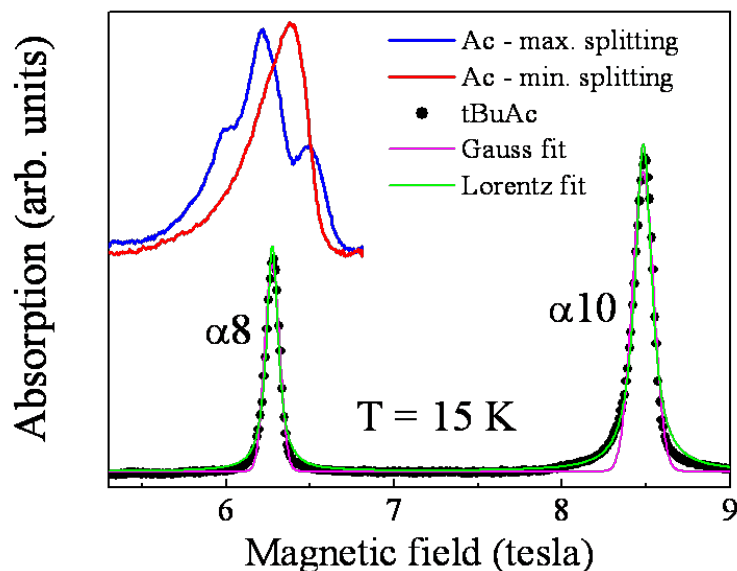


Figure 2-21. A comparison between the hard-plane HF-EPR spectra obtained for **1** and complex **3**, at 15 K and 51.5 GHz. Data for **1**, which have been offset for clarity, are only available below 6.8 T. The solvent disorder in **1** gives rise to fine structures (high- and low-field shoulders) which are well resolved from the central peak for some field orientations within the hard plane (blue curve), and unresolved for others (red curve). These fine structures are completely absent in the data for complex **3**. The thin green and magenta curves are Lorentzian and Gaussian fits to the Mn₁₂-¹BuAc data, respectively.

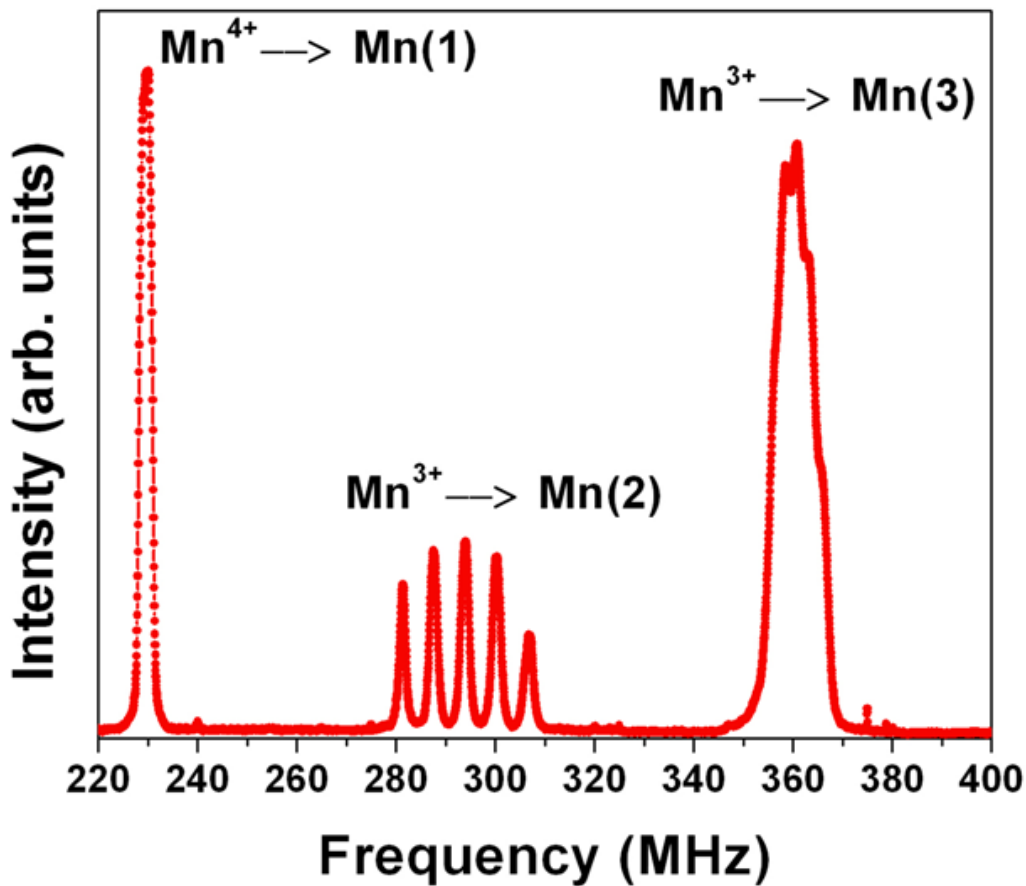


Figure 2-22. Zero-field ^{55}Mn spectrum of **3**. The peaks are assigned as Mn(1), Mn(2), and Mn(3) for ease of discussion.

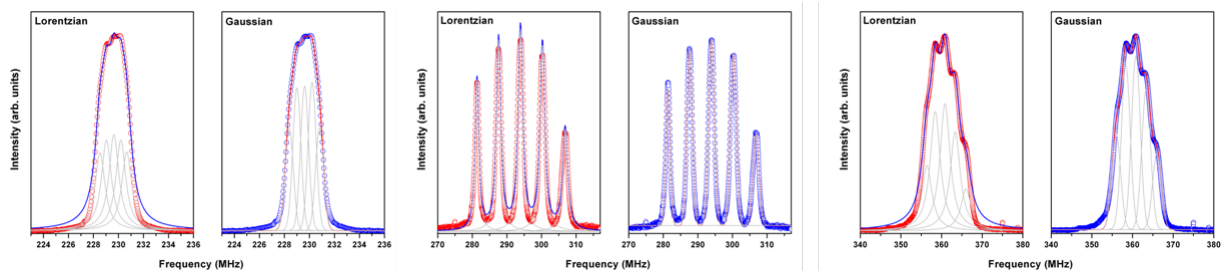


Figure 2-23. Line fits for the Mn(1), Mn(2) and Mn(3) resonances. The left ^{55}Mn spectrum is fit to multiple Lorentzian curves while the right spectrum is fit with multiple Gaussian curves. No spectrum fits perfectly well to either line shape.

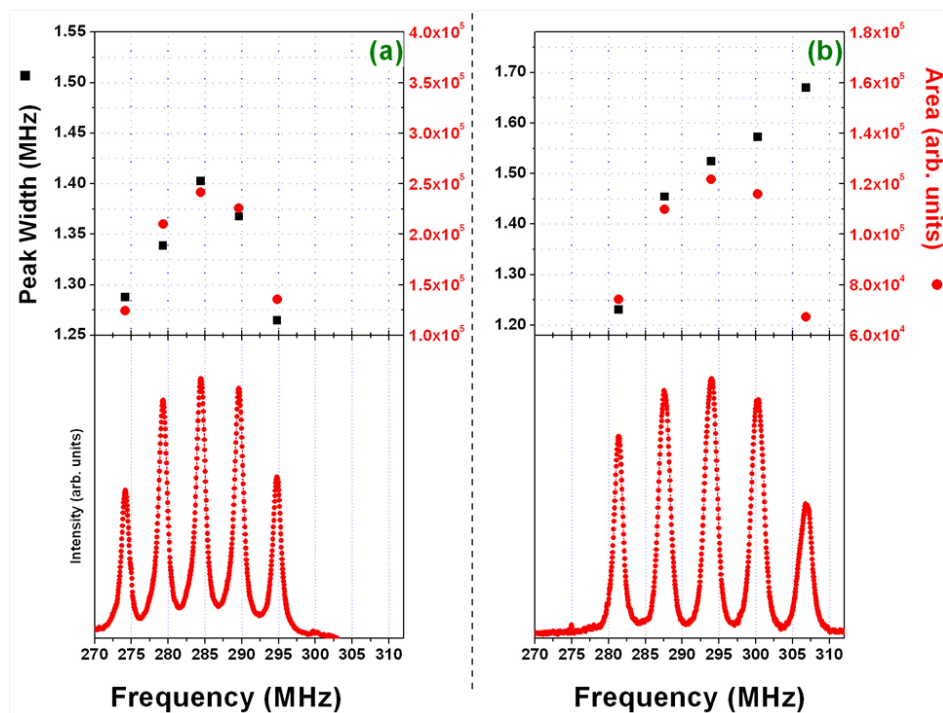


Figure 2-24. Comparison of the line width and peak area of the Mn(2) peaks for (a) Mn₁₂-BrAc and (b) **3**. The peak width for **3** continually increases on moving to higher frequency, unusual behavior which has yet to be fully explained.

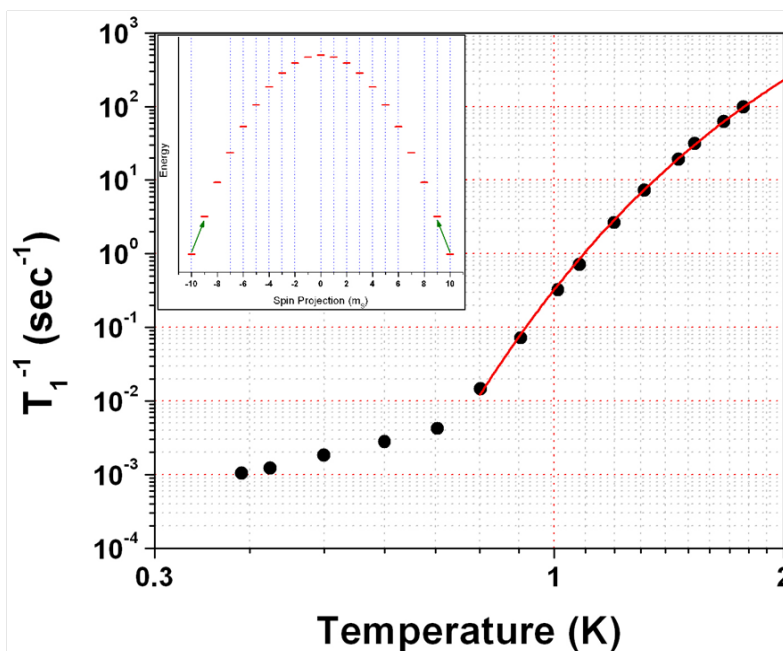


Figure 2-25. Spin-Lattice relaxation rate (T_1^{-1}) of the Mn(1) peak for a single crystal of **3** down to He-3 temperatures. Fit to the data gives the activation barrier between the $m_S = \pm 10$ and $m_S = \pm 9$ states.

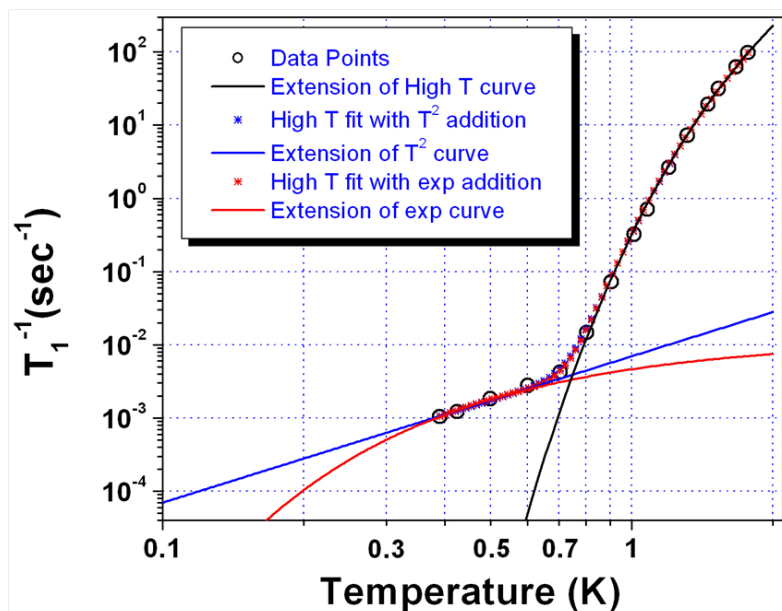


Figure 2-26. T_1^{-1} fits extended down to 100 mK. Dilution fridge studies are necessary to differentiate the fits.

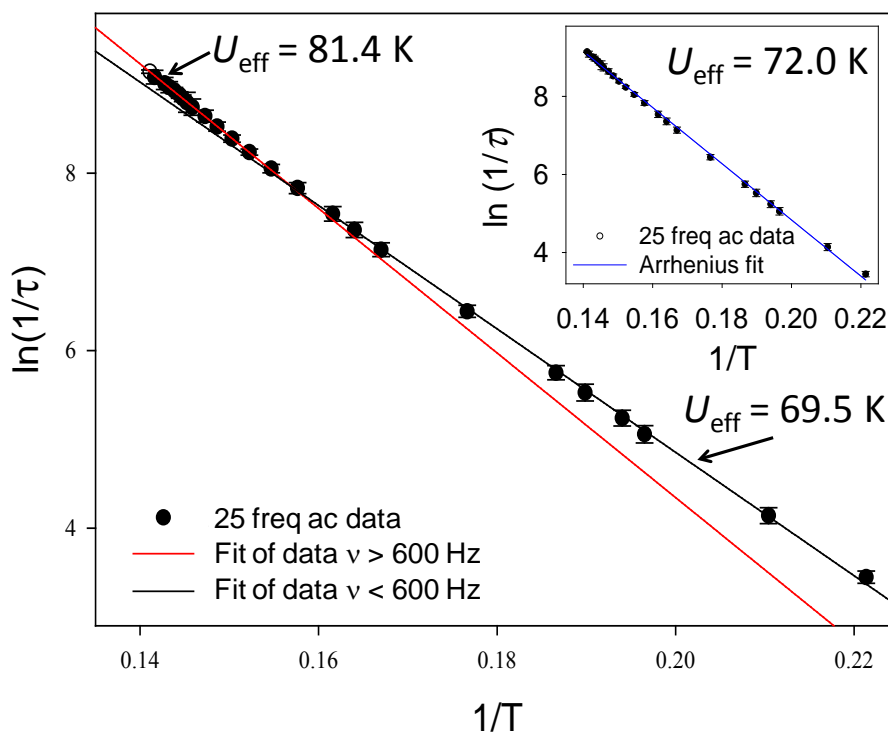


Figure 2-27. Plot of the natural logarithm of the magnetization relaxation rate vs $1/T$ for $3\cdot\text{MeOH}$: solid lines are the separate (two-line) fits of data at $>$ and $<$ 600 Hz to eq 2-17, and are extended to emphasize the different slopes; (inset) the fit of all the data to eq 2-17.

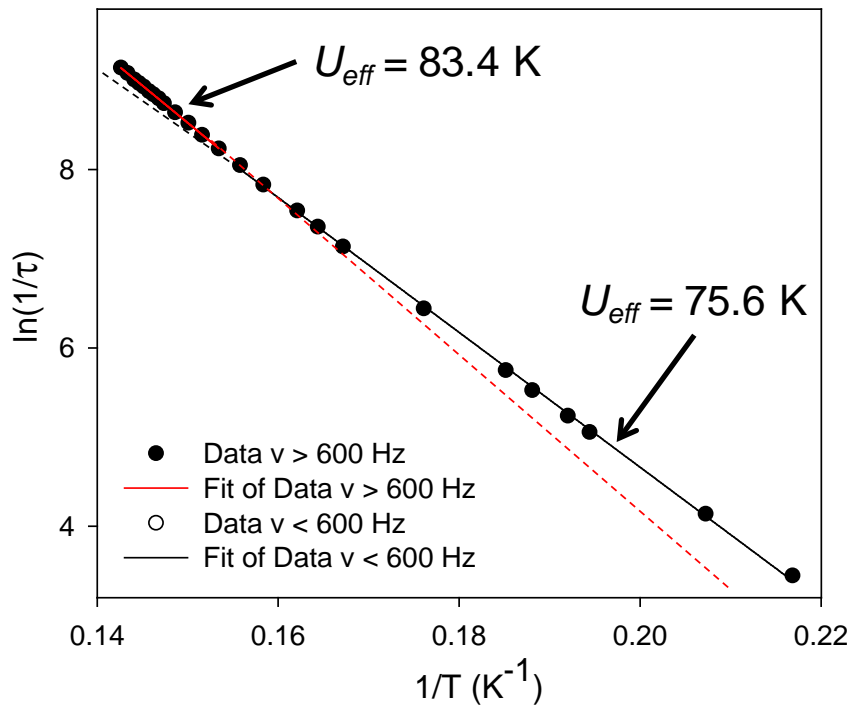


Figure 2-28. Plot of the natural logarithm of the magnetization relaxation rate vs $1/T$ for **2**: solid lines are the separate (two-line) fits of data at $>$ and $<$ 600 Hz to eq 1; dashed lines are extrapolations of the solid lines.

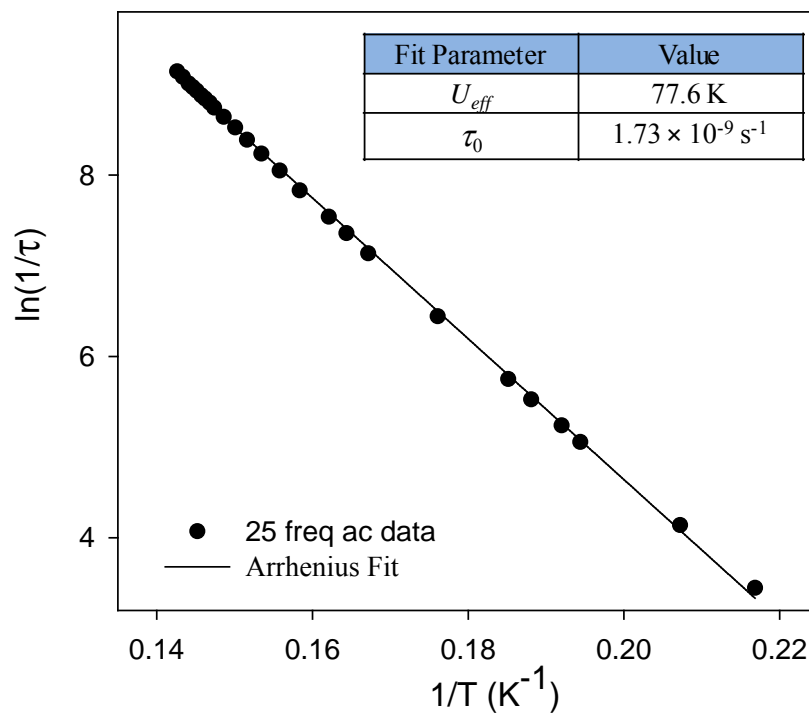


Figure 2-29. The fit of all the data for **2** to eq 2-17.

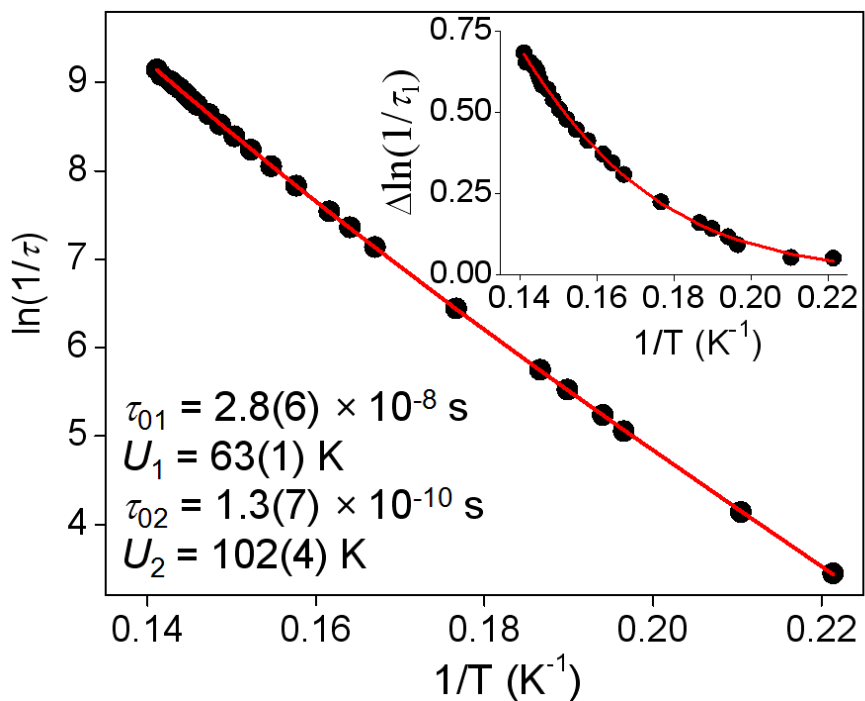


Figure 2-30. Plot of $\ln(1/\tau)$ vs $1/T$ for 3-MeOH. The solid line is the fit to the double-exponential function of eq 2-18. The inset shows the deviation $\Delta\ln(1/\tau_1)$ of the data from the straight line given by the first term of eq 2-18.

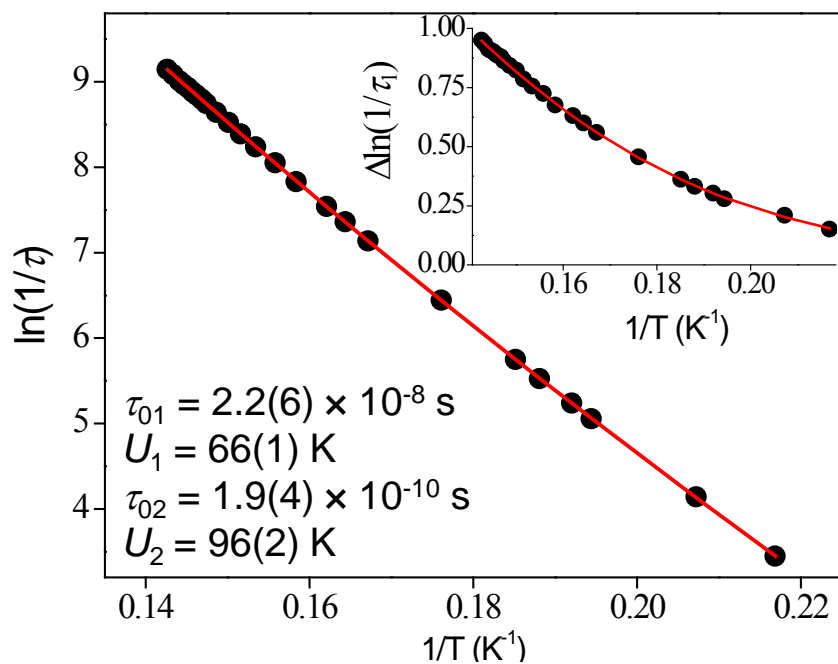


Figure 2-31. Plot of $\ln(1/\tau)$ vs $1/T$ for **2**. The solid line is the fit to the double-exponential function of eq 2-18. The inset shows the deviation $\Delta\ln(1/\tau)$ of the data from the straight line given by the first term of eq 2-18.

CHAPTER 3
NEW PENTA- AND HEXANUCLEAR MIXED-VALENT MANGANESE CLUSTERS FROM
THE USE OF OXIMATO LIGANDS AND AZIDES

3.1 Introduction

There continues to be an intense interest by many groups around the world in the synthesis and study of polynuclear 3d transition metal complexes, not least for their intrinsic architectural beauty and aesthetically pleasing structures.¹²³ Other reasons for this interest are varied. For manganese chemistry, for example, this interest derives from their relevance to two fields. First, the ability of Mn to exist in a number of oxidation states (II-IV) under normal conditions has resulted in this metal being at the active sites of several redox enzymes, the most important of which is the wateroxidizing complex (WOC) on the donor side of photosystem II in green plants and cyanobacteria.¹²⁴⁻¹²⁷ The WOC comprises a tetranuclear Mn cluster, whose exact structure is still unclear, and is responsible for the light-driven, oxidative coupling of two molecules of water into dioxygen.^{128,129} In addition, one Ca plays a crucial role in the WOC activity; without Ca, the WOC does not advance to the S₃ state.^{130,131} Although there is considerable uncertainty about the Mn₄Ca structure obtained from crystallography due to the current resolution,¹³² there is little doubt that the WOC is indeed a heterometallic [Mn₄CaO_x] cluster on the basis of other spectroscopic studies (i.e., XRD^{124,131}, and EXAFS¹³³). Second, polynuclear Mn compounds containing Mn^{III} have been found to often have large, and sometimes abnormally large, ground-state spin values (S), which combined with a large and negative magnetoanisotropy have led to some of these species being able to function as single-molecule magnets (SMMs).²⁶ These are individual molecules that behave as magnets below a certain (“blocking”) temperature.^{49,134} Thus, they represent a molecular, “bottom-up” approach to nanomagnetism.⁴⁹

As a result of the above, we have explored and successfully developed many new routes for the synthesis of polynuclear Mn complexes,^{86,88} with nuclearities currently up to 84.⁵⁶ These

procedures have included comproportionation reactions of simple starting materials,^{34,73} aggregation of clusters of smaller nuclearity,¹³⁵ fragmentation of higher nuclearity clusters,^{136,137} reductive aggregation or fragmentation of preformed clusters,^{17,76,78,80,92,138} and electrochemical oxidation,¹³⁹ disproportionation,¹⁴⁰ or ligand substitution of preformed species,^{135,141,142} among others. As part of this work, we have also explored a wide variety of potentially chelating and/or bridging ligands that might foster formation of high nuclearity products. One such family is the pyridyl alcohols, which have proven to be extremely versatile N,O_x (x = 1, hmpH; x = 2, pdmH₂; Figure 3-1) chelating and bridging groups that have yielded a number of 3d metal clusters with various structural motifs, large S values, and SMM behaviors.^{52,88,141,143-147} More recently, we have been investigating a number of other N- and O-based chelates, and one of these has been the 2-pyridyl oximes, particularly methyl-2-pyridyl ketone oxime (mpkoH; Figure 3-1). We recently reported, for example, the employment of mpkoH in Mn carboxylate chemistry, which gave the initial examples of triangular Mn^{III} SMMs by switching the exchange coupling from the more usual antiferromagnetic to ferromagnetic.^{53,55} As an extension to this work with mpkoH, we have now asked what kind of products might result from the use of non-carboxylate sources of Mn ions, as well as from the addition of another ketone oxime arm onto the mpkoH group but on the other side of the pyridine ring, much like the way that pdmH₂ is hmpH with another hydroxymethyl arm attached at its 6-position (Figure 3-1). The latter resulting molecule, 2,6-diacetylpyridine dioxime (dapdoH₂), is shown in Figure 3-1, where the analogy between the mpkoH/dapdoH₂ and hmpH/pdmH₂ pairs can be clearly seen. Our initial results were very promising, with homometallic Mn clusters with metal nuclearities 6 and 8,¹⁴⁸ and a very interesting Mn^{IV}Gd^{III}₂ heterometallic complex (see Chapter 5).¹⁴⁹ We anticipated that the use of dapdoH₂ in polynuclear transition metal cluster chemistry would give products distinctly

different from those with mpkoH, and we have therefore explored its use initially in Mn chemistry. Except of the few Mn clusters mentioned above, dapdoH₂ has also been employed to date in the literature only for the synthesis of mononuclear [M(dapdoH₂)₂]²⁺ (M = Mn, Fe, Co, Ni, Cu, and Zn) complexes, containing neutral dapdoH₂ groups bound only through their three N atoms,¹⁵⁰ dinuclear [Cu₂(dapdoH)₂]²⁺ where a mono-deprotonated dapdoH⁻ N,N,N-chelates each Cu^{II} ion and links with its deprotonated arm to the neighboring Cu^{II},¹⁵¹ and [Fe(dapdoH)₂{Fe₂OCl₄}], where the two dapdoH⁻ groups N,N,N-chelate to a Fe^{II} ion and bridge through their deprotonated arms to a Fe^{III}₂ unit.¹⁵² In the present investigations, we have deliberately targeted higher nuclearity Mn products by exploring the reactions between mpkoH and dapdoH₂ and various Mn starting materials under basic conditions, in the presence or not of azido ligands. This has successfully led to two pentanuclear and two hexanuclear cluster products, the former containing deprotonated dapdoH⁻ and dapdo²⁻, and the latter incorporating the anion of mpkoH. The syntheses, structures, and magnetochemical characterization of these complexes are described.

3.2 Experimental Section

3.2.1 Syntheses

All manipulations were performed under aerobic conditions using chemicals and solvents as received, unless otherwise stated. mpkoH was prepared as described elsewhere.¹⁵³ dapdoH₂ was synthesized as previously reported.¹⁵⁰ *Warning: Azide and perchlorate salts are potentially explosive; such compounds should be synthesized and used in small quantities, and treated with utmost care at all times.*

3.2.1.1 [Mn₆O₃(N₃)₃(mpko)₆(H₂O)₃](ClO₄)₂ (5)

To a stirred solution of mpkoH (0.14g, 1.0mmol), and NEt₃ (0.14mL, 1.0mmol) in MeOH (30ml) was added solid NaN₃ (0.06g, 1 mmol). After being stirred for about 10 minutes, solid

$\text{Mn}(\text{ClO}_4)_2 \cdot 6\text{H}_2\text{O}$ (0.25g, 1mmol) was added, and the solution soon became dark brown. The reaction mixture was kept under magnetic stirring for another 30 minutes. The solution was then filtered and Et_2O was allowed to slowly diffuse over a period of 2 days, during which time large brown crystals of **5** grew; yield ~50% based on manganese. The crystals of **5** were maintained in the mother liquor for X-ray crystallography and other single-crystal studies, or collected by filtration, washed with diethylether, and dried in vacuo. Anal. Calcd (Found) for **5**: C, 29.62 (29.69)%; H, 3.20 (3.26)%; N, 17.27 (17.21)%. Selected IR data (KBr, cm^{-1}): 3440(b), 2925(w), 2363(w), 2048(vs), 1636(sm), 1601(sm), 1470(bw), 1381(sw), 1333(bw), 1263(bw), 1152(vs), 1080(vs), 782(sm), 705(m), 629(bm).

3.2.1.2 $[\text{Mn}_6\text{O}_3(\text{N}_3)_5(\text{mpko})_6(\text{H}_2\text{O})] \cdot 4\text{H}_2\text{O}$ (**6**)

To a stirred solution of mpkoH (0.27g, 2.0mmol), NEt_3 (0.33mL, 2.3mmol), and NaO_2CMe (0.08g, 1.0mmol) in MeOH (30ml) was added solid NaN_3 (0.06g, 1mmol). After being stirred for about 10 minutes, solid $\text{Mn}(\text{ClO}_4)_2 \cdot 6\text{H}_2\text{O}$ (0.51g, 2.0mmol) was added, and the solution soon became dark brown. The reaction mixture was kept under magnetic stirring for another 30 minutes. The solution was then filtered and Et_2O was allowed to slowly diffuse over a period of 2 days, during which time large brown crystals of **6** grew; yield ~50% based on the total manganese. The crystals of **6** were maintained in the mother liquor for X-ray crystallography and other single-crystal studies, or collected by filtration, washed with diethylether, and dried in vacuo. Anal. Calcd (Found) for **6** (solvent free): C, 32.88 (32.46)%; H, 3.15 (3.27)%; N, 24.65 (24.22)%. Selected IR data (KBr, cm^{-1}): 3421(b), 2362(w), 2336(w), 2038(vs), 1636(bw), 1600(sm), 1554(m), 1474(m), 1435(bw), 1374(w), 1333(w), 1284(w), 1160(sm), 1103(sm), 1068(sm), 1045(sm), 781(m), 706(m), 590(bm).

3.2.1.3 [Mn₅O₂(OMe)₂(N₃)₃(dapdo)₃(py)₂]·py·MeOH (**7**)

To a stirred solution of dapdoH₂ (0.20g, 1.0mmol), NEt₃ (0.28mL, 2.0mmol) in MeOH (20 mL) / pyr (5 mL) was added solid NaN₃ (0.13g, 2.0mmol) in small portions. After being stirred for about 10 minutes, solid MnCl₂ · 4H₂O (0.40 g, 2.0mmol) was added. The reaction mixture was kept under magnetic stirring for another 2hours. The solution was then filtered and Et₂O or Et₂O / hexanes (2:1) was allowed to slowly diffuse over a period of 2 days, during which time large dark brown crystals of **3** grew; yield ~50% based on manganese. The crystals of **7** were maintained in the mother liquor for X-ray crystallography and other single-crystal studies, or collected by filtration, washed with diethylether, and dried in vacuo. Anal. Calcd (Found) for **7**·H₂O: C, 37.64 (37.56)%; H, 3.64 (3.68)%; N, 22.51 (22.88)%. Selected IR data (KBr, cm⁻¹): 3423(bm), 2475(bm), 2082(vs), 1040(w), 1590(sm), 1528(sm), 1442(bm), 1368(bm), 1214(sm), 1190(sm), 1134(vs), 1056(vs), 961(bm), 803(vs), 743(vs), 697(vs), 665(vs), 642(bm), 619(bm), 553(bm).

3.2.1.4 [Mn₅O₂(N₃)_{3.5}(O₂CMe)(dapdo)₃(py)_{2.5}](N₃)_{0.5} (**8**)

To a stirred solution of dapdoH₂ (0.2g, 1mmol), NEt₃ (280μL, 2mmol) in MeCN (25 mL) / pyr (5 mL) was added solid NaN₃ (0.13g, 2mmol) in small portions. After being stirred for about 10 minutes, solid MnCl₂ · 4H₂O (0.40 g, 2mmol) was added. The reaction mixture was kept under magnetic stirring for another 3 hours. The solution was then filtered and Et₂O or Et₂O / hexanes (2:1) was allowed to slowly diffuse over a period of 2 days, during which time small black crystals of **8** grew; yield 20% based on manganese. The crystals of **8** were maintained in the mother liquor for X-ray crystallography and other single-crystal studies, or collected by filtration, washed with diethylether, and dried in vacuo. Anal. Calcd (Found) for **8** (solvent free): C, 33.95 (34.02)%; H, 3.33 (3.47)%; N, 22.42 (21.95)%. Selected IR data (KBr, cm⁻¹): 2910(bm), 2801(bm), 2041(vs), 1952(vs), 1530(m), 1443(bm), 1369(m), 1338(bm), 1284(m),

1215(sm), 1134(vs), 1058(vs), 936(bm), 805(sm), 745(sm), 697(sm), 665(vs), 642(vs), 621(bm), 555(vs).

3.2.2 X-Ray Crystallography

Data for complexes **5**, **7**, and **8** were collected by Dr. K. A. Abboud on a Siemens SMART PLATFORM equipped with a CCD area detector and a graphite monochromator utilizing Mo K α radiation ($\lambda = 0.71073 \text{ \AA}$). Cell parameters were refined using up to 8192 reflections. A full sphere of data (1850 frames) was collected using the ω -scan method (0.3° frame width). The first 50 frames were re-measured at the end of data collection to monitor instrument and crystal stability (maximum correction on I was $< 1 \%$). Absorption corrections by integration were applied based on measured indexed crystal faces. Data for the selected crystal of **6** were collected by Dr. A. J. Tasiopoulos on an Oxford Diffraction Xcalibur-3 diffractometer (equipped with a Sapphire CCD area detector). Cell parameters were refined by using 15920 reflections ($3.1 \leq \theta \leq 30.2^\circ$). Data (792 frames) were collected using the ω -scan method (0.60° frame). Empirical absorption corrections (multi-scan based on symmetry-related measurements) were applied using CrysAlis RED software. The structure was solved by direct methods using SIR2002 and refined on F^2 using full-matrix least-squares with *SHELXL-97*. All non-H atoms were refined anisotropically. Suitable crystals of the complexes were attached to glass fibers using silicone grease and transferred to a goniostat where they were cooled to 173 K for data collection. An initial search of reciprocal space revealed triclinic cell for complex **5**, a monoclinic one for **6**, and **7**, and tetragonal for **8**; the choice of space groups $P\bar{1}$ for **5**, $P2_1/n$ for **6**, $C2/c$ for **7**, and $P4_2/n$ for **8** respectively, was confirmed by the subsequent solution and refinement of the structures. Crystal data and structural refinement parameters for complexes **5-8** are listed in Table D-3.

3.2.2.1 X-ray crystal structure of complex 5

The asymmetric unit consists of a Mn_6 dication cluster, two disordered perchlorate anions, and five water molecules. Both anions are disordered and were refined in two parts each with their site occupation factors dependently refined. Additionally, their structures were constrained to maintain ideal geometries. None of the water molecules protons could be located in Difference Fourier maps and thus were not included in the final refinement model. A total of 811 parameters were refined in the final cycle of refinement using 4501 reflections with $I > 2\sigma(I)$ to yield R_1 and wR_2 of 9.55% and 22.98%, respectively. Refinement was done using F^2 .

3.2.2.2 X-ray crystal structure of complex 6

For complex **6**, the asymmetric unit contains a Mn_6 cluster, and 4 water molecules. A total of 9937 parameters were refined in the final cycle of refinement using 5858 reflections with $I > 2\sigma(I)$ to yield R_1 and wR_2 of 7.91% and 13.43%, respectively. Refinement was done using F^2 .

3.2.2.3 X-ray crystal structure of complex 7

The Mn_5 clusters are located on 2-fold rotation axes. Mn1 and its symmetry equivalent, Mn1a, are bridged by an azide disordered against a methoxy ligand. The 2-fold rotation axis passes through the middle nitrogen of the azide as well as the C-C bond of the methoxy ligand. There is also a pyridine molecule and a methanol molecule in the asymmetric unit. The H atoms of the methanol molecule could not be located in Difference Fourier maps and could not be calculated in idealized positions. Thus they were not included in the final cycle of refinement. A total of 367 parameters were refined in the final cycle of refinement using 4342 reflections with $I > 2\sigma(I)$ to yield R_1 and wR_2 of 8.08% and 21.13%, respectively. Refinement was done using F^2 .

3.2.2.4 X-ray crystal structure of complex 8

For complex **8**, in addition to the Mn_5 cluster, there are four acetonitrile solvent molecules in the unit cell. However, the best refined model shows a disorder in C27 methyl group and

another between the N21 pyridine ligand and the N22 azide ligand. Each was refined with a 50% occupation factor. For charge balance, a half negative charge is needed, which is a half azide anion. Due to the disorder in all four acetonitrile molecules, finding and refining a half azide was not feasible. Thus the final model has only the cluster, while all solvent molecules, including a half azide, were removed by program SQUEEZE, a part of the PLATON package of crystallographic software; thus, the solvent disorder area was calculated and its contribution to the overall intensity data was removed. A total of 679 parameters were refined in the final cycle of refinement using 2977 reflections with $I > 2\sigma(I)$ to yield R_1 and wR_2 of 6.54% and 15.11%, respectively. Refinement was done using F^2 .

3.2.3 Other studies

Infrared spectra were recorded in the solid state (KBr pellets) on a Nicolet Nexus 670 FTIR spectrometer in the 400-4000 cm^{-1} range. Elemental analyses (C, H, and N) were performed by the in-house facilities of the University of Florida Chemistry Department. Variable-temperature dc and ac magnetic susceptibility data were collected at the University of Florida using a Quantum Design MPMS-XL SQUID susceptometer equipped with a 7 T magnet and operating in the 1.8-300 K range. Samples were embedded in eicosane to prevent torquing. Pascal's constants were used to estimate the diamagnetic correction, which was subtracted from the experimental susceptibility to give the molar paramagnetic susceptibility (χ_M).

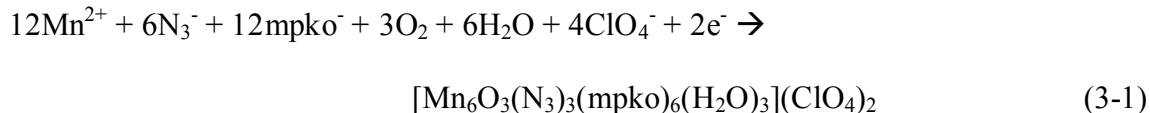
3.3 Results and Discussion

3.3.1 Syntheses

Many synthetic procedures^{53-55,135,148,154} to polynuclear Mn clusters rely on the reactions of carboxylate starting materials (either simple Mn^{II} salts such as $\text{Mn}(\text{O}_2\text{CR})_2$ ($\text{R} = \text{various}$), or preformed higher oxidation Mn_x carboxylate clusters such as $[\text{Mn}_3\text{O}(\text{O}_2\text{CR})_6\text{L}_3]^{0/+155}$ or $[\text{Mn}^{\text{III}}_4\text{O}_2(\text{O}_2\text{CPh})_9(\text{H}_2\text{O})]^{-156}$ with a potentially chelating/bridging ligand. Both routes were

known from previous work^{53-55,157,158} to yield magnetically and structurally interesting complexes upon reaction with mpkoH. In the present study we have investigated the reactions with simple Mn^{II} sources, i.e. MnCl₂ and Mn(ClO₄)₂, in the presence of azides and the absence of carboxylate groups.

A thorough investigation of this reaction system was carried out, including reactions where the reagent identities, ratios, and solvent combinations were varied. The 1:1:1 reaction between Mn(ClO₄)₂, NaN₃, and mpkoH in MeOH in the presence of one equivalent of OH⁻ gave [Mn₆O₃(N₃)₃(mpko)₆(H₂O)₃](ClO₄)₂ (**5**), a mixed-valent Mn^{II}Mn^{III}₅ species; the Mn^{III} ions were clearly formed by aerial oxidation of Mn^{II} in the presence of the base.¹⁵⁸ The reaction is summarized in eq 3-1.

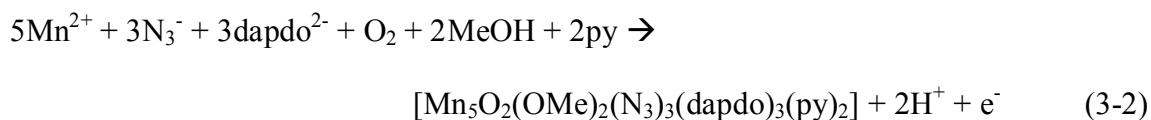


The azido ligands were successfully incorporated in the structure, while their basic character increased the pH of the solution, propagating the oxidation of Mn^{II} ions to Mn^{III}. The order in which the reactants are added during the course of the reaction, follows a common and successfully-used in the past scheme. First the organic ligand was dissolved in the desired solvent (i.e. MeOH), followed by the addition of a base which would foster the chelate's deprotonation. Then, the addition of the azide increases the pH of the solution before dissolving the Mn non-carboxylate salt; addition of the Mn salt is followed by a direct noticeable color change of the solution to dark brown, due to the oxidation of the Mn^{II} ions to Mn^{III}, as a consequence of the basic conditions dominating the reaction mixture. As with many reactions in higher oxidation state Mn chemistry, it is likely that the solution contains a mixture of several species in equilibrium, and what crystallizes out is determined by the relative solubilities, the

nature of any counterions, lattice energies, and related factors.¹⁵⁹ The choice of MeOH as the reaction solvent is consistent with the previously reported experimental observation, where high-nuclearity high-valent complexes have been stabilized in methanolic media.^{148,158}

Similarly, in the case of **6**, the same synthetic methodology was used, with the only difference being the introduction of an additional base, namely NaO₂CMe. The latter was originally intended to afford acetate ions in solution, with the hope being that they would be incorporated giving a different type of product. However, carboxylates were not incorporated and a similar product to **5** was obtained; further investigation of this system did not produce any different results. From the isolation of **6** however, it became apparent that the incorporation of two more terminal azides in the structure of **6**, compared to **5**, caused the final product to be neutral.

The synthesis of complexes **7** and **8** follow a similar general route, only now a mixture of solvents was used. The reaction is summarized in eq 3-2.



For complex **7**, a mixture of MeOH and pyridine was used, whereas for **8** the MeOH was substituted by MeCN. Reactions without pyridine did not produce crystalline products, and this is possibly due to the basic character of pyridine and/or the crystal-lattice dynamics of the products. Thus, the presence of pyridine as a co-solvent was judged to be essential for the isolation of the products, since pyridine acts as an additional base and an ancillary ligand. Note that similar behavior was observed in the synthesis of the Ce₆Mn₄ cluster (complex **9**, Chapter 4). Complex **7** was found to contain two bridging methoxide ions which resulted from the methanolic media. When, MeCN was used instead of MeOH, the incorporation of methoxides

was prevented, and they were replaced by bridging end-on azides in **8** (vide infra). In addition, the end-to-end azide in **7** (vide infra), is now replaced by an acetate in **8**. The acetate ligand is believed to result from metal assisted oxidation of MeCN (as for the Mn^{IV}Gd₂ complex presented in Chapter 5), which is the reaction solvent in the case of **8**. In **7** such a transformation is not possible, since no MeCN was present, thus the end-to-end azide serves as the bridging ligand.

3.3.2 Description of Structures

The structure of complex **5** and a stereopair are presented in Figure 3-2, and the fully labeled core is shown in Figure 3-3. Selected interatomic distances are listed in Table D-4. Complex **5** crystallizes in the triclinic space group $P\bar{1}$. There is a $[\text{Mn}_6\text{O}_3(\text{N}_3)_2]^{9+}$ core consisting of one Mn^{II} (Mn6) and five Mn^{III} atoms bridged by three $\mu_3\text{-O}^{2-}$, and two end-on $\mu_2\text{-N}_3^-$; additional bridges and peripheral ligation is provided by six bidentate mpko⁻ groups (Figure 3-4). The core can be described as three oxide-centered triangular units, each sharing two of its vertices with its closest neighbors, via the end-on azide bridges. All Mn atoms are six-coordinate with near-octahedral geometry, except Mn1 which is five-coordinate with square pyramidal geometry; the oxidation states were established by charge considerations, bond valence sum (BVS) calculations (Table E-1), and the clear Jahn-Teller (JT) distortions (axial elongation) at the Mn^{III} atoms (Mn2, Mn3, Mn4, Mn5), with the JT elongated Mn^{III}-O bonds being at least 0.1-0.2 Å longer than the other Mn^{III}-O bonds. As is usually the case, these JT elongation axes are avoiding the Mn-oxide bonds, in this case pointing toward the end-on azide ions. The triangle edges are each bridged via an oximato group, while the terminal ligation is provided by water molecules (on Mn3 and Mn5), and a terminal azide (on Mn1).

The structure of **6** is very similar to **5**, with the differences being the terminal ligands and the absence of ClO₄⁻ counterions in the lattice. Complex **6** crystallizes in the monoclinic space

group $P2_1/n$; the structure of **6**, and a stereopair are shown in Figure 3-5, while the core is presented in Figure 3-6, and selected distances and angles are listed in Table D-5. The oxidation states of the Mn ions in **6** are the same as in the case of **5**, with the Mn^{II} ion being Mn2, as established by charge considerations, the presence of JT elongations on Mn^{III} ions, and BVS calculations (provided in Table E-1). The $[Mn_6O_3(N_3)_2]^{9+}$ core of the molecule again comprises three triangles each sharing two vertices with its closest neighbors via end-on azide bridges, while the edges of each triangle are bridged by bidentate oximate groups, similar to **5**. Peripheral ligation is provided in **6** by a total of three terminal azides (on Mn4, Mn5, and Mn6), and one H_2O molecule (on Mn5). All Mn ions are six-coordinate with distorted octahedral geometry, except of Mn5 which is five-coordinate with square pyramidal geometry. The main structural differences between complexes **5** and **6** are listed in Table 3-1, of which the most significant ones are the Mn-N-O-Mn torsion angles, and the displacement of the oxide ions away from the Mn_3 plane of the triangle they bridge.

Table 3-1. Structural differences between complexes **5** and **6**.

| Parameter | 5 | 6 |
|---|---------------------|---------------------|
| Mn-N ₃ -Mn angle | 117, 118 | 117, 119 |
| Mn-O ₂ ⁻ - Mn angle (average) | 111.7, 118.7, 121.3 | 113, 119.3, 121 |
| Mn-N-O-Mn torsion angle (average) | 19.25 | 17.24 |
| $Mn_3 - O^{2-}$ | 0.241, 0.343, 0.371 | 0.189, 0.305, 0.335 |

The structure of complex **7** and a stereopair are presented in Figure 3-7, and the fully labeled core is shown in Figure 3-8. Selected interatomic distances are listed in Table D-6. Complex **7** crystallizes in the monoclinic space group C_2/c . There is a $[Mn_5O_2(OMe)_2]^{9+}$ core consisting of two Mn^{II} (Mn1 and its symmetry equivalent partner), one Mn^{III} ion (Mn3), and two Mn^{IV} ions (Mn2 and its symmetry related counterpart), bridged by two μ_4-O^{2-} (O2 and its symmetry equivalent), and two μ_2-OMe^- (O5 and its symmetry related partner) each bridging one Mn^{II} and the single Mn^{III} ion. Additional bridges are provided by three $\eta^1:\eta^3:\eta^1:\mu_3-dapdo^{2-}$

ligands (Figure 3-9), two of which are bridging two Mn^{IV} and one Mn^{II} ions, while the third ligand bridging two Mn^{IV} and one Mn^{III} ions. All three ligands are dissected by the pseudo mirror plane (excluding the terminal azides and the twist of the unique dapdo²⁻ ligand) within the structure, the latter including the para-carbon and the pyridyl nitrogen of each dapdo²⁻ ligand, the oxygen of the μ_2 -OMe⁻ group, the Mn^{III} and the two Mn^{II} ions, and the central nitrogen atom of the bridging end-to-end azide. A true two-fold rotation axis passes through the para-carbon and pyridyl nitrogen of the unique dapdo²⁻ ligand, the Mn^{III} ion, and the central nitrogen of the end-to-end azido bridge. Peripheral ligation is provided by two pyridine groups, and two terminal azides one of each bonded to each Mn^{IV} ion. The two Mn^{II} ions, and the Mn^{III} ion are seven-coordinated with distorted pentagonal bipyramidal geometries, whereas the Mn^{IV} ions are six-coordinate with distorted octahedral geometries; the oxidation were established by charge considerations, and bond valence sum (BVS) calculations (Table E-2).

The structure of complex **8** and a stereopair are presented in Figure 3-10, and the fully labeled core is shown in Figure 3-11. Selected interatomic distances are listed in Table D-7. Complex **8** crystallizes in the tetragonal space group P4₂/n. The structure of **8** is very similar to **7**, with the differences being the replacement of the end-to-end azido group by an acetate, and the replacement of the methoxide ions with end-on azides; similar replacement of MeO⁻ by N₃⁻ groups has been reported for otherwise isostructural molecules by Perlepes and coworkers in Ni₉¹⁶⁰ and Co₉¹⁶¹ complexes. The [Mn₅O₂(N₃)₂]⁹⁺ core consists of two Mn^{II} (Mn4 and Mn2), one Mn^{III} ion (Mn3), and two Mn^{IV} ions (Mn1 and Mn5), bridged by two μ_4 -O²⁻ (O9 and O10), and two μ_2 -N₃⁻ (N14 and N17) each bridging one Mn^{II} and the single Mn^{III} ion. Additional bridges are provided by three $\eta^1:\eta^3:\eta^1:\mu_3$ -dapdo²⁻ ligands (Figure 3-9), two of which are bridging two Mn^{IV} and one Mn^{II} ions, while the third ligand bridging two Mn^{IV} and one Mn^{III} ions. All three

ligands are dissected by the pseudo mirror plane (excluding the terminal azides, the disorder on Mn5 and the twist of the unique dapdo²⁻ ligand) within the structure, the latter including the para-carbon and the pyridyl nitrogen of each dapdo²⁻ ligand, the nitrogen of the μ_2 -N₃⁻ group, the Mn^{III} and the two Mn^{II} ions, and the carboxylate carbon of the bridging acetate. Peripheral ligation is provided by two pyridine groups, and two terminal azides one of each bonded to each Mn^{IV} ion. One of these terminal ligands is disordered between an azide and a pyridine, with the missing half charge counterbalanced by a half azide in the lattice, which did not refine well due to several disordered acetonitrile ligands also present in the lattice; thus, it was not included in the final refinement. The two Mn^{II} ions, and the Mn^{III} ion are seven-coordinated with distorted pentagonal bipyramidal geometries, whereas the Mn^{IV} ions are six-coordinate with distorted octahedral geometries; the oxidation were established by charge considerations, and bond valence sum (BVS) calculations (Table E-2).

3.3.3 Magnetochemistry

3.3.3.1 Direct current magnetic susceptibility studies

Solid-state, variable-temperature ac magnetic susceptibility (χ_M) data were collected on vacuum-dried microcrystalline samples of complexes **5-8**, suspended in eicosane to prevent torquing, in the 5.0-300 K temperature range in a 0.1 tesla (T) (1000 Oe) magnetic field. The obtained data are plotted as $\chi_M T$ vs T in Figure 3-12a for complexes **5** and **6**, and in Figure 3-12b for complexes **7** and **8**. It can be seen that the overall profiles are very similar for complexes **5** and **6**, $\chi_M T$ steadily decreasing with decreasing temperature and thus suggesting dominant antiferromagnetic interactions within the molecules. The $\chi_M T$ values at 300 K for **5** and **6** (14.08 cm³ mol⁻¹ K, and 12.72 cm³ mol⁻¹ K, respectively) are both lower than the expected $\chi_M T$ value for 1 Mn^{II} and 5 Mn^{III} ions, 19.34 cm³ mol⁻¹ K, supporting the presence of dominant

antiferromagnetic interactions of sufficient strength to affect the 300 K χ_{MT} value. The 5 K χ_{MT} value for **5** and **6** ($4.26 \text{ cm}^3 \text{ mol}^{-1} \text{ K}$, and $4.01 \text{ cm}^3 \text{ mol}^{-1} \text{ K}$, respectively) both suggest an $S=5/2$ ground state with $g = 1.95 \pm 3$. The overall similar behavior of the two complexes is as expected, due to the very similar structures, and essentially isostructural cores.

In contrast to this similar behavior of **5** and **6**, the magnetic behaviors of complexes **7** and **8** are distinctively different, as evident from the χ_{MT} vs Temperature plot presented in Figure 3-12b. The χ_{MT} for complex **7** drops from $7.83 \text{ cm}^3 \text{ mol}^{-1} \text{ K}$ at 300 K to $7.09 \text{ cm}^3 \text{ mol}^{-1} \text{ K}$ at 150 K, and then increases to $8.27 \text{ cm}^3 \text{ mol}^{-1} \text{ K}$ at 10 K, before decreasing again to $8.16 \text{ cm}^3 \text{ mol}^{-1} \text{ K}$ at 5 K. The latter decrease can be attributed to zero-field splitting, weak intermolecular interactions, and/or Zeeman effects. The χ_{MT} value at 5 K for **7** suggests an $S = 4$ ground state, with $g \approx 1.82$. For complex **8**, the χ_{MT} decreases continuously from a value of $14.38 \text{ cm}^3 \text{ mol}^{-1} \text{ K}$ at 300 K to $5.81 \text{ cm}^3 \text{ mol}^{-1} \text{ K}$ at 5 K, indicating that predominant antiferromagnetic interactions are present within the magnetic core, with the χ_{MT} at 5 K suggesting an $S = 3$ with $g = 1.97$. The different ground states between **7** and **8** can be rationalized as due to the different ligation within the magnetic cores. In particular, one would expect a partial ferromagnetic character to be present in complex **8** due to the presence of end-on azides; end-on azides are usually referred to as ferromagnetic couplers. For example, the Ni_9 and Co_9 complexes became completely ferromagnetic when MeO^- bridges were replaced by N_3^- ones.^{160,161} Similar behavior was also observed in other Mn complexes, where the use of azides resulted in high spin ground states.^{141,162} For complex **8** the apparent lowering of the ground state, when azides are bridging, is possibly due to the very acute angle ($\theta = 86.7^\circ$) observed between the Mn^{II} and Mn^{III} ions in the core of **8**, as well as the concurrent bridging of the Mn^{II} ions via the introduced acetate group. The above fact merely indicates that the identity of the bridging ligands greatly affects the

magnetic interactions between the metal centers, and in this case the two effects appear to coordinately resulting in a lower ground state spin for complex **8**, compared to its structurally similar, complex **7**.

3.3.3.2 Reduced magnetization studies

In order to confirm the ground state of **5-8**, as well as to obtain an estimate of the axial zfs parameter, D , magnetization data were collected in the 1-70 kOe and 1.8-10.0 K ranges, and these are plotted as reduced magnetization ($M/N\mu_B$) vs H/T in Figures 3-13, 3-14, and 3-15 for complexes **5-8**. We attempted to fit the resulting data using the program MAGNET,⁶⁸ which assumes that only the ground state is populated at these temperatures, includes axial zero-field splitting (ZFS) and the Zeeman interaction, and incorporates a full powder average; the corresponding spin Hamiltonian is given by eq 3-3.

$$\mathcal{H} = D\hat{S}_z^2 + g\mu_B\mu_0\hat{S}\cdot H \quad (3-3)$$

For **5**, the best fit (solid lines in Figure 3-13a) gave $S=5/2$, $D= -1.41(1) \text{ cm}^{-1}$, and $g=1.99(1)$. A D vs g root-mean-square error surface for the fit was generated and is shown in Figure 3-13b; this plots the relative difference between the experimental $M/N\mu_B$ data and those calculated for various combinations of D and g (Figure 3-13b). From the latter plot it is evident that the fit values represent the global minimum for this system, thus confirming our initial estimate of an $S=5/2$ ground state and a very high negative D value; the combination of these two factors explain the appearance of out-of-phase ac susceptibility signals (*vide infra*). For complex **6** the reduced magnetization data is presented in Figure 3-14. An acceptable fit was not attainable, possibly due to lower lying excited states than for **5**. This was originally surprising, taking into account the structural similarity of the two complexes; however, similar patterns (reduced magnetization fitting being only available for one member of a nearly isostructural

family) have been observed in other groups of compounds, like the family of tridecanuclear clusters presented in Chapter 6,¹⁶³ and can be assigned to the sensitivity of the spin state energies to small changes in the relative magnitudes of the J values.

For complexes **7** and **8** the reduced magnetization data are presented in Figure 3-15a and 3-15b, respectively; it is evident that the behavior of the two complexes is distinctively different, which is not surprising taking into account the differences in the magnetic cores of the two molecules. However, we could not obtain an acceptable fit for the data collected in the full field range of 0.1 – 7 T. In our experience, this is the case when there are low-lying excited states that are consequently populated even at these relatively low temperatures, and/or excited states that are more separated from the ground state but have S values greater than that of the ground-state and thus their larger M_S levels rapidly decrease in energy due to the applied magnetic field and approach (or even cross) those of the ground state. Such situations are expected for **7** and **8** because of their high content of Mn^{II} atoms, which give very weak and usually antiferromagnetic exchange interactions, and thus low-lying excited states with larger S values. The above complications can sometimes be avoided by using only data collected at the lowest fields. Indeed, when lower field data were used a satisfactory fit was obtained for both complexes **7** and **8**. For **7**, fitting of only the data collected in the 0.1 – 3.0 T field range (Figure 3-15a) was satisfactory, and gave fit parameters $S= 4$, $D= -0.41(3) \text{ cm}^{-1}$, and $g= 1.99(1)$. For **8**, the best fit (solid lines in Figure 3-15b) was obtained from data collected in the 0.1 – 4.0 T field range, with the fitting parameters being $S= 3$, $D= -0.79(1) \text{ cm}^{-1}$, and $g= 1.99(1)$.

3.3.3.3 Alternating current magnetic susceptibility studies

Alternating-current magnetic susceptibility studies were performed on vacuum-dried microcrystalline samples of **5-8** in the temperature range 1.8-15 K in a zero dc field and a 3.5 Oe ac field oscillating at frequencies between 250-1000 Hz. The resulting data for complexes **5** and

6 are plotted as $\chi_M' T$ vs T and χ_M'' vs T in Figure 3-16a and 3-16b, respectively, where χ_M' and χ_M'' are the in-phase and out-of-phase components of the ac susceptibility. For complexes **5** and **6**, the in-phase and out-of-phase ac signals are very similar, with the in-phase magnetic susceptibility decreasing with decreasing temperature, and a frequency-dependent split becoming evident at temperatures below ~ 3 K. The latter is followed by the concomitant appearance of out-of-phase signals which are also frequency-dependent. Such behavior indicates slow magnetization relaxation, and represents strong evidence for SMM properties. Further confirmation of the SMM behavior of **5** and **6** is needed, but the use of dilution fridge techniques and a micro-SQUID apparatus would be required, since the out-of-phase ac peaks clearly lie below the operating limit of our SQUID (1.8K). A linear extrapolation of the $\chi_M' T$ data above ~ 4 K to 0 K, where only the ground state will be populated, gives $\chi_M' T$ of ~ 4.2 cm³ K mol⁻¹ for both **5** and **6**, which is consistent with an $S = 5/2$ ground state; expected spin-only ($g = 2.0$) values for $S = 3/2, 5/2,$ and $7/2$ are 1.88, 4.38, and 7.88 cm³ K mol⁻¹, respectively calculated by eq 3-4

$$\chi_M' T = (g^2 / 8) \times S (S + 1) \quad (3-4)$$

For complexes **7** and **8** the magnetic behavior is very different. The in-phase component of the ac magnetic susceptibility is presented in Figure 3-17 for complexes **7** and **8**. The overall profiles for the two compounds are very different, with the in-phase ac susceptibility for **7** remaining essentially constant at a value of ~ 8.5 cm³ mol⁻¹ K, indicating the presence of weak interactions between the metal centers, in accordance with the $\chi_M T$ from the dc studies (*vide supra*). In contrast, the susceptibility for **8** drops linearly with temperature, indicating the depopulation of low-lying excited states with S higher than the ground state. The small decrease below 2.2 K is not frequency-dependent, and can be attributed to weak intermolecular interactions becoming evident only at the lowest temperatures. A linear extrapolation of the data

for **7** and **8** to 0 K, where only the ground state will be populated, gives $\chi_M T$ of $\sim 8.5 \text{ cm}^3 \text{ K mol}^{-1}$, and $5.7 \text{ cm}^3 \text{ K mol}^{-1}$ for **7** and **8**, respectively. The latter indicates an $S = 4$ for complex **7** and $S=3$ for **8**, since the expected spin-only ($g = 2.0$) values for $S = 2, 3, 4,$ and 5 are $3, 6, 10,$ and $15 \text{ cm}^3 \text{ K mol}^{-1}$, respectively. This is in satisfying agreement with the dc studies (Figure 3-12b), and the reduced magnetization fit in Figure 3-15.

3.4 Conclusions

The combined use of pyridine oximes and azide ligands has afforded four new mixed-valent clusters with novel metal topologies. Complexes **5** and **6** incorporate the anion of methyl-2-pyridyl ketone oxime (mpkoH), whereas the anions of 2,6-diacetylpyridine dioxime (dapdoH₂) are found in complexes **7** and **8**. All four complexes resulted from the reactions of simple manganese salts with the ligands in basic conditions. Complexes **5** and **6**, even though they possess a small ground state spin of $5/2$, their large and negative zero-field splitting parameter D induces single-molecule magnetism behavior evident in the frequency-dependent out-of-phase ac signals; it should be noted here that SMMs with half integer spin ground states are relatively rare in the literature. The pentanuclear complexes **7** and **8** incorporate manganese ions in three different oxidation states, and represent a rare case where the substitution of bridging methoxides by end-on azides was possible. The ground states of **7** and **8** were found to be $S=4$ and 3 respectively, as evident from reduced magnetization and ac magnetic susceptibility studies. It will be interesting to determine, as this work is extended, to what extent dapdo^{-2-} will continue to provide a route to new metal clusters and to what extent these are related to clusters provided by pyridyl monooximes (mpko⁻) and pyridyl alcohols (pdm⁻²⁻) alone.

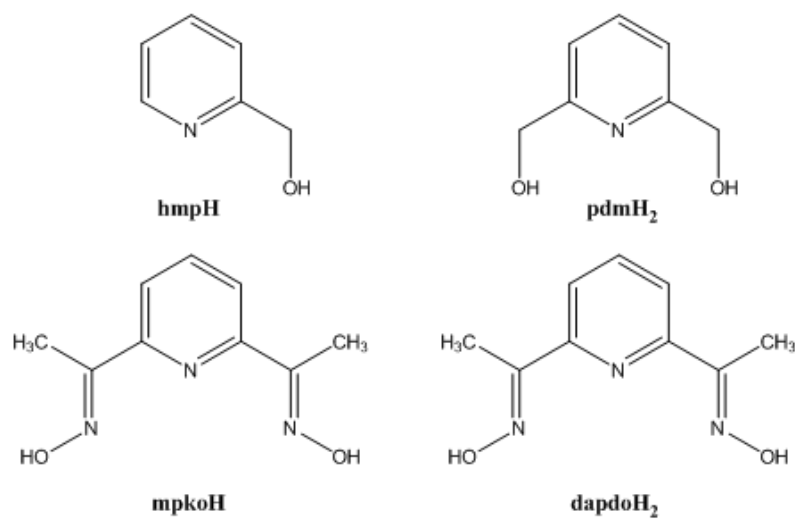


Figure 3-1. A schematic representation of selected pyridine methanols and pyridyl oximes.

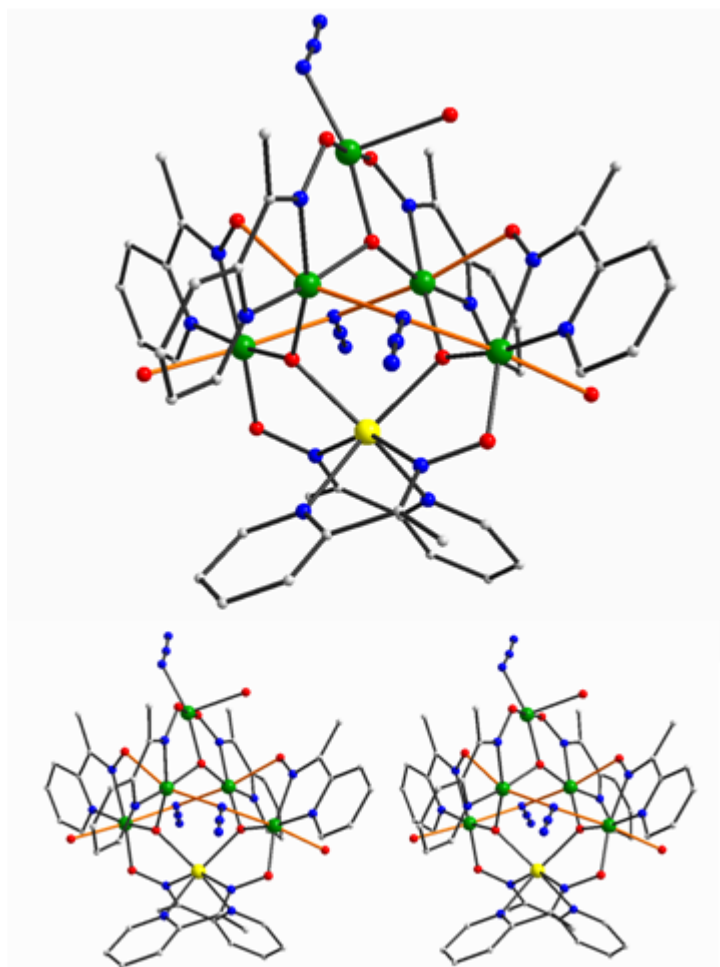


Figure 3-2. The structure and a stereopair of complex **5**. Hydrogen atoms have been omitted for clarity. Color code: Mn^{II} yellow, Mn^{III} green, O red, N blue, C grey.

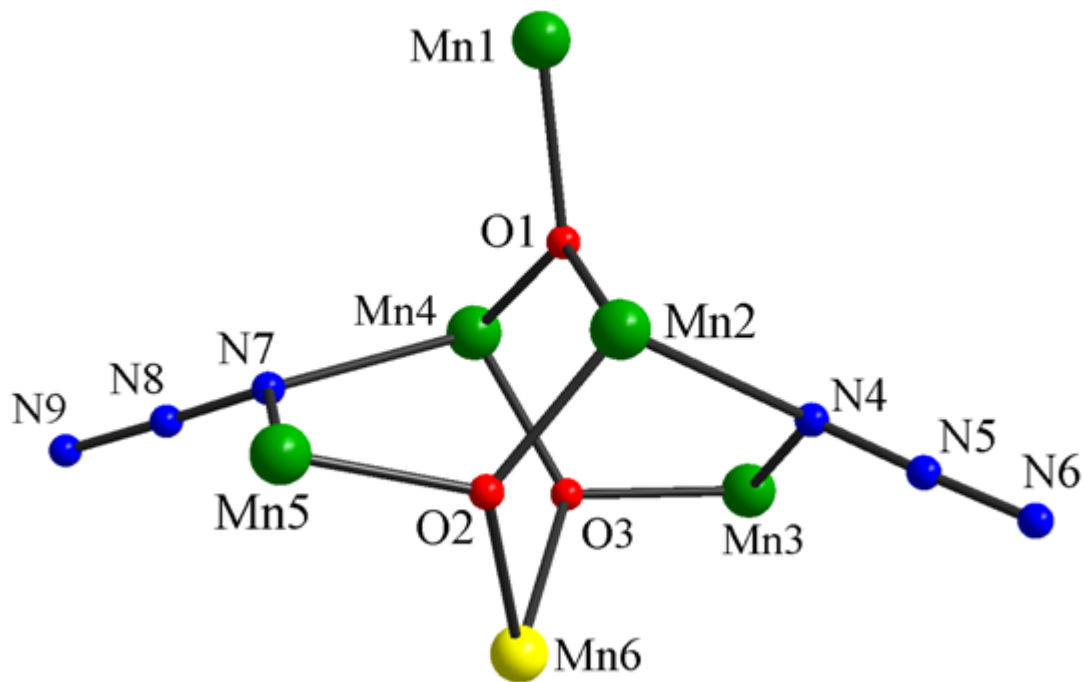


Figure 3-3. The labeled core of complex **5**. Color code: Mn^{II} yellow, Mn^{III} green, O red, N blue, C grey.

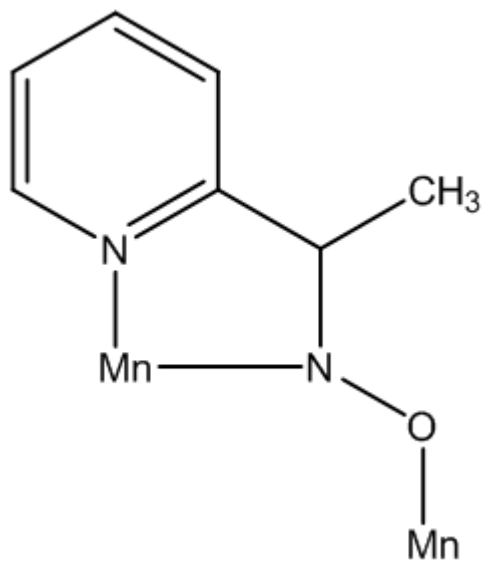


Figure 3-4. The bridging-chelating mode of the mpko⁻ ligand in complexes **5** and **6**.

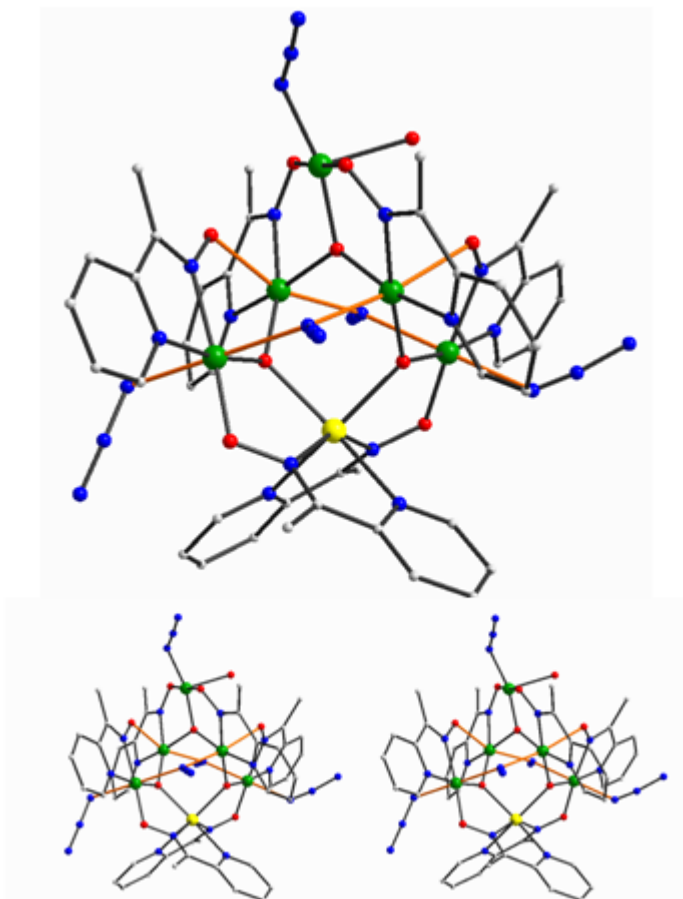


Figure 3-5. The structure and a stereopair of complex **6**. Hydrogen atoms have been omitted for clarity. Color code: Mn^{II} yellow, Mn^{III} green, O red, N blue, C grey.

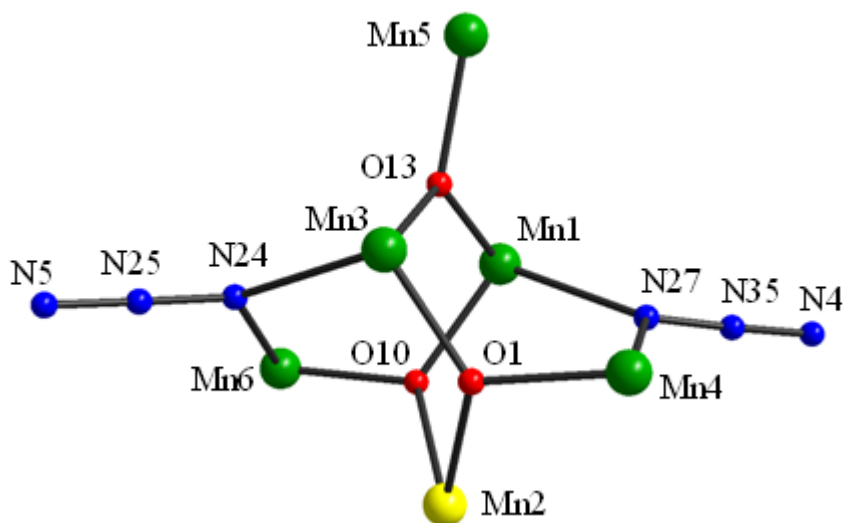


Figure 3-6. The labeled core of complex **6**. Color code: Mn^{II} yellow, Mn^{III} green, O red, N blue, C grey.

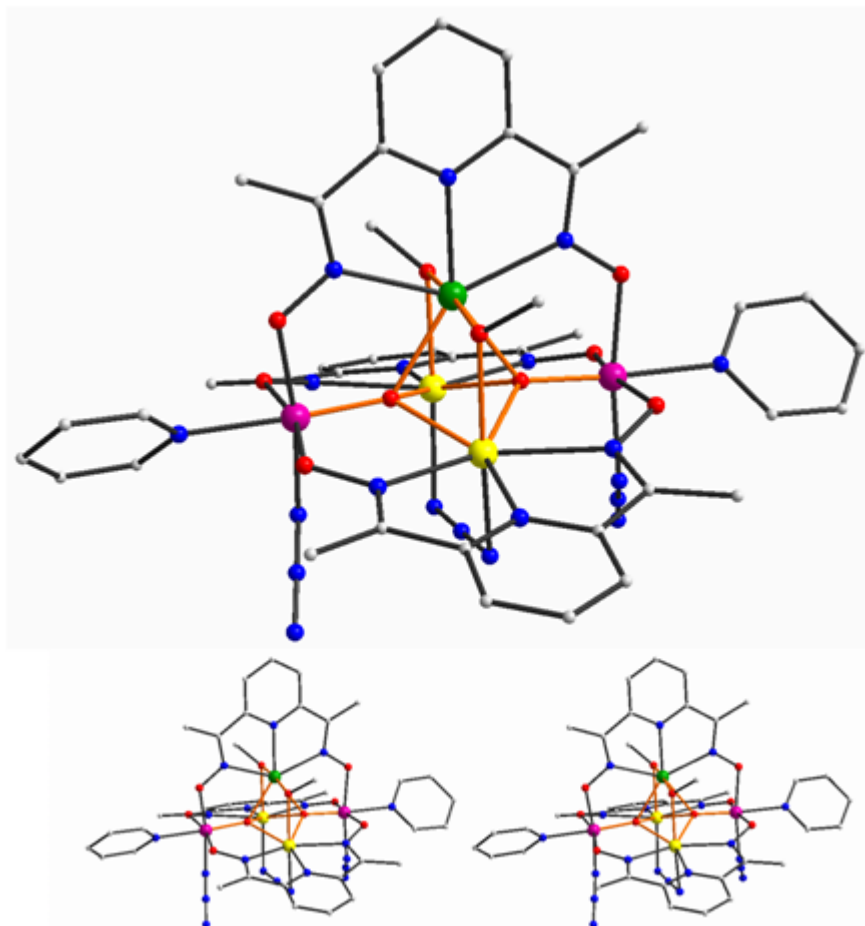


Figure 3-7. The structure and a stereopair of complex **7**. Hydrogen atoms have been omitted for clarity. Color code: Mn^{II} yellow, Mn^{III} green, Mn^{IV} purple, O red, N blue, C grey.

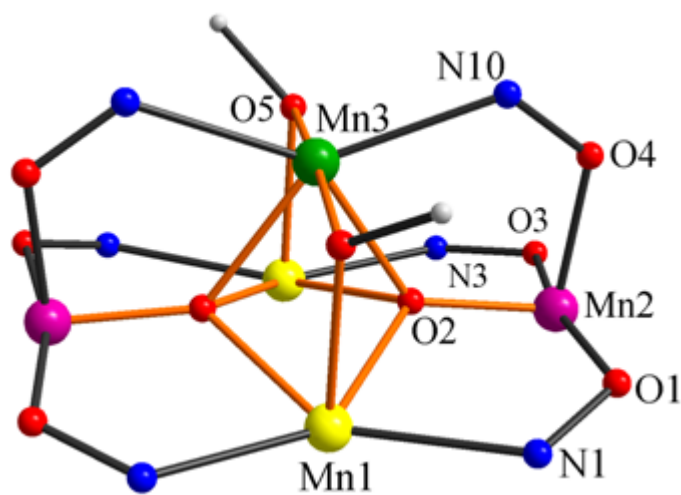


Figure 3-8. The labeled extended core of complex **7**. The asymmetric unit is labeled, and the core is emphasized by orange bonds. Color code: Mn^{II} yellow, Mn^{III} green, Mn^{IV} purple, O red, N blue, C grey.

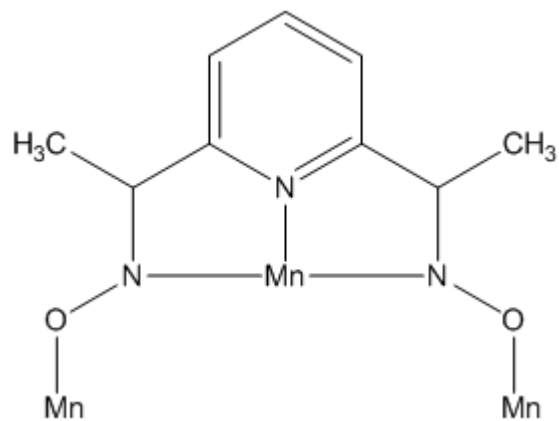


Figure 3-9. The bridging-chelating mode of the dapdo^{2-} ligand in complexes **7** and **8**.

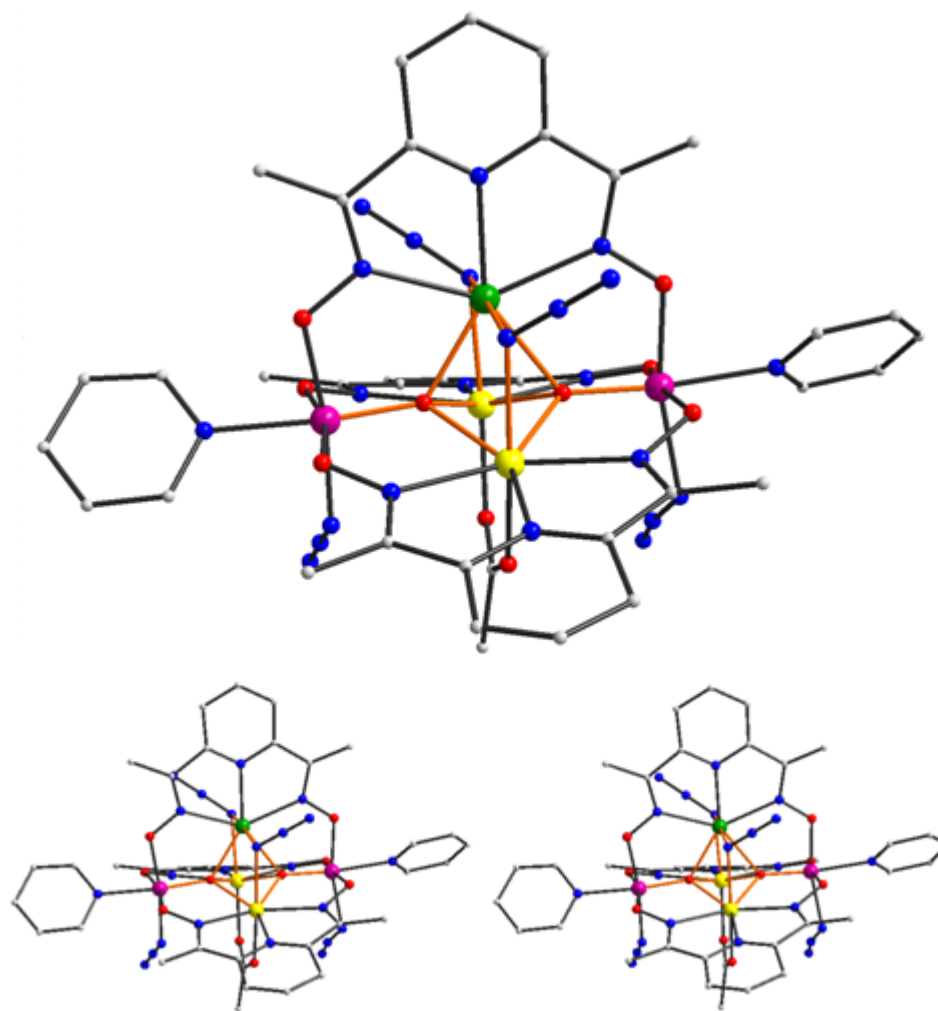


Figure 3-10. The structure and a stereopair of complex **8**. Hydrogen atoms have been omitted for clarity. Color code: Mn^{II} yellow, Mn^{III} green, Mn^{IV} purple, O red, N blue, C grey.

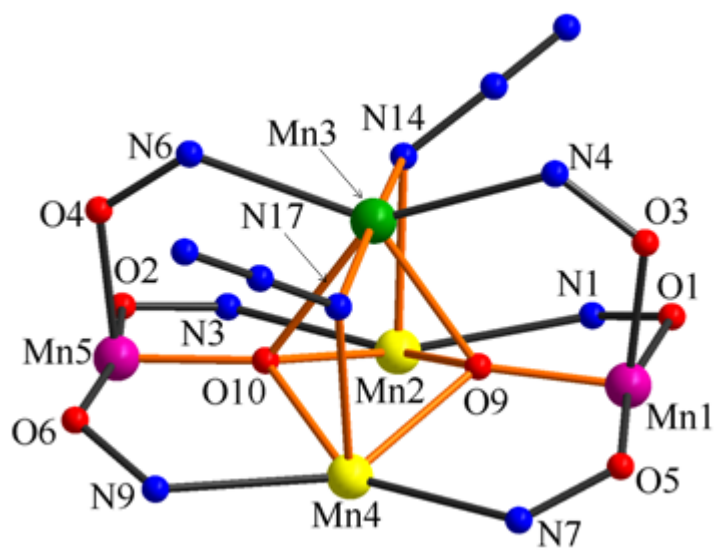
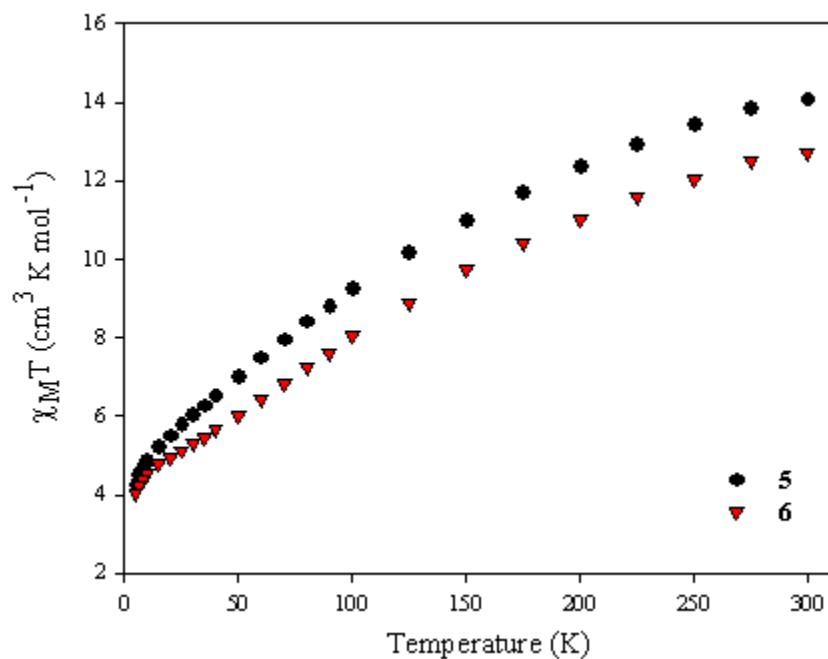
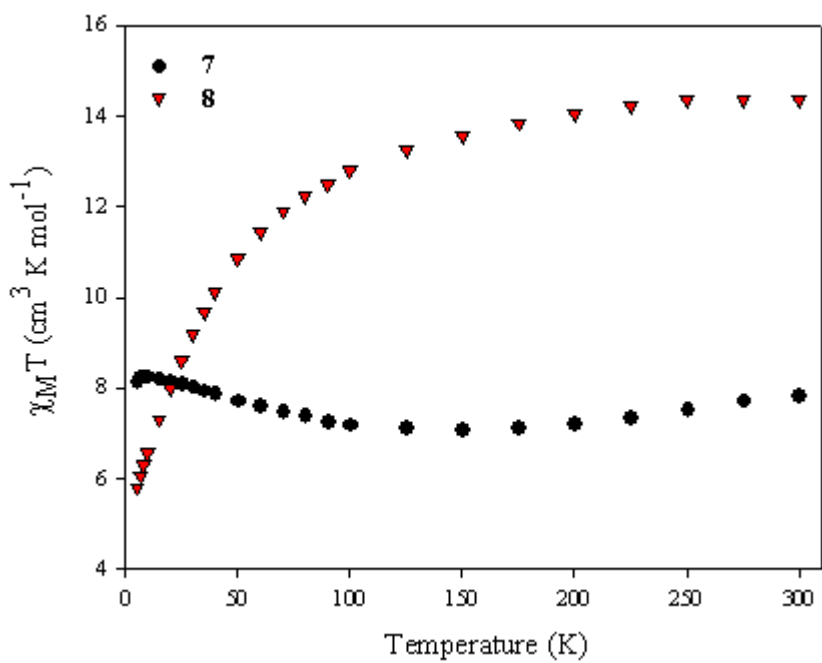


Figure 3-11. The labeled extended core of complex **8**. The asymmetric unit is labeled, and the core is emphasized by orange bonds. Color code: Mn^{II} yellow, Mn^{III} green, Mn^{IV} purple, O red, N blue.

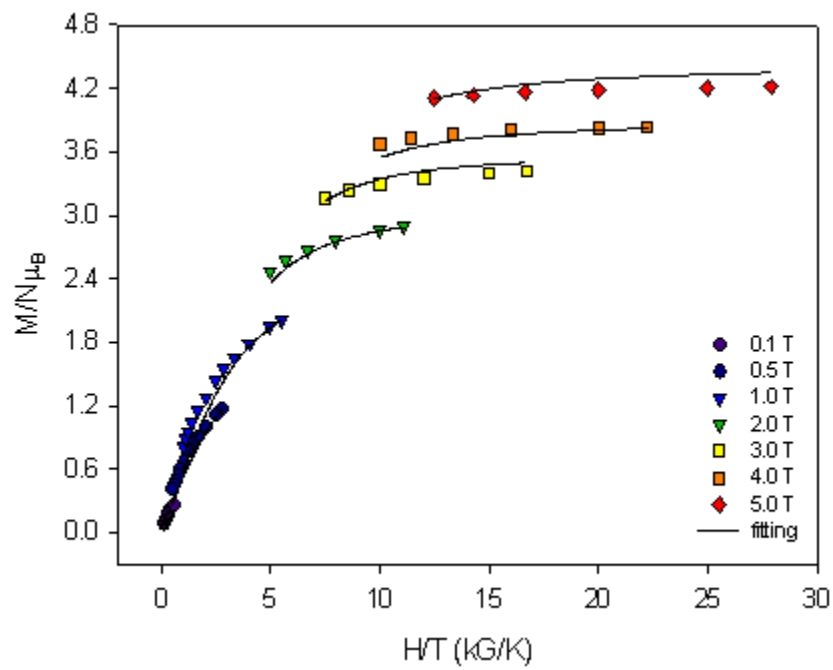


a

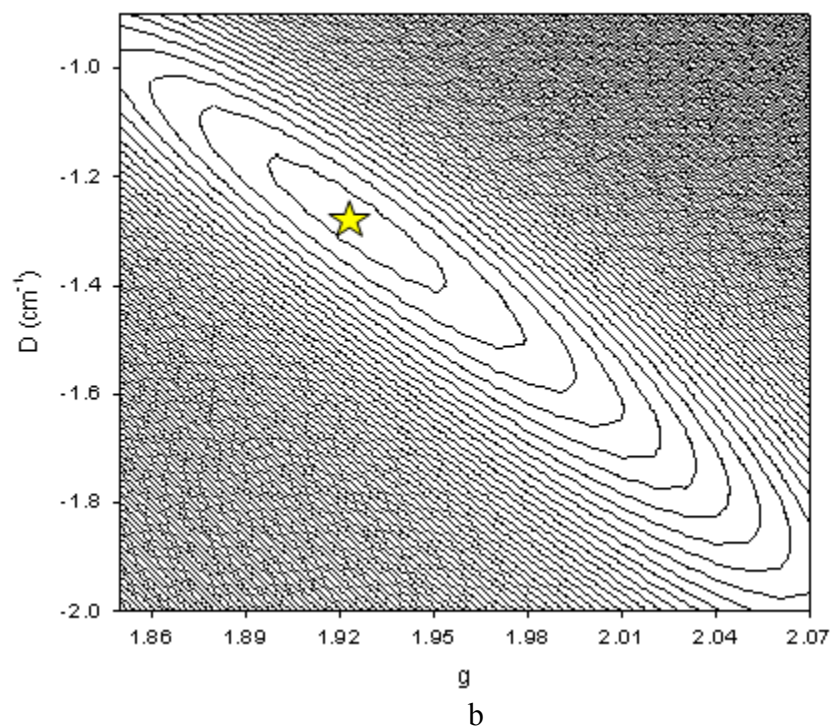


b

Figure 3-12. $\chi_M T$ vs T plots for complexes **5-8** in the temperature range 5.0-300 K in a 0.1 T applied dc field. (a) $\chi_M T$ vs T plots for complexes **5** and **6**; (b) $\chi_M T$ vs T plots for complexes **7** and **8**.



a



b

Figure 3-13. Plots of the reduced magnetization, $M/N\mu_B$, vs H/T for complexes **5** and **6**. The solid lines are the fit with negative D ; see the text for the fit parameters. (a) $M/N\mu_B$, vs H/T plot for **5**; (b) two-dimensional contour plot of the fitting error surface vs D and g for **5**.

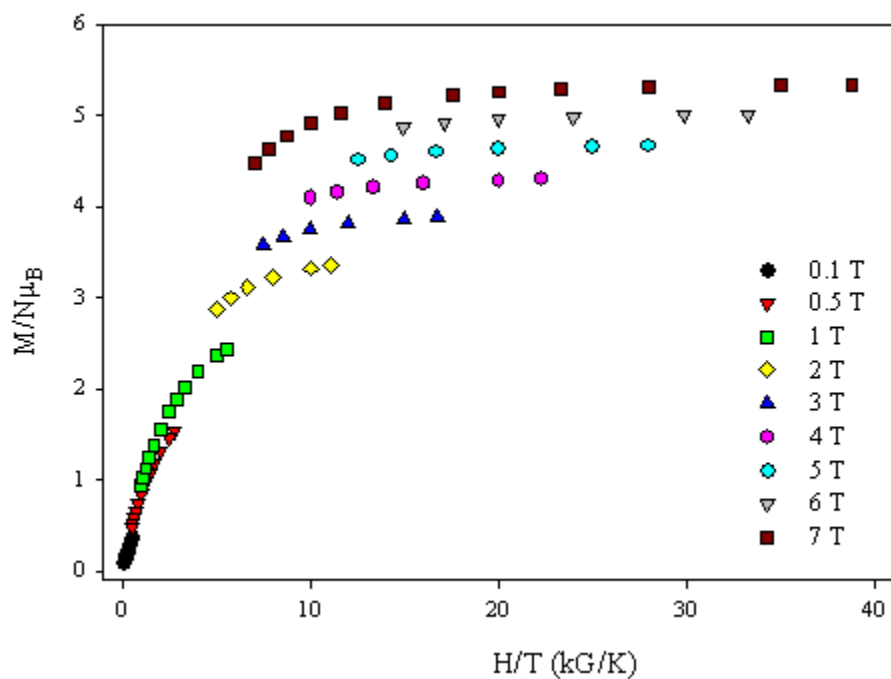


Figure 3-14. $M/N\mu_B$, vs H/T plot for **6**

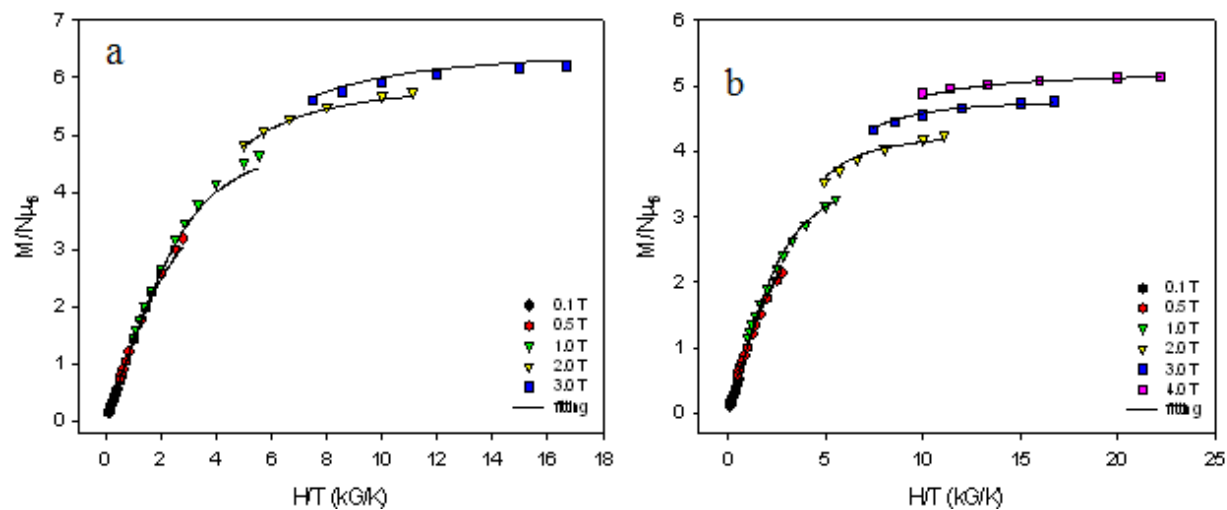


Figure 3-15. Plots of the reduced magnetization, $M/N\mu_B$, vs H/T for complexes **7** and **8**. The solid lines are the fit with negative D ; see the text for the fit parameters. (a) $M/N\mu_B$, vs H/T plot for **7**; (b) $M/N\mu_B$, vs H/T plot for **8**

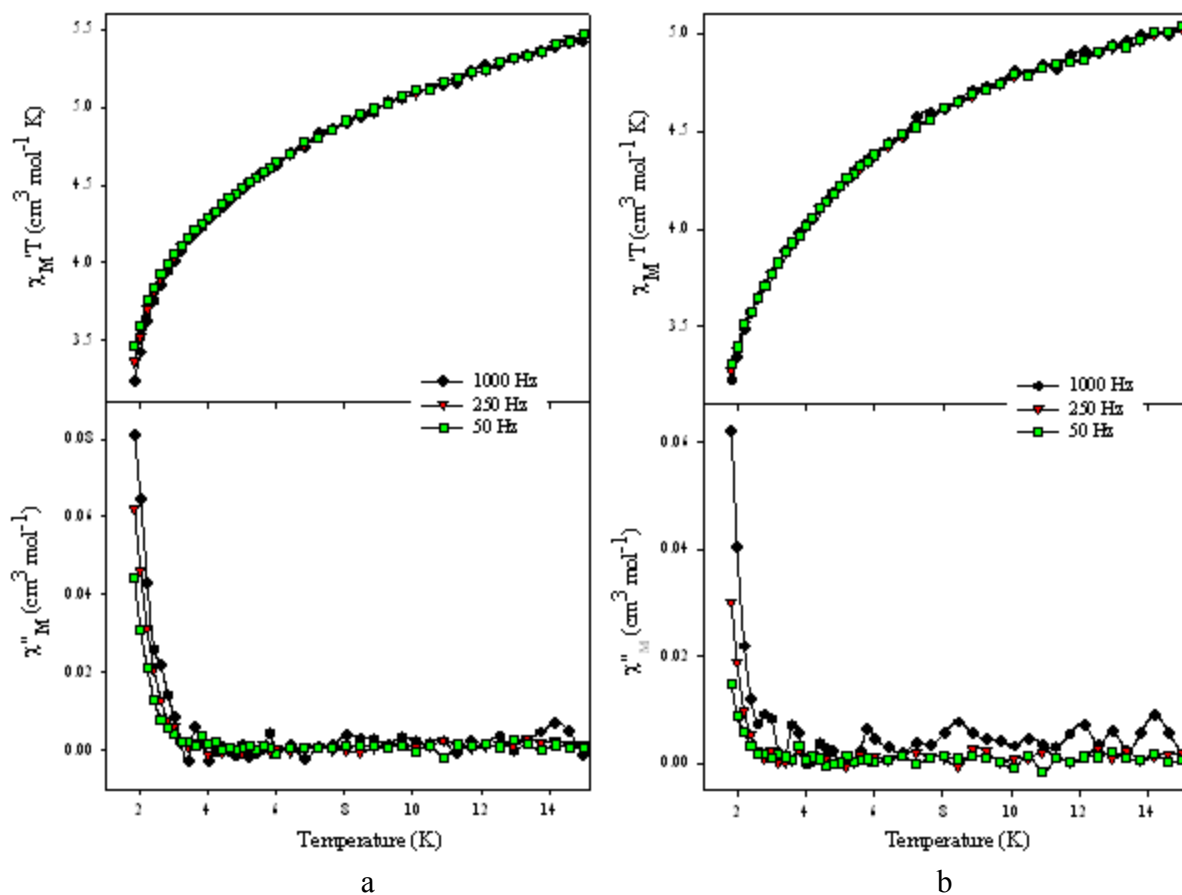


Figure 3-16. Plots of the in-phase (χ'_M) (as $\chi'_M T$) and out-of-phase (χ''_M) ac susceptibility signals of complexes **5** and **6** in a 3.5 G field oscillating at the indicated frequencies. (a) Ac studies of **5**; (b) ac studies of **6**.

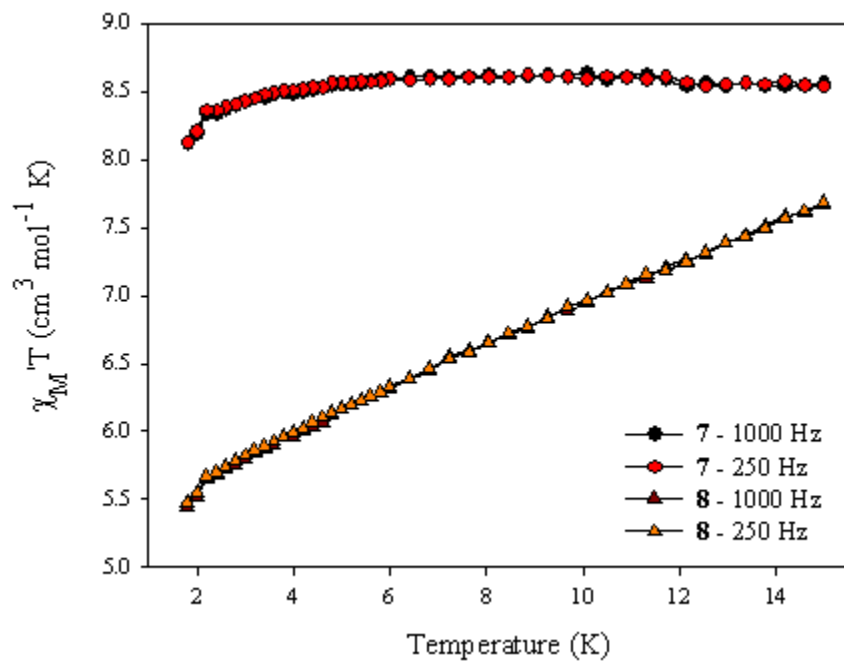


Figure 3-17. Plots of the in-phase (χ'_M) (as $\chi'_M T$) ac susceptibility signals of complexes **7** and **8** in a 3.5 G field oscillating at the indicated frequencies.

CHAPTER 4
BUILDING UP THE SMALL FAMILY OF 3d/4f METAL COMPLEXES:
HETERROMETALLIC HEXA, ENNEA, AND DECANUCLEAR Mn-Ce CLUSTERS

4.1 Introduction

Polynuclear complexes incorporating transition metals have been attracting a great deal of attention for nearly two decades now, due to their aesthetically pleasing chemical structures, as well as the fascinating magnetic properties they often possess. In particular, many of these species exhibit single-molecule magnetism (SMM) behavior, a property which is intrinsic to the individual molecules, and makes them capable of functioning as nanoscale magnetic particles. Such molecules behave as magnets below their blocking temperature (T_B), exhibiting slow magnetization relaxation, and hysteresis loops in magnetization versus dc field scans.^{23,24,26,38,49} This SMM property is primarily due to the high spin ground states of such species (S), and the large and negative Ising (or easy-axis) type of magnetoanisotropy, reflected in the value of the zero-field splitting parameter D . In addition, SMMs are small enough that they truly straddle the classical/quantum interface, displaying not just the classical property of magnetization hysteresis but also the quantum properties of quantum tunneling of the magnetization (QTM)¹¹⁷ through the anisotropy barrier, and quantum phase interference.^{39,42,164}

Inorganic chemical research has been also directed towards the synthesis of high oxidation-state molecular compounds incorporating mixtures of different metals, and such combinations include mixed-transition metal complexes,¹⁶⁵⁻¹⁶⁹ as well as mixed 3d/4f¹⁷⁰⁻¹⁸¹ and 3d/5f¹⁸² compounds. Such complexes provide a wide range of applications in diverse areas involving inorganic, organic, environmental, and industrial chemistry. In particular, Mn-Ce compounds and various polymeric metal oxides have been widely used in all the above mentioned fields, due to their ability to oxidize both inorganic and organic substrates.^{25,127,183-200} The use of Ce^{IV} extends even further to the homogeneous and heterogeneous catalysis of water to molecular

dioxygen by Ru complexes.^{201,202} Furthermore, high oxidation state Mn ions and Ce^{IV} are known in inorganic synthesis for their oxidative ability, and have been employed in the past in the formation of Mn^{III} and/or Mn^{IV} clusters, or mixed-valent Co^{III,IV} complexes.^{25,186-189,203} Also, organic chemists extensively use Mn^{VII}, Mn^{IV}, and Ce^{IV} (as (NH₄)₂[Ce(NO₃)₆]) as oxidizing agents for a vast variety of organic substrates.¹⁹⁰⁻²⁰⁰ In the broader area of catalysis, homo- or heterogeneous, the use of Mn^{III}, Mn^{IV}, and Ce^{IV} oxides has been explored, and it has been shown that they make efficient catalysts for catalysis of the de-NO_x process in car exhausts, either alone or as mixed Mn/Ce oxides.^{204,205} Active research in this direction has shown that Mn and Ce oxides seem to have considerable catalytic activity in the conversion of nitric oxide from the exhaust gases of cars into nitrogen and oxygen, either as impregnated zeolites with Fe, Ce and Mn,²⁰⁴ or as dusts.²⁰⁵ Virtually any combustion process in the high temperature zones produces NO_x mixtures of gases, as well as a variety of chemical processes including the manufacture of nitric acid, the nitration of organic chemicals, the production of adipic acid and the reprocessing of spent nuclear fuel rods.²⁰⁴ For example, Ce^{IV}/Mn^{IV} composite oxides are being widely used in sub- and supercritical catalytic wet oxidations for the treatment of wastewater containing toxic organic pollutants such as ammonia, acetic acid, pyridine, phenol, polyethylene glycol, and others.¹⁹⁵⁻²⁰⁰

The synthesis of Mn-Ce clusters is a challenging task. The synthetic methods for such a synthesis are limited, and involve the treatment of simple manganese salts with Ce^{IV} precursors,^{178,179} or the reaction of preformed species with different Ce sources.^{174,180} In the present work, both these methodologies were successfully employed, and three new clusters, [Ce₆Mn₄O₁₂(O₂CMe)₁₀(NO₃)₄(py)₄]·py·9MeCN (**9**·py·9MeCN), [Mn₈CeO₈(O₂CCH₂Bu^t)₁₂(DMF)₁₄]·1.5DMF (**10**·1.5DMF), and

$[\text{Ce}_2\text{Mn}_4\text{O}_2(\text{O}_2\text{CMe})_6(\text{NO}_3)_4(\text{hmp})_4]\cdot\text{H}_2\text{O}\cdot 6\text{MeCN}$ (**11** $\cdot\text{H}_2\text{O}\cdot 6\text{MeCN}$) (hmpH=2-

(hydroxymethyl)pyridine) have been added to this relatively small family of Mn-Ce compounds.

These three complexes exhibit elaborate metal topologies and clearly illustrate the expediency of the cerium ions' high coordination ability.

4.2 Experimental Section

4.2.1 Syntheses

All manipulations were performed under aerobic conditions using chemicals as received, unless otherwise stated. **1**,²⁵ and $[\text{Mn}_8\text{O}_2(\text{O}_2\text{CCH}_2\text{Bu}^t)_{14}(\text{Bu}^t\text{CH}_2\text{CO}_2\text{H})_4]$ (**12**)²⁰⁶ were prepared as described elsewhere.

4.2.1.1 $[\text{Ce}_6\text{Mn}_4\text{O}_{12}(\text{O}_2\text{CMe})_{10}(\text{NO}_3)_4(\text{py})_4]\cdot\text{py}\cdot 9\text{MeCN}$ (**9** $\cdot\text{py}\cdot 9\text{MeCN}$).

Method A. To a stirred solution of **1** (0.5 g, 0.25 mmol) in MeCN (20 ml) was slowly added solid $(\text{NH}_4)_2[\text{Ce}(\text{NO}_3)_6]$ (0.3 g, 0.5 mmol). The resulting solution was stirred for 30 min during which time the color changed slightly from dark brown to reddish brown. The solution was filtered, and the filtrate was layered with pyridine (5 ml). The solution was left undisturbed for 10 days, during which time black needles slowly grew; the yield was 20%. The crystals were maintained in mother liquor for the X-ray analysis or collected by filtration, washed with Et_2O , and dried in vacuo. Anal. Calcd (Found) for **9** $\cdot\text{py}\cdot 2\text{H}_2\text{O}$: C, 21.92 (21.80); H, 2.41 (2.36); N, 2.84 (2.97) %. Selected IR data (KBr, cm^{-1}): 3422(mb), 2362(m), 2336(m), 1635(w), 1523(mb), 1384(vs), 1022(w), 668(s), 612(mb), 532(m).

Method B. To a stirred solution of **1** (0.5 g, 0.25 mmol) in a solvent mixture comprising MeCN (15 ml) and pyridine (10 ml) was slowly added solid $(\text{NH}_4)_2[\text{Ce}(\text{NO}_3)_6]$ (0.3 g, 0.5 mmol). The resulting solution was stirred for 15 min during which time the color changed slightly from dark brown to reddish brown. The solution was filtered and left undisturbed for a period of 3 days, during which time black needles of **9** $\cdot\text{py}\cdot 9\text{MeCN}$ grew; the yield was 40%. The

identity of the product was confirmed by elemental analysis (C, H, N) and IR spectroscopic comparison with material from method A.

4.2.1.2 [Mn₈CeO₈(O₂CCH₂Bu^t)₁₂(DMF)₁₄·1.5DMF (10·1.5DMF).

To a stirred solution of **12** (0.7 g, 0.25 mmol) in DMF (30 ml) was slowly added solid (NH₄)₂[Ce(NO₃)₆] (0.3 g, 0.5 mmol). The resulting solution was stirred for 30 min during which time the color changed slightly from reddish brown to dark brown. The solution was filtered and left undisturbed for a period of 3 days, during which time black plates slowly grew; the yield was 40%. The crystals were maintained in mother liquor for the X-ray analysis or collected by filtration, washed with Et₂O, and dried in vacuo. Anal. Calcd (Found) for **10** (solvent free): C, 45.01 (44.83); H, 7.19 (7.09); N, 2.50 (2.28) %. Selected IR data (KBr, cm⁻¹): 3446(mb), 2949(m), 1653(s), 1587(s), 1541(s), 1400(vs), 1306(m), 1242(m), 1104(m), 972(w), 903(w), 801(w), 731(s), 685(vs), 592(vs), 505(mb), 424(m).

4.2.1.3 [Ce₂Mn₄O₂(O₂CMe)₆(NO₃)₄(hmp)₄]·H₂O·6MeCN (11·H₂O·6MeCN).

To a stirred solution of (NH₄)₂[Ce(NO₃)₆] (0.55 g, 1.0 mmol) in MeCN (20 ml) was added hmpH (0.10 mL, 1.0 mmol). After stirring for five minutes, solid Mn(O₂CMe)₂·4H₂O (0.25 g, 1.0 mmol) was added. The resulting reddish brown solution was stirred for a further 5 min, and filtered, and the filtrate left undisturbed to concentrate slowly by evaporation. After 5 days, brown crystals of **11**·H₂O·6MeCN were collected by filtration, washed with Et₂O (2 × 5 mL), and dried under vacuum; the yield was 60%. Anal. Calcd (Found) for **11**·2H₂O: C, 27.96 (28.21); H, 3.00 (2.95); N, 3.62 (3.69)%. Selected IR data (KBr, cm⁻¹): 3387(bm), 1613(sm), 1446(s), 1386(s), 1051(sm), 825(sw), 771(sm), 667(sm), 563(bm).

4.2.2 X-Ray Crystallography

Data were collected by Dr. K. A. Abboud on a Siemens SMART PLATFORM equipped with a CCD area detector and a graphite monochromator utilizing Mo K α radiation ($\lambda = 0.71073$

Å). Suitable crystals of the complexes were attached to glass fibers using silicone grease and transferred to a goniostat where they were cooled to 173 K for data collection. An initial search of reciprocal space revealed a monoclinic cell for complex **9**·py·9MeCN and a triclinic one for **10**·1.5DMF and **11**·H₂O·6MeCN; the choice of space groups P2₁/n for **9**·py·9MeCN and $P\bar{1}$ for **10**·1.5DMF and **11**·H₂O·6MeCN, respectively, was confirmed by the subsequent solution and refinement of the structures. Cell parameters were refined using up to 8192 reflections. A full sphere of data (1850 frames) was collected using the ω -scan method (0.3° frame width). The first 50 frames were re-measured at the end of data collection to monitor instrument and crystal stability (maximum correction on I was < 1 %). Absorption corrections by integration were applied based on measured indexed crystal faces. Crystal data and structural refinement parameters for complexes **9**·py·9MeCN, **10**·1.5DMF, and **11**·H₂O·6MeCN are listed in Table D-8.

The structure of complex **9**·py·9MeCN was solved by the direct methods in *SHELXTL6*, and refined using full-matrix least squares. The non-H atoms were treated anisotropically, whereas the hydrogen atoms were calculated in ideal positions and were riding on their respective carbon atoms. The asymmetric unit consists of a half Ce₆Mn₄ cluster, one pyridine molecule, two acetonitrile molecules and two half acetonitrile molecules (located on or close to symmetry elements). A total of 567 parameters were included in the structure refinement on F^2 using 25901 reflections with $I > 2\sigma(I)$ to yield R_1 and wR_2 of 7.17% and 16.76%, respectively.

For complex **10**·1.5DMF, the asymmetric unit contains a CeMn₈ cluster, and one and a half molecules of DMF. The solvent molecule in general position has its O and H atoms disordered, and they were refined in two parts each with their site occupation parameters fixed at 50%. The half solvent molecule comes from a DMF that is disordered around an inversion center. A total

of 1343 parameters were refined in the final cycle of refinement using 22645 reflections with $I > 2\sigma(I)$ to yield R_1 and wR_2 of 3.70% and 9.38%, respectively.

For complex $\mathbf{11} \cdot \text{H}_2\text{O} \cdot 6\text{MeCN}$, the asymmetric unit consists of a half cluster, one half water and three MeCN molecules. The latter were disordered and could not be modeled properly, thus program SQUEEZE, was used to calculate the solvent disorder area and remove its contribution to the overall intensity data. The N3 ligand is half disordered and there is a half water molecule associated with one part of the disorder. The N4 ligand is fully disordered and was refined in two parts with their site occupation factors dependently refined. A total of 356 parameters were included in the structure refinement on F^2 using 6631 reflections with $I > 2\sigma(I)$ to yield R_1 and wR_2 of 3.41% and 9.90%, respectively.

4.2.3 Other Studies

Infrared spectra were recorded in the solid state (KBr pellets) on a Nicolet Nexus 670 FTIR spectrometer in the 400-4000 cm^{-1} range. Elemental analyses (C, H, and N) were performed by the in-house facilities of the University of Florida Chemistry Department. Variable-temperature dc and ac magnetic susceptibility data were collected at the University of Florida using a Quantum Design MPMS-XL SQUID susceptometer equipped with a 7 T magnet and operating in the 1.8-300 K range. Samples were embedded in eicosane to prevent torquing. Pascal's constants were used to estimate the diamagnetic correction, which was subtracted from the experimental susceptibility to give the molar paramagnetic susceptibility (χ_M).

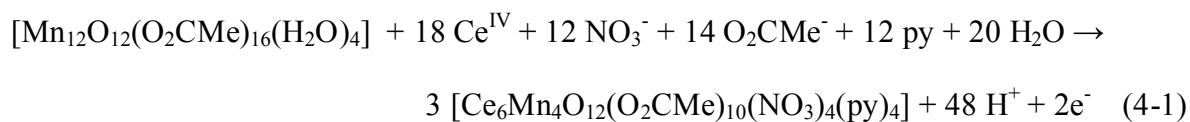
4.3 Results and Discussion

4.3.1 Syntheses

Heterometallic compounds containing first-row transition metals and lanthanides are known in the inorganic literature, but are relatively rare. Our group has previously reported a

series of mixed-metal Mn-Ce compounds^{174,178-181} as well as complexes with other lanthanides (Eu, Gd, Tb, Dy, Ho)^{170,172}, some of which behave as superparamagnets below their blocking temperature.^{172,178,180} Other groups have also explored the reactivity of Ce^{IV} with various first-row transition metal reagents,^{207,208} and great effort was invested in this chemistry both for fundamental understanding of the reactivity, and possible catalytic applications.

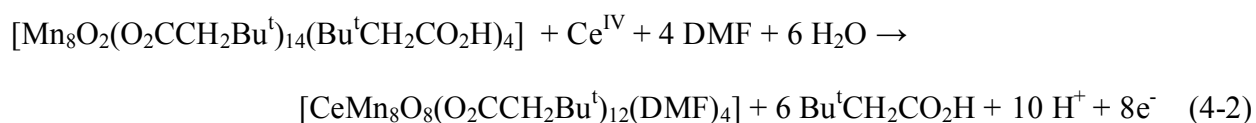
Very few synthetic methodologies have been employed for the synthesis of heterometallic Mn-Ce complexes. One such approach involves aqueous oxidation of simple Mn sources from high-valent Ce^{IV} salts in the presence of organic acids; this synthetic scheme has afforded a variety of high-valent Mn^{IV}-Ce^{IV} products with nuclearities ranging from 3 to 7.¹⁷⁹ Another synthetic route to Mn-Ce clusters is the reactivity of preformed species in the presence of Ce^{IV} salts, which has afforded a series of Mn^{III}₈Ce^{IV} clusters,^{178,180} a Mn^{III}₁₀Ce^{III}₄,¹⁷³ and a Mn^{IV}₄Ce^{III}₂.¹⁷⁴ The preformed species which have been used in the past in similar syntheses are homovalent Mn^{III} compounds. The synthetic approach employed here involves the overall oxidation of mixed-valence Mn₁₂ (average oxidation state +3.33), and Mn₈ (average oxidation state +2.25) with Ce^{IV}, which led to complex **9** (average oxidation state +3.8), and complex **10** (average oxidation state +3.1), respectively. The formation of **9** is summarized in eq 4-1.



Complex **9** was originally synthesized from layering an acetonitrile solution of **1** and (NH₄)₂[Ce(NO₃)₆] with pyridine. With the identity of the product established by x-ray crystallography a superior synthesis was developed using pyridine as a co-solvent in the reaction. The yield was improved substantially and the crystallization time was significantly reduced. (NH₄)₂[Ce(NO₃)₆] has been extensively used in organic synthesis as an oxidizing agent for a

plethora of organic substrates.^{191,193,209} Clearly, this remarkable oxidizer could potentially attack even more complicated systems, and in this case Ce^{IV} attacked the [Mn₁₂O₁₂(O₂CMe)₁₆(H₂O)₄] cluster, and reassembled a different high-nuclearity, high-oxidation state product. During this process, the potentially high coordination number of Ce^{IV}, as well as its preference in binding to the oxygen-rich nitrate anions, had a major effect on the product, and thus Ce^{IV} ions were incorporated into the final cluster. The presence of pyridine was also crucial for the stabilization and therefore isolation of the cluster, since the coordination sphere of the manganese ions was completed by one pyridine per manganese center. Other terminal groups could have been incorporated to facilitate the preference of Mn ions to coordination number 6. The pyridine rings in **9** form π stacks with the pyridine rings of neighboring molecules (*vide infra*). Thus, π - π stacking interactions explain the enhanced stability of the crystal lattice. Complex **9** seems eventually the most thermodynamically favored product, the formation of which is assisted by the presence of the solvent mixture. Crystal lattice dynamics are far complicated, and the formation of a product like this is nearly impossible to predict.

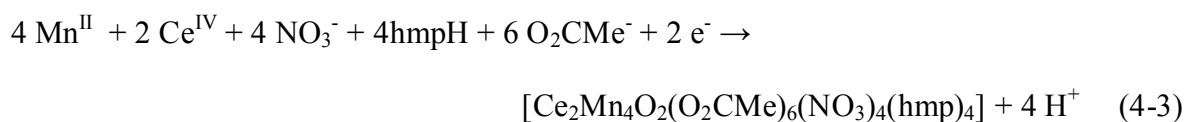
The formation of **10** is summarized in eq 4-2.



The synthesis of **10** involves the oxidative attack of Ce^{IV} on a Mn^{II}₆Mn^{III}₂ species, and the subsequent transformation of the latter to a Ce^{IV}Mn^{III}₈ species where all Mn ions are present in the +3 oxidation state. Thus, the average oxidation state in the resultant complex increases significantly, compared to the starting material. Therefore the use of Ce^{IV} as a means of Mn³⁺ ion inducer has been proven successful. Increase of the Mn₈ to Ce^{IV} ratio, or the use of Ce(ClO₄)₄ instead of (NH₄)₂[Ce(NO₃)₆], does not affect the identity of the product, but only its crystallinity

and isolated yield. Note that the synthesis of this CeMn₈ derivative is different than the previously reported synthesis of the other nearly isostructural clusters.^{178,180}

In the case of compound **11** the synthesis follows a very fruitful synthetic pathway, widely used in manganese cluster chemistry. This synthetic route involves the reaction of a chelating ligand, in this case hmp⁻, with metal-carboxylate precursors, such as Mn(O₂CMe)₂·4H₂O. However, since employment of Ce ions was also desired, a source of the second metal was added to the reaction mixture. The order, in which the reactants are added during the course of the reaction, follows a common scheme successfully used in the past. First the lanthanide non-carboxylate metal source was dissolved in the desired solvent (i.e. MeCN), then the organic pyridyl alcoholate ligand was added in order to increase the pH of the solution, and finally the manganese carboxylate was incorporated, with a direct noticeable color change of the solution to dark red, due to the oxidation of the Mn^{II} ions to Mn^{III} and/or Mn^{IV}, as a consequence of the basic conditions dominating the reaction mixture. The formation of **11** is summarized in eq 4-3.



In the syntheses of both **9** and **11**, nitrate ions are needed to complete the coordination sphere of the Ce^{IV} or Ce^{III} ions. The same reactions were performed using Ce(ClO₄)₄, but due to the absence of nitrates, the clusters were not stabilized and isolated. The latter experimental fact does not imply that the product did not form in solution; however, the analogous compound did not properly crystallize and was not further characterized. Also, performing the same reaction but changing the carboxylate ligation (i.e. using the propionate, or benzoate analogues of Mn₁₂, or the respective simple Mn^{II} salts) also did not produce any crystalline product, possibly due to

steric restrictions within the structure, basicity of the ligands, or other thermodynamic and kinetic factors which we are unable to analyze without any other experimental fact.

4.3.2 Description of Structures

4.3.1 X-ray crystal structure of complex **9**

A PovRay representation of the complete Ce_6Mn_4 molecule of **9** and a stereopair are provided in Figure 4-1. The labeled PovRay representation of the core of **9** is provided in Figure 4-2. Selected interatomic distances and angles are listed in Table D-9. Compound **9** crystallizes in the monoclinic space group $P2_1/n$. It contains six Ce^{IV} , two Mn^{III} and two Mn^{IV} and these are held together by eight $\mu_3\text{-O}^{2-}$ and four $\mu_4\text{-O}^{2-}$. The resulting $[\text{Ce}_6\text{Mn}_4\text{O}_{12}]^{14+}$ core of **9** can be described as one central octahedron of six Ce^{IV} ions with the equatorial Ce atoms belonging also to two outer distorted $[\text{Mn}^{\text{III/IV}}_2\text{Ce}^{\text{IV}}_2]$ cubanes, with the latter held together by two $\mu_4\text{-O}^{2-}$, and two $\mu_3\text{-O}^{2-}$. The oxidation states of the manganese and cerium ions, as well as the protonation level of the triply-bridging oxide bridges were established by bond-valence sum calculations^{210,211} (provided in Tables 4-3 and 4-4, respectively), charge considerations, and the presence of Jahn-Teller (JT) distortions on the Mn^{III} ions. Mn4 and its symmetry equivalent partner (Mn4') have JT axial elongations with, as expected, the elongated $\text{Mn}^{\text{III}}\text{-O}$ and $\text{Mn}^{\text{III}}\text{-N}$ bonds being at least 0.1-0.2 Å longer than the other $\text{Mn}^{\text{III}}\text{-O/N}$ bonds. The Mn and Ce ions are additionally bridged by eight $\eta^1:\eta^1:\mu\text{-MeCO}_2^-$, each bridging one Mn and one equatorial Ce ions. The coordination sphere of each axial Ce^{IV} ion is completed by two chelating NO_3^- groups, with the overall coordination geometry of the eight-coordinate axial Ce^{IV} ions being square antiprismatic.

Based on this overall structure, the equatorial plane of the molecule is defined by the square planar arrangement of Ce2, Ce3 and their symmetry-related partners at the equatorial plane of the central octahedron, and is extended to include the four coplanar $\mu_3\text{-O}^{2-}$ (O11, O12

and their symmetry-related counterparts) in the two cubane-like units at the opposite ends of the cage. The distance between the axial Ce1 and its symmetry equivalent from this plane is 2.614 Å. Within the Ce₆ octahedron, the distance between the axial Ce ions and the equatorial ones is on average 3.670 Å. In the equatorial plane of the central octahedron, there are two short and two longer Ce-Ce distances, namely 3.628 Å for the Ce2 – Ce3' pair and its symmetry equivalent, and 3.800 Å for the Ce2 – Ce3 pair and its symmetry equivalent. The angle between the two best mean planes defined by Ce2, Ce3 and their symmetry-related partners, and Ce1, O7, O9 and their symmetry-equivalent partners, is 89.06°. Another interesting feature of this molecule is the fact that the pyridine rings are not parallel to the plane of the equator and the distance between N4 (which is bound to Mn5) and the equatorial plane is 1.638 Å, whereas the distance between N3 (which is bound to Mn4) and the same plane is 1.506 Å. Inspection of the crystal packing in complex **9** reveals the presence of significant π - π stacking interactions between the clusters in the unit cell, since the distance between two parallel pyridines belonging to two different molecules is in the range of the regular stacking distance (N4 \cdots C13 = 3.604 Å and N3 \cdots C18 = 3.543 Å). The cuboidal structure constructed by two Mn and two Ce ions, to the best of our knowledge, has never been observed before in the literature. Also, the octahedral arrangement of the six Ce^{IV} ions is unprecedented for Ce^{IV}, giving this compound its characteristic structural signature.

4.3.2 X-ray crystal structure of complex **10**

A PovRay representation of the complete CeMn₈ molecule of **10** and the labeled core are provided in Figures 4-3 and 4-4, respectively. Selected interatomic distances and angles are listed in Table D-10. Compound **10** crystallizes in the triclinic space group $P\bar{1}$. It contains one Ce^{IV}, and eight Mn^{III} ions bridged by eight μ_3 -O²⁻ and twelve O₂CCH₂Bu^{t-} groups. The structure can be described as a nonplanar, saddlelike [Mn^{III}₈(μ_3 -O)₈]⁸⁺ loop attached to a central Ce^{IV} ion

via the triply bridging oxides of the loop. The resulting $[\text{CeMn}_8\text{O}_8]^{12+}$ central core is shown in Figure 4-4 and can be seen to comprise eight $[\text{MnO}_2\text{Ce}]$ rhombs fused at the Ce-O^{2-} edges. Four Mn atoms (Mn2, Mn4, Mn6, Mn8) occupy the corners of an almost perfect tetrahedron (Mn2-Ce1-Mn4, Mn2-Ce1-Mn6, Mn2-Ce1-Mn8, Mn4-Ce1-Mn6, Mn4-Ce1-Mn8, Mn8-Ce1-Mn6 angles range from 108.605 to 109.928°), whereas the other four Mn atoms (Mn1, Mn3, Mn5, Mn7) form a distorted (flattened) tetrahedron (Mn1-Ce1-Mn3, Mn1-Ce1-Mn7, Mn3-Ce1-Mn5, Mn5-Ce1-Mn7 angles range from 90.67 to 93.755°). Within this description the Ce^{IV} ion occupies the center of both the Mn_4 tetrahedra. Extending the central core to include the $\mu\text{-OR}^-$ bridges originating at the peripheral carboxylates, the $[\text{CeMn}_8\text{O}_8(\mu\text{-OR})_4]^{8+}$ complete core of **10** can be described as four edge-sharing cubane units, each missing a vertex; the four incomplete cubes are related by a pseudo inversion center located on the central Ce^{IV} . Peripheral ligation around the central core is provided by eight $\eta^1: \eta^1: \mu\text{-O}_2\text{CCH}_2\text{Bu}^{\text{t}-}$, and four $\eta^1: \eta^2: \mu_3\text{-O}_2\text{CCH}_2\text{Bu}^{\text{t}-}$ groups, while four DMF molecules are terminal ligands on four of the Mn^{III} (Mn2, Mn4, Mn6, and Mn8) ions. The Ce atom is eight-coordinate with distorted dodecahedral geometry, and the Ce-O lengths (2.31-2.40 Å) are typical for eight-coordinate Ce^{IV} .²¹¹

Complex **10** is the fifth structurally characterized CeMn_8 complex, with a saddle-like topology and the general formula $[\text{CeMn}_8\text{O}_{12}(\text{O}_2\text{CR})_{12}(\text{L})_4]$ (where R = Me, Ph, HPh₂, and $\text{CH}_2\text{Bu}^{\text{t}-}$, and L = terminal ligands). These complexes span differences in the peripheral ligation, which in turn are significant concerning their magnetic behavior (*vide infra*). Therefore, it is of interest to assess in more detail any structural differences. The main differences between **10** and the other previously reported CeMn_8 clusters are (i) the peripheral ligation, which in **10** is provided by $\text{O}_2\text{CCH}_2\text{Bu}^{\text{t}-}$ groups, compared to O_2CMe^- , O_2CPh^- , or $\text{O}_2\text{CHPh}_2^-$ groups previously employed, and (ii) the terminal ligation in **10** which is provided by DMF molecules,

compared to H₂O, py, MeCN, or dioxane molecules as previously reported.^{178,180} These differences result in small perturbations in the metric parameters within the [CeMn₈O₈]¹²⁺ core, the most important of which are tabulated in Table 4-1. Most of the entries of Table 4-1 are, within the 3σ criterion, identical for all the complexes, with the largest difference arising for the Mn-μ-OR⁻-Mn angle, which is expected to significantly affect the coupling between the Mn centers, which gauges the spin. Overall, we anticipate the collective effect of all the small perturbations to alter the magnetic properties of the different compounds, and/or their SMM behavior, if any (*vide infra*).

4.3.3 X-ray crystal structure of complex **11**

A PovRay representation of the complete Ce₂Mn₄ molecule of **11** and a stereopair are provided in Figure 4-5. The core of the cluster and a schematic representation of the metal topology, and the key structural features within the Ce₂Mn₄ cage are shown in Figures 4-6 and 4-7 respectively. Selected interatomic distances and angles are listed in Table D-1. Compound **11** crystallizes in the triclinic space group $P\bar{1}$. It contains two Ce^{III}, and four Mn^{III} ions and these are held together by two μ₄-O²⁻, four μ-O⁻ from the alkoxo arm of the hmp⁻ ligand, and six total acetate ligands two of which adopt the η¹:η¹:μ bridging mode (bridging two Mn^{III} ions), and two are found to be bridging in the rare η²:η²:μ₃ fashion (bridging two Mn^{III} and one Ce^{III} ions). The resulting [Ce₂Mn₄O₂]¹⁴⁺ core of **11** can be described as a distorted snub octahedron comprising of four manganese ions in the equatorial plane (Mn1, Mn2 and their symmetry related partners), and two cerium centers located at the axial apexes, positioned 2.026 Å above and below the plane. The angle between the Mn₄ plane and the plane which includes both the cerium centers and two diagonally opposing manganese ions (Mn2 and its symmetry related partner) is 86.72°. The parallelogram which the four manganese ions form is 5.115 Å in length and 3.198 Å in

width, as seen in Figure 4-7. The oxidation states of the manganese and cerium ions were established by bond-valence sum calculations^{210,211} (provided in Table E-3), charge considerations, and the presence of Jahn-Teller (JT) distortions on the Mn^{III} ions. Mn1, Mn2 and their symmetry equivalent partners (Mn1' and Mn2') have JT axial elongations with, as expected, the elongated Mn^{III}-O bonds being at least 0.1-0.2 Å longer than the other Mn^{III}-O/N bonds. The JT elongated axes in both the symmetry independent Mn^{III} ions involve the subsequent bond between the manganese ion and the oxygen of the $\eta^2:\eta^2:\mu_3\text{-O}_2\text{CMe}^-$ ligand. The latter coordination mode is relatively rare in the inorganic literature, and it seems to be imposing a significant strain to the structure, making the accommodation of all four JT elongated axes easier at this position.

Complexes **9**, **10** and **11** join a small family of Mn-Ce clusters. Since most of these were reported only relatively recently, we have listed them in Table 4-2 for a convenient comparison of their structural type and pertinent magnetic data such as their ground-state spin (*S*) values (*vide infra*). Examination of Table 4-2 shows that complexes **9** and **11** represent two new structural types, with **9** having the highest reported Ce/Mn ratio of 1.5.

4.3.3 Magnetochemistry

4.3.3.1 Direct current magnetic susceptibility studies

Solid state, variable-temperature magnetic susceptibility measurements were performed on vacuum-dried microcrystalline samples of complex **9**·py·2H₂O, suspended in eicosane to prevent torquing. The dc magnetic susceptibility (χ_M) data were collected in the 5.0-300 K range in a 0.1 T (1000 G) magnetic field. Figure 4-8 shows one half of the molar magnetic susceptibility (χ_M) of complex **9**·py·2H₂O as a $\chi_M T$ versus T plot. The $\chi_M T$ has a value of $\sim 7.2 \text{ cm}^3 \text{ K mol}^{-1}$ at 300 K, gradually decreasing with decreasing temperature to $\sim 3.1 \text{ cm}^3 \text{ K mol}^{-1}$ at 5.0 K. The $\chi_M T$ value at

300 K is higher than the $\sim 4.9 \text{ cm}^3 \text{Kmol}^{-1}$ value expected for two non-interacting Mn centers with the oxidation states found in complex **9** (1 Mn^{III} and 1 Mn^{IV} atom), since Ce^{IV} is diamagnetic (f^0) and has no magnetic contribution. The exchange parameter J between the Mn centers, gauging the interaction within the Mn^{III}-O₂-Mn^{IV} units of **9**, is expected to be affected by the concurrent bonding to the bridging O²⁻ of the strong Lewis acidic Ce^{IV} ion, which weakens the Mn-O bonds that mediate the Mn^{III}Mn^{IV} superexchange interaction.

Thus, complex **9** is anticipated to exhibit the magnetic response of two independent dimeric units; the large diamagnetic octahedron composed of the six Ce^{IV} ions in the middle results in a negligible long range exchange pathway between the dimers at the two opposite ends of the cluster. The isotropic (Heisenberg) spin Hamiltonian describing an exchange-coupled Mn^{III}Mn^{IV} dimeric unit, which is effectively what we expect for complex **9**, is given by eq 4-3, where J is the exchange coupling parameter between the two Mn ions, and $S_1 = 2$ and $S_2 = 3/2$.

$$\hat{H} = -2J(\hat{S}_1\hat{S}_2) \quad (4-3)$$

The eigenvalues of the spin Hamiltonian may be determined using eq 4-4, where S_T is each energy state given by the relationship $S_T = |S_1 + S_2|, |S_1 + S_2 - 1|, \dots, |S_1 - S_2|$; in this case the energy states are $S_{T(1)} = 7/2$, $S_{T(2)} = 5/2$, $S_{T(3)} = 3/2$ and $S_{T(4)} = 1/2$ (Figure 4-8, inset).

$$E(S_T) = -J[S_T(S_T + 1)] \quad (4-4)$$

A theoretical χ_M versus T expression was derived for complex **9** from the use of the Van Vleck equation,^{212,213} and was modified to include a fraction (p) of paramagnetic impurity (assumed to be mononuclear Mn^{II}), and temperature-independent paramagnetism (TIP). The latter was kept constant at $300 \times 10^{-6} \text{ cm}^3 \text{Kmol}^{-1}$. Data below 15 K were ignored for the purpose of this fitting. One of the main reasons is the contribution of the interdimer interaction which becomes significant only at lower temperatures. Note that this fitting model assumes that for the

higher temperature range the exchange coupling constant for the interdimer interaction is orders of magnitude smaller than the intradimer coupling, and thus the parameter that describes this interaction is omitted from our fitting model. Such intercluster communication could be possible through a spin polarization mechanism, and this cannot be ignored for lower temperatures. Other contributing factors are zero-field splitting, weak intermolecular interactions, and Zeeman effects from the use of the dc field. Attempts to fit the complete data using a $2J$ model (including the long-range interaction) gave poor fits and g significantly greater than 2.0. The modified Van Vleck equation (eq 4-5) was used to fit the observed temperature dependence of the molar magnetic susceptibility as a function of the exchange coupling parameter J , and an isotropic g value. The Ω parameter in eq 4-5 is the degeneracy of the S_T state, but for dinuclear compounds Ω is always 1.^{212,213} The obtained fit (solid line in Figure 4-8) gave $J = -45.65 \text{ cm}^{-1}$, $g = 1.95$ and $p = 0.012$ and a ground-state spin value $S_T = 1/2$ (Figure 4-8, inset). The goodness of the fit is evident from the low statistical error, $R^2 = 0.999$.

The $\text{Mn}^{\text{III}}\text{-Mn}^{\text{IV}}$ moiety in **9** is bridged by two $\mu_3\text{-O}^{2-}$ ligands, where the third metal ion is a diamagnetic Ce^{IV} atom (strong Lewis acid). Therefore, the exchange coupling is expected to be weaker than in the case of $\text{Mn}^{\text{III}}\text{-(}\mu_2\text{-O}^{2-}\text{)}_2\text{-Mn}^{\text{IV}}$ dimers where the exchange pathway is mediated by two $\mu_2\text{-O}^{2-}$ ions, and stronger than in the case of $\text{Mn}^{\text{III}}\text{-(}\mu_3\text{-O}^{2-}\text{)-Mn}^{\text{IV}}$ units when there is only one monoatomic bridge between the metal ions. The value of J in the case of complex **9** is, as predicted, significantly lower than the literature values reported for independent $\text{Mn}^{\text{III}}\text{-(}\mu_2\text{-O}^{2-}\text{)}_2\text{-Mn}^{\text{IV}}$ dimers, which range from -102 to -220 cm^{-1} ,^{214,215} and higher than $\text{Mn}^{\text{III}}\text{-(}\mu_3\text{-O}^{2-}\text{)}_2\text{-Mn}^{\text{IV}}$ dimeric units within a larger cluster, with only one bridging $\mu_3\text{-O}^{2-}$ and $J = -18.7, -21, \text{ and } -36 \text{ cm}^{-1}$.²¹⁶

$$\chi_M = (1-p) \frac{Ng^2\beta^2}{3kT} \frac{\sum S_T(S_T+1)(2S_T+1)\Omega(S_T)\exp\left(\frac{-E(S_T)}{kT}\right)}{\sum (2S_T+1)\Omega(S_T)\exp\left(\frac{-E(S_T)}{kT}\right)} + p \frac{35Ng^2\beta^2}{12kT} + TIP \quad (4-5)$$

For complex **10**, the dc magnetic susceptibility data are presented in Figure 4-9. The $\chi_M T$ value of 25.83 cm³Kmol⁻¹ at 300 K increases slightly to a value of 29.92 cm³Kmol⁻¹ at 90 K, and then drops rapidly and reaches a value of 4.69 cm³Kmol⁻¹ at 5 K, indicating a small ground state S for **10**. The spin-only ($g = 2.0$) value for eight noninteracting, high-spin Mn^{III} ions is 24.00 cm³Kmol⁻¹ (Ce^{IV} is diamagnetic, f^0), which is slightly lower than the observed 300 K value for **10**. This suggests that the predominant exchange interactions within the molecule are weakly ferromagnetic at the high temperature range, and then stronger antiferromagnetic interactions assume greater importance at lower temperatures (*vide infra*). Owing to the size and symmetry of the molecule, a matrix diagonalization method to evaluate the various M_2 pairwise exchange parameters (J_{ij}) within the Mn₈Ce core is not easy. Similarly application of the equivalent operator approach based on the Kambe vector coupling method is not possible.²¹⁷

The magnetic data for complex **11**·2H₂O revealed overall antiferromagnetic interactions within the cluster, since the $\chi_M T$ decreases sharply with decreasing temperature, as seen in Figure 4-9. The presence of Ce^{III} atoms in the structure of **11** further complicates the understanding of the magnetic data for this compound, since Ce^{III} has significant spin-orbit coupling. For the lanthanides, paramagnetism is due to unpaired electrons in the f orbitals, which are more buried (lower in energy) than d orbitals and are not as affected by the ligands. Thus, the orbital contribution is not quenched significantly. The spin-orbit coupling for the unpaired electrons in

the *f* orbitals of the lanthanides is a lot stronger than unpaired electrons in the *d* orbitals of the transition metals. Consequently, it is expected that the experimental values obtained for trivalent lanthanides would not be in good agreement with the spin-only values obtained from theory. In this case, the effective magnetic moment, denoted as μ_{eff} , can be calculated from eq 4-6,

$$\mu_{\text{eff}} = g[J(J+1)] \quad (4-6)$$

where *J* is the angular momentum quantum number which includes spin-orbit coupling.

The relationship of μ_{eff} and $\chi_{\text{M}}T$ is given in eq 4-7.

$$\mu_{\text{eff}} = (8\chi_{\text{M}}T)^{1/2} \quad (4-7)$$

Therefore, it is feasible to calculate the $\chi_{\text{M}}T$ for a given lanthanide. In this manner, Ce^{III} has a $\chi_{\text{M}}T$ of $0.8 \text{ cm}^3\text{Kmol}^{-1}$ for the free ion.⁹ Thus, at 300 K we can expect a $\chi_{\text{M}}T$ value corresponding to four Mn^{III} and two Ce^{III} , namely $13.6 \text{ cm}^3\text{Kmol}^{-1}$. The room-temperature $\chi_{\text{M}}T$ value of approximately $10.9 \text{ cm}^3\text{Kmol}^{-1}$ is below that expected for 4 Mn^{III} and 2 Ce^{III} ions ($13.6 \text{ cm}^3\text{Kmol}^{-1}$), which indicates the presence of dominant antiferromagnetic interactions, even at 300 K. The value then drops slowly with decreasing temperature, as seen in Figure 4-9, to a value of $\sim 7.6 \text{ cm}^3\text{Kmol}^{-1}$ at 130 K. Below 130 K, $\chi_{\text{M}}T$ decreases more sharply to a value of $\sim 0.9 \text{ cm}^3\text{Kmol}^{-1}$ at 5.0 K. This behavior is consistent with overall antiferromagnetic exchange interactions between the metal centers with a very low or even diamagnetic spin ground state ($S_{\text{T}} = 0$).

4.3.3.2 Alternating current magnetic susceptibility studies

In order to accurately determine the ground state spin of complex **9**·py·2H₂O, alternating current (ac) magnetic susceptibility measurements were performed in the 1.8–15 K temperature range in a 3.5 G ac field oscillating at 50–1000 Hz. The in-phase component of the ac susceptibility for the complete molecule is shown in Figure 4-10, and reveals two pertinent

features: (i) a linearly decreasing region of the susceptibility at higher temperatures, namely for $T > 7.5$ K in this case, followed by (ii) a lower temperature region where the signal decrease assumes a greater rate. Such slope changes in the in-phase are indicative of slow relaxation of the magnetization, only if they are frequency dependent, and are paired with concomitant growth of out-of-phase ac signals. However, frequency dependence is absent for $\mathbf{9}\cdot\text{py}\cdot 2\text{H}_2\text{O}$ and there are no out-of-phase signals (Figure 4-11). Complex $\mathbf{9}\cdot\text{py}\cdot 2\text{H}_2\text{O}$ is not an SMM and this is anticipated due to the small S value of the cluster.

Also, it is interesting to note that extrapolation of the in-phase ac data to 0 K from the higher temperature region (>7.5 K) corresponds to an $S=5/2$ ground-state, whereas extrapolation from the lower temperature region (1.8 – 7.5 K) supports a ground state of $S = 1$. To account for this behavior it would be useful to consider the possibility of observing the independent response of each $\text{Mn}^{\text{III}}\text{Mn}^{\text{IV}}$ pair at higher temperatures, and at lower ones observing the long-range coupling of the two dimers. One other possible explanation of this behavior could be the Boltzmann population of excited states even at these low temperatures. In the dimeric model used to fit the dc data, any interdimer interaction was ignored, so the energy gap of 137 cm^{-1} between the ground state and the first excited state should not mislead our interpretation, since it may not be applicable for these low temperatures. This long-range coupling becomes stronger at these low temperatures, since the spin polarization mechanism becomes increasingly more significant. Thus, there is further quantum mixing of states, and the effective energy gap between the different spin states is quenched, compared to that predicted from the fitting. Extrapolation of the lower temperature data to 0 K, where only the ground state will be populated, gives a $\chi_M' T$ of $\sim 1\text{ cm}^3\text{ Kmol}^{-1}$, which indicates an $S=1$ for this system; this is indeed what we expect for this dimer-of-dimers, where the intradimer interaction is antiferromagnetic with $S=1/2$ as proven by

the dc studies, and the interdimer interaction is weakly ferromagnetic. Note that interdimer interactions could be mediated either via a spin polarization mechanism through the Ce^{IV}_6 moiety, or via weak intermolecular interactions (through the significant π - π stacking which results from the disposition of the pyridine rings between two neighboring molecules). However, the latter should be much weaker, and rather antiferromagnetic, which is not consistent with the ac data (ac signal clearly heads for $\chi_{\text{M}}' \text{ T} = 1 \text{ cm}^3 \text{ Kmol}^{-1}$). Therefore, on the basis of the relative strength, and the nature of the interactions, we can rule out the possibility of intermolecular interactions being the major contributing factor to the observed behavior.

The in-phase component of the ac magnetic susceptibility of **10** (Figure 4-10) decreases linearly with decreasing temperature and reaches a value of $1.86 \text{ cm}^3 \text{ Kmol}^{-1}$ at 1.8 K. Such linear decrease is consistent with depopulation of excited states, which are thermally populated even at these low temperatures. Such behavior is consistent with the dc measurements, where an apparent competition of exchange couplings is observed. Competition of ferro- and antiferromagnetic interactions often results in lowering of the energy levels of excited states, which in turn complicates our interpretation of the magnetic data. In the case of **10**, however, the linear decrease of the $\chi_{\text{M}}' \text{ T}$ assumes a single slope, and extrapolation of the data to 0 K gives a value of $\chi_{\text{M}}' \text{ T} < 1$, suggestive of a diamagnetic ground state. This ground state, even though it is not well isolated, represents the minimum S state for such a $\text{Ce}^{\text{IV}}\text{Mn}^{\text{III}}_8$ complex, with $S = 16$ being the highest. Note that $S = 16$, as well as other intermediate ground states, have been previously reported,^{178,180} with $S = 0$ for **10** completing the entire range of possible ground states for this family of complexes. These different ground state values are probably different due to the small overall perturbation of the CeMn_8 core, which within this family spans a wide range of peripheral bridging groups from simple acetates, to bulky diphenyl acetates, and now tert-butyl

acetates. The comprehensive effect appears to be significant, and alters the magnetic response of these compounds, whereas the magnetostructural correlation in Table 4-1 reveals the main difference between the family members, which is the angle between the Mn^{III} ions and the monoatomic μ -OR⁻ ion. This particular parameter is thus proven to be of great significance for the nature of the Mn^{III}-Mn^{III} exchange coupling, and the spin of the molecule. Significant differences in the spin ground states could also account for the appearance or not of out-of-phase signals (Figure 4-12), due to SMM behavior (see Table 4-1).

Alternating current magnetic susceptibility measurements for complex **11**·2H₂O were performed in the 1.8–15 K temperature range in a 3.5 G AC field oscillating at 50–1000 Hz. The in-phase component of the ac susceptibility for complex **11**, shown in Figure 4-11, exhibits a linear decrease of the signal with decreasing temperature, similar to **10**, thus confirming the dominant antiferromagnetic interactions within the molecule. In contrast to complex **9**, the $\chi_M' T$ product for **10** is decreasing at a constant rate, and reaches a value of $\sim 0.7 \text{ cm}^3 \text{ mol}^{-1} \text{ K}$ at 1.8 K. Extrapolation of $\chi_M' T$ to 0 K gives a value of $\sim 0.6 \text{ cm}^3 \text{ K mol}^{-1}$ suggestive of an S=1 or an S=0 ground state spin value, with the latter value being more possible due to the symmetry of the molecule, as well as the accordance to the dc magnetic susceptibility data. The spin frustration effects expected within the M₃ triangular units of the Mn₄Ce₂ structure, as well as the thermal population of the spin-orbit (Stark) components of the Ce^{III} ions, can also affect the magnetic response of **10**, and lead to some residual magnetism. Thus it is safe to state that even at these very low temperatures low-lying excited states are populated. From the absence of any signal in the out-of-phase component of the ac (Figure 4-13), it is evident that this complex does not behave as an SMM, as expected for such a low spin system.

Table 4-1. Magnetostructural correlation between **10** and other CeMn₈ clusters with general formula [CeMn₈O₁₂(O₂CR)₁₂(L)₄]

| | 10 (R=CH ₂ Bu ^t , L=DMF) | R=Me L=H ₂ O | R=Me L=py | R=Ph L=MeCN | R=HPh ₂ L=H ₂ O |
|--|---|----------------------------|------------------------------------|-----------------------|--|
| Space group | <i>P</i> -1 | <i>I</i> -4 | <i>P</i> 4 ₂ / <i>n</i> | <i>P</i> 4 <i>n</i> 2 | <i>P</i> 2 ₁ / <i>n</i> |
| Mn ^{III} -Mn | 3.025±0.015 | 3.029(7) | 3.034(1) | 3.011(1) | 3.04±0.01 |
| | 3.235±0.005 | 3.240(8) | 3.237(1) | 3.255(1) | 3.21±0.01 |
| Mn ^{III} -Ce | 3.345±0.025 | 3.345(5) | 3.331(1) | 3.309(1) | 3.36±0.01 |
| | | 3.356(5) | 3.348(1) | 3.320(1) | |
| Mn-μ-OR ⁻ -Mn | 82.09±0.39 | 84.5(1) | 82.4(1) | 81.5(1) | 84.2±1.3 |
| Mn-μ ₃ -O ²⁻ -Mn | 121.00±0.65 | 122(1) | 121.4(2) | 123.3(2) | 119.8±0.6 |
| | 107.45±0.90 | 106(1) | 106.8(2) | 107.0(2) | 102.3±2.6 |
| Mn-μ ₃ -O ²⁻ -Ce | 102.7±1.1 | 102.9±1.1 | 102.35±0.35 | 101.4±0.1 | 102.45±0.65 |
| | 105.5±1.2 | 105.85±0.05 | 105.95±0.65 | 105.25±0.35 | 106.0±0.9 |
| S | 0 | 16 | 4 or 5 | n.r. | 6 ± 1 |
| SMM | No | Yes ^a | No | n.r. | Yes ^b |

^a SMM with exchange-bias due to H-bonded 1D chain formation, ^b SMM with fast tunneling

Table 4-2. Structural types, core descriptions, and ground state S values for heterometallic Mn-Ce clusters

| Complex | Core | Ce/Mn ratio | S |
|--|--|-------------|--------|
| [CeMn ₂ O ₃ (O ₂ CMe)(NO ₃) ₄ (H ₂ O) ₂ (bpy) ₂](NO ₃) ^a | [Ce ^{IV} Mn ^{IV} ₂ (μ-O) ₃] ⁸⁺ | 0.5 | 0 |
| [Ce ₃ Mn ₂ O ₆ (O ₂ CMe) ₆ (NO ₃) ₂ (mhpH) ₄] ^b | [Ce ^{IV} ₃ Mn ^{IV} ₂ (μ ₃ -O) ₆] ⁸⁺ | 1.5 | 0 |
| [Ce ₃ Mn ₂ O ₆ (O ₂ CMe) ₆ (NO ₃) ₂ (pyroH) ₂ (H ₂ O) ₃] ^b | [Ce ^{IV} ₃ Mn ^{IV} ₂ (μ ₃ -O) ₆] ⁸⁺ | 1.5 | 0 |
| [Ce ₂ Mn ₄ O ₂ (O ₂ CMe) ₆ (NO ₃) ₄ (hmp) ₄] ^c | [Ce ^{III} ₂ Mn ^{III} ₄ (μ ₄ -O) ₂ (μ-OR') ₄ (μ-OR'') ₄] ⁶⁺ | 0.5 | 0 or 1 |
| [Ce ₂ Mn ₄ O ₂ (Me-sao) ₆ (NO ₃) ₄ (OAc) ₂ (H ₂ O) ₂] ^d | [Ce ^{III} ₂ Mn ^{IV} ₄ (μ ₃ -O) ₂ (μ-OR') ₄] ⁶⁺ | 0.5 | 3/2 |
| [CeMn ₆ O ₉ (O ₂ CMe) ₉ (NO ₃)(H ₂ O) ₂] ^e | [Ce ^{IV} Mn ^{IV} ₆ (μ ₃ -O) ₆ (μ-O) ₃] ¹⁰⁺ | 0.17 | 0 |
| [CeMn ₆ O ₉ (O ₂ CMe) ₉ (MeOH)(H ₂ O) ₂](ClO ₄) ^e | [Ce ^{IV} Mn ^{IV} ₆ (μ ₃ -O) ₆ (μ-O) ₃] ¹⁰⁺ | 0.17 | 0 |
| [CeMn ₆ O ₉ (O ₂ CMe) ₉ (NO ₃)(H ₂ O) ₂] ^e | [Ce ^{IV} Mn ^{IV} ₆ (μ ₃ -O) ₆ (μ-O) ₃] ¹⁰⁺ | 0.17 | 0 |
| [CeMn ₈ O ₈ (O ₂ CMe) ₁₂ (H ₂ O) ₄] ^f | [Ce ^{IV} Mn ^{III} ₈ (μ ₃ -O) ₈] ¹²⁺ | 0.125 | 16 |
| [CeMn ₈ O ₈ (O ₂ CMe) ₁₂ (py) ₄] ^f | [Ce ^{IV} Mn ^{III} ₈ (μ ₃ -O) ₈] ¹²⁺ | 0.125 | 4 or 5 |
| [CeMn ₈ O ₈ (O ₂ CPh) ₁₂ (MeCN) ₄][CeMn ₈ O ₈ (O ₂ CPh) ₁₂ (dioxane) ₄] ^f | [Ce ^{IV} Mn ^{III} ₈ (μ ₃ -O) ₈] ¹²⁺ | 0.125 | n.r. |
| [CeMn ₈ O ₈ (O ₂ CCHPh ₂) ₁₂ (H ₂ O) ₄] ^f | [Ce ^{IV} Mn ^{III} ₈ (μ ₃ -O) ₈] ¹²⁺ | 0.125 | 6 ± 1 |
| [Mn ₈ CeO ₈ (O ₂ CCH ₂ Bu ^t) ₁₂ (DMF) ₁₄ ·1.5DMF] ^f | [Ce ^{IV} Mn ^{III} ₈ (μ ₃ -O) ₈] ¹²⁺ | 0.125 | 0 |
| [Ce ₆ Mn ₄ O ₁₂ (O ₂ CMe) ₁₀ (NO ₃) ₄ (py) ₄] ^g | [Ce ^{IV} ₆ Mn ^{III} ₂ Mn ^{IV} ₂ (μ ₃ -O) ₈ (μ ₄ -O) ₄] ¹⁴⁺ | 1.5 | 1 |
| [Ce ₄ Mn ₁₀ O ₁₀ (OMe) ₆ (O ₂ CPh) ₁₆ (NO ₃) ₂ (MeOH) ₂ (H ₂ O) ₂] ^h | [Ce ^{IV} ₂ Ce ^{III} ₂ Mn ^{III} ₁₀ (μ ₃ -O) ₄ (μ ₄ -O) ₆ (μ ₂ -OMe) ₄ (μ ₃ -OMe) ₂] ¹⁸⁺ | 0.4 | 4 |

^a {Mn^{IV}₂O₂} rhomb linked to Ce^{IV} via a linear O²⁻; ¹⁷⁹ ^b Ce^{IV}₃ isosceles triangle with two Mn^{IV} being the axial apexes of a trigonal bipyramid; ¹⁷⁹ ^c Mn^{III}₄ parallelogram with 2Ce^{III} ions being the axial apexes of a highly-distorted octahedron; ^d two {Mn^{IV}₂Ce^{III}O} triangles linked through two η²:η²:η¹:μ₄ oximato ligands; ¹⁷⁴ ^e Mn^{IV}₆ wheel connected to a central Ce^{IV} ion via 6 μ₃-O²⁻; ¹⁷⁹ ^f non-planar, saddle-like [Mn₈O₈]⁸⁺ loop attached to the central Ce^{IV} via the O²⁻ ions; ^{178,180} ^g a central Ce^{IV}₆ octahedron with the equatorial Ce atoms also belonging to two outer distorted [Mn^{III/IV}₂Ce^{IV}₂] cubanes; ^h a central [Mn^{III}₄Ce^{IV}₂O₆(OMe)₂] unit attached at either end to a [Mn^{III}₃Ce^{III}O₂(OMe)₂] distorted-cubane unit, giving a tubular structure. ¹⁷³ Abbreviations: bpy=2,2'-bipyridine, mhpH=6-methyl, 2-hydroxypyridine, pyro=2-pyrrolidinone, Me-saoH₂=methyl salicylaloxime, hmpH=2-hydroxymethyl pyridine.

4.4 Conclusions

The versatility of manganese coordination chemistry, in conjunction with the coordination abilities of cerium ions, produced three new clusters, namely $\text{Ce}^{\text{IV}}_6\text{Mn}^{\text{IV}}_2\text{Mn}^{\text{III}}_2$, $\text{Ce}^{\text{IV}}\text{Mn}^{\text{III}}_8$, and $\text{Ce}^{\text{III}}_2\text{Mn}^{\text{III}}_4$, with unprecedented structural characteristics. Specifically, complex **9** is the first example of a 3d/4f molecular species with an octahedral arrangement of the Ce^{IV} ions within the molecular cage. Also, the cubane-like motif consisting of two $\text{Mn}^{\text{III/IV}}$ and two Ce^{IV} ions has no precedent in the literature. Complex **10** is the fifth isolated cluster of the CeMn_8 family, with the previous examples assuming different peripheral ligation, and different magnetic properties. Complex **11** realizes a discrete highly-distorted snub octahedral metal architecture, with a basal parallelogram which is constituted by four Mn^{III} , and two Ce^{III} ions being the axial apexes. Both **9** and **11** are new 3d/4f structural types, they possess aesthetically pleasing cage-like metal topologies, and even though they are not single-molecule magnets, they constitute two new additions to the small family of mixed transition metal-lanthanide molecular clusters. Complex **10** was found to have a diamagnetic ground state, in stark contrast to the rest of the known CeMn_8 clusters, with the magnetostructural correlation highlighting the major contributor to this difference. This chemistry of 3d/4f metal clusters can be extended to different combinations of metals and/or metal/lanthanide ratios, and is likely to produce more polymetallic assemblies, with novel metal topologies. Mixed 3d/4f clusters have the potential of exhibiting exciting properties due to their “hermaphrodite” nature, which includes strongly coupled 3d metal cores, incorporating highly anisotropic lanthanide ions. Such a potential should not be underestimated in the future, as a route to single-molecule and single-chain magnets.

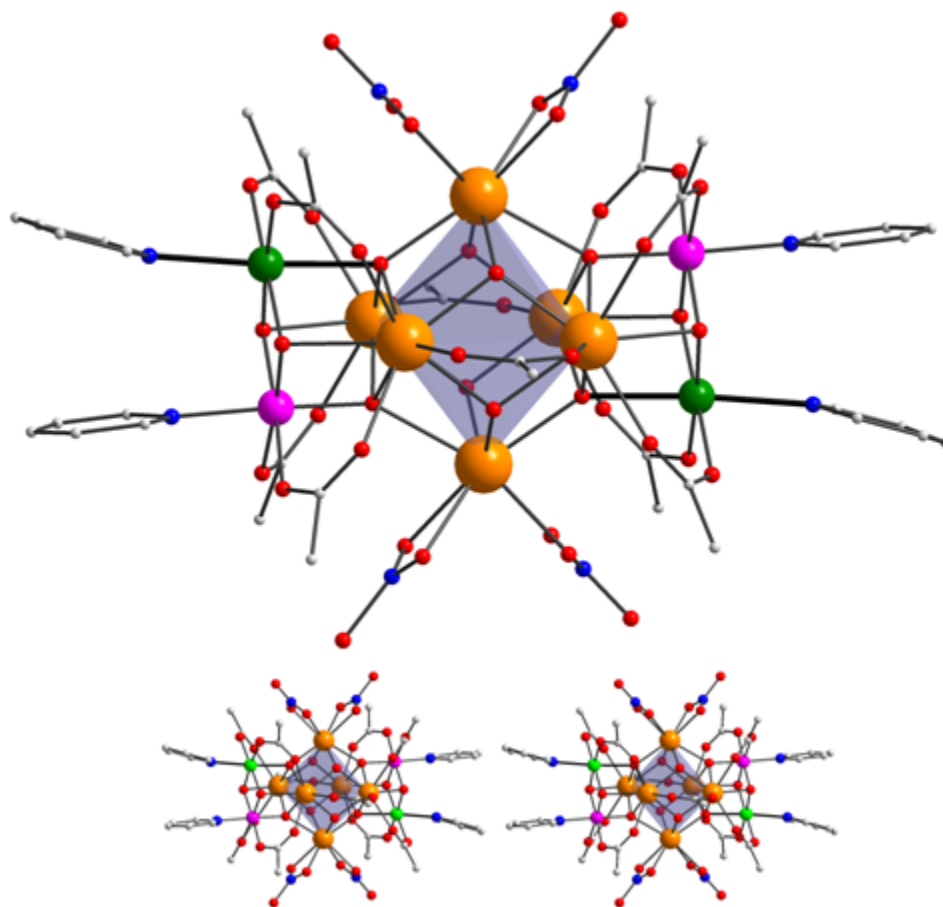


Figure 4-1. The structure and a stereopair of complex **9**. Solid black bonds denote Jahn-Teller elongation axes. Color scheme: Mn^{III} green, Mn^{IV} purple, Ce^{IV} orange, N blue, O red, C grey. H atoms have been omitted for clarity.

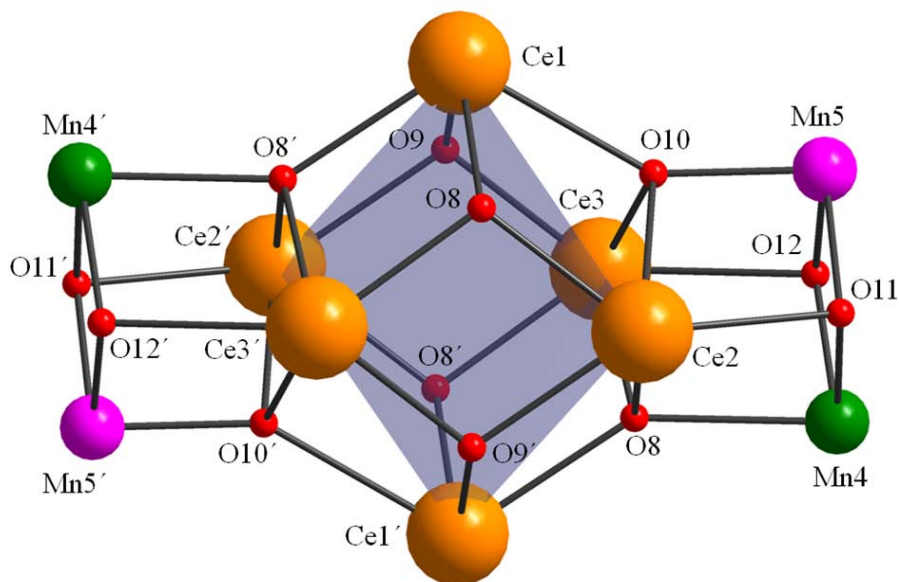


Figure 4-2. Fully labeled core of complex **9**; primed and unprimed atoms are related by the inversion center. Color scheme: Mn^{III} green, Mn^{IV} purple, Ce^{IV} orange, O red.

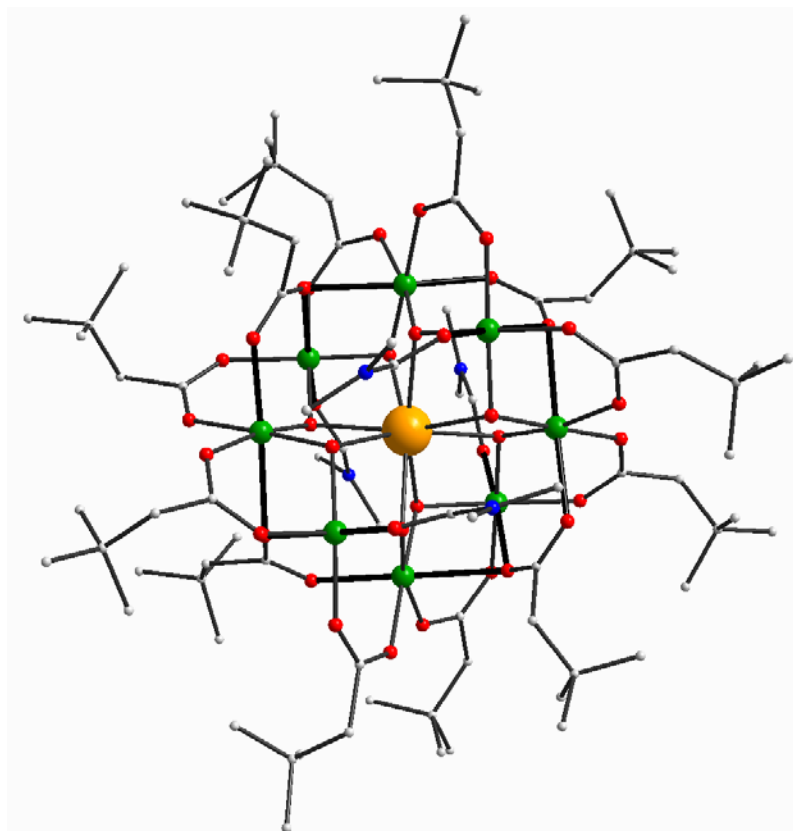


Figure 4-3. The structure of complex **10**. Solid black bonds denote Jahn-Teller elongation axes. Color scheme: Mn^{III} green, Ce^{IV} orange, N blue, O red, C grey. H atoms have been omitted for clarity.

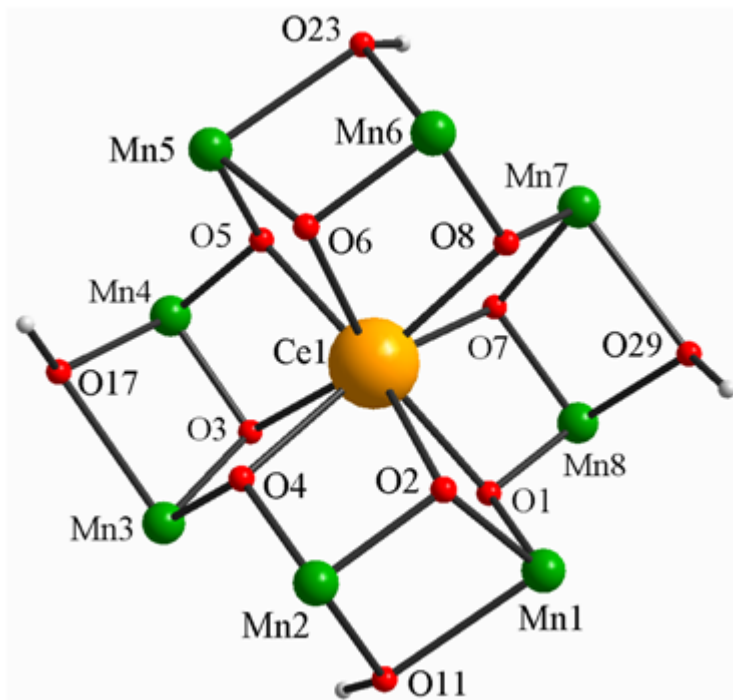


Figure 4-4. Partially labeled core of complex **10**. Color scheme: Mn^{III} green, Ce^{IV} orange, O red.

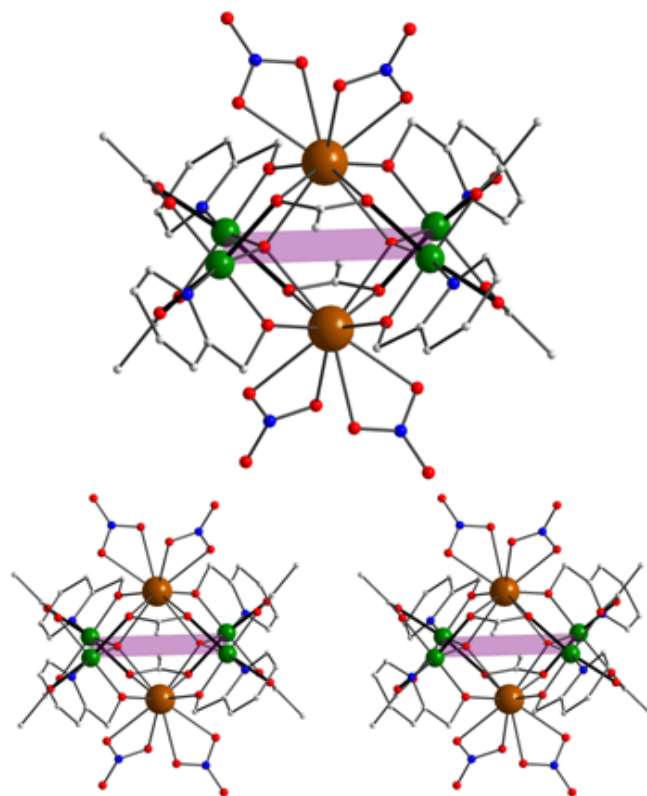


Figure 4-5. The structure and a stereopair of complex **11**. Solid black bonds denote Jahn-Teller elongation axes. Color scheme: Mn^{III} green, Ce^{III} brown, N blue, O red, C grey. H atoms have been omitted for clarity.

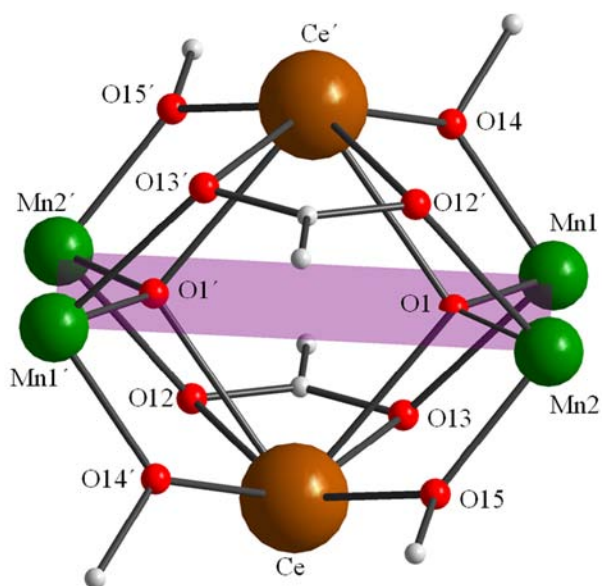


Figure 4-6. The partially labeled core of **11** emphasizing the unusual $\eta^2:\eta^2:\mu_3\text{-O}_2\text{CMe}^-$ ligand; primed and unprimed atoms are related by the inversion center. Color scheme: Mn^{III} green, Ce^{III} brown, O red, C grey. H atoms have been omitted for clarity.

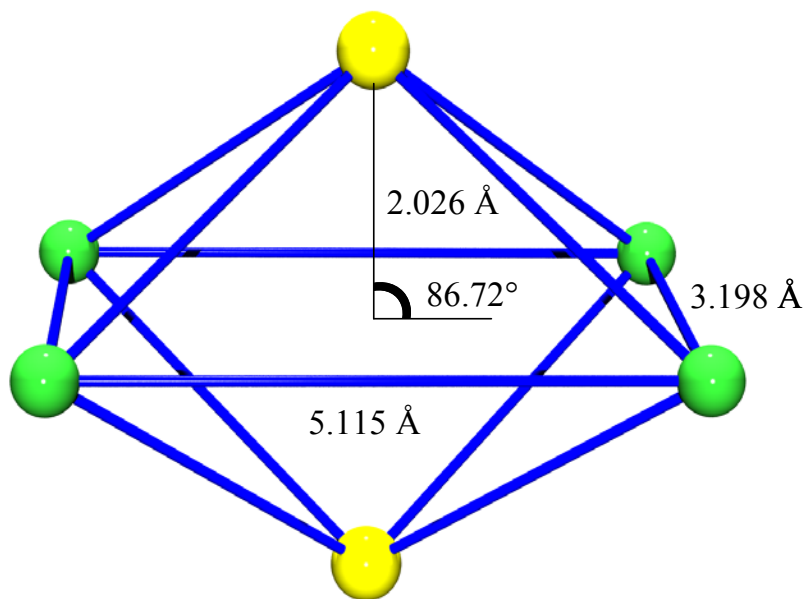


Figure 4-7. Schematic representation of the metal core of **11** and the key structural parameters within.

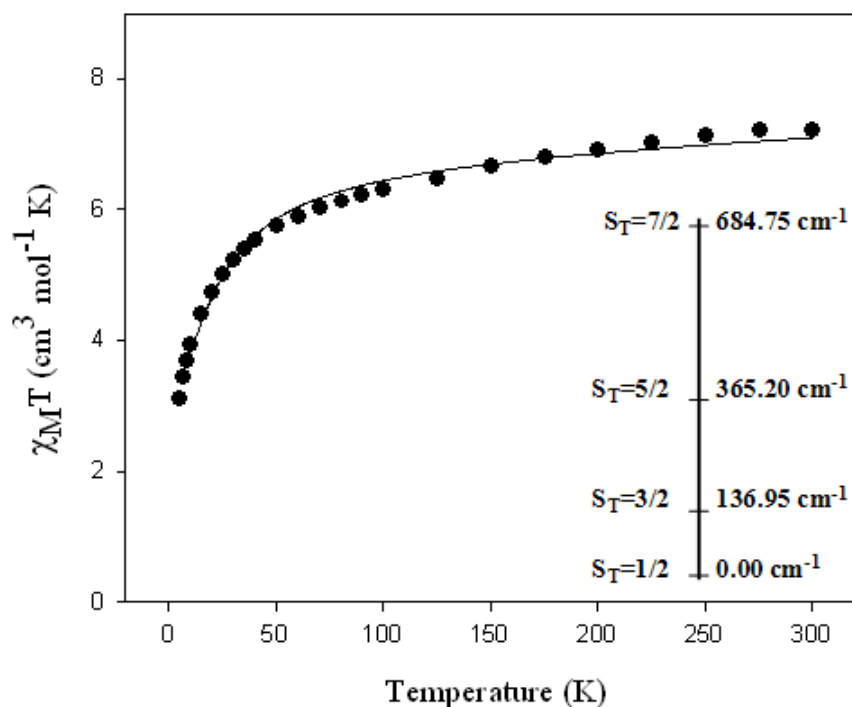


Figure 4-8. Plot of $\chi_M T$ vs temperature for complex **9**. The solid line is the fit of the data to the theoretical equation; see the text for the fit parameters. The inset illustrates the ordering of the energy states for each dimer within **9**, using the calculated exchange parameter J , and the Hamiltonian equation. All states were corrected by 34.24 cm^{-1} in order for the ground state to be at 0 cm^{-1} .

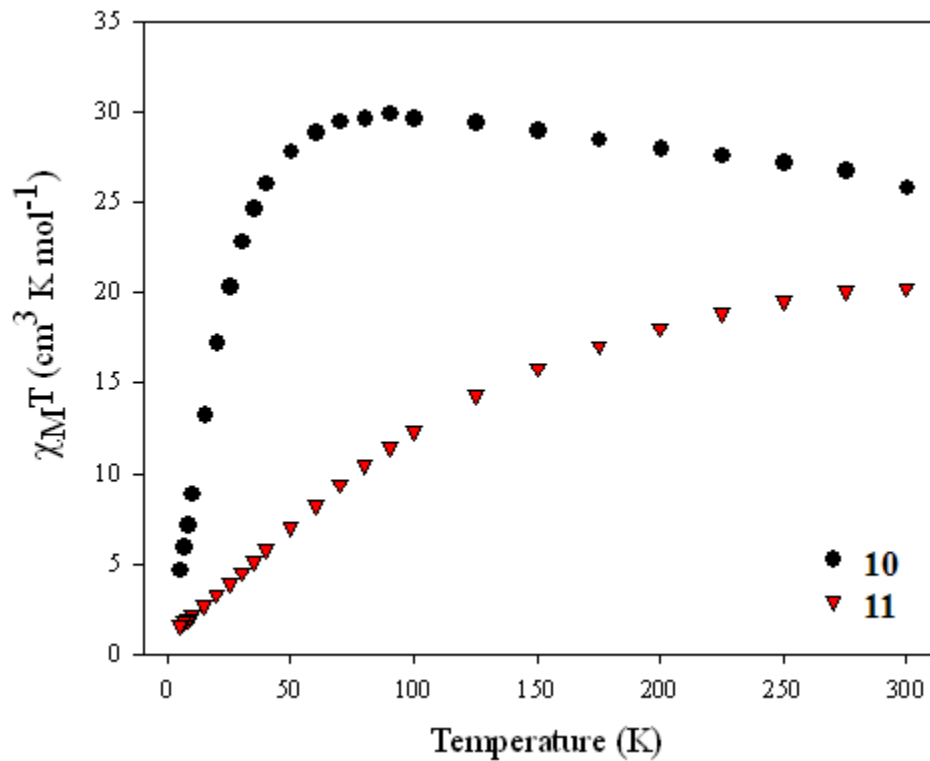


Figure 4-9. Plots of $\chi_M T$ vs temperature for complexes **10** and **11**.

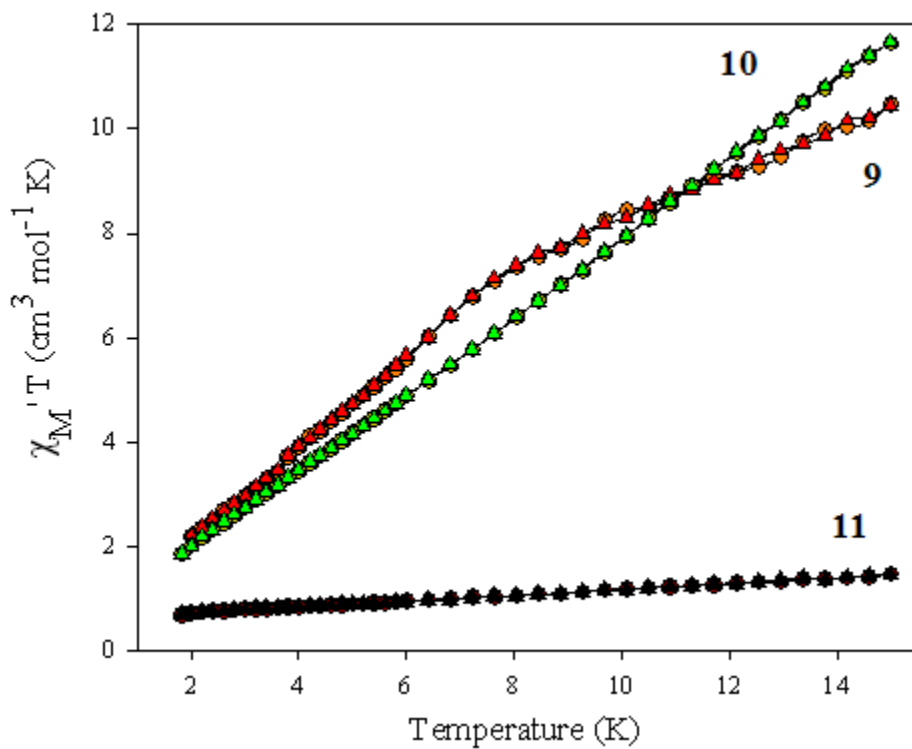


Figure 4-10. Plots of the in-phase ac susceptibility signals, at 500 Hz (\blacklozenge), and 250 Hz (\blacktriangle), for complexes **9**, **10**, and **11**.

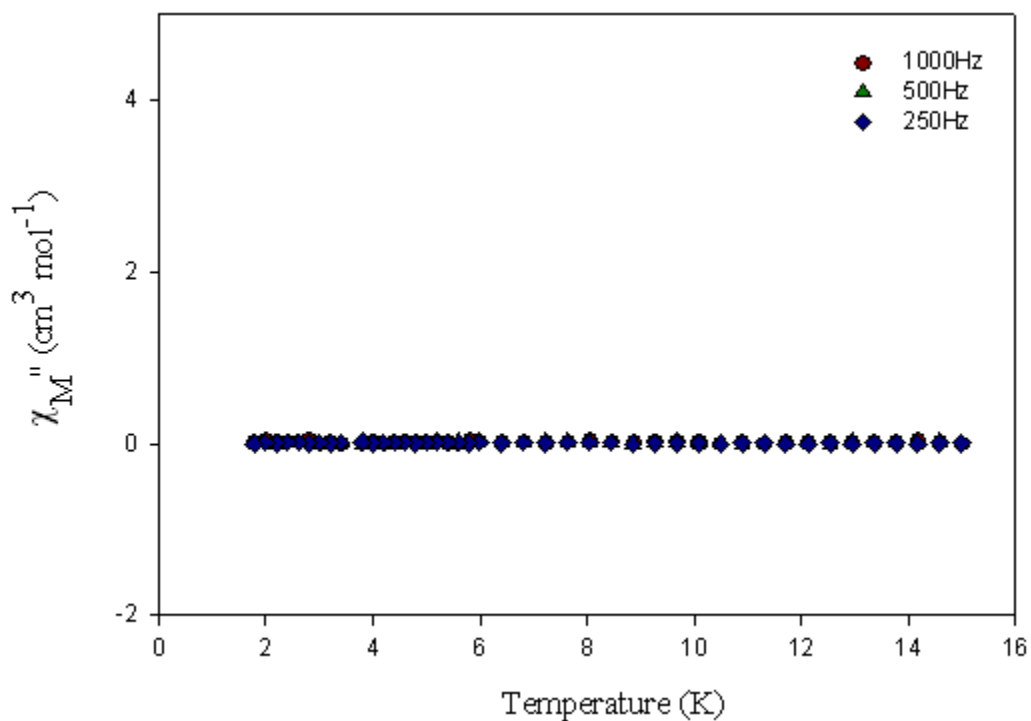


Figure 4-11. Plot of the out-of-phase (χ''_M) AC susceptibility signals of complex **9** in a 3.5 G field oscillating at the indicated frequencies.

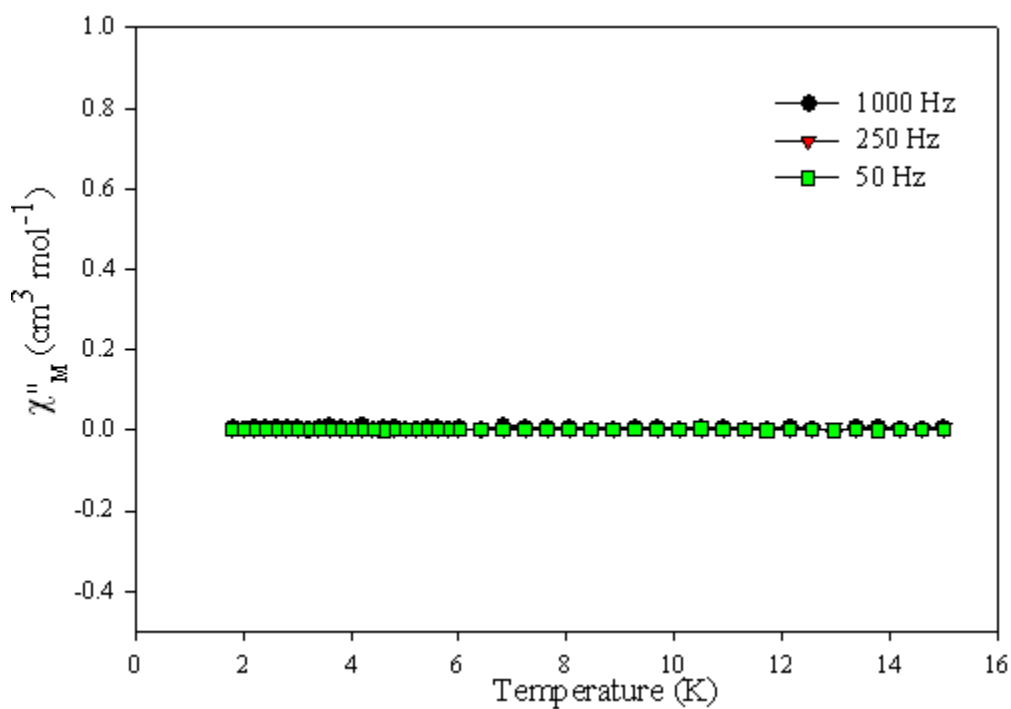


Figure 4-12. Plot of the out-of-phase (χ''_M) AC susceptibility signals of complex **10** in a 3.5 G field oscillating at the indicated frequencies.

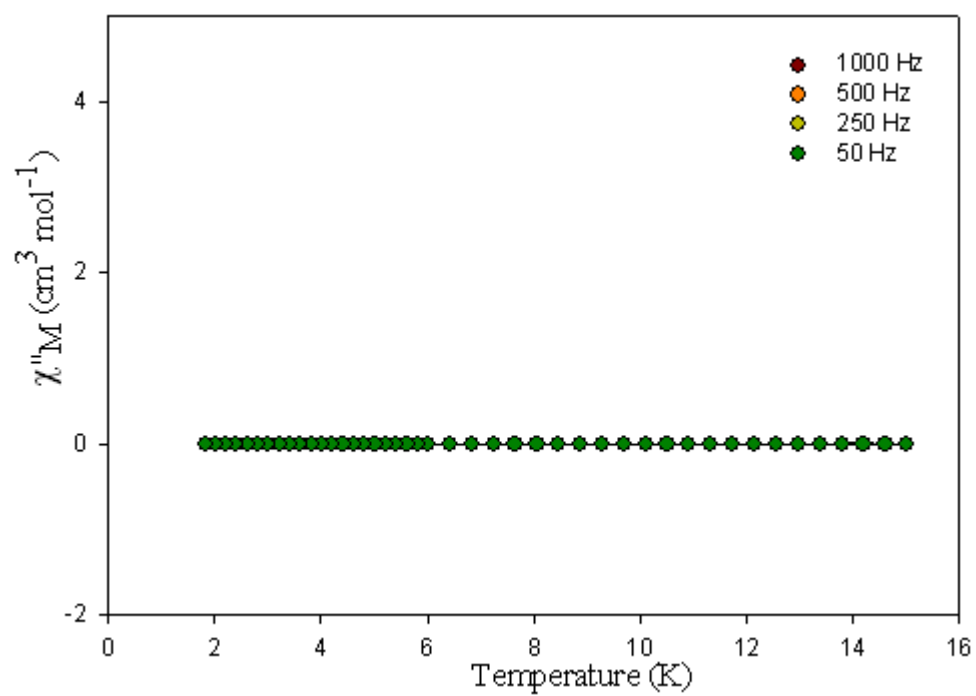


Figure 4-13. Plot of the out-of-phase (χ''_M) AC susceptibility signals of complex **11** in a 3.5 G field oscillating at the indicated frequencies.

CHAPTER 5
PROBING MAGNETIC INTERACTIONS WITH TRIANGULAR CLUSTERS: HOMO- AND
HETEROMETALLIC OXIDE-CENTERED MANGANESE TRIANGLES

5.1 Introduction

Intense attention has been directed in the recent years towards the synthesis of polynuclear 3d-metal clusters.²¹⁸ This field has particularly flourished since the realization that such molecular species will often possess very interesting magnetic properties, and that some of them are single-molecule magnets (SMMs). SMMs are molecules that function as magnets below a critical temperature, providing a new ‘bottom-up’ approach to nanoscale magnetic materials.⁴⁹ SMMs straddle between the classical world and the quantum regime, since their nanoscale dimensions places them on the knife-edge. As such, they display a combination of classical and quantum properties, and thus are excellent model systems for probing novel mesoscopic physical phenomena.²⁴ Several groups have since explored mixed 3d/4f compounds, and particularly Mn/Ln ones, as attractive routes to new SMMs, encouraged by the report of a Cu₂Tb₂ SMM by Matsumoto and co-workers.²¹⁹ The hope has been that a lanthanide’s often significant spin and/or its often large anisotropy will lead to 3d/4f SMMs with properties significantly different from those of homometallic 3d ones. Indeed, this approach has successfully led to several Mn/Ln SMMs, including Mn₁₁Ln₄,¹⁷² Mn₁₁Gd₂,²²⁰ Mn₅Ln₄,²²¹ and Mn₆Dy₆²²² examples.

Additionally, the lanthanide ions are classified as hard-acids forming the most stable complexes with hard-bases as ligands, containing high electronegative and only slightly polarizable donor atoms, such as O, N, and F. Thus, the availability of many oxide bridges within the transition metal cages favors the possible incorporation of lanthanide ions. Due to their specific electronic configurations, lanthanide atoms tend to lose three electrons, usually 5d¹ and 6s², to attain their most stable oxidation state as trivalent ions. The lanthanide trications, feature a Xe core electronic configuration with the addition of n 4f electrons, with n varying

from 0 (for La^{III}) to 14 (for Lu^{III}). This 4fⁿ sub-shell lies inside the ion, shielded by the 5s² and 5p⁶ closed sub-shells. The contracted nature of the 4f orbitals, coupled with their small overlap with the ligand atom orbitals, attaches a predominantly ionic character to lanthanide-ligand atom bonds in complexes. Thus, the mainly electrostatic interactions between the lanthanide trication and the atoms of the ligands result in irregular geometric arrangements and a variety of high coordination numbers.²²³ The latter is very important for the isolation of novel structural types of heterometallic clusters and possibly SMMs.

The Mn/Ln complexes obtained to date have not usually been amenable to detailed studies that can yield the magnitudes of the intramolecular exchange interactions, and a resulting rationalization of how these lead to the observed ground state *S* value. Reasons for this are varied, and include (i) the usually high nuclearity of these molecules, and the consequently large number of pairwise exchange interactions (J_{ij}), many of which are competing and lead to spin frustration effects; (ii) the weak nature of Mn-Ln and Ln-Ln exchange interactions, and (iii) spin-orbit coupling effects which preclude accurate magnetic susceptibility fits for polynuclear systems.²²⁴ For such reasons, we are targeting new synthetic routes that might yield small nuclearity Mn/Ln complexes that are more amenable to an analysis of the sign and nature of their exchange interactions.

Similarly, in homometallic manganese chemistry there is intense interest in the metal-metal interactions, thus smaller clusters are useful in this context. Several structural features have been encountered in metal-oxide clusters, some of which are linear units, oxide-centered [M₃O]ⁿ⁺ triangles, [M₄O₄]ⁿ⁺ cubane-type structures, [M₄O₂]ⁿ⁺ butterflies, among others. Triangles are particularly interesting due to the phenomenon of spin frustration. The concept was originally introduced in the 1970's by solid-state physicists who saw that certain 3D polymeric metal

compounds with repeating M_3 triangular units gave a degenerate ground state spin.²²⁵ The modern chemistry definition of spin frustration no longer includes a requirement for degenerate ground states: in certain M_x topologies (as in triangles), competing exchange interactions of comparable magnitude prevent (frustrate) the spin alignments that would normally be preferred.²²⁶ Spin frustration effects commonly lead to unusual values of ground states, and make the ground state sensitive to the ratio (relative magnitudes) of the competing exchange interactions (J, J' , etc).

Triangular complexes behaving as SMMs have been long sought, and only recently they were discovered.⁵³ These are the family of cationic, oxide-centered, $[Mn^{III}_3O(O_2CR)_3(mpko)_3]^+$ triangular SMMs with mixed oximato/carboxylato ligation. These, and related oximato, complexes are ferromagnetically-coupled with an $S = 6$ ground state, and they exhibit magnetization hysteresis loops. Since then, there have been a number of studies on the origin of the ferromagnetic coupling, as well as the reason for enhanced molecular anisotropy, when compared with other similar triangles.²²⁷ Thus, the synthesis of similar complexes is of particular interest since one of the few methods to understand such an unusual behavior is through a magnetostructural correlation. A comprehensive correlation study would ultimately include all the possible combinations of ligands, and/or ligand ratios. Along these lines, we have been seeking additional examples of ferromagnetically-coupled triangular Mn^{III}_3 complexes for further study, and herein report the synthesis and characterization of a new example of this type. It has been prepared by a reaction that employs 2,6-*bis*(hydroxymethyl)-*p*-cresol ($hmcH_3$), which has been used only sparingly to date in Mn cluster chemistry.¹⁶² This takes advantage of the known ability of groups with multiple alcohol arms to foster formation of metal clusters. The 2,6-*bis*(hydroxymethyl)-*p*-cresol used in the present work incorporates both aromatic and aliphatic

alcohol groups, namely, one phenol and two hydroxymethyl groups (Figure 5-1). An alternative synthetic strategy to high S values involves the use of bridging groups that are known to propagate ferromagnetic coupling, such as the pseudohalides (N_3^- , NCO^- , CN^- , NCS^- , *etc.*).^{88,162}

¹⁴¹ From the amalgamation of carboxylates and NCO^- ligands a new triangular Mn^{III}_3 complex resulted,²²⁸ which we include here merely for a more comprehensive comparison. In addition, we have recently been exploring the use of 2,6-diacetylpyridine dioxime (dapdoH_2) in 3d/4f chemistry (Figure 5-2), and this has led to a new $\text{Gd}^{\text{III}}_2\text{Mn}^{\text{IV}}$ complex with an unusual mix of metal oxidation states. This also represents the initial use of dapdoH_2 in mixed-metal cluster chemistry, having been employed to date only in homometallic $\text{Mn}^{\text{II/III}}$ ¹⁴⁸ and heterometallic $\text{Cr}^{\text{III}}\text{-Cu}^{\text{II}}$ ²²⁹ complexes.²³⁰

5.2 Experimental

5.2.1 Syntheses

All manipulations were performed under aerobic conditions using materials (reagent grade) and solvents as received.

5.2.1.1 $[\text{NEt}_3(\text{CH}_2\text{Cl})]_2[\text{Mn}_3\text{O}(\text{hmcH})_3(\text{hmcH}_2)_3]$ (**13**)

To a stirred solution of hmcH_3 (0.17g, 1.0mmol) and NEt_3 (0.42mL, 3.0mmol) in CH_2Cl_2 (20ml) was added solid $\text{Mn}(\text{O}_2\text{CCH}_3)_2 \cdot 4\text{H}_2\text{O}$ (0.25g, 1.0mmol). After being stirred for about 20 minutes, the pale suspension became dark brown. The reaction mixture was kept under magnetic stirring for another 30 minutes. The solution was then filtered and left undisturbed overnight at ambient temperature, during which time large brown crystals of **13** grew; yield ~50% based on the total manganese. The crystals of **13** were maintained in the mother liquor for X-ray crystallography and other single-crystal studies, or collected by filtration, washed with diethylether, and dried in vacuo. Anal. Calcd (Found) for **13**: C, 55.10 (55.22)%; H, 6.60 (6.65)%; N, 1.89 (1.89)%. Selected IR data (KBr, cm^{-1}): 3423(bm), 2987(sm), 2914(sm),

2864(sm), 2710(sm), 2362(sm), 2335(sw), 1650(bw), 1612(bw), 1469(vs), 1258(vs), 1157(sw), 1004(bm), 866(sw), 809(sm), 599(vs), 567(bm).

5.2.1.2 [MnGd₂O(O₂CPh)₃(O₂CMe)(dapdo)(dapdoH)₂] (**14**)

To a stirred solution of dapdoH₂ (0.19g, 1.0mmol) and NEt₃ (0.28mL, 2.0mmol) in MeCN (30ml) was added solid Mn(O₂CPh)₂ (0.17g, 0.50mmol), and Gd(NO₃)₃•6H₂O (0.23g, 0.50mmol). The reaction mixture was kept under magnetic stirring for 30 minutes during which time the color changed to dark brown. The solution was then filtered and left undisturbed overnight at ambient temperature, during which time large brown crystals of **14** grew; yield ~60% based on the total manganese. The crystals of **14** were maintained in the mother liquor for X-ray crystallography and other single-crystal studies, or collected by filtration, washed with diethylether, and dried in vacuo. Anal. Calc (Found) for dried **14** (solvent-free): C 48.74 (48.62), H 4.34 (4.39), N 10.23 (10.09). Selected IR data (KBr, cm⁻¹): 3421(bm), 3063(sm), 2362(sw), 1599(vs), 1543(bs), 1404(bs), 1179(sw), 1034(sm), 810(sw), 722(sm), 551(bm).

5.2.2 X-Ray Crystallography

Data for complexes **13** and **14** were collected by Dr. K. A. Abboud at 173 K on a Siemens SMART PLATFORM equipped with a CCD area detector and a graphite monochromator utilizing MoK_α radiation ($\lambda = 0.71073 \text{ \AA}$). Cell parameters were refined using up to 8192 reflections. A full sphere of data (1850 frames) was collected using the ω -scan method (0.3° frame width). The first 50 frames were re-measured at the end of data collection to monitor instrument and crystal stability (maximum correction on I was < 1 %). Absorption corrections by integration were applied based on measured indexed crystal faces. The structures were solved by direct methods in SHELXTL6,²³¹ and refined on F^2 using full-matrix least squares. The non-H atoms were treated anisotropically, whereas the H atoms were placed in ideal positions and

refined as riding on their C atoms. Unit cell parameters and structure solution and refinement data are listed in Table D-12.

For **13**, the asymmetric unit consists of two Mn_3 clusters, four cations and six dichloromethane molecules. One of the cations and all six dichloromethane molecules were disordered and could not be modeled properly, thus program SQUEEZE, a part of the PLATON package of crystallographic software, was used to calculate the solvent disorder area and remove its contribution to the overall intensity data. A total of 735 parameters were refined in the final cycle of refinement using 42931 reflections with $I > 2\sigma(I)$ to yield R_1 and wR_2 of 5.40% and 10.90%, respectively.

For **14**, the asymmetric unit consists of the MnGd_2 cluster and 10 MeCN molecules. The cluster has two disorders. The first is the complete disorder of ligand N1-3 with a switching of the coordination mode over a pseudo two-fold rotation. It was refined in two parts with a site occupation factor distribution of 60/40. There is also a disorder in the methyl group C56/C56'. The solvent molecules were disordered and could not be modeled properly, thus program SQUEEZE was used to calculate the solvent disorder area and remove its contribution to the overall intensity data. A total of 655 parameters were refined in the final cycle of refinement using 6822 reflections with $I > 2\sigma(I)$ to yield R_1 and wR_2 of 8.87% and 19.76%, respectively.

5.2.3 Other Studies

Microanalyses (C, H, N) were performed by the in-house facilities of the Chemistry Department at the University of Florida. IR spectra ($4000\text{--}450\text{ cm}^{-1}$) were recorded on a Nicolet Nexus 670 spectrometer with samples prepared as KBr pellets. Variable-temperature dc and ac magnetic susceptibility data were collected at the University of Florida using a Quantum Design MPMS-XL SQUID susceptometer equipped with a 7 Tesla magnet and operating in the 1.8–300

K range. Samples were embedded in solid eicosane to prevent torquing. Pascal's constants were used to estimate the diamagnetic corrections, which were subtracted from the experimental susceptibilities to give the molar paramagnetic susceptibilities (χ_M).

5.3 Results and Discussion

5.3.1 Syntheses

The synthesis of $[\text{NEt}_3(\text{CH}_2\text{Cl})]_2[\text{Mn}_3\text{O}(\text{hmcH})_3(\text{hmcH}_2)_3]$ (**13**) involves the reaction of a simple Mn^{II} salt under basic conditions in the presence of hmcH_3 . A variety of ligands have been employed over the years in the search for new magnetically interesting clusters, and poly-alkoxide groups have proved to be particularly successful. Advantages include their availability in a wide variety of forms, from simple diols⁸ and tripodal triols,²³² to mixed-functionality examples such as pyridine-based polyols.^{52,88,89,141,233,234} The 2,6-*bis*(hydroxymethyl)-*p*-cresol used in the present work incorporates both aromatic and aliphatic alcohol groups, namely, one phenol and two hydroxymethyl groups (Figure 5-1). The unusual $[\text{NEt}_3(\text{CH}_2\text{Cl})]^+$ cation can be attributed to attack by NEt_3 on CH_2Cl_2 solvent molecules.

The ligand dapdoH_2 (Figure 5-2) is a relatively new ligand in transition metal cluster chemistry, with few precedents in the inorganic literature.^{148,229,230} Therefore, dapdoH_2 was thoroughly investigated in Mn/Ln chemistry, including reactions varying the identity of the metal salts, the reagent ratios, and the solvent mixtures. From these synthetic attempts, the reaction of $\text{Mn}(\text{O}_2\text{CPh})_2 \cdot 2\text{H}_2\text{O}$, $\text{Gd}(\text{NO}_3)_3 \cdot 6\text{H}_2\text{O}$, dapdoH_2 , and NEt_3 in a 1:1:2:4 molar ratio in MeCN gave a dark brown solution from which were subsequently isolated brown crystals of $[\text{MnGd}_2\text{O}(\text{O}_2\text{CPh})_3(\text{O}_2\text{CMe})(\text{dapdo})(\text{dapdoH}_2)_2]$ (**14**) in 60% yield as **14**·10MeCN. The acetate anion very likely comes from Mn^{III} or Mn^{IV} catalyzed aerial oxidation of MeCN. Dried solid analyzed satisfactorily (C, H, N) as solvent-free, ruling out the possibility that the acetate is in reality a NO_3^- group; the same reaction in a different solvent does not give complex **14**.

5.3.2 Description of Structures

The structure of complex **13**, a stereopair, and the fully labeled core are presented in Figure 5-3. Selected interatomic distances are listed in Table D-13. Complex **13** crystallizes in the monoclinic space group Cc , and consists of two crystallographically independent Mn_3 anions in the unit cell, which are structurally very similar, and thus only the one containing atoms Mn1-Mn3 will be discussed in detail. The structure of the anion of **13** consists of a near-equilateral Mn^{III}_3 triangle capped by μ_3-O^{2-} ion O19 (BVS calculation gave an effective charge of 1.93 for O19). Each edge is bridged by the deprotonated alkoxide arm (O2, O11, or O17) of an $\eta^1:\eta^2:\mu$ -hmcH²⁻ group, whose phenoxide O atom (O1, O10, or O16) is bound terminally and whose other alcohol arm stays protonated and unbound. Octahedral coordination at each manganese is completed by a chelating $\eta^1:\eta^1$ -hmcH₂⁻ group, which is bound through its deprotonated phenoxide O atom (O4, O7, or O13) and one of its protonated alcohol arms (O5, O8, or O14), with the other protonated arm again remaining unbound. The central oxide ion, atom O19, lies 0.765 Å above the Mn_3 plane. The Mn··Mn separations are within a small range [3.006(4)-3.035(4) Å], almost equivalent within the usual 3σ convention, but the Mn_3 triangle is, nevertheless, best described as isosceles on the basis of the distinctly different central Mn-O²⁻ bonds [Mn1-O19 = 2.001(12) Å; Mn2-O19 = 1.860(11) Å; Mn3-O19 = 1.859(12) Å] and Mn-O19-Mn angles. The Mn^{III} oxidation states were established by charge-balance considerations and inspection of the Mn-O bond distances and confirmed quantitatively by bond valence sum (BVS) calculations (Table E-5). The Mn^{III} atoms are near-octahedral, exhibiting Jahn-Teller (JT) axial elongations, as expected for high-spin d^4 ions in this geometry; the JT axes are O2-Mn1-O5, O14-Mn2-O17, and O8-Mn3-O11.

The structure of complex **14**, a stereopair, and the labeled core are presented in Figure 5-4. Selected interatomic distances are listed in Table D-14. Complex **14** crystallizes in the

monoclinic space group $I2/a$, and consists of an isosceles $\text{Mn}^{\text{IV}}\text{Gd}^{\text{III}}_2$ triangle with a central μ_3 - O^{2-} ion O1; the deprotonated nature was confirmed by a BVS calculation which gave 1.97. Atom O1 lies slightly (0.034 Å) above the MnGd_2 plane. Each dapdoH^- group is a tridentate chelate on a Gd, and forms a diatomic (Gd-N-O-Mn) bridge to Mn1 with its deprotonated NO^- arm. The dapdo^{2-} group is a tridentate chelate on Mn1, and bridges asymmetrically to the Gd atoms: one NO^- arm forms a diatomic (Mn-N-O-Gd) bridge to one Gd whereas the other forms a monoatomic (Mn-O-Gd) bridge to the other Gd. This asymmetric bridging mode is statically disordered in the crystal. The Gd \cdots Gd edge is bridged by a benzoate and an acetate group. Ligation is completed by a chelating (η^2) benzoate group on each Gd. The Mn^{IV} oxidation state was established by bond valence sum (BVS) calculations (Table E-5), charge considerations, and inspection of the metric parameters. Mn1 is six-coordinate with distorted octahedral geometry, whereas each Gd^{3+} ion is nine-coordinate with a distorted capped square antiprismatic geometry. Compound **14** is the first Mn-Ln complex with a triangular topology, and the first 3d/4f cluster with a dioximate ligand.

5.3.3 Magnetochemistry

5.3.3.1 DC magnetic susceptibility of complex 13

Solid-state, direct-current (dc) magnetic susceptibility (χ_M) data for dried complex **13** were collected in the temperature range 5.0-300 K in an applied field of 0.1 T. $\chi_M T$ steadily increases from 9.95 $\text{cm}^3 \text{K mol}^{-1}$ at 300 K to a maximum of 18.85 $\text{cm}^3 \text{K mol}^{-1}$ at 8.0 K before dropping slightly to 18.69 $\text{cm}^3 \text{K mol}^{-1}$ at 5.0 K (Figure 5-5). This behavior is indicative of ferromagnetic exchange between the metal centers and a resulting $S = 6$ ground state, with the low temperature decrease assigned to zfs, Zeeman effects, and/or weak intermolecular antiferromagnetic

interactions. The spin-only ($g = 2$) $\chi_{\text{M}}T$ for an $S = 6$ state is $21 \text{ cm}^3 \text{ K mol}^{-1}$, close to the experimental value at 8.0 K.

In order to determine the Mn_2 pairwise exchange interactions within the molecule, the $\chi_{\text{m}}T$ vs T data for complex **13** were fit to the theoretical $\chi_{\text{m}}T$ vs T expression. It has been noticed previously that the $\chi_{\text{m}}T$ vs T data of $[\text{Mn}_3\text{O}(\text{O}_2\text{CR})_6(\text{L})_3]^{+,0}$ ($\text{R} = \text{various}$, $\text{L} = \text{pyridine, imidazole}$) and related metal complexes of triangular geometry cannot be satisfactorily fit to a $1J$ -model (*i.e.*, an equilateral triangle model).²³⁵ Equilateral triangles undergo Jahn-Teller distortions, resulting in an isosceles ($2J$) magnetic situation. Thus, the data for complex **13** were fit to the theoretical $\chi_{\text{m}}T$ vs T expression for a Mn_3^{III} isosceles triangle derived using the Van Vleck equation. The isotropic (Heisenberg) spin Hamiltonian describing an exchange-coupled Mn^{III}_3 ($S_1 = S_2 = S_3 = 2$) isosceles triangle is given by eq. 5-1, using the numbering scheme shown in the inset of Figure 5-5, where $J = J(\text{Mn1}\cdots\text{Mn2}) = J(\text{Mn2}\cdots\text{Mn3})$ and $J' = J(\text{Mn1}\cdots\text{Mn3})$:

$$\mathcal{H} = -2J(\hat{S}_1 \cdot \hat{S}_2 + \hat{S}_2 \cdot \hat{S}_3) - 2J'(\hat{S}_1 \cdot \hat{S}_3) \quad (5-1)$$

This equation can be expressed in an equivalent form (eq. 5-2) by using Kambe's vector coupling method²¹⁷ and the coupling scheme: $\hat{S}_A = \hat{S}_1 + \hat{S}_3$, and $\hat{S}_T = \hat{S}_A + \hat{S}_2$, where S_T is the spin of the complete Mn_3 molecule.

$$\mathcal{H} = -J(\hat{S}_T^2 - \hat{S}_A^2 - \hat{S}_2^2) - J'(\hat{S}_A^2 - \hat{S}_1^2 - \hat{S}_3^2) \quad (5-2)$$

The eigenvalues of this Hamiltonian are then given by eq. 5-3, where constant terms contributing to all states have been omitted

$$E(S_T, S_A) = -J[S_T(S_T+1) - S_A(S_A+1)] - J'[S_A(S_A+1)] \quad (5-3)$$

A theoretical $\chi_{\text{m}}T$ vs T expression was derived using the S_T values, their energies $E(S_T, S_A)$, and the Van Vleck equation (Appendix B), and this expression was used to fit the experimental data. A temperature-independent paramagnetism (TIP) term was fixed at $600 \times 10^{-6} \text{ cm}^3 \text{ mol}^{-1}$,

and the fit for **13** (solid line in Figure 5-5) gave fit parameter values of $J_1 = +8.7(1) \text{ cm}^{-1}$ $J' = +1.2(2) \text{ cm}^{-1}$, and $g = 1.90(1)$. These give an $S = 6$ ground state and an $S = 5$ first excited state at 44.4 cm^{-1} higher in energy.

5.3.3.2 Reduced magnetization study of complex 13

In order to confirm the ground state of **13**, as well as to obtain an estimate of the axial zfs parameter, D , magnetization data were collected in the 1-70 kOe and 1.8-10.0 K ranges, and these are plotted as reduced magnetization ($M/N\mu_B$) vs H/T in Figure 5-6. The data were fit by matrix diagonalization to a model that assumes that only the ground state is populated, includes axial zfs ($D\hat{S}_z^2$) and the Zeeman interaction, and carries out a full powder average (eq 5-4).

$$\mathcal{H} = D\hat{S}_z^2 + g\mu_B\hat{S}\cdot H \quad (5-4)$$

The best fit (solid lines in Figure 5-6) gave $S = 6$, $D = -0.11(3) \text{ cm}^{-1}$, and $g = 1.86(5)$; the lower-than-expected latter value is no doubt due to the assumption of axial symmetry, the inherent uncertainties in obtaining g from fits of bulk magnetization data, and other experimental errors.

5.3.3.3 AC magnetic susceptibility of complex 13

Alternating-current (ac) magnetic susceptibility studies were also performed on a dried sample of **13** in the temperature range 1.8-15 K, using a 3.5 Oe ac field oscillating at frequencies in the 50-1000 Hz range. The resulting data are plotted as $\chi_M' T$ vs T in Figure 5-7, where χ_M' is the in-phase component of the ac susceptibility. $\chi_M' T$ is essentially constant with decreasing temperature below 15 K at a value of $\sim 20 \text{ cm}^3 \text{ K mol}^{-1}$, indicating an $S = 6$ ground state (with $g \approx 1.95$) that is well isolated from the nearest excited state. This is in agreement with the conclusions from the dc fits. The ac data thus further confirm an $S = 6$ ground state for the

complex. No out-of-phase, χ_M'' , ac signals were observed for **13**, indicating the absence of slow magnetization relaxation.

5.3.3.4 Magnetostructural correlation between **13** and other oxo-centered Mn^{III}_3 triangles

It is of interest to compare **13** and $(n\text{-Bu}_4\text{N})_2[\text{Mn}_3\text{O}(\text{NCO})_6(\text{O}_2\text{CPh})_3]\cdot\text{CH}_2\text{Cl}_2$ (**15** $\cdot\text{CH}_2\text{Cl}_2$) with other complexes with a $[\text{Mn}^{\text{III}}_3(\mu_3\text{-O})]^{7+}$ triangular core. The latter is not uncommon in Mn^{III} chemistry:^{155,236-240} there are antiferromagnetically coupled complexes of the general formula $[\text{Mn}_3\text{O}(\text{O}_2\text{CR})_6\text{L}_3]^+$ (L = monodentate ligand) and recently the $[\text{Mn}^{\text{III}}_3\text{O}(\text{O}_2\text{CR})_3(\text{mpko})_3]^+$ family of carboxylato/oximato complexes that are ferromagnetically coupled, like **13**, and are SMMs.^{53,55} The central $\mu_3\text{-O}^{2-}$ ion in the former lies in the Mn^{III}_3 plane and contains essentially planar Mn-O-C-O-Mn units, whereas the $\mu_3\text{-O}^{2-}$ ion in the latter is displaced out of the plane and the edges are bridged by a combination of carboxylate and oximato ligands; the latter cause a significant Mn-N-O-Mn torsion angle (“twist”). Complexes **13** and **15** are distinctively different from both of these two classes of compounds. In **13** (i) the central $\mu_3\text{-O}^{2-}$ ion lies far above the Mn_3 plane (0.765 Å in **13** vs ~ 0.3 Å in the $[\text{Mn}^{\text{III}}_3\text{O}(\text{O}_2\text{CR})_3(\text{mpko})_3]^+$ complexes), (ii) the complex is carboxylate-free, and (iii) there is no “twist” in **13** because there are only monatomic bridges on each Mn_3 edge. There is one other carboxylate-free triangular Mn^{III}_3 complex with monatomic bridges on the edges, $[\text{Mn}_3\text{O}(\text{5-Br-sap})_3(\text{H}_2\text{O})_3]\text{Cl}$, in which the central O^{2-} ion lies ~ 0.8 Å above the Mn_3 plane, giving the same type of $[\text{Mn}^{\text{III}}_3(\mu_3\text{-O})(\mu\text{-OR})_3]^{4+}$ core as that in **13**.²⁴⁰ However, small structural differences between **13** and $[\text{Mn}_3\text{O}(\text{5-Br-sap})_3(\text{H}_2\text{O})_3]\text{Cl}$, such as larger Mn- μ -OR-Mn angles, are obviously enough to make this compound antiferromagnetically coupled, in contrast to **13**. Although **13** has an $S=6$ ground state, its low $D=-0.11$ cm^{-1} value gives an upper limit to the relaxation barrier of only 3.96 cm^{-1} , with the true barrier being even smaller because of Quantum Tunneling of the Magnetization (QTM), and this is consistent with

the absence of an ac out-of-phase signal (down to 1.8 K at least). The small D is consistent with the propeller-like arrangement of the Mn^{III} JT axes and their relatively small angle with the C_3 symmetry axis ($\theta_{av} \sim 50^\circ$). This is distinctly different from the $[\text{Mn}^{\text{III}}_3\text{O}(\text{O}_2\text{CR})_3(\text{mpko})_3]^+$ complexes, which also have $S=6$ but a larger $D \sim -0.35 \text{ cm}^{-1}$, $\theta_{av} \sim 60^\circ$, and the very recent $[\text{Mn}_3\text{O}(\text{Me-salox})_3(2,4'\text{-bpy})_3(\text{ClO}_4)]$ (Me-H₂salox = 2-hydroxyphenylethanone oxime)²⁴¹ ($D \sim -1.3 \text{ cm}^{-1}$), and which are thus SMMs.

Complex **15** is also different from all other Mn^{III} triangles, since its edges are bridged each by a combination of one monoatomic NCO⁻ ligand and one carboxylate (in this case benzoate). In **15** the central O²⁻ ion lies 0.664 Å above the Mn₃ plane, which is intermediate between the small O²⁻ displacement of ~ 0.3 Å in the $[\text{Mn}^{\text{III}}_3\text{O}(\text{O}_2\text{CR})_3(\text{mpko})_3]^+$ complexes, and the displacement in complex **13**, which is 0.765 Å, or the antiferromagnetically-coupled $[\text{Mn}_3\text{O}(5\text{-Br-sap})_3(\text{H}_2\text{O})_3]\text{Cl}$ complex where the same distance is ~ 0.8 Å. Being in an intermediate situation, **15** appears to have significant anisotropy, and is probably an SMM (see Appendix C). This is likely due to a major contribution from the disposition of the JT axes, gauged by the θ_{av} angle ($\theta_{av} \sim 61^\circ$ in **15**), and a minor contribution from the small but present “twist” in **15**, at the site of the triatomic bridging carboxylate (Mn-O-C-O-Mn torsion angles 3.83, 10.31, 6.81°), which is not possible in **13**, since the latter is bridged only by monoatomic bridges, and thus **13** is not a SMM.

Table 5-1. Magnetostructural correlation between complexes **13** and **15**.

| Parameter | 13 | 15 |
|--|---------------------|---------------------|
| Mn ^{III} ...Mn (Å) | 3.031, 3.031, 3.007 | 3.039, 3.039, 3.041 |
| Mn ^{III} – μ ₃ O ²⁻ (Å) | 1.86, 1.86, 2.01 | 1.85, 1.87, 1.89 |
| Mn ^{III} ₃ ...μ ₃ O ²⁻ (Å) | 0.77 | 0.66 |
| θ_{ave} (°) | 50.0 | 61.2 |
| D (cm ⁻¹) | -0.11(3) | -0.27(3) |
| J | +8.7(1) | +1.2(1) |
| J' | +1.3(1) | +8.3(1) |
| S | 6 | 6 |

Complex **13** thus demonstrates for the first time that it is not necessary to have oximate bridging groups on the edges of a Mn^{III}_3 triangular compound in order to have ferromagnetic coupling, while **15** demonstrates that oximes are not essential to the anisotropy either. However, it is now understood that significant “twist” can come from bridging ligands that are more than diatomic (diatomic oximates, or triatomic carboxylates). While oximate “twists”, when present, no doubt serve to increase the exact magnitude of the observed ferromagnetic exchange parameters, their presence appears not to be essential to obtain ferromagnetic Mn^{III}_3 complexes; i.e., the presence of significant Mn-N-O-Mn torsion angles (“twists”) is not a *sine qua non* for seeing ferromagnetic coupling in such species. The same holds for carboxylate bridges, which we can now prove they are not essential for ferromagnetic coupling either. Instead, as we have argued elsewhere,⁵³ a major contributor to the ferromagnetic coupling in $[\text{Mn}^{\text{III}}_3\text{O}(\text{O}_2\text{CR})_3(\text{mpko})_3]^+$, **13**, and **15** is very likely the displacement of the $\mu_3\text{-O}^{2-}$ ion from the Mn_3 plane, which will weaken the Mn-O²⁻-Mn $d_\pi\text{-}p_\pi\text{-}d_\pi$ antiferromagnetic pathways/contributions to the net exchange coupling parameters, leading to net ferromagnetic coupling. This is due, of course, to the fact that an observed J value (J_{obs}) is the net sum of antiferro- and ferromagnetic contributions, J_{AF} and J_{F} , respectively (eq 5-5).

$$J_{\text{obs}} = J_{\text{AF}} + J_{\text{F}} \quad (5-5)$$

In our opinion, the ferromagnetic coupling in triangular $[\text{Mn}_3\text{O}(\text{bamen})_3]^+$ [$\text{bamenH}_2 = 1,2\text{-bis}(\text{biacetylmonoximeimino})\text{ethane}$] does not argue against this conclusion: this complex is bridged by oximate groups along the edges of the Mn^{III}_3 triangle, and its $\mu_3\text{-O}^{2-}$ ion is *in* the Mn_3 plane, which might at first glance suggest that the oxime twists are the sole cause of the ferromagnetic coupling. However, this complex contains seven-coordinate Mn^{III} : thus, (i) the symmetries and energies of the magnetic orbitals will differ from those in the other Mn^{III}_3

complexes (which contain near octahedral Mn^{III}), and (ii) the Mn^{III}-O²⁻ bonds are slightly longer on average, as expected for an increased coordination number. Thus, the d_{π} - p_{π} - d_{π} overlaps will again be weakened, and antiferromagnetic contributions to the net coupling will be decreased. The [Mn₃O(bamen)₃]⁺ complex, therefore, is to be taken, in our opinion, as merely indicating that anything that affects the antiferromagnetic interactions through the μ_3 -O²⁻ ion will contribute to switching of the coupling to ferromagnetic, whether in addition to oximate “twists” or without them, and that these possibilities include displacement of the μ_3 -O²⁻ ion from the Mn₃ plane, Mn-O²⁻ bond lengthening, increased Mn/O d_{π} - p_{π} orbital energy mismatch, or combinations thereof. All of these will weaken antiferromagnetic contributions to the net exchange coupling via the Mn-O²⁻-Mn pathways.

The presence of small but significant twist however, seems to be essential for observing SMM behavior, and complex **15** represents the first such example. Twists in the other Mn₃ SMMs come from a combination of oximate and carboxylate bridges.^{53,55,238,240} Note that carboxylates are not always enough to make a Mn^{III} triangle behave as a single-molecule magnet, and this is demonstrated in the carboxylate-bridged antiferromagnetically-coupled and thus frustrated triangles with the general formula [Mn₃O(O₂CR)₆L₃]⁺ (L = monodentate ligand), which possess a small ground state spin, and are not SMMs.¹⁵⁵ However, it should be noted here that the major contribution in molecular anisotropy is expected to originate in the large θ_{av} angle (the disposition of the JT axes).

5.3.3.2 DC Magnetic susceptibility of complex 14

Solid-state direct current magnetic susceptibility (χ_M) data on dried **14** were collected in a 1 kG (0.1 T) field in the 5.0–300 K range and are plotted as $\chi_M T$ vs T in Figure 5-8. $\chi_M T$ has a value of 17.60 cm³Kmol⁻¹ at 300 K, and it remains essentially constant down to 50 K and then rapidly increases to 23.62 cm³Kmol⁻¹ at 5 K. The $\chi_M T$ value at 300 K is essentially the same as

the spin-only ($g = 2$) value of $17.64 \text{ cm}^3 \text{Kmol}^{-1}$ for one Mn^{IV} ($S = 3/2$) and two Gd^{III} ($S = 7/2, L = 0$) noninteracting ions. The essentially constant value down to 50 K is consistent with very weak exchange interactions in the molecule, as expected when Ln ions are involved. To determine the individual pairwise exchange parameters J and J' between the Gd–Mn and Gd–Gd pairs, respectively, the χ_{MT} vs T data were fit to the appropriate theoretical expression for an isosceles $\text{Gd}^{\text{III}}_2\text{Mn}^{\text{IV}}$ triangle of C_{2v} symmetry; i.e., we assumed that the GdMn interactions would be very weak and essentially identical despite the slightly different bridges described above. The isotropic spin Hamiltonian describing the exchange interactions within **14** is given by eq 5-6, where \hat{S}_i is the spin operator for metal atom M_i ($i = 1$ for Mn and 2 and 3 for Gd). The eigenvalues of this spin Hamiltonian can be determined analytically with the Kambe vector coupling method.²¹⁷ Thus, using the substitutions $\hat{S}_A = \hat{S}_2 + \hat{S}_3$ and $\hat{S}_T = \hat{S}_A + \hat{S}_1$, where S_T is the total spin of the molecule, allows the spin Hamiltonian to be transformed into the equivalent form given by eq 5-7. The eigenvalues of eq 5-7 are given by eq 5-8, where $E(S_T, S_A)$ is the energy of state S_T arising from S_A , and constant terms contributing to all states have been omitted. For complex **14**, the overall multiplicity of the spin system is 256, made up of 28 spin states ranging from $S_T = 1/2$ to $17/2$. Derivation of the appropriate Van Vleck equation (Appendix B) and its use to fit the χ_{MT} vs T data (shown as the solid line in Figure 5-8) gave $J = +0.49(2) \text{ cm}^{-1}$, $J' = -0.12(3) \text{ cm}^{-1}$, and $g = 1.98(1)$. A temperature-independent paramagnetism term was included and held constant at $900 \times 10^{-6} \text{ cm}^3 \text{ mol}^{-1}$. The exchange interactions are thus both very weak, and of different sign, and predict the complex to have an intermediate $S_T = 13/2$ ground state, the $|S_T, S_A\rangle = |13/2, 5\rangle$ state, with low-lying $S_T = 11/2$ and $15/2$ excited states at 5.32 and 5.62 cm^{-1} , respectively, above the ground state.

$$\mathcal{H} = -2J(\hat{S}_1 \cdot \hat{S}_2 + \hat{S}_1 \cdot \hat{S}_3) - 2J'\hat{S}_2 \cdot \hat{S}_3 \quad (5-6)$$

$$\mathcal{H} = -J(\hat{S}_T^2 - \hat{S}_A^2 - \hat{S}_1^2) - 2J'(\hat{S}_A^2 - \hat{S}_2^2 - \hat{S}_3^2) \quad (5-7)$$

$$E(S_T, S_A) = -J[S_T(S_T + 1) - S_A(S_A + 1)] - J'[S_A(S_A + 1)] \quad (5-8)$$

5.3.3.3 AC Magnetic susceptibility of complex 14

In order to confirm the ground state of **14**, alternating current (ac) magnetic susceptibility studies were performed in the 1.8-10 K temperature range using a 3.5 G ac field oscillating at 250–1000 Hz. The in-phase χ'_{MT} signal (Figure 5-9) rapidly increases with decreasing temperature, indicating depopulation of excited states with S values smaller than the ground state, and reaches a maximum at $25.2 \text{ cm}^3\text{Kmol}^{-1}$ before then decreasing slightly, to $24.7 \text{ cm}^3\text{Kmol}^{-1}$ at 1.8 K. The lowest temperature data thus confirm an $S = 13/2$ state with $g \sim 2$; χ'_{MT} values for $S = 11/2, 13/2,$ and $15/2$ with $g = 2.0$ are $17.9, 24.4,$ and $31.9 \text{ cm}^3\text{Kmol}^{-1}$, respectively. There were no out-of-phase ac signals down to 1.8 K, and **14** is thus not an SMM.

5.3.3.4 Theoretical analysis of the spin frustration in complex 14

A ferromagnetic $J = +0.49(2) \text{ cm}^{-1}$ and an antiferromagnetic $J' = -0.12(3) \text{ cm}^{-1}$ for the Gd–Mn and Gd–Gd interactions, respectively, indicate the presence of competing interactions and spin-frustration effects. This is consistent with the observed $S = 13/2$ ground state, which does not correspond to a simple “spin up/spin down” picture of spin alignments (some examples shown in Figure 5-10). Instead, this value indicates some intermediate (frustrated) alignments resulting from the competing interactions, as is also indicated by the $S_A = 5$ value of the $|S_T, S_A\rangle = |13/2, 5\rangle$ ground state. In such situations, the ground state is usually extremely sensitive to the relative magnitudes of the competing exchange interactions. Because there has been no theoretical analysis to date of the spin-state energies as a ratio of the J values in an isosceles triangle comprising one $S = 3/2$ and two $S = 7/2$ spins, we have carried one out in order to rationalize the observed ground state of **14**.

In Figure 5-11 are plotted the energies (in units of J'), of the 28 spin states of complex **14** as a function of the J/J' ratio, for J ferromagnetic and J' antiferromagnetic values ($J/J' < 0$), and both J and J' antiferromagnetic ($J/J' > 0$). In this discussion, the left half of Figure 5-11 ($J/J' < 0$) will be considered first, followed by the right half. Several important conclusions can be drawn: (i) as expected for a spin-frustrated system, the ground state is indeed very sensitive to the J/J' ratio, with nine different ground states spanning $S_T = 1/2-17/2$ being possible for this combination of signs for J and J' ; (ii) when $J \gg J'$ and as a result $|J/J'| > \sim 4.65$, the ground state is described by $S_T = 17/2$ and $S_A = 7$, i.e., the $|17/2, 7\rangle$ state, arising from J totally overwhelming J' and aligning the two Gd spins parallel to the Mn spin and thus to each other. This is depicted in Figure 5-10a, and corresponds to the antiferromagnetic J' interaction being totally frustrated. As $|J'|$ increases relative to $|J|$, the Gd spins are no longer perfectly parallel but at some intermediate alignment, are determined by the relative magnitudes of J and J' , i.e., the $|J/J'|$ ratio. Thus, as this ratio gets progressively smaller, the Gd spins align less and less parallel and then more and more antiparallel. When $-4.65 < |J/J'| < -4.2$, the ground state is $|15/2, 6\rangle$, and when $\sim -4.2 < |J/J'| < \sim -3.2$, the ground state is the $|13/2, 5\rangle$ found experimentally for **14** (Figure 5-10b). Finally, when $J \ll J'$ and $\sim -0.65 < |J/J'| < 0$, the J interaction is completely frustrated, the Gd spins are perfectly antiparallel, and the ground state is thus $|3/2, 0\rangle$ (Figure 5-10c).

The fit shown in Figure 5-8 gave $J = +0.49(2) \text{ cm}^{-1}$, $J' = -0.12(3) \text{ cm}^{-1}$, and thus $|J/J'| = 4.08$, which is within the range for a $|13/2, 5\rangle$ ground state. Note that if J and J' were (i) both ferromagnetic, (ii) antiferro- and ferromagnetic, respectively, or (iii) both antiferromagnetic, they could not yield an $S = 13/2$ ground state: the first two cases would give $S = 17/2$ and $11/2$ ground states, respectively, for all J/J' ratios, and the third could give a ground state only in the $S = 1/2-11/2$ range. Thus, although we were originally wary about the reliability of the exchange

parameters obtained from the fit, it does appear that the opposite sign and relative magnitudes of J and J' are indeed correct.

For $J/J' > 0$ both J and J' are assumed to be antiferromagnetic. For $0 < J/J' < \sim 0.4$ the ground state of this complex is the same as in the case $\sim 0.65 > |J/J'| > 0$, namely $|3/2, 0\rangle$. Moving to the right, the ground state changes, and for $0.4 < J/J' < 1$ the $|1/2, 1\rangle$ state becomes the ground state. Following the energy diagram further to the right, for the J/J' lying between 1 and 2, the ground state is now the $|1/2, 2\rangle$ magnetic state. For the range of $2 < J/J' < \sim 2.7$ the $|3/2, 3\rangle$ becomes the ground state, while for the small range of J/J' values between ~ 2.7 and ~ 3.3 the ground state changes to the magnetic state $|5/2, 4\rangle$. Following the E/J' vs J/J' plot further to the right, and for values of J/J' between ~ 3.3 and 4 the $|7/2, 5\rangle$ state becomes the ground state. For J being 4 to ~ 4.7 times larger than J' , the ground state is the $|9/2, 6\rangle$ eigenstate, while finally, for $J \gg J'$ (more than ~ 4.7 times) the ground state is the $|11/2, 7\rangle$ eigenstate. The latter represents the situation where the Gd^{III}-Gd pathway is completely frustrated, and the Gd spins are thus aligned parallel, while the Mn^{III}-Gd is strongly antiferromagnetic and dominates (Figure 5-10d).

From this study it is evident that (i) the ground state of **14** is very sensitive to the J/J' ratio, with (ii) 15 out of the total of 28 possible states (54%) being possible ground states, depending on the J/J' ratio. Furthermore, with this study we were able to pinpoint the eigenstate which is the ground state for **14**, based on the relative ratio of the coupling constants, and address the level of spin frustration in an unusual Mn^{IV}Gd^{III}₂ system.

5.4 Conclusions

In the present work two new triangular complexes have been synthesized and characterized. These complexes have allowed for detailed investigation of the intraatomic interactions, and they were used as probes for spin frustration effects. From the study of **14**, we were able to abstract the exchange coupling constants for the Mn^{IV}-Gd^{III} and Gd^{III}-Gd^{III}

interactions, and from their relative magnitudes we were successful in addressing the exact ground state using a theoretical approach. Furthermore, through this approach it became evident that more than half of the total eigenstates resulting from the Hamiltonian describing this system could possibly be the ground state, depending on the exact combination of sign and relative magnitude of exchange parameters. Complexes **13** and **15** represent new examples of homometalic Mn triangles with a core bearing the general formula $[\text{Mn}_3\text{O}]^{7+}$. Both are ferromagnetically coupled with a resulting $S = 6$ ground state, while only complex **15** is a single-molecule magnet.²²⁸ Their differences with the previously reported Mn^{III}_3 triangles, as well as the different ligand combinations found in **13** and **15**, allowed for a more informative magnetostructural correlation. From this correlation, we have now more evidence that the displacement of the O^{2-} ion from the Mn^{III}_3 plane is mostly responsible for the ferromagnetic coupling within the cluster, while the molecular anisotropy is probably a result of the combination of the nearly parallel arrangement of the JT axes, gauged by the θ_{av} angle, and a small structural twist due to the presence of di- and triatomic bridges; the evidence for the latter is that complexes which are ferromagnetically coupled but any twist is absent, are not SMMs. Such a claim is to be further confirmed by extensive theoretical studies and *ab initio* calculations, and attempts towards this direction are already in progress.

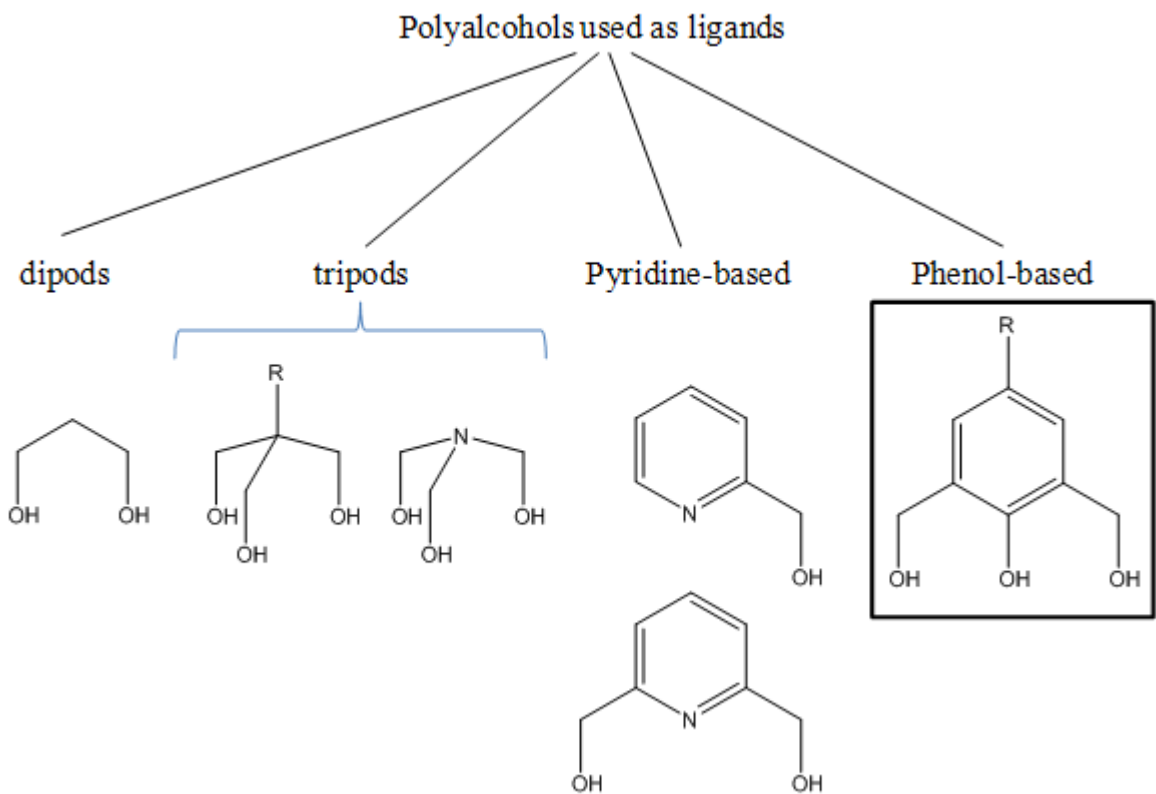


Figure 5-1. Schematic representation of polyalcohols used as ligands. The trialcohol 2,6-bis(hydroxymethyl)-*p*-cresol (hmcH₃) is highlighted (R=CH₃).

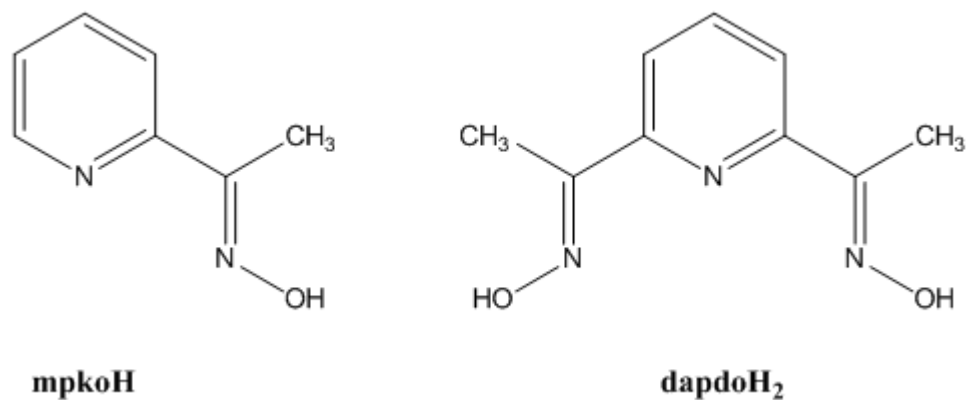


Figure 5-2. Schematic representation of methyl-2-pyridyl ketone oxime, and 2,6-diacetylpyridine dioxime (dapdoH₂).

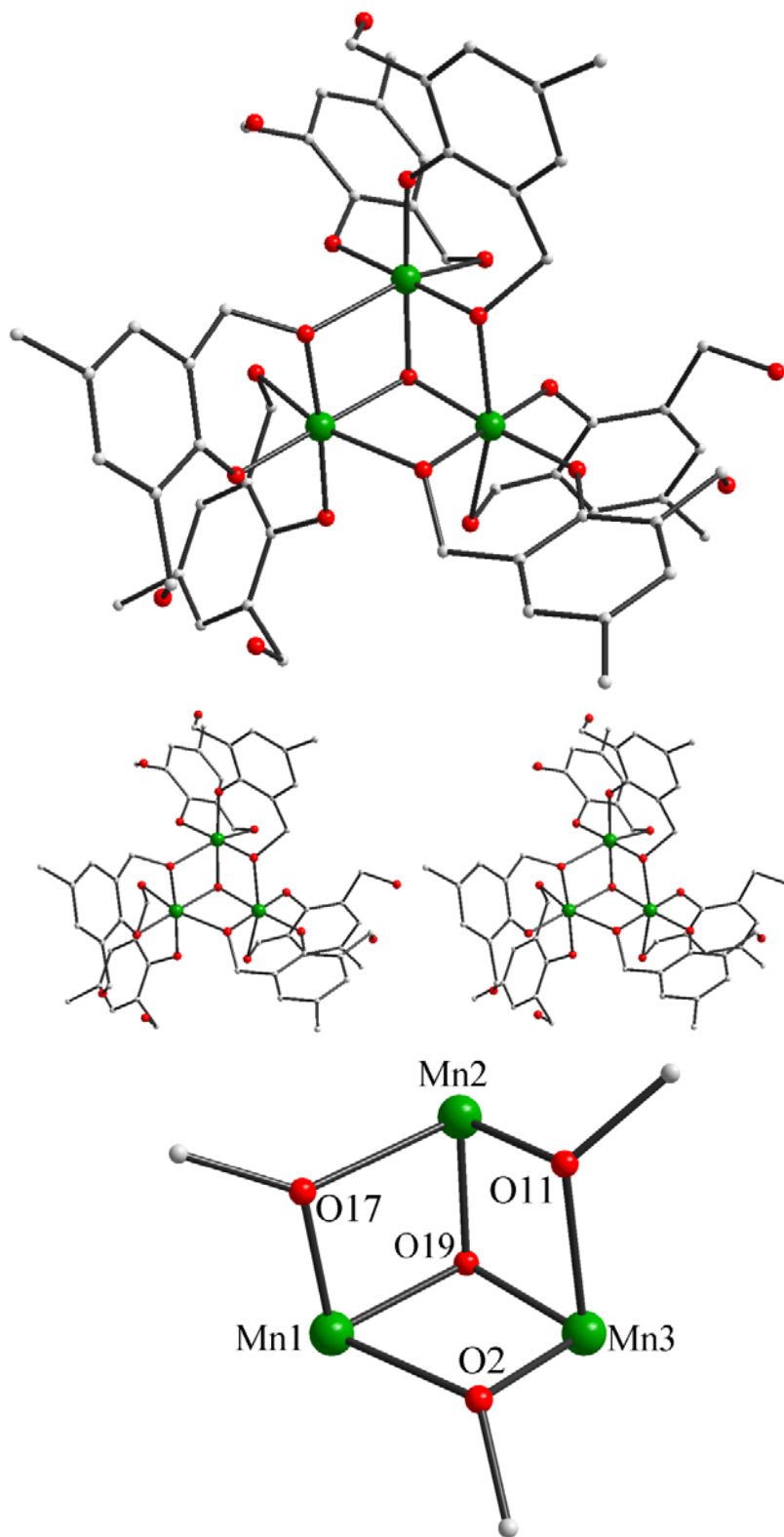


Figure 5-3. The structure, a stereopair, and the partially labeled core of complex **13**. Color code: Mn^{III} green, O red, C grey.

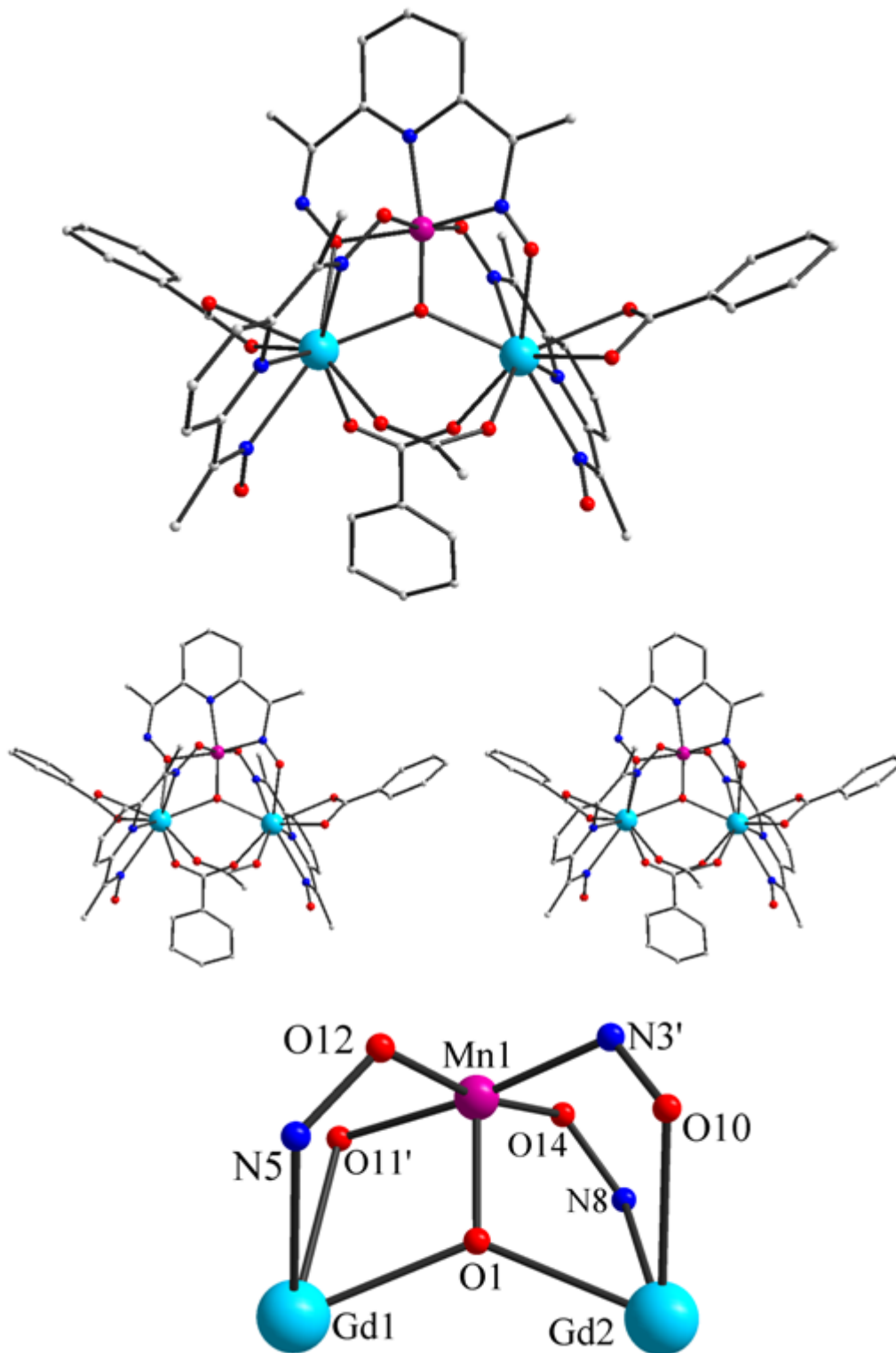


Figure 5-4. The structure, a stereopair, and the labeled core of complex **14**. Hydrogen atoms have been omitted for clarity. Color code: Gd^{III} cyan, Mn^{IV} purple, O red, N blue, C grey.

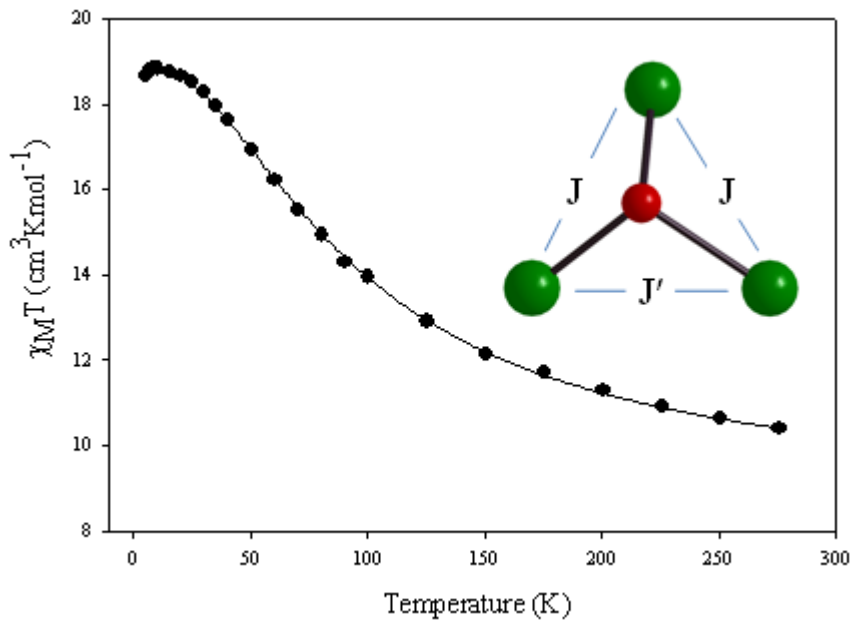


Figure 5-5. $\chi_M T$ vs T plot for complexes **13** in the temperature range 5.0-300 K in a 0.1 T applied dc field; the solid line is the fit to the dc magnetic susceptibility data (see text for fit details).

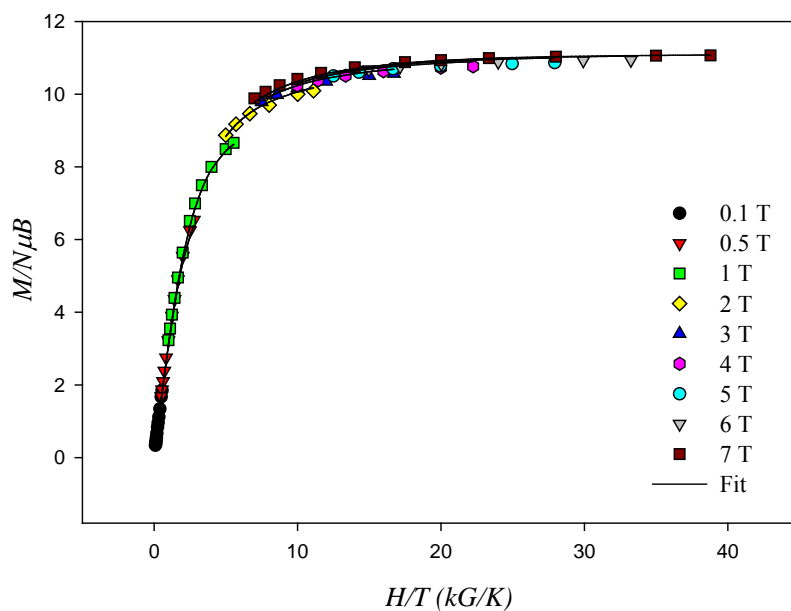


Figure 5-6. Plot of the reduced magnetization, $M/N\mu_B$, vs H/T for complex **13** in the 0.1 – 7 T field range. The solid lines are the fit with negative D ; see the text for the fit parameters.

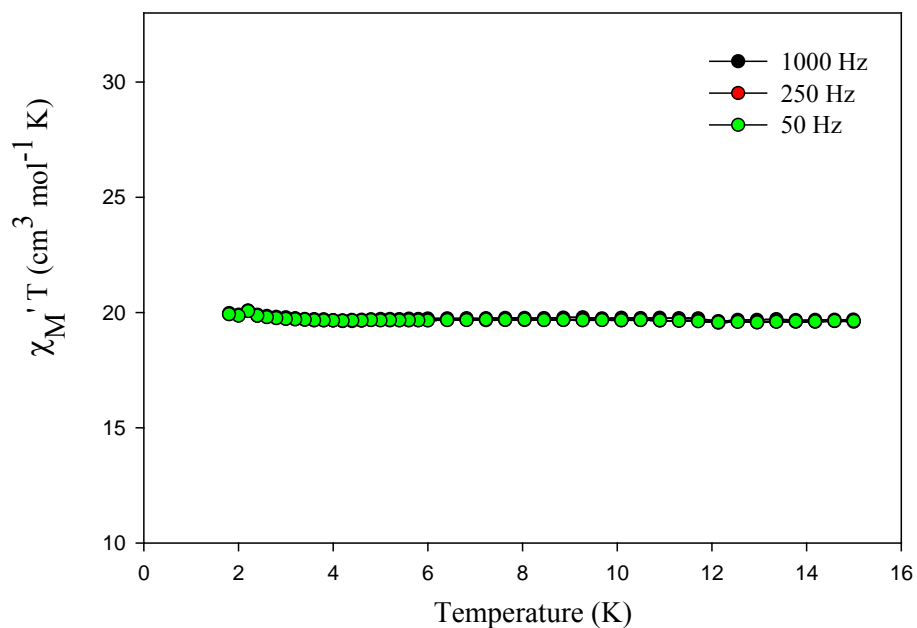


Figure 5-7. Plot of the in-phase (χ_M') ac magnetic susceptibility as $\chi_M'T$ vs T in a 3.5 Oe field oscillating at the indicated frequencies for complex **13**.

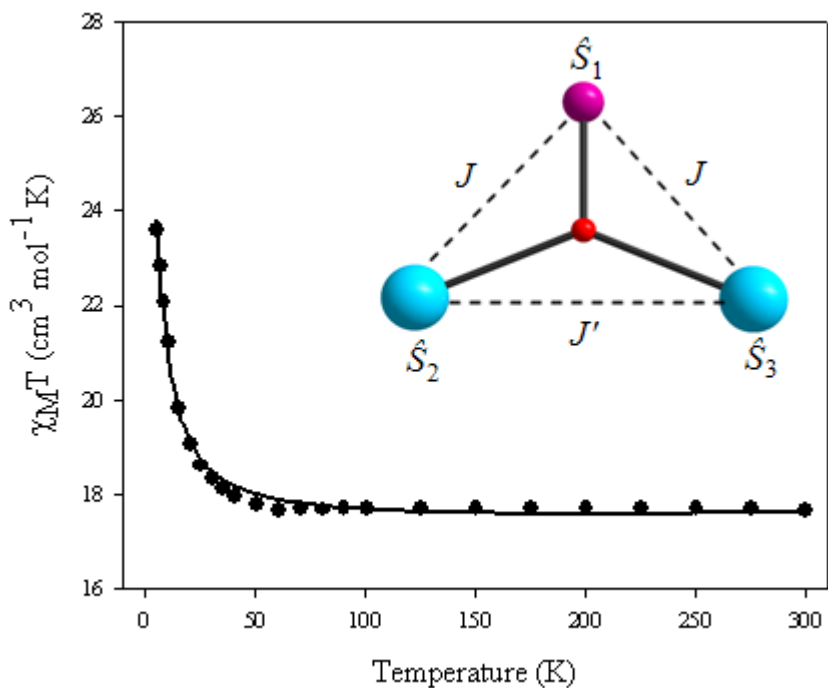


Figure 5-8. $\chi_M T$ vs T plot for complex **14** in the temperature range 5.0-300 K in a 0.1 T applied dc field; the solid line is the fit to the dc magnetic susceptibility data (see text for fit details).

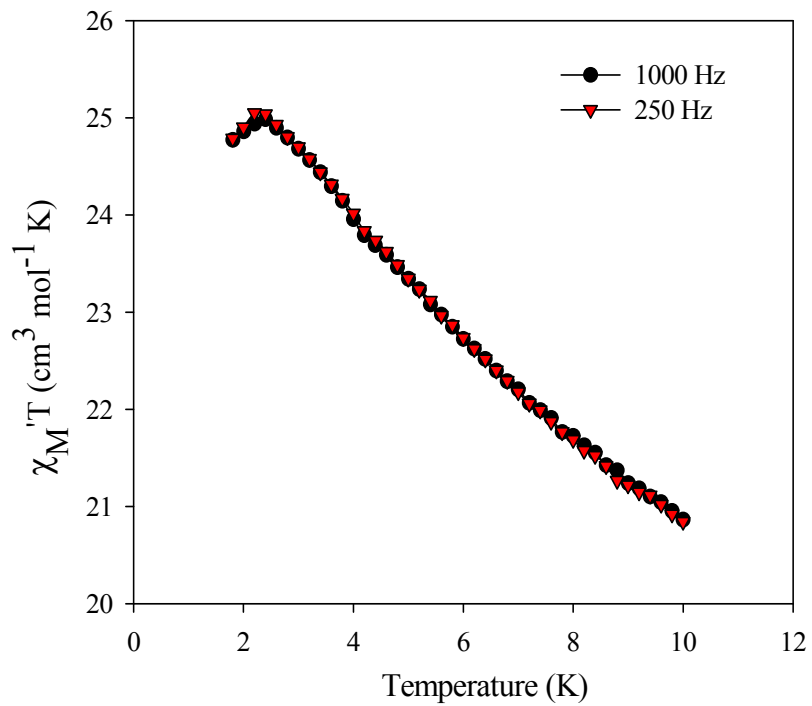


Figure 5-9. Plot of the in-phase (χ_M') ac magnetic susceptibility as $\chi_M'T$ vs T in a 3.5 Oe field oscillating at the indicated frequencies for complex **14**.

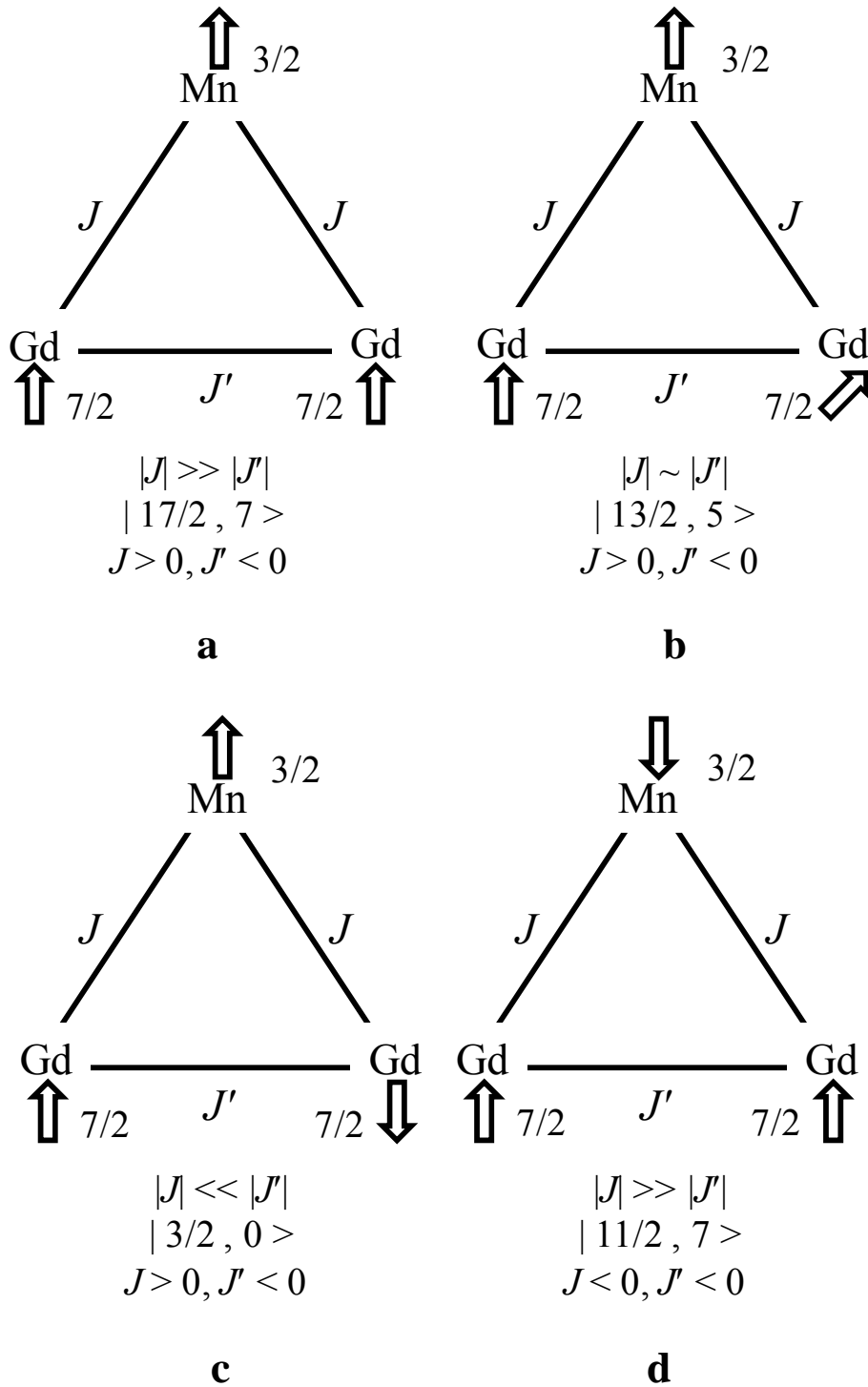


Figure 5-10. Depictions of the indicated $|S_T, S_A\rangle$ states, showing (a) the complete frustration of J' , when $J > 0$ and $J' < 0$, and the resultant $S_T = 17/2$ ground state, (b) the intermediate situation, giving the $S_T = 13/2$ ground state of **14**, (c) the complete frustration of J and the resultant $S_T = 3/2$ ground state, and (d) the complete frustration of J' when $J < 0$ and $J' < 0$, and a resultant $S_T = 11/2$ ground state.

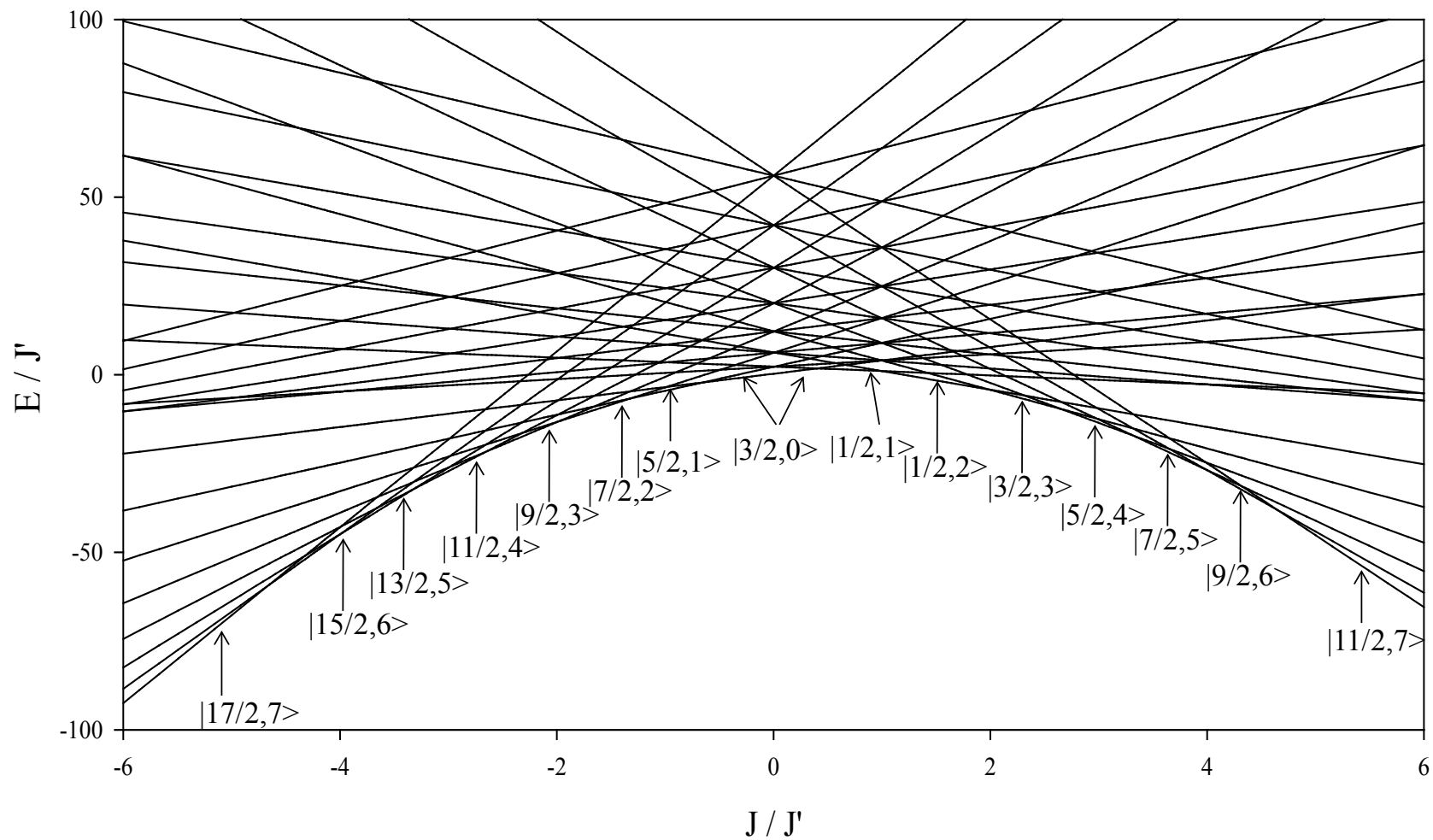


Figure 5-11. Variation of the spin state energies of **14** with the J/J' ratio, showing multiple changes in the ground state; the states are labelled as $|S_T, S_A\rangle$.

CHAPTER 6
SYNTHESIS, MAGNETISM, AND HIGH-FIELD EPR SPECTROSCOPY OF A FAMILY OF
MIXED-VALENT CUBOCTAHEDRAL Mn₁₃ COMPLEXES WITH 1,8-
NAPHTHALENEDICARBOXYLATE LIGANDS

6.1 Introduction

The synthesis and study of large assemblies of paramagnetic 3d transition metal ions has been a well established research area for a long time. Nevertheless, it has been greatly stimulated by being the main source of single-molecule magnets (SMMs). These are molecules, usually of manganese, that can function as molecular superparamagnets, and thus below their blocking temperature (T_B) can function as nanoscale magnets. SMMs combine a large ground state spin (S) with a relatively large easy-axis magnetoanisotropy, corresponding to a negative zero-field splitting parameter, D . As a result, SMMs exhibit magnetization hysteresis in magnetization vs applied field studies, the classical, diagnostic property of a magnet.^{23,24,26,38,49,76,78,242-244}

Manganese clusters have been the main source of SMMs primarily because they often display unusually large ground state S values, and reasonably large D values arising from the presence of Jahn-Teller distorted Mn^{III} ions; the barrier to magnetization reversal has a maximum value given by $S^2|D|$ and $(S^2-1/4)|D|$ for integer and half-integer spins, respectively. In addition, SMMs are small enough that they truly straddle the classical/quantum interface, displaying not just the classical property of magnetization hysteresis but also the quantum properties of quantum tunneling of the magnetization (QTM),¹¹⁷ and quantum phase interference.^{39,42,164}

The rational synthesis of Mn clusters has been a challenge to groups worldwide. Our own group has previously reported Mn SMMs with metal nuclearities ranging from Mn₃^{53,55} to Mn₈₄.⁵⁶ To date, the most well studied SMMs are the [Mn₁₂O₁₂(O₂CR)₁₆(H₂O)₄]^{z-} (R = various; z = 0 - 3) family containing monocarboxylate groups. Indeed, monocarboxylic acids have been the primary ligand type in high-spin clusters to date. In contrast, polynuclear 3d metal clusters

containing dicarboxylate groups are much less common in the inorganic literature. Our own group has reported only a few Mn clusters containing dicarboxylates,^{154,156,216} and we recently decided to extend these investigations. The idea is that the restricted flexibility of two linked carboxylate groups may yield products that are different from those with monocarboxylate groups. This was certainly the case in our previous work with phthalic acid and 2,2'-diethylmalonic acid.^{154,156,216} For the present work, we decided to explore a dicarboxylic acid with an even more restricted flexibility, and chose 1,8-naphthalenedicarboxylic acid (ndcH₂) in which the two carboxylate groups are very close and parallel to each other on a rigid naphthalene backbone (Figure 6-1). We were unaware of any previous use of ndcH₂ in Mn chemistry.

We herein report that the reactions of (ndcH₂) with common Mn starting materials have led to the formation of two new Mn₁₃ clusters. These contain Mn atoms in three oxidation states (II, III and IV). We were also subsequently able to isolate a complex with the same core using only the monocarboxylate ligand benzoate, showing that the dicarboxylate is not strictly speaking essential for forming the Mn₁₃ cluster, although it does yield more robust products. Nevertheless, the benzoate complex has allowed a comparative study of the structures and magnetic properties of this family of related Mn₁₃ complexes.

6.2 Experimental Section

6.2.1 Syntheses

All manipulations were performed under aerobic conditions using chemicals as received, unless otherwise stated. [Mn₃O(O₂CPh)₆(py)₂(H₂O)] was prepared as previously reported.¹⁵⁵

6.2.1.1 [Mn₁₃O₈(OH)₆(ndc)₆] (16)

To a stirred solution of Mn(O₂CMe)₂·4H₂O (0.20 g, 0.8 mmol) in DMF (15 mL) was added dropwise a suspension of 1,8-naphthalic acid anhydride (0.20 g, 1.0 mmol) and NEt₃ (1.40 mL, 10 mmol) in DMF (15 mL), resulting in a dark brown solution. This was stirred for a further 2

hours, filtered, and the filtrate was layered with an equal volume of Et₂O. The solution was left undisturbed at ambient temperature for 2 days, during which time large brown crystals of **16**·xDMF grew; the yield was ~70%. The crystals were maintained in mother liquor for X-ray crystallography and other single-crystal studies, or collected by filtration, washed with Et₂O, and dried in vacuo. Anal. Calcd (Found) for **16**·8DMF·H₂O: C, 40.71 (40.99); H, 3.56 (3.44); N, 3.96 (3.98) %. Selected IR data (KBr disk, cm⁻¹): 3391(w), 2923(m), 2360(m), 1652(s), 1557(s), 1420(s), 1350(s), 1225(m), 1100(m), 843(m), 811(m), 718(s), 610(m), 600(w), 526(s).

6.2.1.2 [Mn₁₃O₈(OEt)₅(OH)(ndc)₆] (**17**)

To a stirred solution of Mn(O₂CMe)₂·4H₂O (0.20 g, 0.8 mmol) in MeCN (20 mL) was added dropwise a suspension of 1,8-naphthalic anhydride (0.20 g, 1.0 mmol) and NEt₃ (1.40 mL, 10 mmol) in EtOH (10 mL), resulting in a dark brown solution. The solution was stirred for a further 2 hours, filtered, and the filtrate was layered with EtOH. The solution was left undisturbed at ambient temperature for 2 days, during which time large brown crystals of **17**·xMeCN formed; the yield was ~65 %. The crystals were maintained in mother liquor for X-ray crystallography and other single-crystal studies, or collected by filtration, washed with cold EtOH, and dried in air. Anal. Calcd (Found) for **17**·6MeCN: C, 42.29 (42.54); H, 3.25 (3.74); N, 3.15 (2.79) %. Selected IR data (KBr, cm⁻¹): 3397(w), 2354(m), 1558(s), 1420(s), 1351(s), 1225(m), 1029(m), 873(m), 839(m), 811(m), 780(s), 613(m), 600(w), 527(s).

6.2.1.3 [Mn₁₃O₈(OEt)₆(O₂CPh)₁₂] (**18**)

To a stirred solution of [Mn₃O(O₂CPh)₆(py)₂(H₂O)] (0.50 g, 0.5 mmol) in a 1:3 (v/v) mixture of MeCN/EtOH (30 mL) was added NEt₃ (0.50 mL, 3.5 mmol) in small portions, resulting in a dark brown solution. The solution was stirred for a further 20 minutes, filtered, and the filtrate was layered with Et₂O. The solution was left undisturbed at ambient temperature for 2 days, during which time large brown crystals of **18**·4MeCN grew; the yield was ~80%. The

crystals were maintained in mother liquor for X-ray crystallography and other single-crystal studies, or collected by filtration, washed with Et₂O, and dried in vacuo. Dried solid appears to be hygroscopic and analyzed as **18**·7H₂O. Anal. Calcd (Found) for **18**·7H₂O: C, 42.54 (42.83); H, 3.48 (3.89) %. Selected IR data (KBr, cm⁻¹): 3397(w), 3059(m), 2969(m), 2923(m), 2878(m), 1597(s), 1553(s), 1410(s), 1402(w), 1379(s), 1176(m), 1027(s), 873(m), 712(s), 685(s), 639(s), 585(s), 560(w), 549(s), 477(s).

6.2.1.4 [Mn₁₃O₈(OMe)₆(ndc)₆] (19)

To a stirred solution of Mn(O₂CMe)₂·4H₂O (0.20 g, 0.8 mmol) in DMF (15 mL) was added dropwise a suspension of 1,8-naphthalic acid anhydride (0.2 g, 1 mmol) and NEt₃ (1.4 mL, 10 mmol) in DMF (15 mL), resulting in a dark brown solution. This was stirred for a further 2 hours, filtered, and layered with an equal volume of MeOH. The solution was left undisturbed at ambient temperature for 2 days, during which time large brown crystals formed; the yield was ~68%. The crystals were collected by filtration, washed with cold MeOH and Et₂O, and dried in vacuo. Anal. Calcd (Found) for **19**·5DMF·H₂O: C, 41.42 (41.27); H, 3.40 (3.40); N, 2.60 (2.94) %. Selected IR data (KBr, cm⁻¹): 3419(w), 2361(m), 2336(m), 1653(s), 1558(s), 1415(s), 1351(s), 1225(m), 1018(m), 843(m), 814(m), 781(s), 645(w), 600(w), 525(s).

6.2.2 X-ray Crystallography

All data were collected by Dr. K. A. Abboud at 173 K on a Siemens SMART PLATFORM equipped with a CCD area detector and a graphite monochromator utilizing MoK_α radiation (λ = 0.71073 Å). Cell parameters were refined using up to 8192 reflections. A full sphere of data (1850 frames) was collected using the ω -scan method (0.3° frame width). The first 50 frames were re-measured at the end of data collection to monitor instrument and crystal stability (maximum correction on I was < 1 %). Absorption corrections by integration were applied based

on measured indexed crystal faces. The structures were solved by the Direct Methods in *SHELXTL6*, and refined on F^2 using full-matrix least squares. The non-H atoms were treated anisotropically, whereas the H atoms were placed in ideal positions and refined as riding on their C atoms. Data collection parameters and structure solution details are listed in Table D-15.

For **16**·xDMF, the asymmetric unit consists of three half clusters and ~19 DMF molecules. The latter were disordered and could not be modeled properly, thus program SQUEEZE, a part of the PLATON package of crystallographic software, was used to calculate the total solvent area and remove its contribution to the overall intensity data. Each half cluster has four bridging OH⁻ groups whose H atoms were located in difference Fourier maps but did not refine properly. Thus they were included in the final refinement cycle in idealized positions and refined riding on their parent atoms. A total of 1666 parameters were refined in the final cycle of refinement using 41405 reflections with $I > 2\sigma(I)$ to yield R_1 and wR_2 of 6.28 and 14.94%, respectively.

For **17**·xMeCN, the asymmetric unit consists of a half cluster and some MeCN molecules. The latter were disordered and could not be modeled properly, thus program SQUEEZE was used to calculate the solvent disorder area and remove its contribution to the overall intensity data. The cluster has one EtO⁻ ligand (O17) with its methyl group disordered, and this was refined in two positions with the site occupation factors dependently refined. Another disorder is located on another EtO⁻ ligand (O19), which is disordered with a OH⁻ group with occupancies of 50:50%; the half-occupancy OH⁻ component is H-bonded to a (half-occupancy) EtOH group. The compound formula is thus $[\text{Mn}_{13}\text{O}_8(\text{OEt})_5(\text{OH})(\text{ndc})_6]$. A total of 598 parameters were refined in the final cycle of refinement using 15010 reflections with $I > 2\sigma(I)$ to yield R_1 and wR_2 of 6.32 and 16.89%, respectively.

For $18 \cdot 4\text{MeCN}$, the asymmetric unit consists of a half cluster and two MeCN molecules. The latter were each disordered about two sites, and they were refined with each site occupation factor fixed at 0.5. A total of 712 parameters were refined in the final cycle of refinement using 9104 reflections with $I > 2\sigma(I)$ to yield R_1 and wR_2 of 4.90 and 7.35%, respectively.

6.2.3 Other Studies

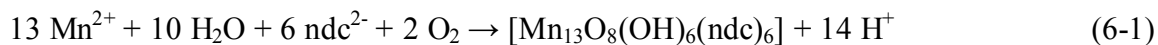
Infrared spectra were recorded in the solid state (KBr pellets) on a Nicolet Nexus 670 FTIR spectrometer in the $400\text{--}4000\text{ cm}^{-1}$ range. Elemental analyses (C, H, and N) were performed by the in-house facilities of the University of Florida Chemistry Department. Variable-temperature dc and ac magnetic susceptibility data were collected at the University of Florida using a Quantum Design MPMS-XL SQUID susceptometer equipped with a 7 T magnet and operating in the 1.8–300 K range. Samples were embedded in solid eicosane to prevent torquing. Magnetization vs field and temperature data were fit using the program MAGNET.⁶⁸ Pascal's constants were used to estimate the diamagnetic correction, which was subtracted from the experimental susceptibility to give the molar paramagnetic susceptibility (χ_M). High frequency (40–160 GHz) Electron Paramagnetic Resonance (HFEPR) measurements were carried out using a Millimeter-wave Vector Network Analyzer (MVNA) in combination with a cavity perturbation technique described elsewhere.⁷⁰ Magnetic fields up to 17 T were provided by an axial superconducting magnet, and angle-dependent HFEPR data were obtained using a cavity which allowed rotation of the sample about one axis perpendicular to the applied field.⁷¹ The temperature was controlled via a variable-flow cryostat situated within the bore of the magnet, using a calibrated Cernox resistor as a reference.

6.3 Results and Discussion

6.3.1 Syntheses

The most commercially convenient source of 1,8-naphthalenedicarboxylic acid is the anhydride 1,8-naphthalic anhydride, and so we employed this in the presence of base to foster in situ formation of the dicarboxylate ndc^{2-} . For completeness, we also prepared and recrystallized the diacid form ndcH_2 , using the published procedure that starts with the anhydride,²⁴⁵ and investigated its use in place of the anhydride in the described reactions. The preformed dicarboxylic acid offers some advantages in being more soluble than the anhydride, but we found that it gives the same products in similar (or lower) yields as the more convenient reactions starting with the anhydride, and so we document only the latter in the Experimental Section. The low solubility of the anhydride was overcome by using DMF and MeCN/EtOH reaction solvents for the syntheses of **16** and **17**, respectively.

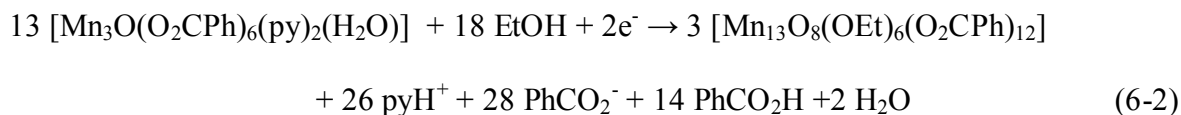
We originally obtained $[\text{Mn}_{13}\text{O}_8(\text{OH})_6(\text{ndc})_6]$ (**16**) from the reaction of $[\text{Mn}_{12}\text{O}_{12}(\text{O}_2\text{CH}_3)_{16}(\text{H}_2\text{O})_4]$ (**1**)²⁵ with eight equivalents of the preformed 1,8-naphthalene dicarboxylic acid, but subsequently derived the superior procedure described. This involves reaction of Mn^{II} with ndc^{2-} formed in situ, followed by air oxidation of Mn under the prevailing basic conditions. The reaction is summarized in eq. 6-1.



The many oxide and OH^- bridges in **16** are thus concluded to be arising from a combination of water in the solvent and the O_2 involved in the reaction. It is thus reasonable that the corresponding reaction in an MeCN/EtOH solvent mixture gives instead $[\text{Mn}_{13}\text{O}_8(\text{OEt})_5(\text{OH})(\text{ndc})_6]$ (**17**). Clearly there is enough water in the employed EtOH and atmosphere to compete sufficiently. In contrast, using the procedure to **16** using DMF as the reaction solvent but layering with methanol, the product is the corresponding methoxide complex

[Mn₁₃O₈(OMe)₆(ndc)₆] (**19**), as concluded from the elemental analysis, infrared spectrum and similar magnetic behavior (vide infra). We also found that **17** was obtained, but in lower yields, when the triangular [Mn₃O(O₂CR)₆(py)₃]⁺ (R = Me, Et, Bu[†]) complexes were employed in an MeCN/EtOH reaction solvent; however, the benzoate complex gives complex **18** (vide infra).

For comparison with complexes **16** and **17**, we attempted to prepare the known complex [Mn₁₃O₈(OEt)₆(O₂CPh)₁₂] (**18**) using the published procedure²⁴⁶ but were unsuccessful. We therefore developed a new, high yield (~80%) synthesis to this compound, the reaction of [Mn₃O(O₂CPh)₆(py)₂(H₂O)] with NEt₃ in MeCN/EtOH. The same product was also obtained from only EtOH solution, but in much lower yield. The Mn₃ reagent is mixed valence (2 Mn^{III}, Mn^{II}) with an average oxidation state of +2.67, almost identical to that in **18** (+2.62), and EtOH can provide reducing equivalents; this likely contributes to the high yield. The formation of **18** is summarized in eq. 6-2.



6.3.2 Description of Structures

The structure of complex **16** and a stereopair are presented in Figure 6-2, and the fully labeled core is shown in Figure 6-3. Selected interatomic distances are listed in Table D-16. Complex **16** crystallizes in the triclinic space group $P\bar{1}$ with the Mn₁₃ molecule lying on an inversion center; for the sake of brevity, reference to specific atoms in the following discussion includes their symmetry-related partners. There is a [Mn₁₃O₈(OH)₆]¹²⁺ core consisting of one Mn^{IV}, six Mn^{III} and six Mn^{II} atoms bridged by six μ₅-O²⁻, two μ₃-O²⁻, and six μ₃-OH⁻ ions; additional bridges and peripheral ligation is provided by six tetradentate ndc²⁻ groups. All Mn atoms are six-coordinate with near-octahedral geometry, and their oxidation states were

established by charge considerations, bond valence sum (BVS) calculations (Table E-6), and the clear Jahn-Teller (JT) distortions (axial elongation) at the Mn^{III} atoms (Mn1, Mn2, Mn5), with the JT elongated Mn^{III}-O bonds being at least 0.1-0.2 Å longer than the other Mn^{III}-O bonds. As is usually the case, these JT elongation axes are avoiding the Mn-oxide bonds, in this case pointing toward carboxylate O atoms.

The views in Figures 6-2 and 6-3 emphasize that the structure can be described as consisting of three layers: there is a central layer comprising a nearly planar ring of six Mn^{II} atoms (Mn3, Mn4, Mn7) with a Mn^{IV} atom (Mn6) at its center. Above and below this Mn₇ layer is an equilateral triangle of three Mn^{III} atoms (Mn1, Mn2, Mn5) capped by a μ₃-O²⁻ ion (O16); these two triangles are staggered in a trigonal antiprismatic fashion. The Mn^{III}₃ triangles are each connected to the central Mn₇ layer by (i) three μ₅-O²⁻ ions (O13, O18, O19), which have square pyramidal geometry and are bound to Mn^{II}₂Mn^{III}₂Mn^{IV} atoms; and (ii) three μ₃-OH⁻ ions (O14, O15, O17) bound to Mn^{II}₂Mn^{III} atoms (the O BVS calculations are presented in Table E-7). The peripheral ligation about the resulting [Mn₁₃O₈(OH)₆]¹²⁺ core is provided by six μ₄-ndc²⁻ groups, each of which has one of its carboxylate groups bridging a Mn^{II}₂ pair, and the other bridging a Mn^{III}₂ pair. The resulting molecule has virtual S₆ symmetry, with the S₆ axis passing through the mid-points of the Mn^{III}₃ triangles and the central Mn^{IV} atom. A view approximately along the S₆ axis is provided in Figure 6-4a.

The [Mn₁₃O₁₄] core can alternatively be described as consisting of eight face-fused [Mn₄O₄] cubane units with a common vertex at the central Mn^{IV} atom (Mn6). Each cubane shares three of its faces with its neighbors, creating a larger cubane-like unit whose eight vertices are all O atoms; in this description, the Mn atoms each lie at the mid-point of an edge and at the

center of the larger cubane. A view emphasizing this cubic description is provided in Figure 6-4b.

It is very interesting and instructive to consider just the Mn atom positions and the resulting Mn₁₃ topology. Shown in Figure 6-5a is the Mn₁₃ unit from a viewpoint similar to those in Figures 6-2 and 6-3, which emphasizes the Mn₃:Mn₇:Mn₃ three-layer arrangement. When viewed from the slightly different viewpoint of Figure 6-5b, the Mn₁₃ unit can now be seen to be a fragment of a body-centered cubic lattice: the fragment comprises one complete body-centered cube with four of its faces capped by the central atoms of four adjacent cubic units. Finally, if the central Mn^{IV} atom is ignored, the remaining Mn₁₂ unit is a cuboctahedron (Figure 6-5c). The cuboctahedron is one of the Archimedean solids: it is a polyhedron consisting of six square faces and eight triangular faces, and possesses twelve identical vertices (i.e., it is ‘vertex transitive’), each representing the meeting point of two triangles and two squares, and twenty-four identical edges, each separating a triangle from a square.²⁴⁷ The Mn₁₃ unit can thus be described as a Mn-centered Mn₁₂ cuboctahedron.

The structure of the core of **17** is presented in Figure 6-6. Selected interatomic distances and angles are listed in Table D-17. Complex **17** crystallizes in the triclinic space group $P\bar{1}$ with the Mn₁₃ molecule again on an inversion center. The complex is again mixed-valence Mn^{IV}Mn^{III}₆Mn^{II}₆, as confirmed by BVS calculations (Table E-6), and is structurally almost identical to that of **16** except that there are now five μ₃-EtO⁻ and one μ₃-OH⁻ ions in place of the six μ₃-OH⁻ ions. Peripheral ligation is again provided by six ndc²⁻ groups, and the molecule has virtual S₆ symmetry (ignoring the one OH⁻ in place of EtO⁻). Complex **19** is concluded to be the same as **17**, but with MeO⁻ groups in place of EtO⁻.

Complex **18** crystallizes in the monoclinic space group $C2/c$, with the Mn_{13} molecule on an inversion center. It contains benzoate rather than ndc^{2-} groups, and the structure of the complete molecule is shown in Figure 6-7. The labeled core and a table of selected interatomic distances are provided in Figure 6-8 and Table D-18, respectively. The complex is $Mn^{IV}Mn^{III}_6Mn^{II}_6$ (Table E-6) and structurally similar to **16** and **17**; its core is the same as that in **17**, with six μ_5-O^{2-} , two μ_3-O^{2-} , and six μ_3-EtO^- ions, but it differs markedly from both **16** and **17** in possessing peripheral ligation by twelve benzoate groups, six bridging Mn^{II}_2 pairs and six bridging Mn^{III}_2 pairs. The complex again has virtual S_6 symmetry.

A number of mixed-valent $Mn^{II/III/IV}$ clusters have been reported. Our own group has reported Mn_9 ,²⁴⁸ Mn_{22} ,²⁴⁹ Mn_{25} ,^{52,88} and Mn_{30} ^{86,250} examples, of which the Mn_{25} family are of particular relevance to complexes **16-19** in also consisting of Mn_x layers. In particular, the central layer in the Mn_{25} complexes consists of a Mn^{IV} -centered Mn^{III}_6 hexagon, structurally similar to the Mn^{IV} -centered Mn^{II}_6 hexagon of **16-19**. Some other multi-layered structures include a Mn_{19} family of coordination polymers with a pyramidal structure,²⁵¹ a Mn_{13} complex with a dumbbell shape,²⁵² a Mn_{26} discrete pyramid,²⁵³ a Mn_{18} cluster,²⁵⁴ a Mn_{10} cage,²⁵⁵ and a Mn_{19} cluster,¹⁶² as well as the heterometallic $Mn_{10}Th_6$,^{173,182} $Mn_{12}Cu_8$,²⁵⁶ and $Cu_{17}Mn_{28}$,¹⁶⁹ cages, amongst others. As already mentioned, complex **18** was briefly reported elsewhere,²⁴⁶ and the the Mn_{13} core has also been obtained with ferrocene-1,1'-dicarboxylate,²⁵⁷ and very recently with another benzoate derivative analogous to **18**.²⁵⁸

6.3.3 Structural Comparison of Complexes 16-18

Since complexes **16-18** structurally span differences both in the core (OH^- vs EtO^-) and in the peripheral ligation (ndc^{2-} vs $PhCO_2^-$), and since they display somewhat different magnetic properties (vide infra), it is of interest to assess in more detail any structural differences. Pertinent structural parameters are thus collected in Table 6-1, and close inspection reveals few

major differences. The biggest, of course, is the carboxylate C...C separation between two adjacent carboxylate groups. In **16** and **17**, the average separation is only 2.899(42) and 2.909(17) Å, respectively, since the two carboxylate groups are attached to the naphthalene backbone, and these are much shorter than the 3.434(43) Å between two separate benzoate groups in **18**. It is thus logical to assume that this would cause some significant structural perturbation of the core, but on the contrary it does not appear to have a significant effect on the metric parameters within the [Mn₁₃O₁₄] core; those for **18** are essentially all within the ranges for either **16** or **17**, or both. In approximately half the entries in Table 6-1, there are no differences between the three complexes. Among the remainder, it is interesting to note that for some parameters (Mn^{III}...Mn^{III} and Mn^{II}...Mn^{III} distances, and Mn^{III}-μ₃-O²⁻-Mn^{III} angles), the values for **16** are closer to those for **18** than those for **17**. This suggests that for many of the metric parameters, changes caused by the HO⁻-to-EtO⁻ substitution (**16** to **17**) are essentially equal and

Table 6-1. Structural Comparison between Complexes **16**, **17**, and **18**.

| Parameter ^a | 16 | 17 | 18 |
|--|--------------|--------------|--------------|
| C...C (Å) | 2.899(42) | 2.909(17) | 3.434(43) |
| Mn ^{III} ...Mn ^{III} | 2.945(4) | 2.987(10) | 2.952(3) |
| Mn ^{II} ...Mn ^{III} | 3.186(13) | 3.177(38) | 3.202(43) |
| Mn ^{II} ...Mn ^{IV} | 3.239(21) | 3.195(7) | 3.206(8) |
| Mn ^{II} ...Mn ^{II} | 3.250(31) | 3.208(41) | 3.207(20) |
| Mn ^{III} ...Mn ^{IV} | 3.018(8) | 3.054(10) | 3.061(80) |
| Mn ^{III} -μ ₅ -O ²⁻ -Mn ^{III} | 86.17(18) | 86.43(19) | 84.35(35) |
| Mn ^{III} -μ ₃ -O ²⁻ -Mn ^{III} | 103.85(75) | 102.25(45) | 104.20(40) |
| Mn ^{II} -O ²⁻ -Mn ^{IV} | 99.93(1.08) | 98.54(1.30) | 98.85(2.75) |
| Mn ^{III} -O ²⁻ -Mn ^{IV} | 97.16(6.94) | 97.42(6.78) | 97.40(7.80) |
| Mn ^{II} -O ²⁻ -Mn ^{II} | 88.18(53) | 88.15(1.70) | 88.41(50) |
| trans Mn ^{II} -μ ₅ -O ²⁻ -Mn ^{III} | 162.15(7.65) | 162.60(7.90) | 161.85(6.55) |
| cis Mn ^{II} -μ ₅ -O ²⁻ -Mn ^{III} | 90.66(5.03) | 90.41(5.20) | 91.55(6.65) |
| Mn ^{II} -RO ⁻ -Mn ^{III} | 102.30(1.60) | 101.11(1.26) | 100.80(1.60) |
| Mn ^{II} -RO ⁻ -Mn ^{II} | 96.49(2) | 94.66(54) | 92.30(30) |
| O ²⁻ to Mn ₃ ^{III} plane | 0.782 | 0.837 | 0.769 |
| Mn ^{IV} to Mn ₃ ^{III} plane | 2.492 | 2.520 | 2.543 |

^a Average values, in Å and ° - the range in the values is indicated in parentheses.

opposite to those due to the ndc^{2-} -to- PhCO_2^- substitution (**17** to **18**), resulting in some parameters for **16** being the same as those for **18**. In other cases, the values for **17** are closest to those for **18** (e.g. $\text{Mn}^{\text{II}}\cdots\text{Mn}^{\text{II}}$, $\text{Mn}^{\text{II}}\cdots\text{Mn}^{\text{IV}}$ and $\text{Mn}^{\text{III}}\cdots\text{Mn}^{\text{IV}}$ distances, $\text{Mn}^{\text{II}}-\text{O}^{2-}-\text{Mn}^{\text{IV}}$ angles) showing the values are dominated by the EtO^- vs HO^- difference.

With respect to the magnetic properties to be discussed below, a probably significant difference within Table 6-1 is found in the $\text{Mn}^{\text{II}}-\text{RO}^--\text{Mn}^{\text{II}}$ angles, where R = H (**16**) or Et (**17**, **18**). In this case, the values for the latter two are both smaller than that of **16**. This is likely a contributory factor in the observed differences in magnetic properties to be discussed below, because it is well known that even very small changes in the angles at mono-atomic bridges between two metal atoms can have a significant effect on the magnitude of the resulting superexchange interaction;⁹ this was first demonstrated in the classic work on bis-hydroxo-bridged Cu(II) dimers.²⁵⁹

6.4.4 Magnetochemistry

6.3.4.1 DC Magnetic Susceptibility Studies on Complexes 16-19

Solid-state, variable-temperature ac magnetic susceptibility (χ_M) data were collected on vacuum-dried microcrystalline samples of complexes **16-19**, suspended in eicosane to prevent torquing, in the 5.0-300 K temperature range in a 0.1 tesla (T) (1000 Oe) magnetic field. The obtained data are plotted as $\chi_M T$ vs T in Figure 6-9, and it can be seen that the overall profiles are very similar for the four complexes, $\chi_M T$ steadily decreasing with decreasing temperature and thus suggesting dominant antiferromagnetic interactions within the molecules. However, the plots for **16** and **18** are the most similar, which is in agreement with the fact that these two complexes have very similar core metric parameters, as described above. Similarly, complexes **17** and **19** exhibit very similar $\chi_M T$ vs T profiles, and this is reasonable since the two compounds

differ only in the EtO⁻ vs MeO⁻ difference. We did not pursue the crystal structure of **19** because we did not anticipate that the EtO⁻ vs MeO⁻ difference would cause any significant structural difference between the two compounds, and the very similar magnetic properties seem to agree with and support this assertion.

For all three compounds, the 5.0 K data suggest that the complexes all possess ground states with significant S values. This would not be unexpected for such a complicated Mn₁₃ topology with multiple inequivalent exchange parameters, most of which, if not all, being almost certainly antiferromagnetic. This is because of the spin frustration effects expected within the many Mn₃ triangular units within the Mn₁₃ structure. We define spin frustration here in its more general form as competing exchange interactions of comparable magnitude that prevent (frustrate) the preferred pairwise antiparallel spin alignments that would give small (0 or 1/2) ground states.

In order to determine the ground states of complexes **16-19**, magnetization (M) data were collected in the magnetic field and temperature ranges of 0.1-7 T and 1.8-10 K (Figure 6-10, inset). We attempted to fit the resulting data using the program MAGNET,⁶⁸ which assumes that only the ground state is populated at these temperatures, includes axial zero-field splitting (ZFS) and the Zeeman interaction, and incorporates a full powder average; the corresponding spin Hamiltonian is given by eq. 6-3.

$$\mathcal{H} = D\hat{S}_z^2 + g\mu_B\mu_0\hat{S}\cdot\mathbf{H} \quad (6-3)$$

However, we could not get an acceptable fit. In our experience, this is the case when there are low-lying excited states that are consequently populated even at these relatively low temperatures, and/or excited states that are more separated from the ground state but have S values greater than that of the ground-state and thus their larger M_S levels rapidly decrease in

energy due to the applied magnetic field and approach (or even cross) those of the ground state. Such situations are expected for **16-19** because of their high content of Mn^{II} atoms, which give very weak and usually antiferromagnetic exchange interactions, and thus low-lying excited states with larger S values.

As we have described elsewhere on multiple occasions,^{52,86-88,249} the above complications can sometimes be avoided by using only data collected at the lowest fields. Indeed, a satisfactory fit was obtained for complex **16** using only data collected in the 0.1 – 0.8 T field range (Figure 6-10) with fit parameters $S = 9/2$, $g = 2.00$ (1) and $D = -0.14$ (2) cm⁻¹. It is usually the case in fitting powder magnetization data that comparable fits can be obtained with positive and negative D values, and this was also the case for **16**, giving an alternative fit with $S = 9/2$, $g = 2.00$ (1) and $D = +0.22$ (2) cm⁻¹. To assess which fit was superior, a D vs g root-mean-square error surface for the fit was generated and is shown in Figure 6-11; this plots the relative difference between the experimental $M/N\mu_B$ data and those calculated for various combinations of D and g . It is clear from Figure 6-10 that the two fits are of comparable quality and that the minima are fairly soft, leading to the significant uncertainties quoted for the fit parameters. Thus, although D values for Mn^{III}-containing Mn_x clusters are almost always negative, this could not be concluded in the present case for **16**. This point was probed further in the EPR studies (vide infra).

For complexes **17-19**, attempted fits using data collected at only the lower fields still did not lead to acceptable fits. We will not discuss these further, because in any case we resorted to the use of more reliable methods employing ac magnetic susceptibility measurements,^{87,250,260} which do not employ a dc field, to identify the ground spins of **17-19**, and also to confirm or otherwise our initial conclusion of an $S = 9/2$ ground state for **16**.

6.3.4.2 AC Magnetic Susceptibility Studies of Complexes 16-19

Alternating-current magnetic susceptibility studies were performed on vacuum-dried microcrystalline samples of **16-19** in the temperature range 1.8-15 K in a zero dc field and a 3.5 Oe ac field oscillating at frequencies between 250-1000 Hz. The resulting data are plotted as $\chi_M' T$ vs. T in Figure 6-12, where χ_M' is the in-phase component of the ac susceptibility. For all four complexes, $\chi_M' T$ decreases essentially linearly with decreasing temperature, this downward slope supporting a decreasing population of excited states with a larger S than the ground state, in agreement with the statements above re the dc magnetization fitting problems. A linear extrapolation of the data for **16** to 0 K, where only the ground state will be populated, gives $\chi_M' T$ of $\sim 13 \text{ cm}^3 \text{ K mol}^{-1}$, indicating an $S = 9/2$ ground state (expected spin-only ($g = 2.0$) values for $S = 7/2, 9/2,$ and $11/2$ are 7.88, 12.4, and $17.88 \text{ cm}^3 \text{ K mol}^{-1}$). This is in satisfying agreement with the dc magnetization fit in Figure 6-10. For **17** and **19**, the plots are almost superimposed and the $\chi_M' T$ values are significantly higher, extrapolating to values in the $16.0 - 16.5 \text{ cm}^3 \text{ K mol}^{-1}$ range at 0 K, consistent with an $S = 11/2$ ground state for these complexes. Again, their anticipated similarity in structure is supported by their almost identical magnetic properties. For **18**, the $\chi_M' T$ vs. T plot is noticeably higher than those for the other complexes, and appears to be heading for a value in the $18.5 - 19.0 \text{ cm}^3 \text{ K mol}^{-1}$ range. Again, this is suggestive of an $S = 11/2$ ground state, since the expected spin-only value for an $S = 13/2$ state is much higher at $24.38 \text{ cm}^3 \text{ K mol}^{-1}$. The slightly high value for **18** is likely due to one or more particularly low-lying excited states whose depopulation does not become evident in the $\chi_M' T$ vs. T plot until the very lowest temperatures, below the 1.8 K operating limit of our SQUID magnetometer. The same may apply for the slightly high value for **16**. Note that deviations of g from 2.0 should be below not above this value for Mn.

It is interesting that complexes **16** and **18** have the overall more similar $\chi_M T$ vs. T behavior up to 300 K (Figure 6-9) but that **17**, **18**, and **19** are the more similar in ground state (Figure 6-12). The former observation is consistent with the many structural similarities between **16** and **18** seen in Table 6-1, even though they differ in both the EtO^- vs HO^- and benzoate vs ndc^{2-} identities, whereas the difference in ground state is perhaps due to the significantly different $\text{Mn}^{\text{II}}\text{Mn}^{\text{II}}$ exchange interactions via the $\text{Mn}^{\text{II}}\text{-RO}^-\text{-Mn}^{\text{II}}$ ($\text{R} = \text{H, Et}$) superexchange pathways. These are likely the weakest interactions in the molecule, their impact thus becoming evident only at the lowest temperatures; given the significant difference in these angles, it seems reasonable that it could cause a flip in the relative energies of some of the closely-separated, lowest-lying spin states, causing a change in the ground state. In contrast, the MeO^- vs EtO^- difference between **17** and **19** has essentially no impact on the magnetic properties. Finally, none of the compounds exhibited a frequency-dependent drop in the $\chi_M T$ vs. T plot at the lowest temperatures, or an out-of-phase χ_M'' signal, and we conclude that they are not SMMs. The tiny dips in the plots of Figure 6-12 at ~ 2 K are not frequency-dependent, and are likely due to very weak intermolecular interactions.

6.3.4.3 Single-crystal, High-Field EPR Spectroscopy of Complex 16

HF-EPR spectra on a single crystal of representative complex **16**·xDMF were obtained at 51.8 GHz to probe the magnitude and sign of the D value. The spectra revealed a single broad peak throughout the 2.5-20 K range, with no discernible fine structure (Figure 6-13). The position of this peak (1.86 T) corresponds very precisely to the isotropic $g = 2.00(1)$ value. A very faint peak can be seen at ~ 0.93 T, but this corresponds simply to a double quantum ($g = 4.00$) transition, i.e. this peak is observed at exactly half the field of the main peak. Measurements were also carried out at several higher frequencies (Figure 6-14), and these gave

the same conclusions, i.e. the peak positions lie on two straight lines corresponding to $g = 2.000(5)$ and $3.98(3)$. We also carried out angle-dependent studies at 10 K (Figure 6-13a), and these revealed no detectable variation in the position of the 1.86 T peak for 180° of rotation. These combined data suggest that complex **16**·xDMF possesses little or no magnetic anisotropy.

The only slight hint that magnetic anisotropy could be present for **16**·xDMF was obtained upon cooling the sample to 2.5 K (Figure 6-13b), whereupon the main EPR peak became broader and displayed slight asymmetry. This behavior may be indicative of the appearance of unresolved fine-structure caused by weak ZFS.²⁶¹ However, given that it is not possible to resolve any fine-structure splitting, we are unable to make any quantitative statements about either the magnitude of the ground state S value or the axial ZFS parameter (D) for **16**·xDMF on the basis of these EPR measurements.

Overall, the EPR studies suggest that complex **16** is essentially isotropic, i.e. $D \sim 0$. Indeed, on the basis of the EPR linewidth, it is unlikely that the magnitude of D could be greater than 0.05 cm^{-1} . The latter is somewhat different from that obtained from the dc magnetization fit, which was $D = -0.14 (2) \text{ cm}^{-1}$ (assuming the negative value). Of course, the inversion symmetry of the Mn_{13} molecules, and the arrangement of the Mn^{III} JT axes (Figure 6-3) suggest D should indeed be essentially zero. We note three pertinent points: (i) the HF EPR studies were on a single crystal of **16**·xDMF ($x \sim 19$) kept wet with mother liquor, whereas the dc magnetization data were collected on dried samples analyzing as **16**·8DMF·H₂O. It is quite possible that solvent loss could cause some crystal lattice collapse and resulting small perturbations of the Mn_{13} molecules affecting its D value; (ii) the low-lying excited states may be particularly problematic in this case, and the obtained D value thus artificially high; and (iii) bulk magnetization studies are not the most accurate way to determine D , and although there is usually better agreement

between magnetization fits and EPR data, it is possible in this case that the former are particularly unreliable. Points (ii) and (iii) are likely cause-and-effect, and in fact it is very possible that all three points (i)-(iii) are contributing to the difference in D from the magnetization and HFEPR studies in the present work.

6.4 Conclusions

The initial use of the ndc^{2-} dicarboxylate group in Mn chemistry has led to three mixed-valent Mn_{13} clusters containing three different oxidation states of this metal and differing only in the HO^- vs MeO^- vs EtO^- identity of some of the bridging ligands. In addition, a rational and convenient synthesis has been developed for the known benzoate version. This Mn_{13} family has a very interesting core structure, with the Mn_{13} topology comprising a Mn-centered cuboctahedron, or alternatively a fragment of a body-centered cubic lattice. Comparison of the structural parameters of **16-18** reveal that the inflexible ndc^{2-} group imposes only minor structural changes on the cores of **16** and **17** compared with the monocarboxylate benzoate ligation in **18**. Nevertheless, complex **16** has a lower ground state spin of $S = 9/2$ whereas the others have $S = 11/2$ ground states. As expected from the distribution and orientation of the Mn^{III} JT distortion axes, the complexes have little magnetoanisotropy, as reflected in the axial ZFS parameter, D . HFEPR studies on single crystals of the representative complex **16**·xDMF revealed it to be essentially isotropic, a relatively rare situation for such a high nuclearity cluster. As a result, there was no possibility of these compounds functioning as SMMs. Nevertheless, the unusual $\eta^1:\eta^1:\eta^1:\eta^1:\mu_4$ coordination mode adopted by the ndc^{2-} group suggests that it may yet prove a route to many other high nuclearity products, both homo- and heterometallic, and some of these could well be new members of the SMM family. Further studies are thus in progress along these lines.

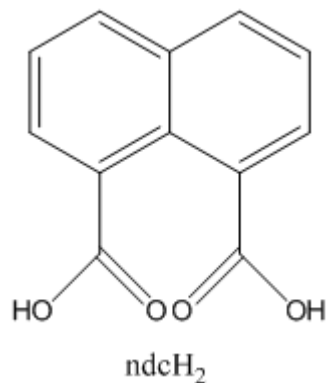


Figure 6-1. Schematic representation of 1,8-naphthalene dicarboxylic acid (ndcH₂)

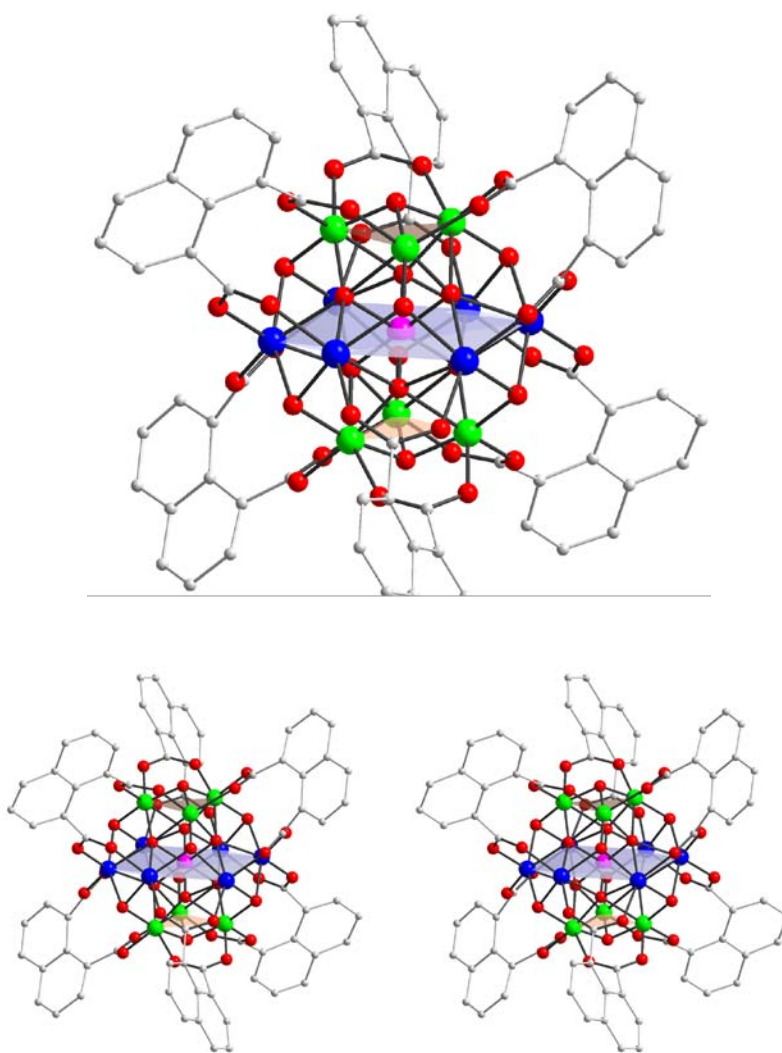


Figure 6-2. The structure and a stereopair of complex **16**. Hydrogen atoms have been omitted for clarity. Color code: Mn^{II} blue, Mn^{III} green, Mn^{IV} purple, O red, C grey.

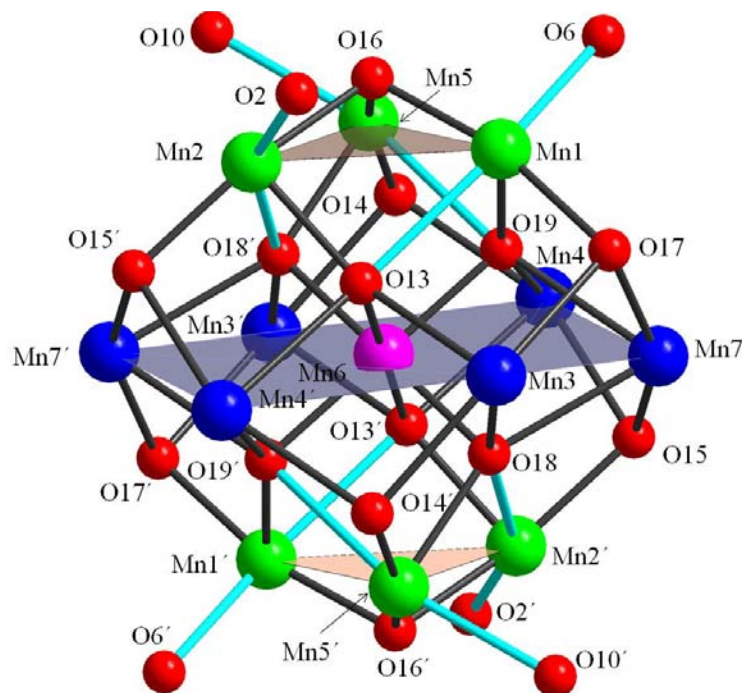


Figure 6-3. Fully labeled core of complex **16**; primed and unprimed atoms are related by the inversion center. The Mn^{III} Jahn-Teller elongation axes are denoted as sky-blue bonds. Color code: Mn^{II} blue, Mn^{III} green, Mn^{IV} purple, O red.

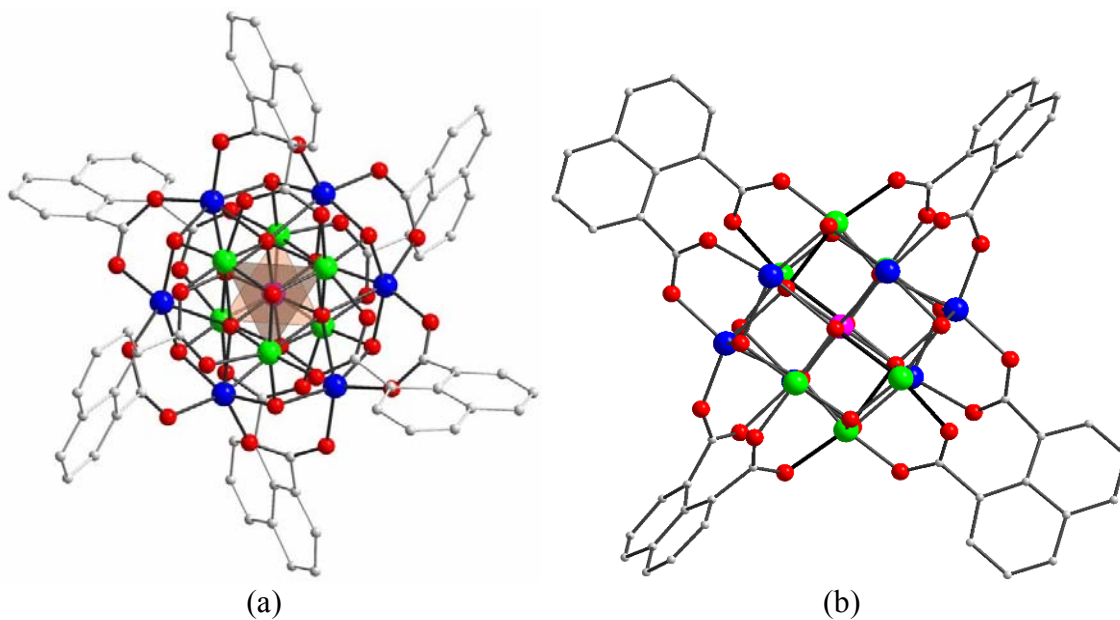


Figure 6-4. Alternate views of complex **16**. (a) View of complex **16** approximately along the virtual S_6 symmetry axis. (b) View approximately perpendicular to two opposite square faces (with their two bridging ndc^{2-} groups removed for clarity) emphasizing the cubic description of the Mn_{13} core.

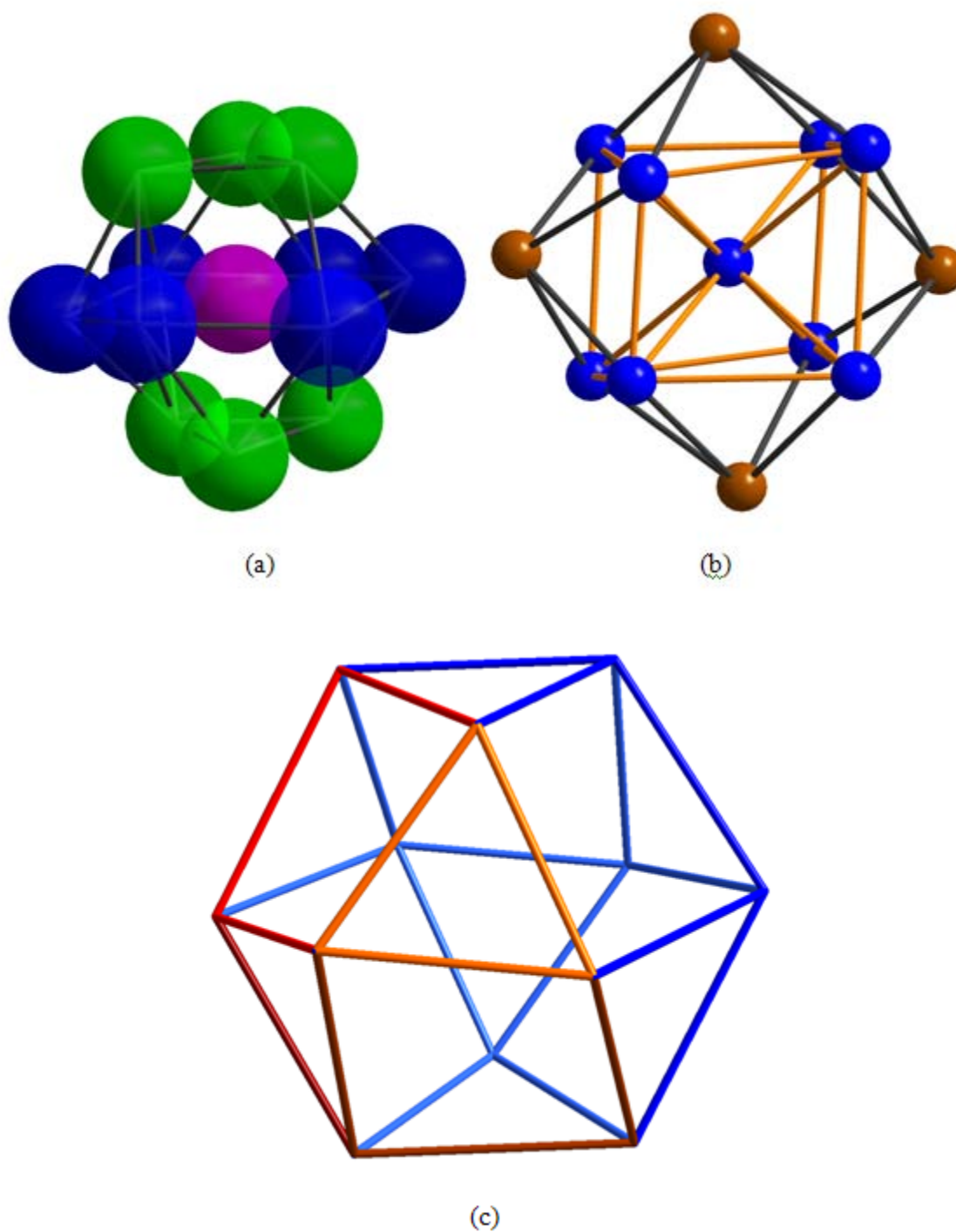


Figure 6-5. Alternate views of the Mn_{13} topology: (a) Mn_3 , Mn_7 , Mn_3 layers, with color code Mn^{IV} purple, Mn^{III} green, Mn^{II} blue; (b) fragment of a body-centered cubic lattice, the brown atoms are the central atoms of neighboring cubic units; (c) the Mn_{12} cuboctahedron, with the Mn^{IV} at the center omitted.

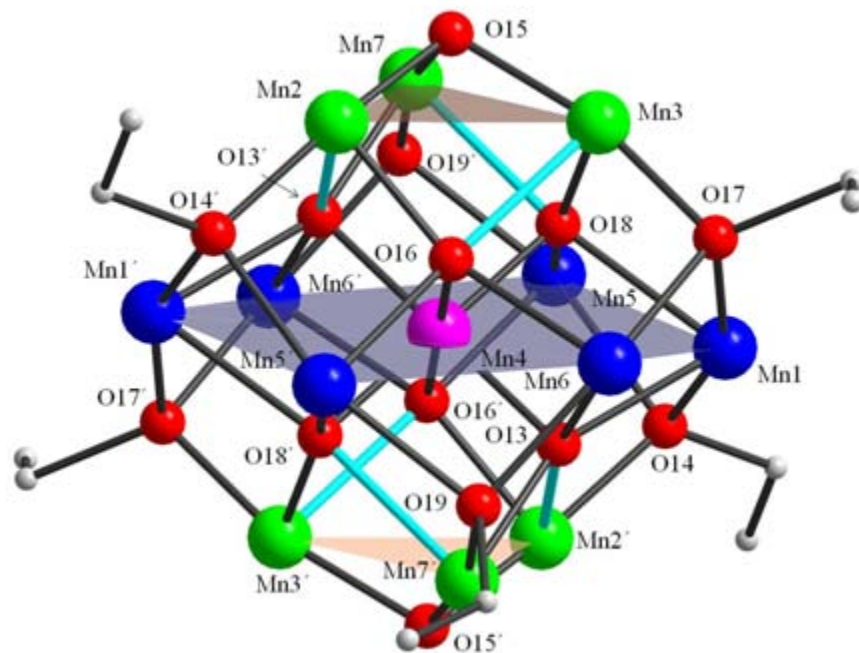


Figure 6-6. The labeled core of complex **17**; the Mn^{III} JT elongation axes are shown as blue bonds. Color code: Mn^{II} blue, Mn^{III} green, Mn^{IV} purple, O red, C grey.

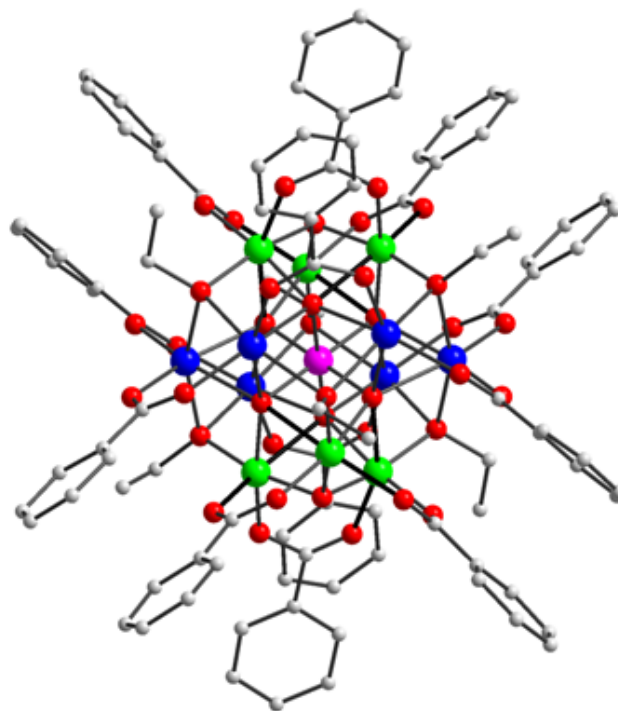


Figure 6-7. The complete molecule of complex **18**; the Mn^{III} JT elongation axes are shown as thicker black bonds. Mn^{II} blue, Mn^{III} green, Mn^{IV} purple, O red, C grey.

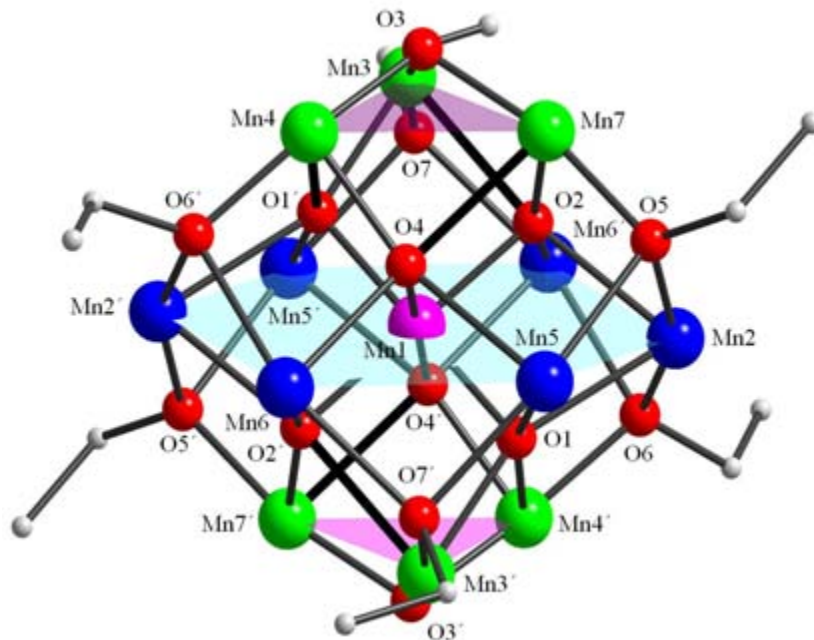


Figure 6-8. Representation of the core of complex **18**. Black solid bonds denote the position of the JT elongations, however half of the elongated axes are shown in the interest of clarity. Color code: Mn^{II} blue, Mn^{III} green, Mn^{IV} purple, O red, C grey.

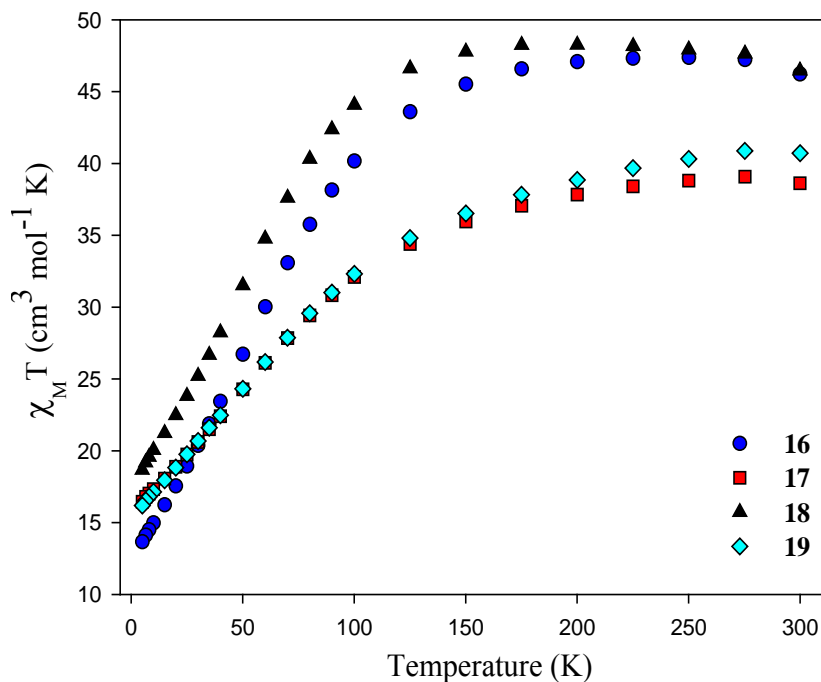


Figure 6-9. $\chi_M T$ vs T plots for complexes **16-19** in the temperature range 5.0-300 K in a 0.1 T applied dc field.

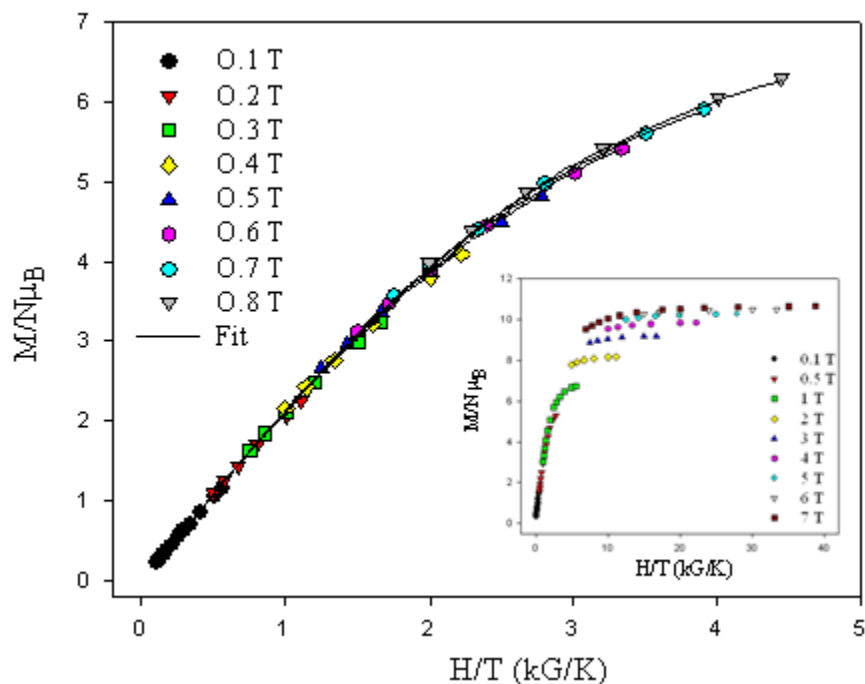


Figure 6-10. Plot of the reduced magnetization, $M/N\mu_B$, vs H/T for complex **16** in the 0.1 – 0.8 T field range. The solid lines are the fit with negative D ; see the text for the fit parameters. The inset displays the plot of the reduced magnetization in the field range 0.1 – 7 T.

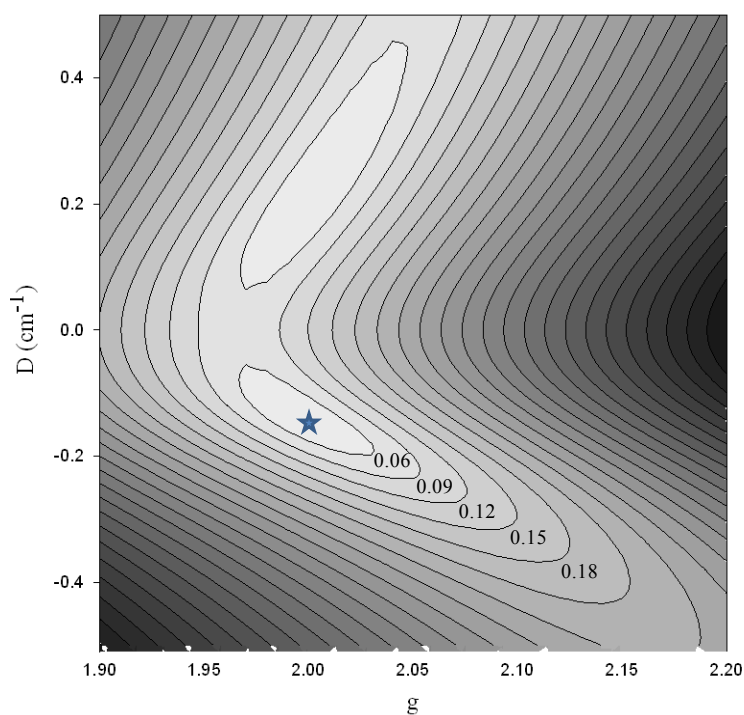


Figure 6-11. Two-dimensional contour plot of the fitting-error surface vs D and g for **16**.

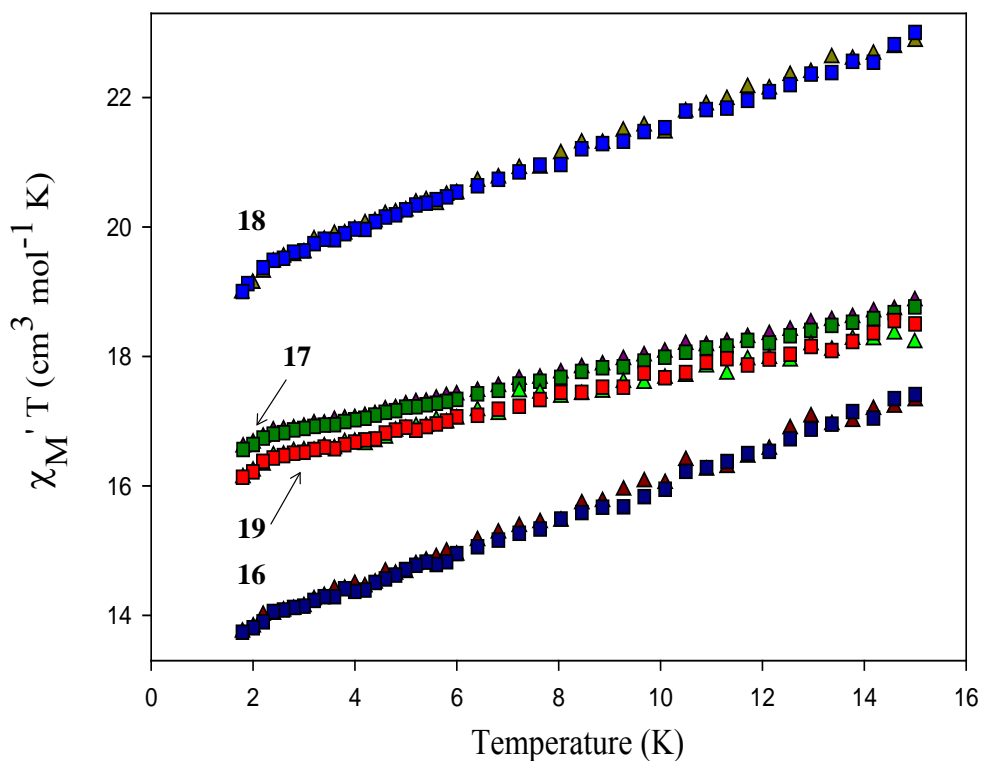


Figure 6-12. Plot of the in-phase (χ_M') ac magnetic susceptibility as $\chi_M' T$ vs T in a 3.5 Oe field oscillating at 250 (\blacktriangle) and 1000 (\blacksquare) Hz for complexes **16-19**.

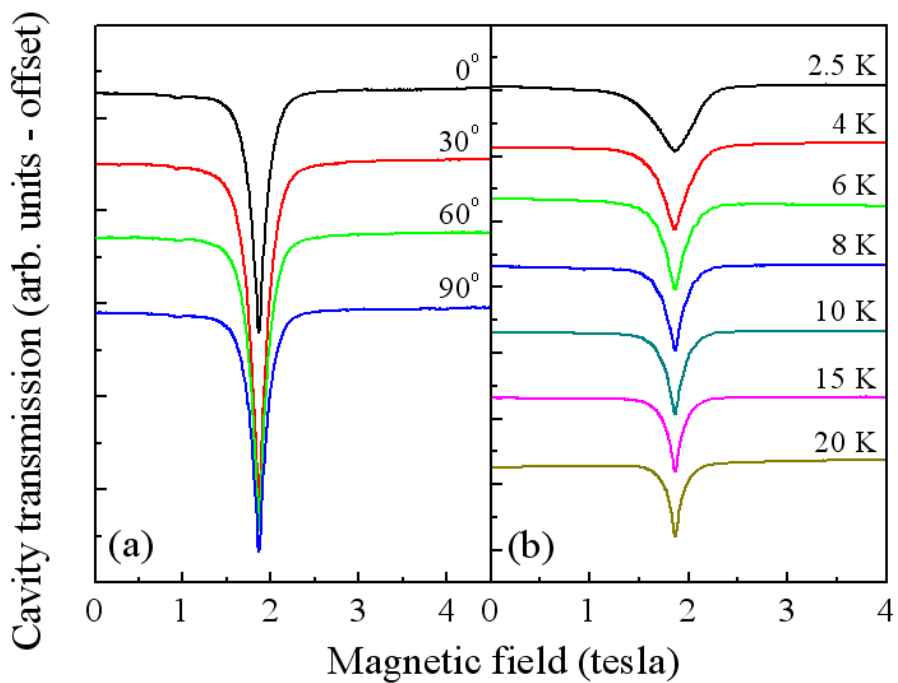


Figure 6-13. High-field EPR data for complex **16**. (a) Angle-dependent EPR spectra obtained at 51.8 GHz and 10 K. (b) Temperature dependence of the EPR spectrum at 51.8 GHz.

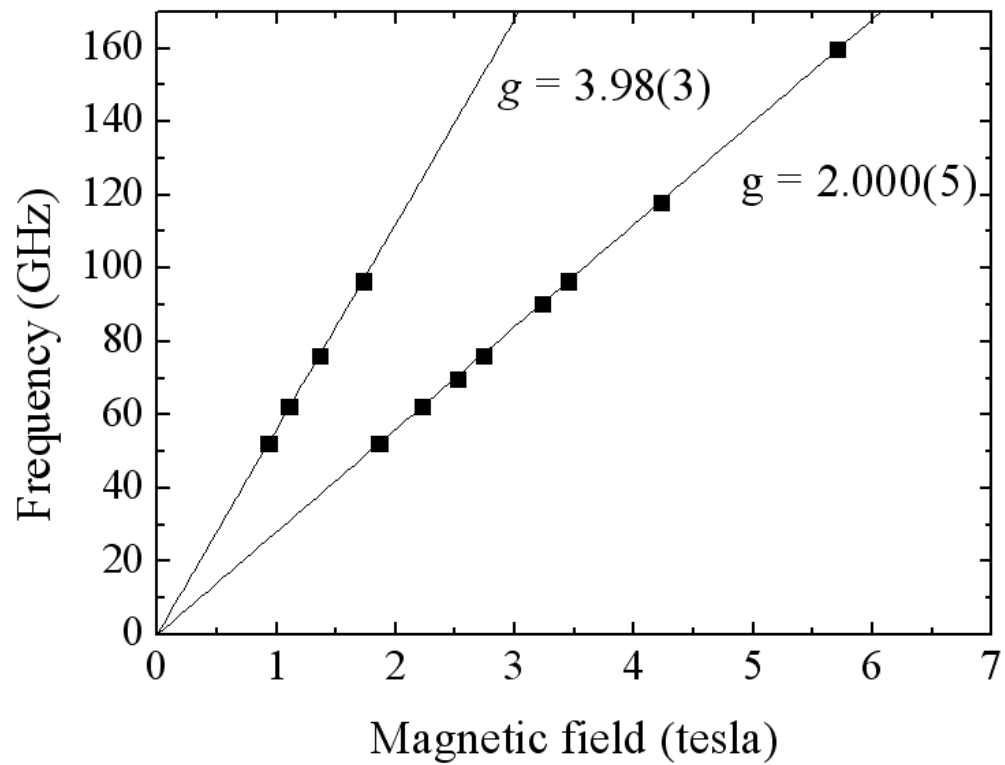


Figure 6-14. Frequency dependence of the EPR spectrum. The solids lines are the fits and the obtained g values.

APPENDIX A
LIST OF COMPOUNDS

- [Mn₁₂O₁₂(O₂CMe)₁₆(H₂O)₄]·2MeCO₂H·4H₂O (1)
- [Mn₁₂O₁₂(O₂CCH₂Br)₁₆(H₂O)₄] (2)
- [Mn₁₂O₁₂(O₂CCH₂Bu^t)₁₆(MeOH)₄]·MeOH (3)
- [Mn₁₂O₁₂(O₂CCH₂Bu^t)₁₆(H₂O)₄]·CH₂Cl₂·CH₃NO₂ (4)
- [Mn₆O₃(N₃)₃(mpko)₆(H₂O)₃](ClO₄)₂ (5)
- [Mn₆O₃(N₃)₅(mpko)₆(H₂O)]·4H₂O (6)
- [Mn₅O₂(OMe)₂(N₃)₃(dapdo)₃(py)₂]·py·MeOH (7)
- [Mn₅O₂(N₃)_{3.5}(O₂CMe)(dapdo)₃(py)_{2.5}](N₃)_{0.5} (8)
- [Ce₆Mn₄O₁₂(O₂CMe)₁₀(NO₃)₄(py)₄]·2py·9MeCN (9)
- [Mn₈CeO₈(O₂CCH₂Bu^t)₁₂(DMF)₁₄]·1.5DMF (10)
- [Ce₂Mn₄O₂(O₂CMe)₆(NO₃)₄(hmp)₄]·H₂O·6MeCN (11)
- [Mn₈O₂(O₂CCH₂Bu^t)₁₄(Bu^tCH₂CO₂H)₄] (12)
- [NEt₃(CH₂Cl)]₂[Mn₃O(hmcH)₃(hmcH₂)₃] (13)
- [MnGd₂O(O₂CPh)₃(O₂CMe)(dapdo)(dapdoH)₂] (14)
- (*n*-Bu₄N)₂[Mn₃O(NCO)₆(O₂CPh)₃]·CH₂Cl₂ (15)
- [Mn₁₃O₈(OH)₆(ndc)₆] (16)
- [Mn₁₃O₈(OEt)₅(OH)(ndc)₆] (17)
- [Mn₁₃O₈(OEt)₆(O₂CPh)₁₂] (18)
- [Mn₁₃O₈(OMe)₆(ndc)₆] (19)

APPENDIX B
VAN VLECK EQUATIONS

p = paramagnetic impurity

$$c = N\mu_B^2 / 3k$$

N = Avogadro's number

g = Lande's factor

k = Boltzmann constant

T = Temperature

TIP = Temperature independent paramagnetism

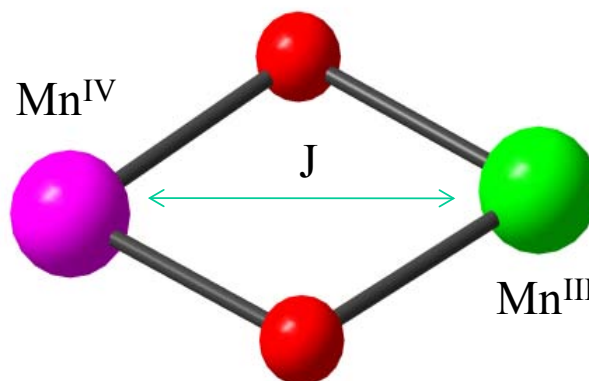


Figure B-1. Dimeric model used to fit the dc magnetic susceptibility of complex **9**.

$$\text{num} = + 1.5000 \cdot \exp(0.7500 \cdot m) + 15.0000 \cdot \exp(3.7500 \cdot m) + 52.5000 \cdot \exp(8.7500 \cdot m) + 126.0000 \cdot \exp(15.7500 \cdot m)$$

$$\text{den} = + 2.0000 \cdot \exp(0.7500 \cdot m) + 4.0000 \cdot \exp(3.7500 \cdot m) + 6.0000 \cdot \exp(8.7500 \cdot m) + 8.0000 \cdot \exp(15.7500 \cdot m)$$

$$m = J1/0.695052552/x$$

$$C = 0.1250415518$$

$$TIP = 300 \times 10^{-6}$$

$$f = (1-p) \cdot (C \cdot g^2)/(x) \cdot \text{num/den} + p \cdot (35 \cdot C \cdot g^2)/(x^4) + TIP$$

$$h = f \cdot T$$

fit h to $\chi_M T$

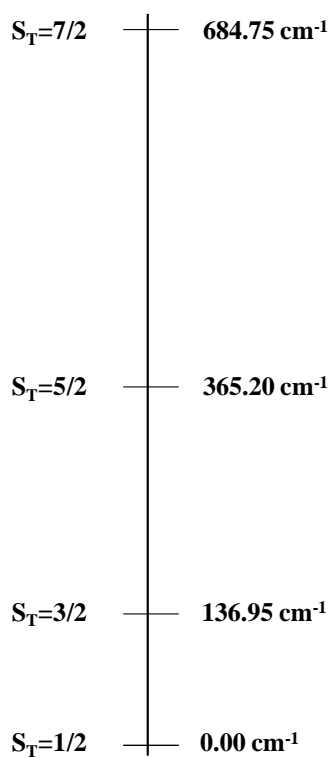


Figure B-2. The ordering of the energy states for each dimer within **9**, using the calculated exchange parameter J , and the Hamiltonian equation. All states were corrected by 34.24 cm^{-1} in order for the ground state to be at 0 cm^{-1} .

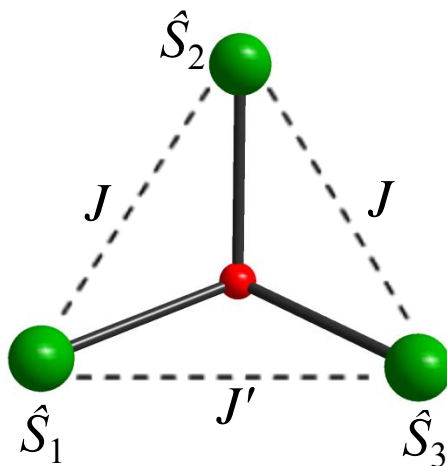


Figure B-3. Triangular model used to fit the dc magnetic susceptibility of complex **13**.

$$\begin{aligned} \text{num} = & + 30.0000 \cdot \exp(6.0000 \cdot m + 0.0000 \cdot n) + 6.0000 \cdot \exp(0.0000 \cdot m + 2.0000 \\ & * n) + 30.0000 \cdot \exp(4.0000 \cdot m + 2.0000 \cdot n) + 84.0000 \cdot \exp(10.0000 \cdot m + 2.0000 \cdot n) + \\ & 0.0000 \cdot \exp(-6.0000 \cdot m + 6.0000 \cdot n) + 6.0000 \cdot \exp(-4.0000 \cdot m + 6.0000 \cdot n) + 30.0000 \\ & * \exp(0.0000 \cdot m + 6.0000 \cdot n) + 84.0000 \cdot \exp(6.0000 \cdot m + 6.0000 \cdot n) + 180.0000 \cdot \exp(\\ & 14.0000 \cdot m + 6.0000 \cdot n) + 6.0000 \cdot \exp(-10.0000 \cdot m + 12.0000 \cdot n) + 30.0000 \cdot \exp(- \\ & 6.0000 \cdot m + 12.0000 \cdot n) + 84.0000 \cdot \exp(0.0000 \cdot m + 12.0000 \cdot n) + 180.0000 \cdot \exp(\\ & 8.0000 \cdot m + 12.0000 \cdot n) + 330.0000 \cdot \exp(18.0000 \cdot m + 12.0000 \cdot n) + 30.0000 \cdot \exp(- \\ & 14.0000 \cdot m + 20.0000 \cdot n) + 84.0000 \cdot \exp(-8.0000 \cdot m + 20.0000 \cdot n) + 180.0000 \cdot \exp(\\ & 0.0000 \cdot m + 20.0000 \cdot n) + 330.0000 \cdot \exp(10.0000 \cdot m + 20.0000 \cdot n) + 546.0000 \cdot \exp(\\ & 22.0000 \cdot m + 20.0000 \cdot n) \end{aligned}$$

$$\begin{aligned} \text{den} = & + 5.0000 \cdot \exp(6.0000 \cdot m + 0.0000 \cdot n) + 3.0000 \cdot \exp(0.0000 \cdot m + 2.0000 \cdot n) + \\ & 5.0000 \cdot \exp(4.0000 \cdot m + 2.0000 \cdot n) + 7.0000 \cdot \exp(10.0000 \cdot m + 2.0000 \cdot n) + 1.0000 \cdot \exp(- \end{aligned}$$

$$\begin{aligned}
& 6.0000 *m+ 6.0000 *n) + 3.0000 *exp(-4.0000 *m+ 6.0000 *n) + 5.0000 *exp(0.0000 *m+ \\
& 6.0000 *n) + 7.0000 *exp(6.0000 *m+ 6.0000 *n) + 9.0000 *exp(14.0000 *m+ 6.0000 *n) + \\
& 3.0000 *exp(-10.0000 *m+ 12.0000 *n) + 5.0000 *exp(-6.0000 *m+ 12.0000 *n) + 7.0000 \\
& *exp(0.0000 *m+ 12.0000 *n) + 9.0000 *exp(8.0000 *m+ 12.0000 *n) + 11.0000 *exp(\\
& 18.0000 *m+ 12.0000 *n) + 5.0000 *exp(-14.0000 *m+ 20.0000 *n) + 7.0000 *exp(-8.0000 \\
& *m+ 20.0000 *n) + 9.0000 *exp(0.0000 *m+ 20.0000 *n) + 11.0000 *exp(10.0000 *m+ \\
& 20.0000 *n) + 13.0000 *exp(22.0000 *m+ 20.0000 *n)
\end{aligned}$$

$$m = J1/0.695052552/x$$

$$n = J2/0.695052552/x$$

$$C = 0.1250415518$$

$$TIP = 400 \times 10^{-6}$$

$$f = (C * g^2) / (x) * num / den + TIP$$

$$h = f * T$$

$$\text{fit } h \text{ to } \chi_M T$$

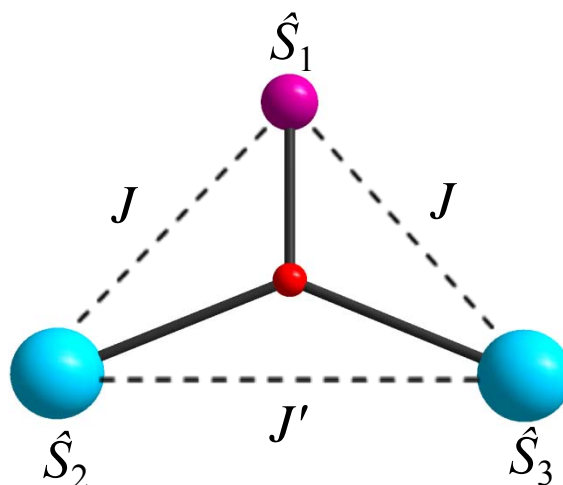


Figure B-4. Triangular model used to fit the dc magnetic susceptibility of complex **14**.

$$\begin{aligned}
 \text{num} = & + 15.0000 * \exp(3.7500 * m + 0.0000 * n) + 1.5000 * \exp(-1.2500 * m + 2.0000 * n) + \\
 & 15.0000 * \exp(1.7500 * m + 2.0000 * n) + 52.5000 * \exp(6.7500 * m + 2.0000 * n) + 1.5000 * \exp(- \\
 & 5.2500 * m + 6.0000 * n) + 15.0000 * \exp(-2.2500 * m + 6.0000 * n) + 52.5000 * \exp(2.7500 * m + \\
 & 6.0000 * n) + 126.0000 * \exp(9.7500 * m + 6.0000 * n) + 15.0000 * \exp(-8.2500 * m + 12.0000 * n) \\
 & + 52.5000 * \exp(-3.2500 * m + 12.0000 * n) + 126.0000 * \exp(3.7500 * m + 12.0000 * n) + \\
 & 247.5000 * \exp(12.7500 * m + 12.0000 * n) + 52.5000 * \exp(-11.2500 * m + 20.0000 * n) + \\
 & 126.0000 * \exp(-4.2500 * m + 20.0000 * n) + 247.5000 * \exp(4.7500 * m + 20.0000 * n) + \\
 & 429.0000 * \exp(15.7500 * m + 20.0000 * n) + 126.0000 * \exp(-14.2500 * m + 30.0000 * n) + \\
 & 247.5000 * \exp(-5.2500 * m + 30.0000 * n) + 429.0000 * \exp(5.7500 * m + 30.0000 * n) + \\
 & 682.5000 * \exp(18.7500 * m + 30.0000 * n) + 247.5000 * \exp(-17.2500 * m + 42.0000 * n) + \\
 & 429.0000 * \exp(-6.2500 * m + 42.0000 * n) + 682.5000 * \exp(6.7500 * m + 42.0000 * n) + \\
 & 1020.0000 * \exp(21.7500 * m + 42.0000 * n) + 429.0000 * \exp(-20.2500 * m + 56.0000 * n) +
 \end{aligned}$$

$$682.5000 * \exp(-7.2500 * m + 56.0000 * n) + 1020.0000 * \exp(7.7500 * m + 56.0000 * n) + 1453.5000 * \exp(24.7500 * m + 56.0000 * n)$$

$$\begin{aligned} \text{den} = & + 4.0000 * \exp(3.7500 * m + 0.0000 * n) + 2.0000 * \exp(-1.2500 * m + 2.0000 * n) + \\ & 4.0000 * \exp(1.7500 * m + 2.0000 * n) + 6.0000 * \exp(6.7500 * m + 2.0000 * n) + 2.0000 * \exp(- \\ & 5.2500 * m + 6.0000 * n) + 4.0000 * \exp(-2.2500 * m + 6.0000 * n) + 6.0000 * \exp(2.7500 * m + \\ & 6.0000 * n) + 8.0000 * \exp(9.7500 * m + 6.0000 * n) + 4.0000 * \exp(-8.2500 * m + 12.0000 * n) + \\ & 6.0000 * \exp(-3.2500 * m + 12.0000 * n) + 8.0000 * \exp(3.7500 * m + 12.0000 * n) + 10.0000 \\ & * \exp(12.7500 * m + 12.0000 * n) + 6.0000 * \exp(-11.2500 * m + 20.0000 * n) + 8.0000 * \exp(- \\ & 4.2500 * m + 20.0000 * n) + 10.0000 * \exp(4.7500 * m + 20.0000 * n) + 12.0000 * \exp(15.7500 \\ & * m + 20.0000 * n) + 8.0000 * \exp(-14.2500 * m + 30.0000 * n) + 10.0000 * \exp(-5.2500 * m + \\ & 30.0000 * n) + 12.0000 * \exp(5.7500 * m + 30.0000 * n) + 14.0000 * \exp(18.7500 * m + 30.0000 \\ & * n) + 10.0000 * \exp(-17.2500 * m + 42.0000 * n) + 12.0000 * \exp(-6.2500 * m + 42.0000 * n) + \\ & 14.0000 * \exp(6.7500 * m + 42.0000 * n) + 16.0000 * \exp(21.7500 * m + 42.0000 * n) + 12.0000 \\ & * \exp(-20.2500 * m + 56.0000 * n) + 14.0000 * \exp(-7.2500 * m + 56.0000 * n) + 16.0000 * \exp(\\ & 7.7500 * m + 56.0000 * n) + 18.0000 * \exp(24.7500 * m + 56.0000 * n) \end{aligned}$$

$$m = J1/0.695052552/x$$

$$n = J2/0.695052552/x$$

$$C = 0.1250415518$$

$$F = (C * g^2)/(x) * \text{num}/\text{den} + \text{TIP}$$

$$\text{TIP} = 900 \times 10^{-6}$$

$$h = f * T$$

$$\text{fit } h \text{ to } \chi_M T$$

APPENDIX C
STRUCTURE AND MAGNETIC PROPERTIES OF COMPLEX 15

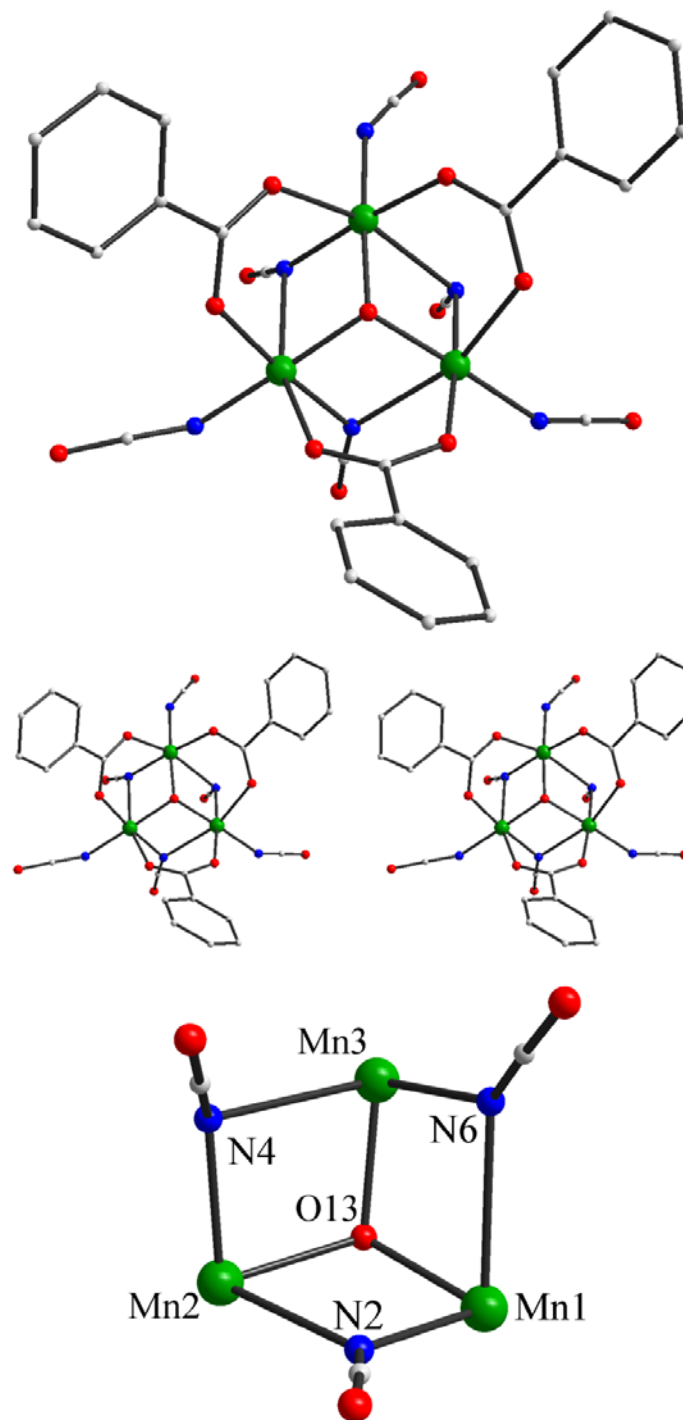


Figure C-1. The structure, a stereopair, and the partially labeled core of complex **15**. Color code: Mn^{III} green, O red, N blue, C grey.

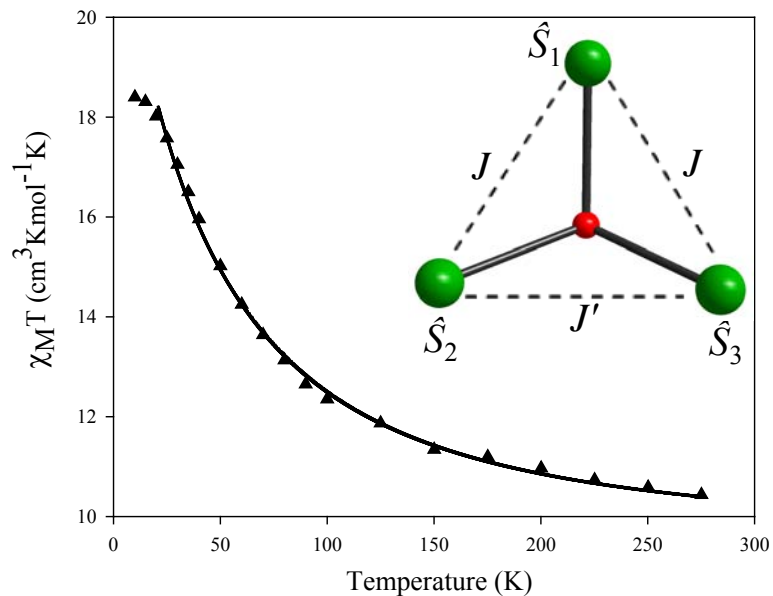


Figure C-2. $\chi_M T$ vs T plot for complex **15** in a 1 kG field. The solid lines are the fit of the data to the theoretical expression; fitting parameters $J = 1.31 \text{ cm}^{-1}$, $J' = 8.26 \text{ cm}^{-1}$, and $g = 1.98$.

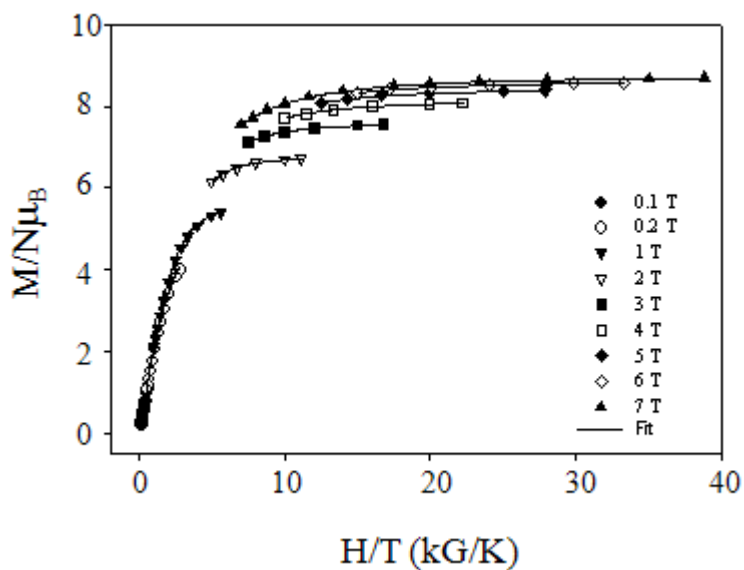


Figure C-3. Plot of the reduced magnetization, $M/N\mu_B$, vs H/T for complex **15** in the 0.1 – 7 T field range. The solid lines are the fit; fitting parameters $S = 6$, $g = 1.87(5)$, and $D = -0.27(3) \text{ cm}^{-1}$.

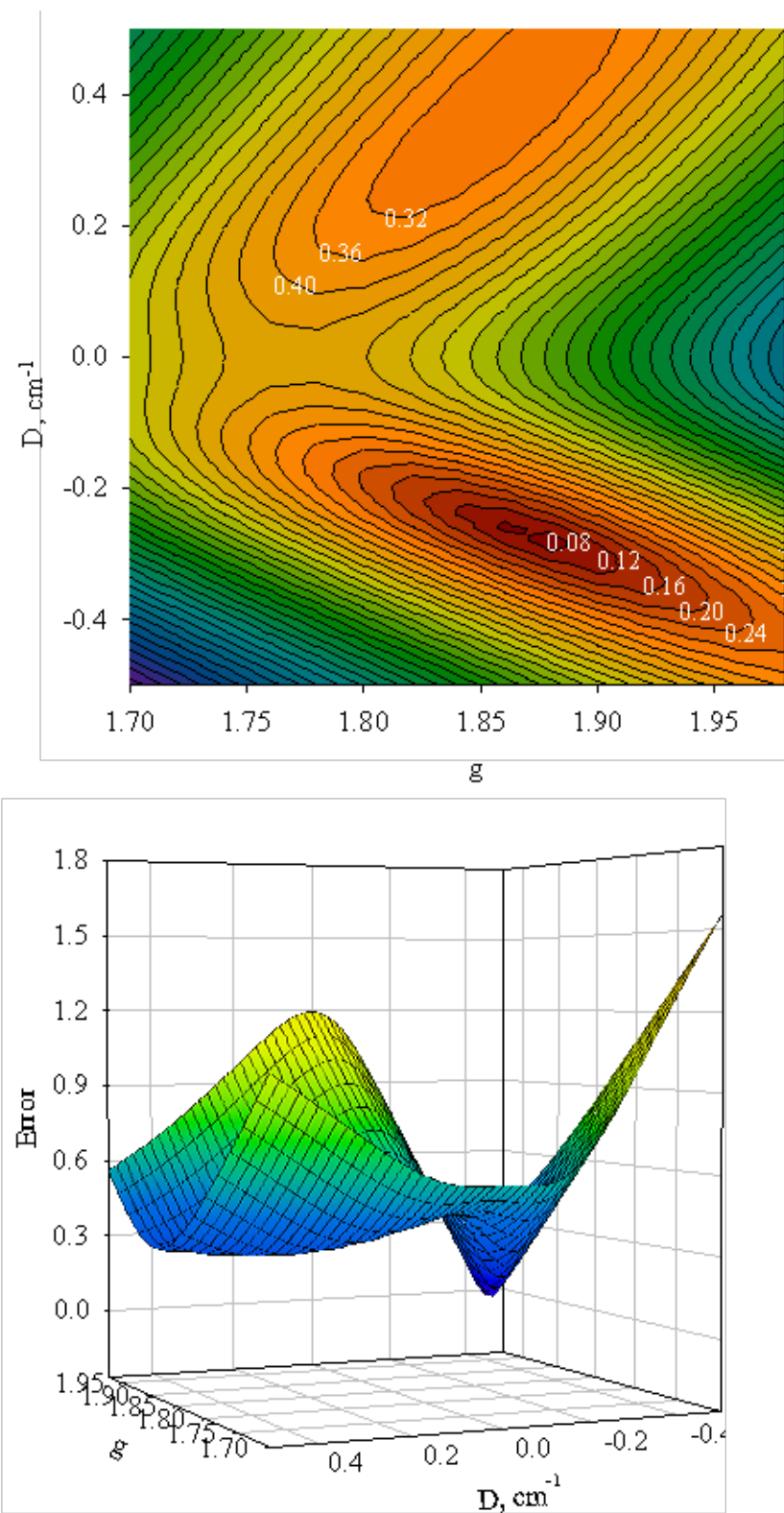


Figure C-4. Representations of the error surface for the D vs g fit of reduced magnetization ($M/N\mu_B$) vs H/T for complex **15** (Figure C-3). Top: two-dimensional contour plot. Bottom: three-dimensional mesh plot.

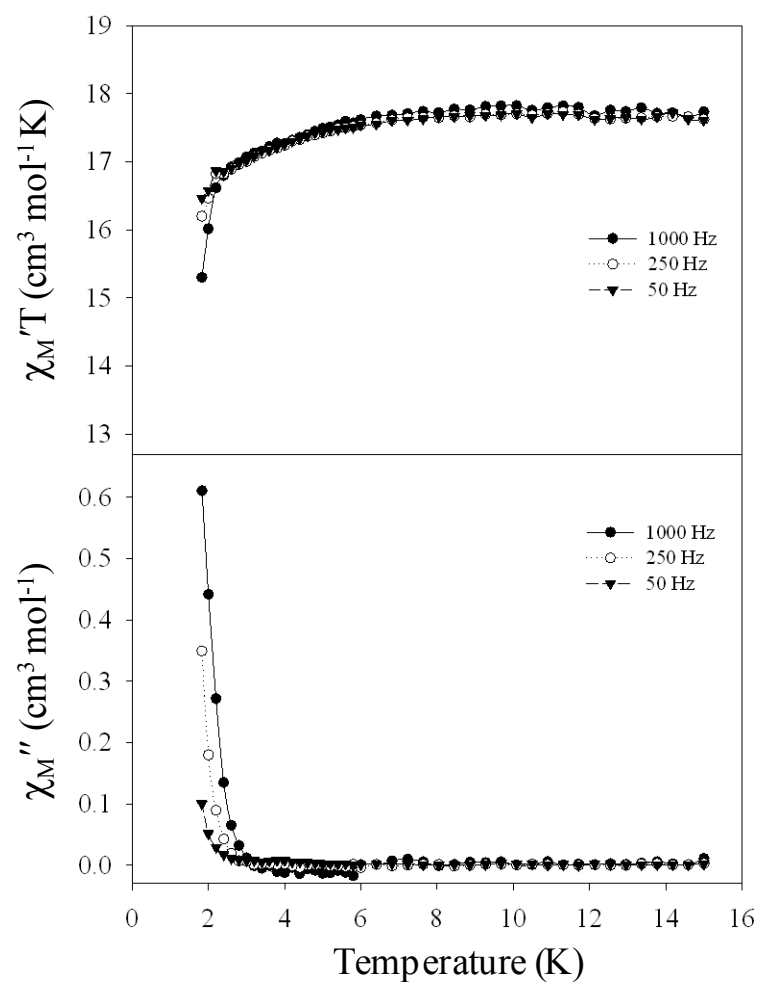


Figure C-5. Plot of the in-phase (χ'_M) (as $\chi'_M T$) and out-of-phase (χ''_M) AC susceptibility signals of complex **15** in a 3.5 G field oscillating at the indicated frequencies.

APPENDIX D
X-RAY CRYSTALLOGRAPHY TABLES

Table D-1. Crystallographic Data for **3**

| Parameter | 3 |
|---|--------------------|
| formula ^a | C101 H192 Mn12 O49 |
| fw, g mol ⁻¹ | 2849.83 |
| space group | <i>I</i> -4 |
| <i>a</i> , Å | 21.5248(6) |
| <i>b</i> , Å | 21.5248(6) |
| <i>c</i> , Å | 15.2323(8) |
| <i>V</i> , Å ³ | 7057.4(5) |
| <i>Z</i> | 2 |
| <i>T</i> , °C | -100(2) |
| radiation, Å ^b | 0.71073 |
| ρ_{calc} , g cm ⁻³ | 1.341 |
| μ , cm ⁻¹ | 11.08 |
| <i>R</i> 1 (<i>wR</i> 2), % ^{c,d} | 3.64 (10.35) |

^a Including solvent molecules. ^b Graphite monochromator. ^c $R1 = \sum ||F_o| - |F_c|| / \sum |F_o|$. ^d $wR2 = [\sum [w(F_o^2 - F_c^2)^2] / \sum [w(F_o^2)^2]]^{1/2}$ where $S = [\sum [w(F_o^2 - F_c^2)^2] / (n-p)]^{1/2}$, $w = 1/[\sigma^2(F_o^2) + (m^*p)^2 + n^*p]$, $p = [\max(F_o^2, 0) + 2^*F_c^2]/3$, and *m* and *n* are constants.

Table D-2. Selected Bond Distances (Å) and Angles (deg) for **3**·MeOH

| Parameter | 3 ·MeOH |
|--|---------------------------------|
| Mn ^{IV} – O _c (ax) | 1.931(2) |
| Mn ^{IV} – O _c (eq) | 1.908(2), 1.907(2) |
| Mn ^{IV} – O _r | 1.874(1), 1.880(2) |
| Mn ^{IV} – O _{ax} | 1.913(2) |
| Mn ^{IIIb} – O _r | 1.895(2), 1.899(2) |
| Mn ^{IIIc} – O _r | 1.882(2), 1.892(2) |
| Mn ^{IIIb} – O _{eq} | 1.956(2), 1.932(2) |
| Mn ^{IIIc} – O _{eq} | 2.118(2), 1.970(2) |
| Mn ^{IIIb} – O _{ax} | 2.166(2), 2.177(2) |
| Mn ^{IIIc} – O _{ax} | 2.118(2) |
| Mn ^{IIIc} – O _M | 2.225(2) |
| O _r – Mn ^{IV} – O _r | 84.97(8) |
| O _r – Mn ^{IIIb} – O _r | 83.84(8) |
| O _r – Mn ^{IIIc} – O _r | 93.62(8) |
| Mn ^{IV} ...Mn ^{IV} | 2.831(1), 2.831(1), 2.928(1) |
| Mn ^{IIIb} ...Mn ^{IIIc} | 3.339(1), 3.425(1) |
| Mn ^{IIIb} ...Mn ^{IV} ...Mn ^{IV} | 178.36(2), 121.18(2), 122.73(2) |
| Mn ^{IIIb} ...Mn ^{IV} | 2.7720(6) |
| Mn ^{IIIc} ...Mn ^{IV} | 3.456(2), 3.467(1) |

^a O_c = cubane O²⁻, O_r = ring O²⁻, O_{ax} = axial carboxylate, O_{eq} = equatorial carboxylate, O_M = methanol. ^b Mn^{III} atom Mn(2). ^c Mn^{III} atom Mn(3).

Table D-3. Crystal Data and Structure Refinement Parameters for Complexes **5-8**.

| Parameter | 5 | 6 ·4H ₂ O | 7 ·py·MeOH | 8 |
|---|---|---|--------------------------------------|---|
| Formula ^a | C ₄₂ H ₅₈ Cl ₂ Mn ₆ N ₂₁ O ₂₅ | C ₄₂ H ₅₀ Mn ₆ N ₂₇ O ₁₄ | C ₄₃ H ₅₃ MnNO | C _{49.5} H _{54.5} Mn ₅ N ₂₆ O ₁₀ |
| fw, g/mol ^a | 1657.63 | 1486.65 | 654.80 | 1448.39 |
| Space group | <i>P</i> $\bar{1}$ | P2 ₁ /n | C2/c | P4(2)/n |
| <i>a</i> , Å | 13.173(3) | 15.3962(4) | 21.381(2) | 24.482(1) |
| <i>b</i> , Å | 15.530(3) | 25.5091(8) | 14.8529(17) | 24.482(1) |
| <i>c</i> , Å | 16.658(4) | 16.2520(4) | 21.326(2) | 19.714(2) |
| α , deg | 85.820(4) | 90 | 90 | 90 |
| β , deg | 75.620(3) | 95.838(2) | 114.746(2) | 90 |
| γ , deg | 80.578(4) | 90 | 90 | 90 |
| <i>V</i> , Å ³ | 3254.7(12) | 6349.76(3) | 6150.5(12) | 11815.7(15) |
| <i>Z</i> | 2 | 4 | 6 | 8 |
| <i>T</i> , K | 173(2) | 173(2) | 173(2) | 173(2) |
| Radiation, Å ^b | 0.71073 | 0.71073 | 0.71073 | 0.71073 |
| ρ_{calc} , g cm ⁻³ | 1.691 | 1.547 | 1.061 | 1.628 |
| μ , mm ⁻¹ | 1.304 | 1.152 | 0.351 | 1.120 |
| R1 ^{c,d} | 0.0955 | 0.0791 | 0.0808 | 0.0654 |
| wR2 ^e | 0.2298 | 0.1343 | 0.2113 | 0.1511 |

^a Including solvate molecules. ^b Graphite monochromator. ^c $I > 2\sigma(I)$. ^d $R1 = 100\sum(|F_o| - |F_c|)/\sum|F_o|$. ^e $wR2 = 100[\sum[w(F_o^2 - F_c^2)^2]/\sum[w(F_o^2)^2]]^{1/2}$, $w = 1/[\sigma^2(F_o^2) + [(ap)^2 + bp]$, where $p = [\max(F_o^2, O) + 2F_c^2]/3$.

Table D-4. Selected bond distances (Å) and angles (°) for complex **5**

| | | | |
|---------|----------|-------------|----------|
| Mn1-O1 | 1.891(9) | Mn5-N12 | 2.047(1) |
| Mn1-O8 | 1.950(1) | Mn5-N13 | 2.055(1) |
| Mn1-O5 | 1.955(1) | Mn5-N7 | 2.273(1) |
| Mn1-N1 | 1.991(1) | Mn5-O12 | 2.280(1) |
| Mn1-O4 | 2.204(1) | Mn6-O2 | 2.133(1) |
| Mn2-O2 | 1.858(9) | Mn6-O3 | 2.165(1) |
| Mn2-O1 | 1.887(9) | Mn6-N18 | 2.195(1) |
| Mn2-N10 | 2.006(1) | Mn6-N20 | 2.201(1) |
| Mn2-N11 | 2.030(1) | Mn6-N21 | 2.285(1) |
| Mn2-O6 | 2.226(1) | Mn6-N19 | 2.320(1) |
| Mn2-N4 | 2.328(1) | Mn1 ... Mn2 | 3.078(3) |
| Mn3-O3 | 1.861(8) | Mn2 ... Mn5 | 3.184(3) |
| Mn3-O9 | 1.898(9) | Mn3 ... Mn4 | 3.162(3) |
| Mn3-N14 | 2.016(1) | Mn4-O1-Mn2 | 125.6(5) |
| Mn3-N15 | 2.044(1) | Mn4-O1-Mn1 | 120.4(5) |
| Mn3-O11 | 2.306(1) | Mn2-O1-Mn1 | 109.1(5) |
| Mn3-N4 | 2.354(1) | Mn2-O2-Mn5 | 117.7(5) |
| Mn4-O3 | 1.830(9) | Mn2-O2-Mn6 | 118.9(4) |
| Mn4-O1 | 1.865(1) | Mn5-O2-Mn6 | 114.2(4) |
| Mn4-N16 | 2.019(1) | Mn4-O3-Mn3 | 117.9(4) |
| Mn4-N17 | 2.033(1) | Mn4-O3-Mn6 | 119.0(4) |
| Mn4-O7 | 2.237(9) | Mn3-O3-Mn6 | 112.3(4) |
| Mn4-N7 | 2.357(1) | Mn2-N4-Mn3 | 117.6(5) |
| Mn5-O2 | 1.862(9) | Mn5-N7-Mn4 | 118.1(5) |
| Mn5-O10 | 1.904(1) | | |

Table D-5. Selected bond distances (Å) and angles (°) for complex **6**

| | | | |
|---------|----------|-------------|----------|
| Mn1-O9 | 2.245(2) | Mn5-O11 | 1.957(2) |
| Mn1-O10 | 1.851(2) | Mn5-O13 | 1.849(2) |
| Mn1-O13 | 1.884(2) | Mn5-O15 | 1.970(2) |
| Mn1-N22 | 2.012(2) | Mn5-O16 | 2.160(2) |
| Mn1-N27 | 2.310(2) | Mn5-N9 | 1.947(2) |
| Mn1-N28 | 2.039(2) | Mn6-O8 | 1.911(2) |
| Mn2-O10 | 2.118(2) | Mn6-O10 | 1.853(2) |
| Mn2-N17 | 2.317(2) | Mn6-N24 | 2.330(2) |
| Mn2-N18 | 2.324(2) | Mn6-N30 | 2.021(2) |
| Mn2-O1 | 2.134(2) | Mn6-N31 | 2.048(2) |
| Mn2-N20 | 2.185(2) | Mn3 ... Mn5 | 3.117(3) |
| Mn3-O13 | 1.886(2) | Mn1 ... Mn6 | 3.176(3) |
| Mn3-O14 | 2.209(2) | Mn1-O10-Mn2 | 119.3(5) |
| Mn3-O1 | 1.849(2) | Mn1-O10-Mn6 | 118.0(5) |
| Mn3-N21 | 2.036(2) | Mn2-O10-Mn6 | 115.3(5) |
| Mn3-O24 | 2.356(2) | Mn2-O1-Mn4 | 111.5(5) |
| Mn3-N26 | 2.017(2) | Mn2-O1-Mn3 | 121.1(5) |
| Mn4-O12 | 1.915(2) | Mn3-O1-Mn4 | 118.8(5) |
| Mn4-O1 | 1.882(2) | Mn1-O13-Mn3 | 122.7(5) |
| Mn4-N27 | 2.315(2) | Mn1-O13-Mn5 | 121.1(5) |
| Mn4-N29 | 2.043(2) | Mn3-O13-Mn5 | 113.1(5) |
| Mn4-N32 | 2.012(2) | Mn1-N27-Mn4 | 119.8(5) |
| Mn4-N1 | 2.209(2) | Mn3-N24-Mn6 | 117.5(5) |

Table D-6. Selected bond distances (Å) and angles (°) for complex **7**

| | | | |
|---------|-----------|-------------|------------|
| Mn1-O2' | 2.213(3) | Mn3-O5 | 1.885(4) |
| Mn1-N4 | 2.253(15) | Mn3-O2 | 2.171(4) |
| Mn1-O5 | 2.260(4) | Mn3-N11 | 2.192(7) |
| Mn1-O2 | 2.260(4) | Mn3-N10 | 2.287(5) |
| Mn1-N2 | 2.276(4) | Mn1 ... Mn3 | 2.962(3) |
| Mn1-N3 | 2.284(5) | Mn1 ... Mn2 | 3.499(3) |
| Mn1-N1 | 2.304(4) | Mn2-O2-Mn3 | 128.96(19) |
| Mn2-O2 | 1.767(4) | Mn2-O2-Mn1' | 122.69(19) |
| Mn2-O3 | 1.891(4) | Mn3-O2-Mn1' | 85.04(12) |
| Mn2-O1 | 1.904(4) | Mn2-O2-Mn1 | 120.99(17) |
| Mn2-O4 | 1.920(4) | Mn3-O2-Mn1 | 83.89(13) |
| Mn2-N7 | 1.990(5) | Mn1'-O2-Mn1 | 105.06(14) |
| Mn2-N6 | 2.116(5) | Mn3-O5-Mn1 | 90.78(15) |

Table D-7. Selected bond distances (Å) and angles (°) for complex **8**

| | | | |
|---------|-----------|-------------|-----------|
| Mn1-O9 | 1.762(7) | Mn3-N4 | 2.285(10) |
| Mn1-O1 | 1.878(9) | Mn4-O8 | 2.103(8) |
| Mn1-O3 | 1.914(8) | Mn4-O9 | 2.208(7) |
| Mn1-O5 | 1.914(8) | Mn4-O10 | 2.222(7) |
| Mn1-N11 | 1.974(9) | Mn4-N8 | 2.275(9) |
| Mn1-N10 | 2.147(10) | Mn4-N7 | 2.305(10) |
| Mn2-O7 | 2.093(8) | Mn4-N9 | 2.316(10) |
| Mn2-O10 | 2.196(7) | Mn4-N17 | 2.366(9) |
| Mn2-O9 | 2.238(7) | Mn5-O10 | 1.745(7) |
| Mn2-N2 | 2.271(10) | Mn5-O4 | 1.871(7) |
| Mn2-N1 | 2.324(11) | Mn5-O6 | 1.899(8) |
| Mn2-N3 | 2.326(10) | Mn5-O2 | 1.906(8) |
| Mn2-N14 | 2.393(10) | Mn5-N22 | 1.98(2) |
| Mn3-N14 | 2.012(12) | Mn5-N20 | 2.156(12) |
| Mn3-N17 | 2.066(9) | Mn2 ... Mn3 | 3.001(2) |
| Mn3-O9 | 2.153(7) | Mn3 ... Mn4 | 3.025(2) |
| Mn3-N5 | 2.209(9) | Mn3-N14-Mn2 | 85.4(3) |
| Mn3-N6 | 2.27(1) | Mn3-N17-Mn4 | 85.8(3) |
| Mn3-O10 | 2.281(7) | | |

Table D-8. Crystal data and structure refinement parameters for complexes **9**, **10**, and **11**.

| | 9 ·py·9MeCN | 10 ·1.5DMF | 11 ·H ₂ O·6MeCN |
|---|---|--|---|
| formula ^a | C ₆₂ H ₇₈ Ce ₆ Mn ₄ N ₁₆ O ₄₄ | C _{88.5} H _{170.5} Ce Mn ₈ N _{5.5} O _{37.5} | C ₄₈ H ₆₂ Ce ₂ Mn ₄ N ₁₄ O ₃₁ |
| Fw, g mol ⁻¹ | 2811.88 | 2491.44 | 1831.12 |
| space group | P2 ₁ /n | <i>P</i> $\bar{1}$ | <i>P</i> $\bar{1}$ |
| a, Å | 14.0419(2) | 17.2684(11) | 11.5998(9) |
| b, Å | 14.3165(2) | 17.5059(11) | 12.0750(9) |
| c, Å | 24.551(3) | 23.2553(14) | 13.1809(1) |
| α , deg | 90 | 79.510(1) | 108.886(1) |
| β , deg | 104.253(2) | 76.190(1) | 104.727(1) |
| γ , deg | 90 | 62.780(1) | 90.137(1) |
| V, Å ³ | 4783.5(9) | 6049.1(7) | 1682.2(2) |
| Z | 2 | 2 | 1 |
| T, K | 173(2) | 173(2) | 173(2) |
| Radiation, Å ^b | 0.71073 | 0.71073 | 0.71073 |
| ρ_{calc} , g cm ⁻³ | 1.952 | 1.368 | 1.808 |
| μ , mm ⁻¹ | 3.394 | 1.247 | 2.149 |
| R1 ^{c, d} | 0.0717 | 0.0370 | 0.0341 |
| wR2 ^e | 0.1795 | 0.0938 | 0.1009 |

^a Including solvate molecules. ^bGraphite monochromator. ^c $I > 2\sigma(I)$. ^d $R1 = 100\Sigma(|F_o| - |F_c|)/\Sigma|F_o|$. ^e $wR2 = 100[\Sigma [w(F_o^2 - F_c^2)^2] / \Sigma [w(F_o^2)^2]]^{1/2}$, $w = 1/[\Sigma^2(F_o^2) + [(ap)^2 + bp]$, where $p = [\max(F_o^2, O) + 2F_c^2]/3$.

Table D-9. Selected bond distances (Å) and angles (°) for complex **9**

| | | | |
|--------------|----------|--------------|----------|
| Ce1 – O9' | 2.139(8) | Ce3 – O10 | 2.402(8) |
| Ce1 – O7 | 2.153(8) | Ce3 – O12 | 2.407(7) |
| Ce1 – O8 | 2.332(8) | Ce3 – O20 | 2.414(9) |
| Ce1 – O5 | 2.427(1) | Mn4 – O12 | 1.879(8) |
| Ce1 – O4 | 2.443(1) | Mn4 – O11 | 1.885(8) |
| Ce1 – O2 | 2.468(1) | Mn4 – O13 | 1.943(9) |
| Ce1 – O1 | 2.475(1) | Mn4 – O17 | 1.954(9) |
| Ce1 – O10' | 2.506(8) | Mn4 – O8 | 2.256(7) |
| Ce1 – N2 | 2.816(2) | Mn4 – N3 | 2.313(1) |
| Ce1 – N1 | 2.880(2) | Mn5 – O11 | 1.835(8) |
| Ce2 – O7' | 2.245(7) | Mn5 – O12 | 1.856(9) |
| Ce2 – O9' | 2.280(8) | Mn5 – O10 | 1.910(8) |
| Ce2 – O8 | 2.340(8) | Mn5 – O15 | 1.948(9) |
| Ce2 – O10 | 2.372(8) | Mn5 – O19 | 1.965(9) |
| Ce2 – O21 | 2.376(8) | Mn5 – N4 | 2.062(1) |
| Ce2 – O14 | 2.383(9) | Ce1 … Ce3 | 3.667(1) |
| Ce2 – O16 | 2.387(9) | Ce1 … Ce2 | 3.673(1) |
| Ce2 – O11 | 2.390(7) | Ce2 … Mn5 | 3.269(2) |
| Ce3 – O7 | 2.251(8) | Ce2 … Mn4 | 3.368(2) |
| Ce3 – O9 | 2.251(7) | Ce2 … Ce3' | 3.628(9) |
| Ce3 – O8 | 2.289(8) | Ce3 … Mn5 | 3.277(2) |
| Ce3 – O22' | 2.382(8) | Ce3 … Mn4 | 3.371(2) |
| Ce3 – O18 | 2.385(9) | Mn4 … Mn5 | 2.809(3) |
| Ce1-O7-Ce2' | 116.7(3) | Mn5-O10-Ce2 | 99.0(3) |
| Ce1-O7-Ce3 | 112.7(3) | Mn4-O12-Ce3 | 103.0(3) |
| Ce2'-O7-Ce3 | 107.6(3) | Mn5-O10-Ce3 | 98.2(3) |
| Mn4-O8-Ce3 | 95.8(3) | Ce2-O10-Ce3 | 105.5(3) |
| Mn4-O8-Ce1 | 145.5(4) | Mn5-O10-Ce1' | 149.4(4) |
| Ce3-O8-Ce1 | 105.0(3) | Ce2-O10-Ce1' | 100.2(3) |
| Mn4-O8-Ce2 | 94.2(3) | Ce3-O10-Ce1' | 99.4(3) |
| Ce3-O8-Ce2 | 110.4(3) | Mn5-O11-Mn4 | 98.0(4) |
| Ce1-O8-Ce2 | 103.7(3) | Mn5-O11-Ce2 | 100.6(3) |
| Ce1'-O9-Ce3 | 117.0(3) | Mn4-O11-Ce2 | 103.4(3) |
| Ce1'-O9-Ce2' | 112.4(3) | Mn5-O12-Mn4 | 97.5(4) |
| Ce3-O9-Ce2' | 106.4(3) | Mn5-O12-Ce3 | 99.7(3) |
| | | Mn4-O12-Ce3 | 103.0(3) |

Symmetry code: ' = 1 -x+1, -y+1, -z

Table D-10. Selected bond distances (Å) and angles (°) for complex **10**

| | | | |
|------------|----------|-------------|----------|
| Ce1 – O1 | 2.336(2) | Mn5 – O5 | 1.875(2) |
| Ce1 – O2 | 2.399(2) | Mn5 – O6 | 1.876(2) |
| Ce1 – O3 | 2.399(2) | Mn5 – O20 | 1.966(2) |
| Ce1 – O4 | 2.320(2) | Mn5 – O21 | 1.976(2) |
| Ce1 – O5 | 2.314(2) | Mn5 – O18 | 2.147(2) |
| Ce1 – O6 | 2.388(2) | Mn5 – O23 | 2.308(2) |
| Ce1 – O7 | 2.389(2) | Mn6 – O6 | 1.876(2) |
| Ce1 – O8 | 2.316(2) | Mn6 – O8 | 1.857(2) |
| Mn1 – O1 | 1.865(2) | Mn6 – O22 | 1.986(2) |
| Mn1 – O2 | 1.867(2) | Mn6 – O25 | 1.983(2) |
| Mn1 – O9 | 1.969(2) | Mn6 – O23 | 2.298(2) |
| Mn1 – O32 | 1.964(2) | Mn6 – O34 | 2.206(2) |
| Mn1 – O11 | 2.371(2) | Mn7 – O7 | 1.876(2) |
| Mn1 – O30 | 2.183(2) | Mn7 – O8 | 1.869(2) |
| Mn2 – O2 | 1.883(2) | Mn7 – O26 | 1.969(2) |
| Mn2 – O4 | 1.858(2) | Mn7 – O27 | 1.973(2) |
| Mn2 – O10 | 1.993(2) | Mn7 – O24 | 2.143(2) |
| Mn2 – O13 | 1.973(2) | Mn7 – O29 | 2.321(2) |
| Mn2 – O11 | 2.240(2) | Mn8 – O1 | 1.857(2) |
| Mn2 – O33 | 2.215(2) | Mn8 – O7 | 1.878(2) |
| Mn3 – O3 | 1.881(2) | Mn8 – O28 | 1.984(2) |
| Mn3 – O4 | 1.856(2) | Mn8 – O31 | 1.988(2) |
| Mn3 – O14 | 1.972(2) | Mn8 – O29 | 2.247(2) |
| Mn3 – O15 | 1.978(2) | Mn8 – O36 | 2.225(2) |
| Mn3 – O12 | 2.165(2) | Mn1 … Mn2 | 3.041(1) |
| Mn3 – O17 | 2.303(2) | Mn1 … Mn8 | 3.229(1) |
| Mn4 – O3 | 1.879(2) | Mn2 … Mn3 | 3.238(1) |
| Mn4 – O5 | 1.857(2) | Mn5 … Mn6 | 3.013(1) |
| Mn4 – O16 | 1.983(2) | Mn7 … Mn8 | 3.008(1) |
| Mn4 – O19 | 1.981(2) | Mn1 … Ce1 | 3.330(1) |
| Mn4 – O17 | 2.289(2) | Mn3 … Ce1 | 3.338(1) |
| Mn4 – O35 | 2.221(2) | Mn5 … Ce1 | 3.323(1) |
| Mn1-O1-Mn8 | 120.4(1) | Mn5-O5-Ce1 | 104.5(1) |
| Mn1-O1-Ce1 | 104.4(1) | Mn6-O6-Mn5 | 106.9(1) |
| Mn8-O1-Ce1 | 106.4(1) | Mn6-O6-Ce1 | 102.9(1) |
| Mn1-O2-Mn2 | 108.3(1) | Mn5-O6-Ce1 | 101.7(1) |
| Mn1-O2-Ce1 | 101.9(1) | Mn7-O7-Mn8 | 106.6(1) |
| Mn2-O2-Ce1 | 102.7(1) | Mn7-O7-Ce1 | 101.6(1) |
| Mn4-O3-Mn3 | 106.8(1) | Mn8-O7-Ce1 | 103.7(1) |
| Mn4-O3-Ce1 | 102.7(1) | Mn6-O8-Mn7 | 121.6(1) |
| Mn3-O3-Ce1 | 101.8(1) | Mn6-O8-Ce1 | 106.3(1) |
| Mn3-O4-Mn2 | 121.3(1) | Mn7-O8-Ce1 | 104.5(1) |
| Mn2-O4-Ce1 | 106.5(1) | Mn2-O11-Mn1 | 82.5(1) |
| Mn3-O4-Ce1 | 105.6(1) | Mn4-O17-Mn3 | 82.2(1) |
| Mn4-O5-Mn5 | 120.7(1) | Mn6-O23-Mn5 | 81.7(1) |

Table D-11. Selected bond distances (Å) and angles (°) for complex **11**

| | | | |
|------------|----------|-------------|------------|
| Ce – O14' | 2.470(2) | Mn2-O11 | 1.927(2) |
| Ce – O15 | 2.153(8) | Mn2-N4 | 2.005(7) |
| Ce – O1 | 2.557(2) | Mn2-O9 | 2.157(3) |
| Ce – O2 | 2.561(3) | Mn2-O13 | 2.329(2) |
| Ce – O1' | 2.563(2) | Mn1 ... Mn2 | 3.1984(7) |
| Ce – O6 | 2.566(2) | Mn2 ... Ce' | 3.5337(5) |
| Ce – O5 | 2.619(2) | | |
| Ce – O3 | 2.628(3) | | |
| Ce – O13 | 2.638(2) | Mn2-O1-Mn1 | 115.62(10) |
| Ce – O12 | 2.716(2) | Mn2-O1-Ce | 113.12(9) |
| Mn1 – O15 | 1.879(2) | Mn1-O1-Ce | 104.94(8) |
| Mn1 – O1 | 1.893(2) | Mn2-O1-Ce' | 104.10(8) |
| Mn1 – O8 | 1.927(2) | Mn1-O1-Ce' | 113.35(9) |
| Mn1 – N3 | 2.039(3) | Ce-O1-Ce' | 105.45(7) |
| Mn1 – O10 | 2.160(2) | Mn1'-O12-Ce | 96.73(8) |
| Mn1 – O12' | 2.274(2) | Mn2-O13-Ce | 97.02(8) |
| Mn2 – O1 | 1.887(2) | Mn2-O14-Ce' | 107.61(9) |
| Mn2 – O14 | 1.888(2) | Mn1-O15-Ce | 107.63(9) |

Symmetry code: ' = -x+1, -y+1, -z

Table D-12. Crystal Data and Structure Refinement Parameters for Complexes **13** and **14**.

| Parameter | 13 | 14 |
|--|--|---|
| Formula ^a | C ₇₀ H ₇₅ Gd ₂ Mn N ₁₉ O ₁₅ | C ₁₄₂ H ₂₀₆ C ₁₁₂ Mn ₆ N ₄ O ₃₈ |
| fw, g/mol ^a | 1791.93 | 3332.15 |
| Space group | I2/a | Cc |
| a, Å | 19.424(2) | 26.380(1) |
| b, Å | 27.132(3) | 29.954(6) |
| c, Å | 30.071(3) | 19.741(4) |
| α, deg | 90 | 90 |
| β, deg | 90.155(2) | 93.560(1) |
| γ, deg | 90 | 90 |
| V, Å ³ | 15848(3) | 15569(5) |
| Z | 8 | 4 |
| T, K | 173(2) | 173(2) |
| Radiation, Å ^b | 0.71073 | 0.71073 |
| ρ _{calc} , g cm ⁻³ | 1.502 | 1.422 |
| μ, mm ⁻¹ | 1.884 | 0.754 |
| R1 ^{c,d} | 0.0887 | 0.0537 |
| wR2 ^e | 0.1976 | 0.1082 |

^a Including solvent molecules. ^b Graphite monochromator. ^c $I > 2\sigma(I)$. ^d $R1 = 100\sum(|F_o| - |F_c|)/\sum|F_o|$. ^e $wR2 = 100[\sum[w(F_o^2 - F_c^2)^2]/\sum[w(F_o^2)^2]]^{1/2}$, $w = 1/[\sigma^2(F_o^2) + [(ap)^2 + bp]$, where $p = [\max(F_o^2, O) + 2F_c^2]/3$.

Table D-13. Selected Core Interatomic Distances (Å) and angles (°) for complex **13**.

| | | | |
|-----------|----------|-----------------|----------|
| Mn1...Mn2 | 3.035(4) | Mn3 – O7 | 1.850(2) |
| Mn1...Mn3 | 3.033(5) | Mn3 – O1 | 1.850(2) |
| Mn2...Mn3 | 3.006(4) | Mn3 – O19 | 1.880(2) |
| Mn1 – O17 | 1.860(2) | Mn3 – O2 | 1.880(2) |
| Mn1 – O16 | 1.900(2) | Mn3 – O11 | 2.210(2) |
| Mn1 – O4 | 1.980(2) | Mn3 – O8 | 2.350(2) |
| Mn1 – O19 | 1.980(2) | | |
| Mn1 – O2 | 2.270(2) | Mn1 – O19 – Mn2 | 104.7(6) |
| Mn1 – O5 | 2.350(2) | Mn2 – O19 – Mn3 | 107.6(6) |
| Mn2 – O19 | 1.850(2) | Mn3 – O19 – Mn1 | 103.6(6) |
| Mn2 – O11 | 1.880(2) | Mn1 – O17 – Mn2 | 92.3(5) |
| Mn2 – O10 | 1.930(2) | Mn2 – O11 – Mn3 | 94.5(5) |
| Mn2 – O13 | 1.970(2) | Mn3 – O2 – Mn1 | 93.4(5) |
| Mn2 – O14 | 2.270(2) | | |
| Mn2 – O17 | 2.330(2) | | |

Table D-14. Selected Core Interatomic Distances (Å) and angles (°) for Complex **14**.

| | | | |
|------------|-----------|----------------|-----------|
| Mn1...Gd1 | 3.358(2) | Mn1...Gd2 | 3.390(2) |
| Gd1 – O1 | 2.309(8) | Gd2 – O1 | 2.317(7) |
| Gd1 – O3 | 2.372(8) | Gd2 – O8 | 2.378(9) |
| Gd1 – O9 | 2.381(10) | Gd2 – O2 | 2.399(10) |
| Gd1 – O5 | 2.474(9) | Gd2 – O10 | 2.504(9) |
| Gd1 – O4 | 2.507(8) | Gd2 – O6 | 2.505(10) |
| Gd1 – N5 | 2.543(9) | Gd2 – N8 | 2.551(9) |
| Gd1 – O11 | 2.560(1) | Gd2 – O7 | 2.565(9) |
| Gd1 – N6 | 2.568(1) | Gd2 – N9 | 2.581(10) |
| Gd1 – N4 | 2.598(8) | Gd2 – N7 | 2.599(9) |
| Mn1 – O1 | 1.724(8) | | |
| Mn1 – N3' | 1.860(2) | Mn1 – O1 – Gd1 | 112.0(4) |
| Mn1 – O14 | 1.903(7) | Mn1 – O1 – Gd2 | 113.2(4) |
| Mn1 – O12 | 1.932(7) | Gd1 – O1 – Gd2 | 134.7(4) |
| Mn1 – N1 | 2.040(1) | N5 – O12 – Mn1 | 112.6(6) |
| Mn1 – O11' | 2.020(2) | N8 – O14 – Mn1 | 114.5(6) |

Table D-15. Crystal Data and Structure Refinement Parameters for Complexes **16-18**.

| Parameter | 16 ·xDMF | 17 ·xMeCN | 18 ·4MeCN |
|---|---|---|---|
| Formula ^a | C ₃₃₀ H ₃₆₀ Mn ₃₉ N ₃₈ O ₁₅₂ | C ₉₁ H ₈₀ Mn ₁₃ N ₄ O ₃₉ | C ₁₀₄ H ₁₀₂ Mn ₁₃ N ₄ O ₃₈ |
| fw, g/mol ^a | 9433.22 | 2567.81 | 2730.12 |
| Space group | $P\bar{1}$ | $P\bar{1}$ | C2/c |
| <i>a</i> , Å | 17.1761(10) | 15.0588(2) | 25.580(3) |
| <i>b</i> , Å | 22.9617(14) | 15.2249(2) | 15.1050(15) |
| <i>c</i> , Å | 24.9168(15) | 15.3862(2) | 28.771(3) |
| α , deg | 74.456(1) | 112.591(2) | 90 |
| β , deg | 85.032(1) | 118.922(2) | 100.315(2) |
| γ , deg | 86.978(1) | 94.82(2) | 90 |
| <i>V</i> , Å ³ | 9427.5(10) | 2687.1(3) | 10937(2) |
| <i>Z</i> | 1 | 1 | 4 |
| <i>T</i> , K | 173(2) | 173(2) | 173(2) |
| Radiation, Å ^b | 0.71073 | 0.71073 | 0.71073 |
| ρ_{calc} , g cm ⁻³ | 1.662 | 1.587 | 1.658 |
| μ , mm ⁻¹ | 1.352 | 1.552 | 1.530 |
| <i>R1</i> ^{c,d} | 0.0628 | 0.0632 | 0.0490 |
| <i>wR2</i> ^e | 0.1718 | 0.1830 | 0.1019 |

^a Including solvate molecules. ^b Graphite monochromator. ^c $I > 2\sigma(I)$. ^d $R1 = 100\Sigma(|F_o| - |F_c|)/\Sigma|F_o|$. ^e $wR2 = 100[\Sigma[w(F_o^2 - F_c^2)^2]/\Sigma[w(F_o^2)^2]]^{1/2}$, $w = 1/[\sigma^2(F_o^2) + [(ap)^2 + bp]$, where $p = [\max(F_o^2, O) + 2F_c^2]/3$.

Table D-16. Selected Core Interatomic Distances (Å) for Complex **16**.^a

| | | | |
|-----------|----------|-----------|----------|
| Mn1···Mn2 | 2.948(2) | Mn2···Mn6 | 3.010(1) |
| Mn1···Mn3 | 3.173(2) | Mn2···Mn7 | 3.187(1) |
| Mn1···Mn5 | 2.949(2) | Mn3···Mn6 | 3.218(1) |
| Mn1···Mn6 | 3.015(1) | Mn4···Mn7 | 3.219(2) |
| Mn2···Mn4 | 3.205(2) | Mn5···Mn6 | 3.026(1) |
| Mn2···Mn5 | 2.941(2) | Mn4-O15 | 2.143(5) |
| Mn1-O16 | 1.860(5) | Mn4-O19 | 2.315(5) |
| Mn1-O17 | 1.912(5) | Mn4-O14 | 2.188(5) |
| Mn1-O19' | 1.950(5) | Mn5-O16' | 1.866(5) |
| Mn1-O13 | 2.330(4) | Mn5-O14 | 1.921(5) |
| Mn2-O13 | 1.960(5) | Mn5-O18 | 1.954(4) |
| Mn2-O16 | 1.890(5) | Mn5-O19 | 2.353(5) |
| Mn2-O15 | 1.921(4) | Mn6-O13 | 1.878(5) |
| Mn2-O18' | 2.339(5) | Mn6-O18 | 1.882(5) |
| Mn3-O18 | 2.318(5) | Mn6-O19 | 1.894(4) |
| Mn3-O12 | 2.126(6) | Mn7-O17' | 2.163(5) |
| Mn3-O14 | 2.179(5) | Mn7-O15 | 2.171(5) |
| Mn3-O17 | 2.202(5) | Mn7-O19 | 2.333(5) |
| Mn3-O13 | 2.300(5) | Mn7-O18' | 2.350(4) |
| Mn4-O13 | 2.391(5) | | |

^a The values are for molecule A of the three independent molecules in the unit cell.

Table D-17. Selected Core Interatomic Distances (Å) for **17**.

| | | | |
|------------|----------|------------|----------|
| Mn1...Mn2 | 3.174(1) | Mn3...Mn6 | 3.197(1) |
| Mn1...Mn4 | 3.188(1) | Mn4...Mn7 | 3.054(1) |
| Mn1...Mn6 | 3.194(1) | Mn5...Mn6 | 3.167(1) |
| Mn2...Mn3 | 2.977(1) | Mn5...Mn7 | 3.147(1) |
| Mn2...Mn4 | 3.064(1) | Mn6...Mn7 | 3.139(1) |
| Mn3...Mn4 | 3.044(1) | Mn4 – O16 | 1.896(4) |
| Mn1 – O14 | 2.165(5) | Mn4 – O13 | 1.896(4) |
| Mn1 – O17' | 2.182(4) | Mn5 – O19 | 2.168(5) |
| Mn1 – O18' | 2.272(5) | Mn5 – O14 | 2.235(4) |
| Mn1 – O13 | 2.291(4) | Mn5 – O16 | 2.285(4) |
| Mn2 – O15 | 1.921(5) | Mn5 – O18' | 2.329(4) |
| Mn2 – O14 | 1.960(4) | Mn6 – O19 | 2.139(5) |
| Mn2 – O13 | 1.992(4) | Mn6 – O17 | 2.182(5) |
| Mn2 – O16 | 2.358(4) | Mn6 – O13' | 2.262(4) |
| Mn3 – O15 | 1.891(4) | Mn6 – O16 | 2.340(4) |
| Mn3 – O17 | 1.915(4) | Mn7 – O19 | 1.898(4) |
| Mn3 – O10' | 1.956(4) | Mn7 – O15' | 1.941(4) |
| Mn3 – O16 | 1.961(4) | Mn7 – O18' | 1.994(5) |
| Mn3 – O18 | 2.357(4) | Mn7 – O13' | 2.373(4) |
| Mn4 – O18' | 1.887(4) | | |

Table D-18. Selected bond distances (Å) and angles (deg) for **18**.

| | | | |
|-----------|----------|------------|----------|
| Mn1 – O1 | 1.911(5) | Mn5 – O5 | 2.199(6) |
| Mn1 – O2 | 1.889(5) | Mn5 – O7 | 2.271(5) |
| Mn1 – O4 | 1.890(5) | Mn5 – O10 | 2.071(6) |
| Mn2 – O1 | 2.237(5) | Mn5 – O18 | 2.051(6) |
| Mn2 – O2 | 2.386(5) | Mn6 – O2 | 2.244(6) |
| Mn2 – O5 | 2.230(5) | Mn6 – O4 | 2.347(6) |
| Mn2 – O6 | 2.225(6) | Mn6 – O6 | 2.227(7) |
| Mn2 – O8 | 2.035(6) | Mn6 – O7 | 2.214(6) |
| Mn2 – O11 | 2.104(6) | Mn6 – O9 | 2.106(6) |
| Mn3 – O1 | 2.379(6) | Mn6 – O19 | 2.081(5) |
| Mn3 – O2 | 1.954(6) | Mn7 – O2 | 2.421(5) |
| Mn3 – O3 | 1.859(5) | Mn7 – O3 | 1.881(5) |
| Mn3 – O7 | 1.899(5) | Mn7 – O4 | 1.980(5) |
| Mn3 – O13 | 2.130(6) | Mn7 – O5 | 1.941(6) |
| Mn3 – O15 | 1.941(6) | Mn7 – O12 | 1.944(6) |
| Mn4 – O1 | 1.976(5) | Mn7 – O16 | 2.102(6) |
| Mn4 – O3 | 1.868(5) | Mn1...Mn3 | 3.054(1) |
| Mn4 – O4 | 2.405(6) | Mn1...Mn4 | 3.069(1) |
| Mn4 – O6 | 1.913(6) | Mn2...Mn6 | 3.219(2) |
| Mn4 – O14 | 2.115(6) | Mn3...Mn4 | 2.949(2) |
| Mn4 – O17 | 1.937(6) | Mn3...Mn7 | 2.955(2) |
| Mn5 – O1 | 2.353(5) | Mn4...Mn2' | 3.159(2) |
| Mn5 – O4 | 2.258(5) | | |

APPENDIX E
BOND VALENCE SUM (BVS) CALCULATIONS

Table E-1. Bond valence sum calculations for the Mn ions for complexes **5** and **6**.^a

| Atom | 5 | | | 6 | | |
|------|------------------|-------------------|------------------|------------------|-------------------|------------------|
| | Mn ^{II} | Mn ^{III} | Mn ^{IV} | Mn ^{II} | Mn ^{III} | Mn ^{IV} |
| Mn1 | 2.90 | <u>2.70</u> | 2.77 | 3.32 | <u>3.12</u> | 3.14 |
| Mn2 | 3.33 | <u>3.13</u> | 3.15 | <u>2.12</u> | 2.01 | 1.99 |
| Mn3 | 3.18 | <u>2.99</u> | 3.01 | 3.31 | <u>3.11</u> | 3.13 |
| Mn4 | 3.37 | <u>3.17</u> | 3.19 | 3.29 | <u>3.11</u> | 3.10 |
| Mn5 | 3.18 | <u>2.99</u> | 3.01 | 3.08 | <u>2.86</u> | 2.93 |
| Mn6 | <u>2.08</u> | 1.97 | 1.95 | 3.32 | <u>3.14</u> | 3.13 |

^a The underlined value is the one closest to the charge for which it was calculated. The oxidation state of a particular atom can be taken as the whole number nearest to the bond value.

Table E-2. Bond valence sum calculations for the Mn ions for complexes **7** and **8**.^a

| Atom | 7 | | | 8 | | |
|------|------------------|-------------------|------------------|------------------|-------------------|------------------|
| | Mn ^{II} | Mn ^{III} | Mn ^{IV} | Mn ^{II} | Mn ^{III} | Mn ^{IV} |
| Mn1 | <u>2.07</u> | 1.96 | 1.95 | 4.24 | 3.94 | <u>4.04</u> |
| Mn2 | 4.22 | 3.92 | <u>4.02</u> | <u>2.10</u> | 1.98 | 1.99 |
| Mn3 | 3.12 | <u>2.91</u> | 2.97 | 2.80 | <u>2.68</u> | 2.62 |
| Mn4 | | | | <u>2.13</u> | 2.01 | 2.01 |
| Mn5 | | | | 4.32 | 4.02 | <u>4.12</u> |

^a The underlined value is the one closest to the charge for which it was calculated. The oxidation state of a particular atom can be taken as the whole number nearest to the bond value.

Table E-3. Bond valence sum calculations and assignments for the Ce and Mn ions in **9**, **10**, and **11**.^a

| | atom | Ce ^{III} | Ce ^{IV} | atom | Mn ^{II} | Mn ^{III} | Mn ^{IV} |
|-----------|------|-------------------|------------------|------|------------------|-------------------|------------------|
| 9 | Ce1 | 4.31 | <u>3.80</u> | Mn4 | 3.79 | <u>2.90</u> | 3.04 |
| | Ce2 | 4.29 | <u>3.78</u> | Mn5 | 3.93 | 3.59 | <u>3.77</u> |
| | Ce3 | 4.30 | <u>3.79</u> | | | | |
| 10 | Ce | 4.33 | <u>3.81</u> | Mn1 | 3.20 | <u>2.93</u> | 3.07 |
| | | | | Mn2 | 3.19 | <u>2.91</u> | 3.06 |
| | | | | Mn3 | 3.22 | <u>2.95</u> | 3.06 |
| | | | | Mn4 | 3.16 | <u>2.89</u> | 3.04 |
| | | | | Mn5 | 3.21 | <u>2.94</u> | 3.09 |
| | | | | Mn6 | 3.17 | <u>2.90</u> | 3.04 |
| | | | | Mn7 | 3.23 | <u>2.95</u> | 3.10 |
| | | | | Mn8 | 3.18 | <u>2.91</u> | 3.05 |
| 11 | Ce | <u>2.99</u> | 2.63 | Mn1 | 3.16 | <u>2.89</u> | 3.04 |
| | | | | Mn2 | 3.17 | <u>2.90</u> | 3.04 |

^a The underlined value is the one closest to the charge for which it was calculated. The oxidation state can be taken as the whole number nearest to the bond value.

Table E-4. Bond valence sum calculations and assignments for the μ_3 -O^a in complexes **9**, and **10**.

| | atom | BVS | Assignment |
|-----------|------|------|-----------------|
| 9 | O7 | 2.01 | O ²⁻ |
| | O9 | 1.98 | O ²⁻ |
| | O11 | 1.83 | O ²⁻ |
| | O12 | 1.78 | O ²⁻ |
| 10 | O1 | 1.91 | O ²⁻ |
| | O2 | 1.78 | O ²⁻ |
| | O3 | 1.76 | O ²⁻ |
| | O4 | 1.95 | O ²⁻ |
| | O5 | 1.93 | O ²⁻ |
| | O6 | 1.79 | O ²⁻ |
| | O7 | 1.79 | O ²⁻ |
| | O8 | 1.93 | O ²⁻ |

^a An O BVS in the ~1.8-2.0, ~1.0-1.2 and ~0.2-0.4 ranges is indicative of non-, single- and double-protonation, respectively.

Table E-5. BVS Calculations for the Mn^a atoms of **13** and **14**.

| Atom | 13 | | | 14 | | |
|------|------------------|-------------------|------------------|------------------|-------------------|------------------|
| | Mn ^{II} | Mn ^{III} | Mn ^{IV} | Mn ^{II} | Mn ^{III} | Mn ^{IV} |
| Mn1 | 3.07 | <u>2.80</u> | 2.94 | 4.13 | 3.86 | <u>3.91</u> |
| Mn2 | 3.23 | <u>2.95</u> | 3.10 | | | |
| Mn3 | 3.58 | <u>3.27</u> | 3.43 | | | |

^a The underlined value is the one closest to the charge for which it was calculated. The oxidation state can be taken as the whole number nearest to the bond value.

Table E-6. Bond valence sum calculations for the Mn ions for complexes **16**, **17** and **18**.^a

| Atom | 16 | | | 17 | | | 18 | | |
|------|------------------|-------------------|------------------|------------------|-------------------|------------------|------------------|-------------------|------------------|
| | Mn ^{II} | Mn ^{III} | Mn ^{IV} | Mn ^{II} | Mn ^{III} | Mn ^{IV} | Mn ^{II} | Mn ^{III} | Mn ^{IV} |
| Mn1 | 3.26 | <u>2.98</u> | 3.13 | <u>1.95</u> | 1.79 | 1.88 | 4.20 | 3.84 | <u>4.03</u> |
| Mn2 | 3.10 | <u>2.84</u> | 2.98 | 2.96 | <u>2.71</u> | 2.84 | <u>1.92</u> | 1.76 | 1.85 |
| Mn3 | <u>1.92</u> | 1.77 | 1.84 | 3.25 | <u>3.01</u> | 3.10 | 3.48 | <u>3.24</u> | 3.31 |
| Mn4 | <u>1.85</u> | 1.69 | 1.78 | 4.25 | 3.90 | <u>4.10</u> | 3.19 | <u>2.92</u> | 3.06 |
| Mn5 | 3.20 | <u>2.93</u> | 3.07 | <u>1.87</u> | 1.71 | 1.79 | <u>1.93</u> | 1.77 | 1.85 |
| Mn6 | 4.34 | 3.97 | <u>4.17</u> | <u>1.99</u> | 1.82 | 1.91 | <u>1.89</u> | 1.73 | 1.82 |
| Mn7 | <u>1.92</u> | 1.76 | 1.85 | 2.99 | <u>2.73</u> | 2.87 | 3.10 | <u>2.83</u> | 2.97 |

^a The underlined value is the one closest to the charge for which it was calculated. The oxidation state of a particular atom can be taken as the whole number nearest to the bond value.

Table E-7. Bond valence sum calculations for the μ_3 -O^a ions for complex **16**.^a

| | BVS | Assignment |
|-----|------|-----------------|
| O14 | 1.17 | OH ⁻ |
| O15 | 1.21 | OH ⁻ |
| O16 | 1.96 | O ²⁻ |
| O17 | 1.19 | OH ⁻ |

^aAn O BVS in the ~1.8-2.0, ~1.0-1.2 and ~0.2-0.4 ranges is indicative of non-, single- and double-protonation, respectively.

LIST OF REFERENCES

- (1) McCartney, S. *ENIAC: The Triumphs and Tragedies of the World's First Computer*; Walker: New York, 1999.
- (2) Moore, G. E. *Electronics* **1965**, 38, 114.
- (3) Lehn, J.-M. *Supramolecular Chemistry. Concepts and Perspectives*; VCH: Weinheim, 1995.
- (4) Miller, J. S.; Epstein, A. J. *MRS Bulletin* **2000**, 25, 21.
- (5) West, A. R.; Wiley: New York, 1984, p 553.
- (6) Kahn, O.; Editor *Magnetism: A Supramolecular Function*, 1996.
- (7) J. E. Huheey, E. A. Keiter, R. L. Keiter *Inorganic Chemistry: Principles of structure and reactivity*; 4th ed.; Harper Collins College: New York, 1993.
- (8) Jiles, D. *Introduction to Magnetism and Magnetic Materials*; Chapman and Hall: New York, 1991.
- (9) Kahn, O. *Molecular Magnetism*; VCH Publishers: New York, 1993.
- (10) West, A. R. *Basic Solid State Chemistry*; Wiley: New York, 1988.
- (11) Miller, J. S.; Epstein, A. J. *Angew. Chem. Int. Ed.* **1994**, 33, 385.
- (12) Epstein, A. J. *MRS Bull.* **2000**, 25, 33.
- (13) E. Grochowski, R. D. H. *IBM Syst. J.* **2003**, 42, 338.
- (14) Balzani, V.; Credi, A.; Venturi, M. In *Stimulating Concepts in Chemistry*; Shibasaki, M., Stoddart, J. F., Vogtle, F., Eds.; Willey-VCH: Weinheim, 2000.
- (15) Gatteschi, D.; Kahn, O.; Miller, J. S.; Palacio, F.; Editors *NATO ASI Series, Ser. E: Applied Sciences, Vol. 198: Magnetic Molecular Materials*, 1991.
- (16) Aubin, S. M. J.; Wemple, M. W.; Adams, D. M.; Tsai, H.-L.; Christou, G.; Hendrickson, D. N. *J. Am. Chem. Soc.* **1996**, 118, 7746.
- (17) Eppley, H. J.; Tsai, H.-L.; de Vries, N.; Folting, K.; Christou, G.; Hendrickson, D. N. *J. Am. Chem. Soc.* **1995**, 117, 301.
- (18) Miller, J. S. *Adv. Mater.* **1994**, 6, 322.
- (19) Wickman, H. H.; Trozzolo, A. M.; Williams, H. J.; Hull, G. W.; Merritt, F. R. *Phys. Rev.* **1967**, 155, 563.

- (20) Miller, J. S.; Calabrese, J. C.; Rommelmann, H.; Chittipeddi, S. R.; Zhang, J. H.; Reiff, W. M.; Epstein, A. J. *J. Am. Chem. Soc.* **1987**, *109*, 769.
- (21) Miller, J. S.; Epstein, A. J.; Reiff, W. M. *Chem. Rev.* **1988**, *88*, 201.
- (22) Kahn, O.; Pei, Y.; Nakatani, K.; Journaux, Y. *Mol. Cryst. Liq. Cryst.* **1989**, *176*, 481.
- (23) Sessoli, R.; Tsai, H. L.; Schake, A. R.; Wang, S.; Vincent, J. B.; Folting, K.; Gatteschi, D.; Christou, G.; Hendrickson, D. N. *J. Am. Chem. Soc.* **1993**, *115*, 1804.
- (24) Sessoli, R.; Gatteschi, D.; Caneschi, A.; Novak, M. A. *Nature* **1993**, *365*, 141.
- (25) Lis, T. *Acta Crystallogr., Sect. B: Struct. Sci* **1980**, *B36*, 2042.
- (26) Christou, G.; Gatteschi, D.; Hendrickson, D. N.; Sessoli, R. *MRS Bull.* **2000**, *25*, 66.
- (27) Aromi, G.; Aubin, S. M. J.; Bolcar, M. A.; Christou, G.; Eppley, H. J.; Folting, K.; Hendrickson, D. N.; Huffman, J. C.; Squire, R. C.; Tsai, H.-L.; Wang, S.; Wemple, M. W. *Polyhedron* **1998**, *17*, 3005.
- (28) Aubin, S. M. J.; Ruiz, D.; Rumberger, E.; Sun, Z.; Albela, B.; Wemple, M. W.; Dilley, N. R.; Ribas, J.; Maple, M. B.; Christou, G.; Hendrickson, D. N. *Mol. Cryst. Liq. Cryst.* **1999**, *335*, 1083.
- (29) Caneschi, A.; Gatteschi, D.; Sessoli, R.; Barra, A. L.; Brunel, L. C.; Guillot, M. *J. Am. Chem. Soc.* **1991**, *113*, 5873.
- (30) Chakov, N., E.; Lee, S.-C.; Harter, A., G.; Kuhns, P., L.; Reyes, A., P.; Hill, S., O.; Dalal, N. S.; Wernsdorfer, W.; Abboud, K., A.; Christou, G. *J. Am. Chem. Soc.* **2006**, *128*, 6975.
- (31) Thomas, L.; Lioni, F.; Ballou, R.; Gatteschi, D.; Sessoli, R.; Barbara, B. *Nature* **1996**, *383*, 145.
- (32) Hendrickson, D. N.; Christou, G.; Ishimoto, H.; Yoo, J.; Brechin, E. K.; Yamaguchi, A.; Rumberger, E. M.; Aubin, S. M. J.; Sun, Z.; Aromi, G. *Polyhedron* **2001**, *20*, 1479.
- (33) Ruiz, D.; Sun, Z.; Aubin, S. M. J.; Rumberger, E.; Incarvito, C.; Folting, K.; Rheingold, A. L.; Christou, G.; Hendrickson, D. N. *Mol. Cryst. Liq. Cryst.* **1999**, *335*, 1125.
- (34) Ruiz, D.; Sun, Z.; Albela, B.; Folting, K.; Ribas, J.; Christou, G.; Hendrickson, D. N. *Angew. Chem. Int. Ed.* **1998**, *37*, 300.
- (35) Barra, A. L.; Debrunner, P.; Gatteschi, D.; Schulz, C. E.; Sessoli, R. *Europhys. Lett.* **1996**, *35*, 133.
- (36) Wernsdorfer, W. *Adv. Chem. Phys.* **2001**, *118*, 99.
- (37) Hill, S.; Edwards, R. S.; Aliaga-Alcalde, N.; Christou, G. *Science (Washington, DC, United States)* **2003**, *302*, 1015.

- (38) Wernsdorfer, W.; Aliaga-Alcalde, N.; Hendrickson David, N.; Christou, G. *Nature* **2002**, *416*, 406.
- (39) Wernsdorfer, W.; Soler, M.; Christou, G.; Hendrickson, D. N. *J. Appl. Phys.* **2002**, *91*, 7164.
- (40) Barra, A. L.; Gatteschi, D.; Sessoli, R. *Phys. Rev. B: Condens. Matter* **1997**, *56*, 8192.
- (41) Caneschi, A.; Ohm, T.; Paulsen, C.; Rovai, D.; Sangregorio, C.; Sessoli, R. *J. Magn. Magn. Mater.* **1998**, *177-181*, 1330.
- (42) Wernsdorfer, W.; Chakov, N. E.; Christou, G. *Phys. Rev. Lett.* **2005**, *95*, 037203/1.
- (43) Leuenberger, M. N.; Loss, D. *Nature* **2001**, *410*, 789.
- (44) Caneschi, A.; Gatteschi, D.; Sangregorio, C.; Sessoli, R.; Sorace, L.; Cornia, A.; Novak, M. A.; Paulsen, C.; Wernsdorfer, W. *J. Magn. Magn. Mater.* **1999**, *200*, 182.
- (45) Awschalom, D. D.; Divincenzo, D. P. *Physics Today* **1995**, *48*, 43.
- (46) Tejada, J.; Chudnovsky, E. M.; del Barco, E.; Hernandez, J. M.; Spiller, T. P. *Nanotechnology* **2001**, *12*, 181.
- (47) Zhong, Y.; Sarachik, M. P.; Friedman, J. R.; Robinson, R. A.; Kelley, T. M.; Nakotte, H.; Christianson, A. C.; Trouw, F.; Aubin, S. M. J.; Hendrickson, D. N. *J. Appl. Phys.* **1999**, *85*, 5636.
- (48) Tsai, H.-L.; Eppley, H. J.; De Vries, N.; Folting, K.; Christou, G.; Hendrickson, D. N. *Molecular Crystals and Liquid Crystals Science and Technology, Section A: Molecular Crystals and Liquid Crystals* **1995**, *274*, 823.
- (49) Christou, G. *Polyhedron* **2005**, *24*, 2065.
- (50) Milios, C. J.; Vinslava, A.; Wernsdorfer, W.; Moggach, S.; Parsons, S.; Perlepes, S. P.; Christou, G.; Brechin, E. K. *J. Am. Chem. Soc.* **2007**, *129*, 2754.
- (51) Milios, C. J.; Vinslava, A.; Wood, P. A.; Parsons, S.; Wernsdorfer, W.; Christou, G.; Perlepes, S. P.; Brechin, E. K. *J. Am. Chem. Soc.* **2007**, *129*, 8.
- (52) Stamatatos, T. C.; Abboud, K. A.; Wernsdorfer, W.; Christou, G. *Angew. Chem. Int. Ed.* **2007**, *46*, 884.
- (53) Stamatatos, T. C.; Foguet-Albiol, D.; Lee, S. C.; Stoumpos, C. C.; Raptopoulou, C. P.; Terzis, A.; Wernsdorfer, W.; Hill, S. O.; Perlepes, S. P.; Christou, G. *J. Am. Chem. Soc.* **2007**, *129*, 9484.
- (54) Stamatatos, T. C.; Foguet-Albiol, D.; Stoumpos, C. C.; Raptopoulou, C. P.; Terzis, A.; Wernsdorfer, W.; Perlepes, S. P.; Christou, G. *Polyhedron* **2007**, 2165.

- (55) Stamatatos Theocharis, C.; Foguet-Albiol, D.; Stoumpos Constantinos, C.; Raptopoulou Catherine, P.; Terzis, A.; Wernsdorfer, W.; Perlepes Spyros, P.; Christou, G. *J. Am. Chem. Soc.* **2005**, *127*, 15380.
- (56) Tasiopoulos, A. J.; Vinslava, A.; Wernsdorfer, W.; Abboud, K. A.; Christou, G. *Angew. Chem. Int. Ed.* **2004**, *43*, 2117.
- (57) Takahashi, S.; Edwards, R. S.; North, J. M.; Hill, S.; Dalal, N. S. *Physical Review B* **2004**, *70*.
- (58) Chudnovsky, E. M.; Garanin, D. A. *Phys. Rev. Lett.* **2001**, 8718.
- (59) Garanin, D. A.; Chudnovsky, E. M. *European Physical Journal B* **2002**, *29*, 3.
- (60) Cornia, A.; Fabretti, A. C.; Sessoli, R.; Sorace, L.; Gatteschi, D.; Barra, A. L.; Daiguebonne, C.; Roisnel, T. *Acta Crystallographica, Section C: Crystal Structure Communications* **2002**, C58, m371.
- (61) Tsai, H. L.; Chen, D. M.; Yang, C. I.; Jwo, T. Y.; Wur, C. S.; Lee, G. H.; Wang, Y. *Inorg. Chem. Commun.* **2001**, *4*, 511.
- (62) An, J.; Chen, Z. D.; Zhang, X. X.; Raubenheimer, H. G.; Esterhuysen, C.; Gao, S.; Xu, G. X. *Journal of the Chemical Society-Dalton Transactions* **2001**, 3352.
- (63) Wernsdorfer, W.; Murugesu, M.; Christou, G. *Physical Review Letters* **2006**, *96*, 057208/1.
- (64) Harter, A. G.; Lampropoulos, C.; Murugesu, M.; Kuhns, P.; Reyes, A.; Christou, G.; Dalal, N. S. *Polyhedron* **2007**, 2320.
- (65) Cornia, A.; Sessoli, R.; Sorace, L.; Gatteschi, D.; Barra, A. L.; Daiguebonne, C. *Phys. Rev. Lett.* **2002**, *89*, 257201/1.
- (66) Soler, M.; Wernsdorfer, W.; Sun, Z.; Huffman, J. C.; Hendrickson, D. N.; Christou, G. *Chemical Communications (Cambridge, United Kingdom)* **2003**, 2672.
- (67) Sun, Z.; Ruiz, D.; Hendrickson, D. N.; Dilley, N. R.; Maple, M. B.; Soler, M.; Folting, K.; Christou, G.; Ribas, J. *Chemical Communications (Cambridge)* **1999**, 1973.
- (68) Davidson, E. R. In *MAGNET*; Indiana University: Bloomington, 1999.
- (69) Davidson, E. R. In *GRID*; Indiana University: Bloomington, 1999.
- (70) Mola, M.; Hill, S.; Goy, P.; Gross, M. *Rev. Sci. Instrum.* **2000**, *71*, 186.
- (71) Takahashi, S.; Hill, S. *Rev. Sci. Instrum.* **2005**, *76*, 10.
- (72) Artus, P.; Boskovic, C.; Yoo, J.; Streib, W. E.; Brunel, L. C.; Hendrickson, D. N.; Christou, G. *Inorg. Chem.* **2001**, *40*, 4199.

- (73) Soler, M.; Artus, P.; Folting, K.; Huffman, J. C.; Hendrickson, D. N.; Christou, G. *Inorg. Chem.* **2001**, *40*, 4902.
- (74) Chakov, N. E.; Abboud, K. A.; Zakharov, L. N.; Rheingold, A. L.; Hendrickson, D. N.; Christou, G. *Polyhedron* **2003**, *22*, 1759.
- (75) Brockman, J. T.; Abboud, K. A.; Hendrickson, D. N.; Christou, G. *Polyhedron* **2003**, *22*, 1765.
- (76) Soler, M.; Wernsdorfer, W.; Abboud, K. A.; Hendrickson, D. N.; Christou, G. *Polyhedron* **2003**, *22*, 1777.
- (77) Soler, M.; Wernsdorfer, W.; Sun, Z.; Ruiz, D.; Huffman, J. C.; Hendrickson, D. N.; Christou, G. *Polyhedron* **2003**, *22*, 1783.
- (78) Soler, M.; Wernsdorfer, W.; Abboud, K. A.; Huffman, J. C.; Davidson, E. R.; Hendrickson, D. N.; Christou, G. *J. Am. Chem. Soc.* **2003**, *125*, 3576.
- (79) Eppley, H. J.; Christou, G.; Law, N. A.; Pecoraro, V. L. *Inorg. Synth.* **2002**, *33*, 61.
- (80) Chakov, N. E.; Soler, M.; Wernsdorfer, W.; Abboud, K. A.; Christou, G. *Inorg. Chem.* **2005**, *44*, 5304.
- (81) Coronado, E.; Forment-Aliaga, A.; Alejandro, G.-A.; Gimenez-Saiz, C.; Romero, F. M.; Wernsdorfer, W. *Angew. Chem. Int. Ed.* **2004**, *43*, 6152.
- (82) Redler, G.; Lampropoulos, C.; Datta, S.; Stamatatos, T. C.; Chakov, N. E.; Hill, S.; Christou, G. *Physical review B*, to be submitted.
- (83) Palenik, G. J. *Inorg. Chem.* **1997**, *36*, 4888.
- (84) Aliaga-Alcalde, N.; Edwards, R. S.; Hill, S. O.; Wernsdorfer, W.; Folting, K.; Christou, G. *J. Am. Chem. Soc.* **2004**, *126*, 12503.
- (85) Chakov, N. E.; Wernsdorfer, W.; Abboud, K. A.; Christou, G. *Inorg. Chem.* **2004**, *43*, 5919.
- (86) Soler, M.; Wernsdorfer, W.; Folting, K.; Pink, M.; Christou, G. *J. Am. Chem. Soc.* **2004**, *126*, 2156.
- (87) Sanudo, E. C.; Wernsdorfer, W.; Abboud, K. A.; Christou, G. *Inorg. Chem.* **2004**, *43*, 4137.
- (88) Murugesu, M.; Habrych, M.; Wernsdorfer, W.; Abboud, K. A.; Christou, G. *J. Am. Chem. Soc.* **2004**, *126*, 4766.
- (89) Brechin, E. K.; Sanudo, E. C.; Wernsdorfer, W.; Boskovic, C.; Yoo, J.; Hendrickson, D. N.; Yamaguchi, A.; Ishimoto, H.; Concolino, T. E.; Rheingold, A. L.; Christou, G. *Inorg. Chem.* **2005**, *44*, 502.

- (90) Aubin, S. M.; Sun, Z.; Eppley, H. J.; Rumberger, E. M.; Guzei, I. A.; Folting, K.; Gantzel, P. K.; Rheingold, A. L.; Christou, G.; Hendrickson, D. N. *Inorg. Chem.* **2001**, *40*, 2127.
- (91) Aubin, S. M. J.; Sun, Z.; Eppley, H. J.; Rumberger, E. M.; Guzei, I. A.; Folting, K.; Gantzel, P. K.; Rheingold, A. L.; Christou, G.; Hendrickson, D. N. *Polyhedron* **2001**, *20*, 1139.
- (92) Aubin, S. M. J.; Sun, Z.; Pardi, L.; Krzystek, J.; Folting, K.; Brunel, L.-C.; Rheingold, A. L.; Christou, G.; Hendrickson, D. N. *Inorg. Chem.* **1999**, *38*, 5329.
- (93) Boskovic, C.; Brechin, E. K.; Streib, W. E.; Folting, K.; Bollinger, J. C.; Hendrickson, D. N.; Christou, G. *J. Am. Chem. Soc.* **2002**, *124*, 3725.
- (94) Novak, M. A.; Sessoli, R. *NATO ASI Series, Series E: Applied Sciences* **1995**, *301*, 171.
- (95) Bian, G. Q.; Kuroda-Sowa, T.; Gunjima, N.; Maekawa, M.; Munakata, M. *Inorg. Chem. Commun.* **2005**, *8*, 208.
- (96) Hill, S.; Perenboom, J.; Dalal, N. S.; Hathaway, T.; Stalcup, T.; Brooks, J. S. *Phys. Rev. Lett.* **1998**, *80*, 2453.
- (97) Hill, S.; Maccagnano, S.; Park, K.; Achey, R. M.; North, J. M.; Dalal, N. S. *Physical Review B* **2002**, *65*.
- (98) Hill, S.; Edwards, R. S.; Jones, S. I.; Dalal, N. S.; North, J. M. *Phys. Rev. Lett.* **2003**, *90*.
- (99) del Barco, E.; Kent, A. D.; Hill, S.; North, J. M.; Dalal, N. S.; Rumberger, E. M.; Hendrickson, D. N.; Chakov, N.; Christou, G. *J. Low Temp. Phys.* **2005**, *140*, 119.
- (100) Perenboom, J.; Brooks, J. S.; Hill, S.; Hathaway, T.; Dalal, N. S. *Physical Review B* **1998**, *58*, 330.
- (101) Hill, S.; Anderson, N.; Wilson, A.; Takahashi, S.; Petukhov, K.; Chakov, N. E.; Murugesu, M.; North, J. M.; del Barco, E.; Kent, A. D.; Dalal, N. S.; Christou, G. *J. Appl. Phys.* **2005**, *97*, 10M50.
- (102) del Barco, E.; Kent, A. D.; Rumberger, E. M.; Hendrickson, D. N.; Christou, G. *Europhys. Lett.* **2002**, *60*, 768.
- (103) Mertes, K. M.; Suzuki, Y.; Sarachik, M. P.; Paltiel, Y.; Shtrikman, H.; Zeldov, E.; Rumberger, E.; Hendrickson, D. N.; Christou, G. *Phys. Rev. Lett.* **2001**, *87*, 227205/1.
- (104) Park, K.; Novotny, M. A.; Dalal, N. S.; Hill, S.; Rikvold, P. A. *Physical Review B* **2002**, *65*.
- (105) Park, K.; Novotny, M. A.; Dalal, N. S.; Hill, S.; Rikvold, P. A. *Physical Review B* **2002**, *66*.

- (106) Parks, B.; Loomis, J.; Rumberger, E.; Hendrickson, D. N.; Christou, G. *Physical Review B: Condensed Matter and Materials Physics* **2001**, *64*, 184426/1.
- (107) Wernsdorfer, W.; Sessoli, R.; Gatteschi, D. *Europhys. Lett.* **1999**, *47*, 254.
- (108) Harter, A. G.; Chakov, N. E.; Achey, R.; Reyes, A.; Kuhns, P.; Christou, G.; Dalal, N. S. *Polyhedron* **2005**, *24*, 2346.
- (109) Kubo, T.; Goto, T.; Koshiha, T.; Takeda, K.; Awaga, K. *Physical Review B* **2002**, *65*, 2244425.
- (110) Lascialfari, A.; Jang, Z. H.; Borsa, F.; Carretta, P.; Gatteschi, D. *Phys. Rev. Lett.* **1998**, *81*, 3773.
- (111) Furukawa, Y.; Watanabe, K.; Kumagai, K.; Borsa, F.; Gatteschi, D. *Physical Review B: Condensed Matter and Materials Physics* **2001**, *64*, 104401/1.
- (112) Morello, A.; Bakharev, O. N.; Brom, H. B.; Sessoli, R.; de Jongh, L. J. *Phys. Rev. Lett.* **2004**, *93*, 197202/1.
- (113) Morello, A.; Bakharev, O. N.; Brom, H. B.; de Jongh, L. J. *Polyhedron* **2003**, *22*, 1745.
- (114) Goto, T.; Kubo, T.; Koshiha, T.; Fujii, Y.; Oyamada, A.; Arai, J.; Takeda, K.; Awaga, K. 2000, p 1227.
- (115) Morello, A.; de Jongh, L. J. *Physical Review B* **2007**, *76*.
- (116) Hennion, M.; Pardi, L.; Mirebeau, I.; Suard, E.; Sessoli, R.; Caneschi, A. *Phys. Rev. B: Condens. Matter* **1997**, *56*, 8819.
- (117) Friedman, J. R.; Sarachik, M. P.; Tejada, J.; Ziolo, R. *Phys. Rev. Lett.* **1996**, *76*, 3830.
- (118) Gomes, A. M.; Novak, M. A.; Sessoli, R.; Caneschi, A.; Gatteschi, D. *Physical Review B: Condensed Matter and Materials Physics* **1998**, *57*, 5021.
- (119) Blinc, R.; Zalar, B.; Gregorovic, A.; Arcon, D.; Kutnjak, Z.; Filipic, C.; Levstik, A.; Achey, R. M.; Dalal, N. S. *Physical Review B* **2003**, *67*, 094401.
- (120) Lampropoulos, C.; Lawrence, J.; Harter, A. G.; Wernsdorfer, W.; Hill, S. O.; Dalal, N. S.; Abboud, K. A.; Christou, G. *J. Am. Chem. Soc.* **2009**, *submitted*.
- (121) Petukhov, K.; Hill, S.; Chakov, N. E.; Abboud, K. A.; Christou, G. *Physical Review B* **2004**, *70*, 054426.
- (122) Datta, S.; Bolin, E.; Milios, C. J.; Brechin, E. K.; Hill, S. *Polyhedron*, *in press*, DOI:10.1016.
- (123) Wang, X. J.; Langetepe, T.; Persau, C.; Kang, B. S.; Sheldrick, G. M.; Fenske, D. *Angewandte Chemie-International Edition* **2002**, *41*, 3818.

- (124) Ferreira, K. N.; Iverson, T. M.; Maghlaoui, K.; Barber, J.; Iwata, S. *Science* **2004**, *303*, 1831.
- (125) Carrell, T. G.; Tyryshkin, A. M.; Dismukes, G. C. *J. Biol. Inorg. Chem.* **2002**, *7*, 2.
- (126) Cinco, R. M.; Rompel, A.; Visser, H.; Aromi, G.; Christou, G.; Sauer, K.; Klein, M. P.; Yachandra, V. K. *Inorg. Chem.* **1999**, *38*, 5988.
- (127) Yachandra, V. K.; Sauer, K.; Klein, M. P. *Chem. Rev.* **1996**, *96*, 2927.
- (128) Law, N. A.; Caudle, M. T.; Pecoraro, V. L. In *Advances in Inorganic Chemistry, Vol 46* 1999; Vol. 46, p 305.
- (129) Yocum, C. F.; Pecoraro, V. L. *Curr. Opin. Chem. Biol.* **1999**, *3*, 182.
- (130) Cinco, R. M.; Holman, K. L. M.; Robblee, J. H.; Yano, J.; Pizarro, S. A.; Bellacchio, E.; Sauer, K.; Yachandra, V. K. *Biochemistry* **2002**, *41*, 12928.
- (131) Loll, B.; Kern, J.; Saenger, W.; Zouni, A.; Biesiadka, J. *Nature* **2005**, *438*, 1040.
- (132) Dau, H.; Liebisch, P.; Haumann, M. *PCCP* **2004**, *6*, 4781.
- (133) Yano, J.; Kern, J.; Sauer, K.; Latimer, M. J.; Pushkar, Y.; Biesiadka, J.; Loll, B.; Saenger, W.; Messinger, J.; Zouni, A.; Yachandra, V. K. *Science* **2006**, *314*, 821.
- (134) Gatteschi, D.; Sessoli, R. *Angew. Chem. Int. Ed.* **2003**, *42*, 268.
- (135) Tsai, H.-L.; Wang, S.; Folting, K.; Streib, W. E.; Hendrickson, D. N.; Christou, G. *J. Am. Chem. Soc.* **1995**, *117*, 2503.
- (136) Bhaduri, S.; Pink, M.; Christou, G. *Chem. Commun.* **2002**, 2352.
- (137) Canada-Vilalta, C.; Pink, M.; Christou, G. *Dalton Transactions* **2003**, 1121.
- (138) Soler, M.; Chandra, S. K.; Davidson, E. R.; Christou, G.; Ruiz, D.; Hendrickson, D. N. *Chem. Commun.* **2000**, 2417.
- (139) Aliaga, N.; Folting, K.; Hendrickson, D. N.; Christou, G. *Polyhedron* **2001**, *20*, 1273.
- (140) Perlepes, S. P.; Huffman, J. C.; Christou, G. *J. Chem. Soc., Chem. Commun.* **1991**, 1657.
- (141) Stamatatos Theocharis, C.; Abboud Khalil, A.; Wernsdorfer, W.; Christou, G. *Angew. Chem. Int. Ed. Eng.* **2006**, *45*, 4134.
- (142) Canada-Vilalta, C.; Huffman, J. C.; Christou, G. *Polyhedron* **2001**, *20*, 1785.
- (143) Harden, N. C.; Bolcar, M. A.; Wernsdorfer, W.; Abboud, K. A.; Streib, W. E.; Christou, G. *Inorg. Chem.* **2003**, *42*, 7067.

- (144) Yoo, J.; Brechin, E. K.; Yamaguchi, A.; Nakano, M.; Huffman, J. C.; Maniero, A. L.; Brunel, L. C.; Awaga, K.; Ishimoto, H.; Christou, G.; Hendrickson, D. N. *Inorg. Chem.* **2000**, *39*, 3615.
- (145) Boskovic, C.; Wernsdorfer, W.; Folting, K.; Huffman, J. C.; Hendrickson, D. N.; Christou, G. *Inorg. Chem.* **2002**, *41*, 5107.
- (146) Yang, E.-C.; Harden, N.; Wernsdorfer, W.; Zakharov, L.; Brechin, E. K.; Rheingold, A. L.; Christou, G.; Hendrickson, D. N. *Polyhedron* **2003**, *22*, 1857.
- (147) Yang, E.-C.; Hendrickson, D. N.; Wernsdorfer, W.; Nakano, M.; Zakharov, L. N.; Sommer, R. D.; Rheingold, A. L.; Ledezma-Gairaud, M.; Christou, G. *J. Appl. Phys.* **2002**, *91*, 7382.
- (148) Stamatatos, T. C.; Luisi, B. S.; Moulton, B.; Christou, G. *Inorg. Chem.* **2008**, *47*, 1134.
- (149) Lampropoulos, C.; Stamatatos, T. C.; Abboud, K. A.; Christou, G. *Inorg. Chem.* **2009**, *48*, 429.
- (150) Glynn, C. W.; Turnbull, M. M. *Transition Met. Chem.* **2002**, *27*, 822.
- (151) Nicholson, G. A.; Lazarus, C. R.; McCormick, B. J. *Inorg. Chem.* **1980**, *19*, 192.
- (152) Vasilevsky, I.; Stenkamp, R. E.; Lingafelter, E. C.; Rose, N. J. *J. Coord. Chem.* **1988**, *19*, 171.
- (153) Orama, M.; Saarinen, H.; Korvenranta, J. *J. Coord. Chem.* **1990**, *22*, 183.
- (154) Squire, R. C.; Aubin, S. M. J.; Folting, K.; Streib, W. E.; Christou, G.; Hendrickson, D. N. *Inorg. Chem.* **1995**, *34*, 6463.
- (155) Vincent, J. B.; Chang, H. R.; Folting, K.; Huffman, J. C.; Christou, G.; Hendrickson, D. N. *J. Am. Chem. Soc.* **1987**, *109*, 5703.
- (156) Wemple, M. W.; Tsai, H.-L.; Wang, S.; Claude, J. P.; Streib, W. E.; Huffman, J. C.; Hendrickson, D. N.; Christou, G. *Inorg. Chem.* **1996**, *35*, 6437.
- (157) Stoumpos, C. C.; Stamatatos, T. C.; Psycharis, V.; Raptopoulou, C. P.; Christou, G.; Perlepes, S. P. *Polyhedron* **2008**, *27*, 3703.
- (158) Stoumpos, C. C.; Stamatatos, T. C.; Sartzi, H.; Roubeau, O.; Tasiopoulos, A. J.; Nastopoulos, V.; Teat, S. J.; Christou, G.; Perlepes, S. P. *Dalton Transactions* **2009**, article asap.
- (159) Stamatatos, T. C.; Abboud, K. A.; Christou, G. *J. Mol. Struct.* **2008**, *890*, 263.
- (160) Papaefstathiou, G. S.; Escuer, A.; Vicente, R.; Font-Bardia, M.; Solans, X.; Perlepes, S. P. *Chem. Commun.* **2001**, 2414.

- (161) Papaefstathiou, G. S.; Perlepes, S. P.; Escuer, A.; Vicente, R.; Font-Bardia, M.; Solans, X. *Angew. Chem. Int. Ed.* **2001**, *40*, 884.
- (162) Ako, A. M.; Hewitt, I. J.; Mereacre, V.; Clerac, R.; Wernsdorfer, W.; Anson, C. E.; Powell, A. K. *Angew. Chem. Int. Ed.* **2006**, *45*, 4926.
- (163) Lampropoulos, C.; Koo, C.; Hill, S. O.; Abboud, K.; Christou, G. *Inorg. Chem.* **2008**, *47*, 11180.
- (164) Wernsdorfer, W.; Sessoli, R. *Science (Washington, D. C.)* **1999**, *284*, 133.
- (165) Oshio, H.; Nihei, M.; Koizumi, S.; Shiga, T.; Nojiri, H.; Nakano, M.; Shirakawa, N.; Akatsu, M. *J. Am. Chem. Soc.* **2005**, *127*, 4568.
- (166) Goodgame, D. M. L.; Williams, D. J.; Winpenny, R. E. P. *Angew. Chem.* **1987**, *99*, 1053.
- (167) Timco, G. A.; Batsanov, A. S.; Larsen, F. K.; Murn, C. A.; Overgaard, J.; Teat, S. J.; Winpenny, R. E. P. *Chemical Communications (Cambridge, United Kingdom)* **2005**, 3649.
- (168) Wernsdorfer, W.; Mailly, D.; Timco, G. A.; Winpenny, R. E. P. *Physical Review B: Condensed Matter and Materials Physics* **2005**, *72*, 060409/1.
- (169) Wang, W. G.; Zhou, A. J.; Zhang, W. X.; Tong, M. L.; Chen, X. M.; Nakano, M.; Beedle, C. C.; Hendrickson, D. N. *J. Am. Chem. Soc.* **2007**, *129*, 1014.
- (170) Murugesu, M.; Mishra, A.; Wernsdorfer, W.; Abboud, K. A.; Christou, G. *Polyhedron* **2006**, *25*, 613.
- (171) Mishra, A.; Wernsdorfer, W.; Abboud, K. A.; Christou, G. *Chemical Communications (Cambridge, United Kingdom)* **2005**, 54.
- (172) Mishra, A.; Wernsdorfer, W.; Abboud, K. A.; Christou, G. *J. Am. Chem. Soc.* **2004**, *126*, 15648.
- (173) Mishra, A.; Tasiopoulos, A. J.; Wernsdorfer, W.; Abboud, K. A.; Christou, G. *Inorg. Chem.* **2007**, *46*, 3105.
- (174) Milios, C. J.; Wood, P. A.; Parsons, S.; Foguet-Albiol, D.; Lampropoulos, C.; Christou, G.; Perlepes, S. P.; Brechin, E. K. *Inorg. Chim. Acta* **2007**, 3932.
- (175) Prasad, T. K.; Rajasekharan, M. V.; Costes, J. P. *Angewandte Chemie-International Edition* **2007**, *46*, 2851.
- (176) Zaleski, C. M.; Kampf, J. W.; Mallah, T.; Kirk, M. L.; Pecoraro, V. L. *Inorg. Chem.* **2007**, *46*, 1954.
- (177) Liu, F. C.; Zeng, Y. F.; Jiao, J.; Li, J. R.; Bu, X. H.; Ribas, J.; Batten, S. R. *Inorg. Chem.* **2006**, *45*, 6129.

- (178) Tasiopoulos, A. J.; Wernsdorfer, W.; Moulton, B.; Zaworotko, M. J.; Christou, G. *J. Am. Chem. Soc.* **2003**, *125*, 15274.
- (179) Tasiopoulos, A. J.; O'Brien, T.; Abboud, K. A.; Christou, G. *Angew. Chem. Int. Ed.* **2004**, *43*, 345.
- (180) Mishra, A.; Tasiopoulos, A. J.; Wernsdorfer, W.; Moushi, E. E.; Moulton, B.; Zaworotko, M. J.; Abboud, K. A.; Christou, G. *Inorg. Chem.* **2008**, *47*, 4832.
- (181) Tasiopoulos, A. J.; Mishra, A.; Christou, G. 2007, p 2183.
- (182) Mishra, A.; Abboud, K. A.; Christou, G. *Inorg. Chem.* **2006**, *45*, 2364.
- (183) Nugent, J. *Biochimica Et Biophysica Acta-Bioenergetics* **2001**, *1503*, 1.
- (184) Manchanda, R.; Brudvig, G. W.; Crabtree, R. H. *Coord. Chem. Rev.* **1995**, *144*, 1.
- (185) Yagi, M.; Kaneko, M. *Chem. Rev.* **2001**, *101*, 21.
- (186) Tasiopoulos, A. J.; Abboud, K. A.; Christou, G. *Chemical Communications (Cambridge, United Kingdom)* **2003**, 580.
- (187) Bhaduri, S.; Tasiopoulos, A. J.; Bolcar, M. A.; Abboud, K. A.; Streib, W. E.; Christou, G. *Inorg. Chem.* **2003**, *42*, 1483.
- (188) Reddy, K. R.; Rajasekharan, M. V.; Padhye, S.; Dahan, F.; Tuchagues, J. P. *Inorg. Chem.* **1994**, *33*, 428.
- (189) Dimitrou, K.; Brown, A. D.; Christou, G.; Concolino, T. E.; Rheingold, A. L. *Chemical Communications (Cambridge, United Kingdom)* **2001**, 1284.
- (190) Snider, B. B. *Chem. Rev.* **1996**, *96*, 339.
- (191) Nair, V.; Mathew, J.; Prabhakaran, J. *Chem. Soc. Rev.* **1997**, *26*, 127.
- (192) Cao, H.; Suib, S. L. *Journal of the American Chemical Society* **1994**, *116*, 5334.
- (193) Arndt, D. *Manganese Compounds as Oxidizing Agents in Organic Chemistry*; Open Court Publishing Company: Illinois, USA, 1981.
- (194) Trovarelli, A. *Catalysis Reviews - Science and Engineering* **1996**, *38*, 439.
- (195) Matatov-Meytal, Y. I.; Sheintuch, M. *Industrial & Engineering Chemistry Research* **1998**, *37*, 309.
- (196) Imamura, S.; Doi, A.; Ishida, S. *Industrial & Engineering Chemistry Product Research and Development* **1985**, *24*, 75.
- (197) Hamoudi, S.; Belkacemi, K.; Larachi, F. *Chemical Engineering Science* **1999**, *54*, 3569.

- (198) Hamoudi, S.; Belkacemi, K.; Sayari, A.; Larachi, F. *Chemical Engineering Science* **2001**, *56*, 1275.
- (199) Ding, Z. Y.; Frisch, M. A.; Li, L.; Gloyna, E. F. *Industrial & Engineering Chemistry Research* **1996**, *35*, 3257.
- (200) Ding, Z. Y.; Li, L.; Wade, D.; Gloyna, E. F. *Industrial & Engineering Chemistry Research* **1998**, *37*, 1707.
- (201) Ruettinger, W.; Dismukes, G. C. *Chemical Reviews (Washington, D. C.)* **1997**, *97*, 1.
- (202) Yagi, M.; Kaneko, M. *Chemical reviews* **2001**, *101*, 21.
- (203) Reddy, K. R.; Rajasekharan, M. V.; Arulsamy, N.; Hodgson, D. J. *Inorg. Chem.* **1996**, *35*, 2283.
- (204) Ott, K. C.; (USA). US, 2006, p 17 pp.
- (205) Qi, G. S.; Yang, R. T. *Chem. Commun.* **2003**, 848.
- (206) Boskovic, C.; Huffman, J. C.; Christou, G. *Chemical Communications (Cambridge, United Kingdom)* **2002**, 2502.
- (207) Lin, X.; Doble, D. M. J.; Blake, A. J.; Harrison, A.; Wilson, C.; Schroeder, M. *J. Am. Chem. Soc.* **2003**, *125*, 9476.
- (208) Mills, A. M.; Ruck, M. *Inorg. Chem.* **2006**, *45*, 5172.
- (209) Snider, B. B. *Chemical Reviews (Washington, D. C.)* **1996**, *96*, 339.
- (210) Liu, W. T.; Thorp, H. H. *Inorg. Chem.* **1993**, *32*, 4102.
- (211) Roulhac, P. L.; Palenik, G. J. *Inorg. Chem.* **2003**, *42*, 118.
- (212) Vleck, J. H. V. *The theory of Electric and Magnetic Susceptibilities*; Oxford University Press: London, 1932.
- (213) O'Connor, C. J. *Progress in Inorganic Chemistry* **1982**, *29*, 203.
- (214) Plaksin, P. M.; Stoufer, R. C.; Mathew, M.; Palenik, G. J. *Journal of the American Chemical Society* **1972**, *94*, 2121.
- (215) Lippard, S. J.; Editor *Progress in Inorganic Chemistry, Vol. 38: Bioinorganic Chemistry*, 1990.
- (216) Canada-Vilalta, C.; Streib, W. E.; Huffman, J. C.; O'Brien, T. A.; Davidson, E. R.; Christou, G. *Inorganic Chemistry* **2004**, *43*, 101.
- (217) Kambe, K. *J. Phys. Soc. Jpn.* **1950**, *5*, 48.

- (218) Winpenny, R. E. P. In *Comprehensive Coordination Chemistry II*; McCleverty, J. A., M., T. J., E., Eds.; Elsevier: Amsterdam, 2004; Vol. 7, p 125.
- (219) Osa, S.; Kido, T.; Matsumoto, N.; Re, N.; Pochaba, A.; Mrozinski, J. *J. Am. Chem. Soc.* **2004**, *126*, 420.
- (220) Mereacre, V. M.; Ako, A. M.; Clerac, R.; Wernsdorfer, W.; Filoti, G.; Bartolome, J.; Anson, C. E.; Powell, A. K. *J. Am. Chem. Soc.* **2007**, *129*, 9248.
- (221) Mereacre, V.; Ako, A. M.; Clerac, R.; Wernsdorfer, W.; Hewitt, I. J.; Anson, C. E.; Powell, A. K. *Chemistry-a European Journal* **2008**, *14*, 3577.
- (222) Zaleski, C. M.; Depperman, E. C.; Kampf, J. W.; Kirk, M. L.; Pecoraro, V. L. *Angewandte Chemie-International Edition* **2004**, *43*, 3912.
- (223) Cotton, F. A.; Wilkinson, G.; Bochmann, M.; Murillo, C. *Advanced Inorganic Chemistry, 6th Edition*; Wiley: Chichester, 1998.
- (224) Panagiotopoulos, A.; Zafiroopoulos, T. F.; Perlepes, S. P.; Bakalbassis, E.; Masson-Ramade, I.; Kahn, O.; Terzis, A.; Raptopoulou, C. P. *Inorg. Chem.* **1995**, *34*, 4918.
- (225) Toulouse, G. *Communications on Physics* **1977**, *2*, 115.
- (226) Kahn, O. *Chem. Phys. Lett.* **1997**, *265*, 109.
- (227) Cano, J.; Cauchy, T.; Ruiz, E.; Milios, C. J.; Stoumpos, C. C.; Stamatatos, T. C.; Perlepes, S. P.; Christou, G.; Brechin, E. K. *Dalton Transactions* **2008**, 234.
- (228) Vinslava, A., University of Florida, 2006.
- (229) Khanra, S.; Weyhermuller, T.; Chaudhuri, P. *Dalton Transactions* **2008**, 4885.
- (230) Lampropoulos, C.; Vinslava, A.; Abboud, K. A.; Christou, G. *Inorg. Chem.* **2009**, *to be submitted*.
- (231) Bruker-AXS Madison, WI, 2000.
- (232) Brechin, E. K. *Chemical Communications (Cambridge, United Kingdom)* **2005**, 5141.
- (233) Murugesu, M.; Wernsdorfer, W.; Abboud, K. A.; Christou, G. *Polyhedron* **2005**, *24*, 2894.
- (234) Stamatatos, T. C.; Foguet-Albiol, D.; Perlepes, S. P.; Raptopoulou, C. P.; Terzis, A.; Patrickios, C. S.; Christou, G.; Tasiopoulos, A. J. *Polyhedron* **2006**, *25*, 1737.
- (235) Basler, R.; Chaboussant, G.; Canada-Vilalta, C.; Christou, G.; Mutka, H.; Janssen, S.; Altorfer, F.; Gudel, H. U. *Polyhedron* **2003**, *22*, 2471.

- (236) Wu, R.; Poyraz, M.; Sowrey, F. E.; Anson, C. E.; Wocadlo, S.; Powell, A. K.; Jayasooriya, U. A.; Cannon, R. D.; Nakamoto, T.; Katada, M.; Sano, H. *Inorg. Chem.* **1998**, *37*, 1913.
- (237) Bhula, R.; Gainsford, G. J.; Weatherburn, D. C. *J. Am. Chem. Soc.* **1988**, *110*, 7550.
- (238) Li, J.; Yang, S. M.; Zhang, F. X.; Tang, Z. X.; Ma, S. L.; Shi, Q. Z.; Wu, Q. J.; Huang, Z. X. *Inorg. Chim. Acta* **1999**, *294*, 109.
- (239) Sreerama, S. G.; Pal, S. *Inorg. Chem.* **2002**, *41*, 4843.
- (240) Nihei, M.; Hoshino, N.; Ito, T.; Oshio, H. *Chem. Lett.* **2002**, 1016.
- (241) Yang, C.-I.; Wernsdorfer, W.; Cheng, K.-H.; Nakano, M.; Lee, G.-H.; Tsai, H.-L. *Inorg. Chem.* **2008**, *47*, 10184.
- (242) Andres, H.; Basler, R.; Blake, A. J.; Cadiou, C.; Chaboussant, G.; Grant, C. M.; Gudel, H.-U.; Murrie, M.; Parsons, S.; Paulsen, C.; Semadini, F.; Villar, V.; Wernsdorfer, W.; Winpenny, R. E. P. *Chem. Eur. J.* **2002**, *8*, 4867.
- (243) Brechin, E. K.; Soler, M.; Christou, G.; Helliwell, M.; Teat, S. J.; Wernsdorfer, W. *Chemical Communications (Cambridge, United Kingdom)* **2003**, 1276.
- (244) Price, D. J.; Batten, S. R.; Moubaraki, B.; Murray, K. S. *Chemical Communications (Cambridge, United Kingdom)* **2002**, 762.
- (245) Fitzgerald, L. J.; Gallucci, J. C.; Gerkin, R. E. *Acta Crystallographica Section B-Structural Science* **1991**, *47*, 776.
- (246) Sun, Z.; Gantzel, P. K.; Hendrickson, D. N. *Inorg. Chem.* **1996**, *35*, 6640.
- (247) Keppert, D. L. *Inorganic Stereochemistry*; Springer—Verlag: Berlin, 1982.
- (248) Brechin, E. K.; Soler, M.; Christou, G.; Davidson, J.; Hendrickson, D. N.; Parsons, S.; Wernsdorfer, W. *Polyhedron* **2003**, *22*, 1771.
- (249) Murugesu, M.; Raftery, J.; Wernsdorfer, W.; Christou, G.; Brechin, E. K. *Inorganic Chemistry* **2004**, *43*, 4203.
- (250) Soler, M.; Rumberger, E.; Folting, K.; Hendrickson, D. N.; Christou, G. *Polyhedron* **2001**, *20*, 1365.
- (251) Moushi, E. E.; Stamatatos, T. C.; Wernsdorfer, W.; Nastopoulos, V.; Christou, G.; Tasiopoulos, A. J. *Angewandte Chemie (International ed. in English)* **2006**, *118*, 7886.
- (252) Shanmugam, M.; Chastanet, G.; Mallah, T.; Sessoli, R.; Teat, S. J.; Timco, G. A.; Winpenny, R. E. P. *Chemistry—a European Journal* **2006**, *12*, 8777.

- (253) Zaleski, C. M.; Depperman, E. C.; Dendrinou-Samara, C.; Alexiou, M.; Kampf, J. W.; Kessissoglou, D. P.; Kirk, M. L.; Pecoraro, V. L. *J. Am. Chem. Soc.* **2005**, *127*, 12862.
- (254) Brechin, E. K.; Clegg, W.; Murrie, M.; Parsons, S.; Teat, S. J.; Winpenny, R. E. P. *J. Am. Chem. Soc.* **1998**, *120*, 7365.
- (255) Goldberg, D. P.; Caneschi, A.; Lippard, S. J. *J. Am. Chem. Soc.* **1993**, *115*, 9299.
- (256) Yamashita, S.; Shiga, T.; Kurashina, M.; Nihei, M.; Nojiri, H.; Sawa, H.; Kakiuchi, T.; Oshio, H. *Inorg. Chem.* **2007**, *46*, 3810.
- (257) Kondo, M.; Shinagawa, R.; Miyazawa, M.; Kabir, M. K.; Irie, Y.; Horiba, T.; Naito, T.; Maeda, K.; Utsuno, S.; Uchida, F. *Dalton Transactions* **2003**, 515.
- (258) Ferguson, A.; Thomson, K.; Parkin, A.; Cooper, P.; Milios, C. J.; Brechin, E. K.; Murrie, M. *Dalton Transactions* **2007**, 728.
- (259) Crawford, V. H.; Richardson, H. W.; Wasson, J. R.; Hodgson, D. J.; Hatfield, W. E. *Inorg. Chem.* **1976**, *15*, 2107.
- (260) Brechin, E. K.; Boskovic, C.; Wernsdorfer, W.; Yoo, J.; Yamaguchi, A.; Sanudo, E. C.; Concolino, T. R.; Rheingold, A. L.; Ishimoto, H.; Hendrickson, D. N.; Christou, G. *J. Am. Chem. Soc.* **2002**, *124*, 9710.
- (261) Murugesu, M.; Takahashi, S.; Wilson, A.; Abboud, K. A.; Wernsdorfer, W.; Hill, S.; Christou, G. *Inorg. Chem.* **2008**, *47*, 9459.

BIOGRAPHICAL SKETCH

Christos Lampropoulos was born in Patras, Greece on May 13, 1981. He performed his high school studies at the General Lyceum in Kamares and graduated with highest honors and GPA 19.8 out of 20. He then travelled to the United States and began his undergraduate studies at Harper Community College in Palatine, IL. After two semesters at Harper, he transferred to the University of Illinois at Chicago (UIC) where he was a biology major for the first year. Since his sophomore year at UIC, he was performing undergraduate research in the group of Prof. John A. Morrison on the synthesis of trifluoromethyl-containing organometallic compounds of platinum, and molybdenum. His interest in synthetic inorganic chemistry made him change his major and he received a bachelor's degree with honors in chemistry. In the fall of 2004, Christos joined the group of Drago Professor George Christou at the Chemistry Department of the University of Florida. He received his Master in Science degree in 2007, and in October of 2008 he got engaged to Evangelia Anninos. Christos was the recipient of the graduate student award in teaching (2007), the graduate student award in Chemical Education awarded by the center of research in the Bio-Nano interface (2008), the Crow Stasch award for excellence in scientific publication (2009), and the Howard Hughes Medical Institute (HHMI) Science for Life graduate student mentor award (2009). Christos received his Ph.D. in May of 2009, and his doctoral research primarily involved the synthesis of polynuclear transition metal, and mixed transition metal-lanthanide clusters, in search for new metal topologies, single-molecule magnets, and novel physical phenomena.